Title

Electrochemical systems for wearable applications

Author

Zamarayeva, Alla

Publication Date

2019

Peer reviewed|Thesis/dissertation

Electrochemical systems for wearable applications

By

Alla Zamarayeva

A dissertation submitted in partial satisfaction of the

requirements for the degree of

Doctor of Philosophy

in

Engineering - Materials Science & Engineering

in the

Graduate Division

of the

University of California, Berkeley

Committee in charge:

Professor Ana Claudia Arias, Co-chair
Professor Andrew Minor, Co-chair
Professor James W. Evans
Professor Kristofer Pister

Fall 2019

Electrochemical systems for wearable applications

Abstract

Electrochemical systems for wearable applications

by

Alla Zamarayeva

Doctor of Philosophy in Engineering – Materials Science and Engineering

University of California, Berkeley

Professor Andrew Minor, Co-chair

Professor Ana Arias, Co-chair

Non-invasive detection of biomarkers in sweat is of great interest for assessing the body's response to physical activity, as well as for clinical diagnostics. Moreover, if fabricated in a form factor of a wearable device, sweat sensors offer advantages of continuous data acquisition, high performance and low cost. Despite significant progress up to date, major developments in fabrication of reliable sensing components still have to be realized in order to implement the vision of using sweat for continuous health monitoring. Commercially viable sweat sensors should demonstrate fast response, sensitivity to physiologically relevant concentrations of analyte, batch to batch reproducibility, stable performance under continuous operation, specificity, i.e. insensitivity to other analytes present in sweat, long-term storage, and ideally, no calibration requirement.

These sensors are designed to be compliant and nearly imperceptible to the wearer. The need to power these devices while retaining their mechanical properties has been driving active innovation in the field of wearable compliant batteries. Unfortunately, incorporating additional functionalities commonly compromises the energy storage capacity of the wearable devices: they usually show lower gravimetric or volumetric capacity than those of commercially available systems. It remains important to maximize the energy density of wearable batteries. Additionally, despite numerous innovative design strategies for the compliant batteries, there are few reports of batteries that exhibit fatigue resistance satisfactory enough for applications in wearable systems which are likely to undergo thousands of deformation cycles throughout their lifetime. Not to mention, the disposal of batteries becomes a concern with increased worldwide use of these devices. At the same time, the bulk of the demonstrations are based on Li-ion ion battery chemistry, which often relies on toxic and/or flammable components. Designing non-toxic systems comprising more abundant and disposable materials is of great importance.

This thesis focuses on addressing some of the existing shortcomings in the development of the wearable electrochemical devices: both electrochemical sensors for sweat monitoring and batteries. We demonstrate several unique design strategies to achieve high-performance flexible and stretchable batteries for wearable applications. For example, we develop an electrode composite with interpenetrated binder network to achieve a flexible battery with energy density matching that of the commercial AA alkaline battery. We also show wire-shaped batteries based on helical band springs that are resilient to fatigue and retain electrochemical performance over 17,000 flexure cycles. Both of these innovations address important limitations of existing flexible battery systems. Moreover, we use intrinsically safe, non-toxic silver-zinc (Ag/Zn) and zinc-manganese dioxide (Zn/MnO_2) battery chemistries, which are highly desirable for wearable applications. For electrochemical sensors, we outline optimization steps to achieve printed flexible sensors for continuous monitoring of the lactate, Na^+ or NH_4^+ ions and show how different optimization parameters affect the sensor performance. Last but not the least, we point out aspects that remain to be studied and/or addressed before such system can be claimed to be commercially viable.

To my family:
Nataliya and Michail Zamarayev

Contents

Acknowledgements

I am grateful to my advisors, Professor Ana Arias and Professor Andrew Minor, for supporting me in pursuing research topics that I found meaningful. Additional thank you to Professor Ana Arias for providing resources for my research and advancing my personal and professional development throughout graduate school. I could not have imagined a better place for my graduate studies.

I thank the Department of Materials Science at UC Berkeley for giving me the chance to pursue my Ph.D, and to the student advisor Ariana Castro for being helpful throughout. I am indebted to Professor Oscar Dubon for motivating me to pursue this doctoral journey. I thank Professor Phillip Messersmith for the rewarding experience of being a teaching assistant in his class.

I acknowledge with gratitude the National Science Foundation and William Floyd Jr. Fellowship for funding.

I would like to thank Professor Jim Evans, Professor Miki Lustig, Professor Vivek Subramanian and Professor Paul Wright for creating collaborative research environment that greatly contributed to the work for this dissertation. I am obliged to Professor Vivek Subramanian, Professor Oscar Dubon for being on my qualifying examination committee and to Professor Kristofer Pister and Professor Jim Evans for being on both qualifying examination and thesis committees. Their insightful suggestions helped me shape the research that constitutes this thesis.

I have had an incredible luck to work alongside, collaborate with and learn from the talented individuals in the Arias' and Minor's groups – Nate Velez, Mahsa Sadeghi, Dr. Yasser Khan, Dr. Balthazar Lechene, Dr. Joe Corea, Karthik Gopalan, Dr. Aminy Ostfeld, Dr. Adrien Pierre, Dr. Claire Lochner, Dr. Donggeon Han, Jonathan Ting, Maruf Ahmed, Dr. Abhinav Gaikwad, Dr. Igal Deckman, Dr. Natasha Yamomoto, Maggie Paine, Dr. Anju Toor, Juan Zhu, Payton Goodrich, Carol Baumbauer. I am especially grateful to Dr. Abhinav Gaikwad and Dr. Igal Deckman who mentored me throughout the Ph.D. program and helped me grow as a researcher. I am thankful to Dr. Natasha Yamomoto and Maggie Paine for being wonderful collaborators on the sweat sensing projects; Dr. Joe Corea and Karthik Gopalan for teaching me how to use tools for building functional hardware, Dr. Aminy Ostfeld, Dr. Balthazar Lechene, Dr. Abhinav Gaikwad, Dr. Igal Deckman for making the work on flexible power sources possible, through sharing ideas, insights on experimental design, providing solar cells, performing experiments.

I would like to acknowledge Professor Daniel Steingart from Columbia University for astute critique of some of my scientific hypothesis. Additionally, I thank his group members Greg Davies, Michael Wang for their help with the mechanical modeling of the flexible battery architectures. I would also like to express my gratitude to Guiomar Hernandez and Nerea Casado Perez from CIC Energigune for including me in their exciting project on all-organic polymer batteries.

I would like to thank Veronika Pister, Akshaya Jegraj, Cheryl Chang, Jerica Duey, Austin Chou, Michael Wang, Kelvin Pang whom I have been fortunate to mentor throughout the Ph.D. Among everything else, they have inspired me to strive to be a better person.

Last but not the least, I am forever indebted to my parents – Nataliya and Michail Zamarayev, my family and friends who supported me on countless occasions.

CHAPTER 1

Introduction

1.1 Introduction

Major developments in the wearable electronics field are being realized in order to implement the vision of personalized, point-of-care health monitoring. Wearable sensors can continuously measure various bio-signals and provide comprehensive feedback. For example, these devices can continuously collect vital signs such as temperature, heart rate, respiration rate, and blood pressure from physical signals of the patient and make this information available to the healthcare provider (*1*, *2*). This approach is invaluable for monitoring chronically ill patients in home settings, as it can timely notify the wearer in case of health emergency. Additionally, continuous monitoring of performance markers has broad applicability in sports and fitness.

In addition to vital signs, non-invasive detection of biomarkers in bodily fluids is of great interest for assessing the body's response to physical activity, as well as for clinical diagnostics. For example, non-invasive monitoring of glucose for diabetes management has potential to improve the quality of life for millions of people. Monitoring drug efficacy is another example that requires continuous analyte measurements. Sweat, saliva and tears are three biofluids that can be continuously sensed for non-invasive real-time monitoring of various analytes. Compared to saliva and tears, sweat has advantages of more straightforward biofluid access, which allows to sample analytes quickly, avoiding degradation or contamination (*3*). Additionally, sensors for sweat monitoring can be worn with more comfort than the sensors placed in the eye or mouth. As a result, development of wearable sensors for non-invasive detection of biomarkers has been directed primarily towards sweat sensing. Up to date, different sensing mechanisms have been used for wearable sweat sensors. Impedance-based sensors have been shown to be effective in monitoring sweat rate (*4*, *5*). Sensors based on colorimetric readouts were coupled with microfluidic sweat supply and removal systems to obtain wearable multimetabolite sweat sensing platforms (*6*, *7*). Optical sweat sensing was also investigated (*8*, *9*). Electrochemical sensors gained the most traction due to their high specificity, low cost and commercially available material systems (*10–12*). Wearable sensors

for monitoring single (*13–21*) and multiple (*4*, *8*, *22–27*) analytes in sweat were developed using electrochemical sensing mechanisms. Some of the demonstrations were adapted to fit large-scale, roll-to-roll manufacturing approaches.

In spite of significant progress up to date, major developments in sweat sensing field have still to be realized in order to implement the vision of using sweat for individualized health monitoring. Algorithms for processing vast amounts of data from multiple sensors need to be developed to build a representative picture of individual's health. Models for biomarker transport mechanisms from blood plasma into the sweat, and from sweat duct to the skin surface have to be developed for each species of interest. In addition to developments around data processing, a significant effort has to be directed towards fabrication of reliable sensing components for multiple sweat analytes. Commercially viable sweat sensors should demonstrate fast response, sensitivity to physiologically relevant concentrations of analyte, batch to batch reproducibility, stable performance under continuous operation, specificity, i.e. insensitivity to other analytes present in sweat, long-term storage, and ideally, no calibration requirement.

These sensors can be worn directly on the body or integrated into clothes or accessories. They should be designed to be compliant and nearly imperceptible to the wearer. The need to power these devices while retaining their mechanical properties has been driving active innovation in the field of wearable compliant batteries. Wearable batteries should be able to withstand bending, folding, and stretching while maintaining safe performance under deformation. The initial demonstrations were flexible batteries based on planar structures, assembled through stacking of the thin film battery components (*28–31*). Flexible electrodes for such batteries were fabricated either by dip coating electroactive materials in a mesh that served as a mechanical support, or by printing thin layer of the electrode slurry on a flexible substrate. Despite apparent simplicity of the planar architecture significant amount of innovation was required to prevent loss of contact between the battery components, leakage of electrolyte, internal short-circuits, cracking and delamination of the battery electrodes during flexing. The planar designs evolved into more advanced form factors that enabled omnidirectional flexibility. Batteries in the shape of a fiber or wire (*32–45*), for example, can be twisted, tied and weaved into fabrics, allowing integration with wearable garments. In addition, the ability of the battery systems to withstand stretching is critical for integration with electronic devices that are likely to undergo compression and stretching throughout their lifetime. Several mechanic-guided engineering approaches to designing stretchable batteries were developed in the last decade and will be reviewed in the following section of this chapter. However, in spite of numerous innovative design strategies for the compliant batteries, there are very few reports of batteries that exhibit fatigue resistance sufficient for applications in wearable systems that are likely to undergo thousands of deformation cycles throughout their lifetime.

Unfortunately, incorporating additional functionalities commonly introduces additional inactive components to the battery structure. This compromises energy storage capacity of the wearable devices that usually show lower gravimetric or volumetric capacity than those of commercially available systems. In case of wearable applications, aesthetic features and compliant characteristics might be of higher priority than the cost or the energy density of the battery. Nevertheless, the energy storage capability should not be substantially compromised when

additional functionality is added. It remains important to maximize energy density, since the dimensions of the battery are often limited with the size of the device being powered. An optimum system would match the commercial product in terms of energy density and at the same time have a flexible form factor. And finally, with increased worldwide use of these devices, disposal of the batteries becomes a concern. At the same time, the bulk of the demonstrations are based on Li-ion ion battery chemistry, which often relies on toxic and/or flammable components. More attention could be devoted to non-toxic systems comprising more abundant, disposable materials.

This thesis focuses on addressing some of the existing shortcomings in the development of the wearable electrochemical devices: electrochemical sensors for sweat monitoring, as well as batteries. We demonstrate several unique design strategies to achieve high-performance flexible and stretchable batteries for wearable applications. For example, we develop an electrode composite with interpenetrated binder network to achieve flexible battery with energy density matching that of the commercial AA Duracell. We also show wire-shaped batteries based on helical band springs that are resilient to fatigue and retain electrochemical performance over 17,000 flexure cycles. Both of these innovations address important limitations of existing flexible battery systems. Moreover, we use intrinsically safe, non-toxic silver-zinc (Ag/Zn) and zinc-manganese dioxide (Zn/MnO_2) battery chemistries, which are highly desirable for wearable applications. For electrochemical sensors, we outline optimization steps to achieve printed flexible sensors for continuous monitoring of the lactate, Na^+ or NH_4^+ ions. Tracking the change in the concentration of these species during the exercise can provide important information for optimizing individual's sport/fitness routine, as well as for prevention of complications that could be dangerous to the overall health. We show how different optimization parameters affect the sensor performance. Importantly, we point out aspects that remain to be studied and/or addressed before such system can be claimed to be commercially viable.

The fundamentals of operation specific to each system described in this work are incorporated in the corresponding chapters. In this chapter we will give a background information on the flexible batteries and electrochemical sensors, review the existing design strategies to achieve wearable batteries and electrochemical sensors. We will conclude with the outline of the thesis.

1.2 Background

Electrochemical sensors

A chemical sensor is a device that selectively utilizes chemical composition of a sample to produce a signal suitable for analytical analyses. Electrochemical sensors directly transform chemical information into an electrical signal. Such direct conversion makes this technique precise, sensitive, simple and low cost, which in turn allows miniaturization of these systems. An electrochemical sensor consists of two main components – receptor and transducer. The receptor interacts with the target analyte in the sample to produce an electrochemical signal that is related to the concentration of analyte of interest. The transducer converts the signal into a detectable

value. The receptor should possess high selectivity towards the specific analyte in the sample to avoid false positive results. In electrochemical sweat sensor devices, the receptor often consists of biologically derived species like enzymes and proteins therefore these devices belong to the category of biosensors. Depending on the type of signal transduction the sweat sensors can be classified as potentiometric, voltammetric and conductimetric.

The electrochemical cell is designed differently depending on the type of sensor. The conductimetric sensors do not rely on electrochemical interaction of species but rather detect changes in conductivity of specific ions. Therefore, they are more appropriately considered to be electrical sensors instead of electrochemical and will not be addressed here. The potentiometric and amperometric (a subclass of voltammetric) sensors have been most intensely studied and used and therefore will be a focus of further discussion.

The analytical information in potentiometric sensors is obtained through the potential signal. The electrochemical setup for this type of sensor consists of two electrodes. The potential is generated by the difference in charge concentration between two electrodes – the working electrode, functionalized with certain indicator material, and the reference electrode comprised of a material composite that retains stable potential regardless of the composition of the sample. Potentiometric measurements do not require any current application. Ideally, the relationship between potential signal and the concentration of target species obeys the Nernst equation and is logarithmically proportional. The working electrode should be designed to have fast and reversible response to the change in concentration of target species.

Amperometric sensors utilize a three-electrode setup with working, reference and counter electrodes. The active material of the working electrode is usually enzyme that promotes electrochemical reaction - oxidation of analyte species from the sample with the generation of electrons. The amount of generated current is related to the concentration of analyte in the sample. The reference electrode is composed of material composite with stable potential, like silver/silver chloride, and the counter electrode is usually a chemically stable conductor material. The electrochemical reaction between enzyme and analyte occurs at a certain value of potential. Therefore, a constant voltage of the appropriate magnitude is applied between working and reference electrodes and the resulting current is measured between working and counter electrodes. The voltage value is set to the lowest value that would facilitate chemical reaction between analyte in the sample and active material of the working electrode to avoid occurrence of undesired side reactions that could compromise the precision of the measurements.

The “Golden Age” of electrochemical sensor technology falls in 1960-1970s owing to the rise of polymer science. During this time period sensor devices drastically changed their form factor, transforming from glass electrodes with the enclosed sensing solution to self-supported solid polymeric films. This started the stage of so-called solid contact sensor electrodes. These sensors are designed to effectively entrap the sensing substance within the polymeric matrix. Utilizing polymeric films instead of liquid media allowed utilizing low cost mass production technologies such as screen printing to fabricate electrochemical sensors on a large scale.

During this time Adams invented the paste-like material that consisted of carbon powder combined with the polymeric binder (*46–48*). It had good conduction properties, was electrochemically inert and had a large surface area that increased the rate of electrochemical reactions. It replaced the metal conductors in electrochemical sensor devices and gained a broad popularity in the field of analytical chemistry and beyond (*48*). Since then, various carbon materials (e.g., glassy carbon fibers, graphene, carbon nanotubes) and binder combinations were explored to construct carbon electrodes (*49–53*). In addition to previously mentioned advantages, carbon paste could be easily deposited on a variety of substrates via large scale roll to roll and screen-printing technologies, which had profound impact on fabrication of electrochemical sensor strips for mass consumption. The plastic flat electrochemical sensing devices were optimized by Eastman Kodak's Ektachem project in the early 1970s and by the late 1970s the variety of commercial products such as dip-style micropotentiomentric sensors found their way to the market (*54*). To date the majority of commercially available electrochemical sensors, including glucose sensors, utilize printed carbon paste as working electrode (*55*, *56*).

The broad diversity of polymeric materials stimulated development of material composites to advance the solid-state electrode technology not only from the perspective of more practical solid film device configuration but also from the standpoint of improved performance characteristics. To date it represents a very active research area with great potential. The technology was advanced further to achieve trace-level detection limits (*57–59*), and combine advanced ion sensors with solid state reference electrodes to fabricate miniature devices (*60–65*). Developments in the fields of plasticizer-free membranes (*66–73*) and covalently bound ionophores (*74–77*) further enhanced the performance characteristics of solid state sensors, such as durability and lower detection limit. Novel membrane materials such as anion-sensitive epoxy resins (*78*), ionophores (*79*) and liquid crystal dispersed in a polymer matrix have been demonstrated. In addition, discovery of polymers with novel properties, like conducting polymers that won Heeger, Macdiarmid and Shirakawa the Nobel Prize in Chemistry in 2000 resulted in extensive development of efficient electron to ion transducers for electrochemical sensors (*80–85*). These developments led to enhanced stability, sensitivity, immobilization characteristics of the sensing component due to elimination of the blocked interface between conductor and polymeric sensing component of the working electrode (*83*, *86*).

Advancements in the scientific understanding and instrumentation allowed for controlled synthesis of materials with nanoscale features. Incorporating nanomaterials and their composites into electrochemical sensing technology enabled devices with improved stability, detection limits and biocompatibility (*87*, *88*). For example, the analytical response can be significantly enhanced by incorporating gold nanoparticles into the electrode matrix (*19*). Another critical advancement in the electrochemical sensing technology was the introduction of carbon nanotubes by Iijima in 1991 (*89*). Since the first report there has been a number of original papers pertaining to their application in electrochemical sensing due to their electrocatalytic properties (*90*, *91*) and ability to immobilize enzymes (*92*, *93*).

The present day sweat sensor development is focused on utilizing nanomaterial composites to further miniaturize these devices while achieving improved performance characteristics. This would lead to reduced manufacturing costs and improved portability. The intensive area of device

engineering research is related to fabricating wearable sensors on flexible substrates that can conform to the body movements without disrupting comfort of the wearer. Another challenge yet to be resolved is how to efficiently incorporate flexible circuitry and flexible energy sources with the sensing components. Development of such multicomponent systems is crucial to enable autonomous operation of wearable sweat sensing devices.

Batteries for wearables

The key components of a battery are the anode, cathode, separator, current collectors and electrolyte. The anode is the negative pole of a battery and typically consists of a strong reducing agent such as lithium or zinc. The cathode is the positive pole comprising an oxidizing agent such as lithium cobalt oxide, manganese oxide, and silver oxide. Two current collectors facilitate electron transport to and from the battery electrodes. The separator is typically an ionically conductive but electronically insulating microporous polymer membrane. The assembly is soaked in the electrolyte that facilitates electrochemical reaction and maintains charge neutrality. The potential difference between electrodes drives the electrons from the anode to cathode generating a current that can be used to power an external load.

The choice of electroactive materials determines potential (V), capacity (mAh/g) and, consequently, theoretical energy density (Wh/kg) of the battery. Since commercialization by Sony in 1991, Lithium (Li)-ion batteries have been the most broadly used energy storage source due to their high energy density and well-engineered stability. However, anticipated increase in the number of battery-powered wearable and portable devices raises concerns about the limited availability of the Li-ion battery materials, as well as end-of-life battery disposal. Moreover, the organic electrolytes used in Li-ion batteries are generally toxic and flammable. Although a number of preventive approaches, such as utilization of chemical additives for stable electrode/electrolyte interfaces (*94*, *95*), solid-state batteries based on inorganic electrolytes (*96*, *97*), and incorporating flame-retardant additives (*98*), batteries with intrinsically safe aqueous electrolytes are highly preferred for wearable applications. Moreover, Li-ion batteries require high barrier multilayer encapsulation, limiting the compliance of the final system.

Batteries based on Zn appeared as an attractive alternative to Li-ion batteries due to higher safety and environmentally friendly characteristics. Zn anodes were widely explored in many flexible battery systems, such as alkaline Zn–MnO_2 batteries (*29*, *99*), zinc–nickel batteries (*100*, *101*), and zinc–silver batteries (*102*, *103*). Zn – air is one of the most explored options among flexible batteries based on Zn, mainly due to its high theoretical energy density (*104*, *105*). Innovations in materials' design were used to enhance electrochemical and mechanical performance of these batteries. To date, growing catalyst nanomaterials onto the carbon cloths (*106–109*), carbon fiber films (*110*, *111*), nanowire arrays (*112*), graphene materials (*113*, *114*), carbon nanotube structures (*115–117*) have been demonstrated. These approaches enable freestanding flexible electrodes and also ensure high accessibility of the catalytic sites and a low contact resistance. However, such materials are expensive to manufacture. Among mainstream battery chemistries with low-cost and well-established material production routes, zinc-manganese dioxide (Zn/MnO_2) is well-suited to power wearable electronics (*104*).

The commercial battery manufacturing process starts with preparing the battery slurry. The slurries consist of a mixture of electrochemically active particles, conductive additives, and polymeric binder. Conductive additives are incorporated to improve the conductivity and typically comprise the mixture of graphite and carbon black. Binder is added to maintain integrity of the electrode. It typically consists of polymers such as polyvinylidene difluoride, polytertrafluoroethylene, styrene butadiene rubbers and carboxymethylcellulose. The components of the slurry are dispersed in a solvent and mixed. Additives or thickening agents might also be added. Slurries of the predetermined thickness are cast onto one or both sides of the current collectors that serve as a support for the electrodes. The current collectors typically consist of the metal foils that are chemically compatible with the active components. The resulting electrodes are dried and compressed (calendared) to achieve desired electrode porosity and to improve particle-to-particle contact. Next, the electrodes and the separator are cut corresponding to the dimensions of the final product, stacked, and inserted into packaging and filled with electrolyte, which is typically in a liquid form. Various configurations of the electrolyte have been developed: gel, polymer and solid-state electrolytes that can serve the dual function of both separator and ion conductor. The practical energy density of the fully assembled battery comprises <50% of its theoretical value due to contribution of the inactive components to the weight and volume of the batteries (*118*). The commercial cells are optimized to have high volumetric energy density and do not meet esthetic and mechanical (flexibility/stretchability) requirements of wearable systems. The approaches described in the following sections enable battery flexibility/stretchability and seamless integration into wearables without disrupting esthetics of the garments. However, these additional features usually come at a cost of the energy density of the device, which is usually lower than that of commercially available systems, based on the same chemistry.

1.3 Design strategies for wearable electrochemical systems

The two key strategies for achieving compliance of the electrochemical systems are through either synthesizing intrinsically compliant materials (including active materials) or through innovating device/electrode composite design improvements, while using commercially available materials. This thesis focuses solely on device/electrode composite innovation and, therefore, design of the compliant materials is not reviewed. Device/electrode composite design strategies can be broken into three key categories: structural designs, fiber-based designs and electrode composite designs **(Fig. 1.1)**, although some devices rely on the combination of these approaches. Each category is reviewed below, supported with the representative examples.

Structural designs

High-performance electrochemical systems commonly rely on hard and brittle components from inorganic materials. For example, metal current collectors and electrodes for batteries, or transducer electrodes for electrochemical sensors typically withstand elastic strains of not more than 1% before plastic deformation and eventual failure. The following structural device designs

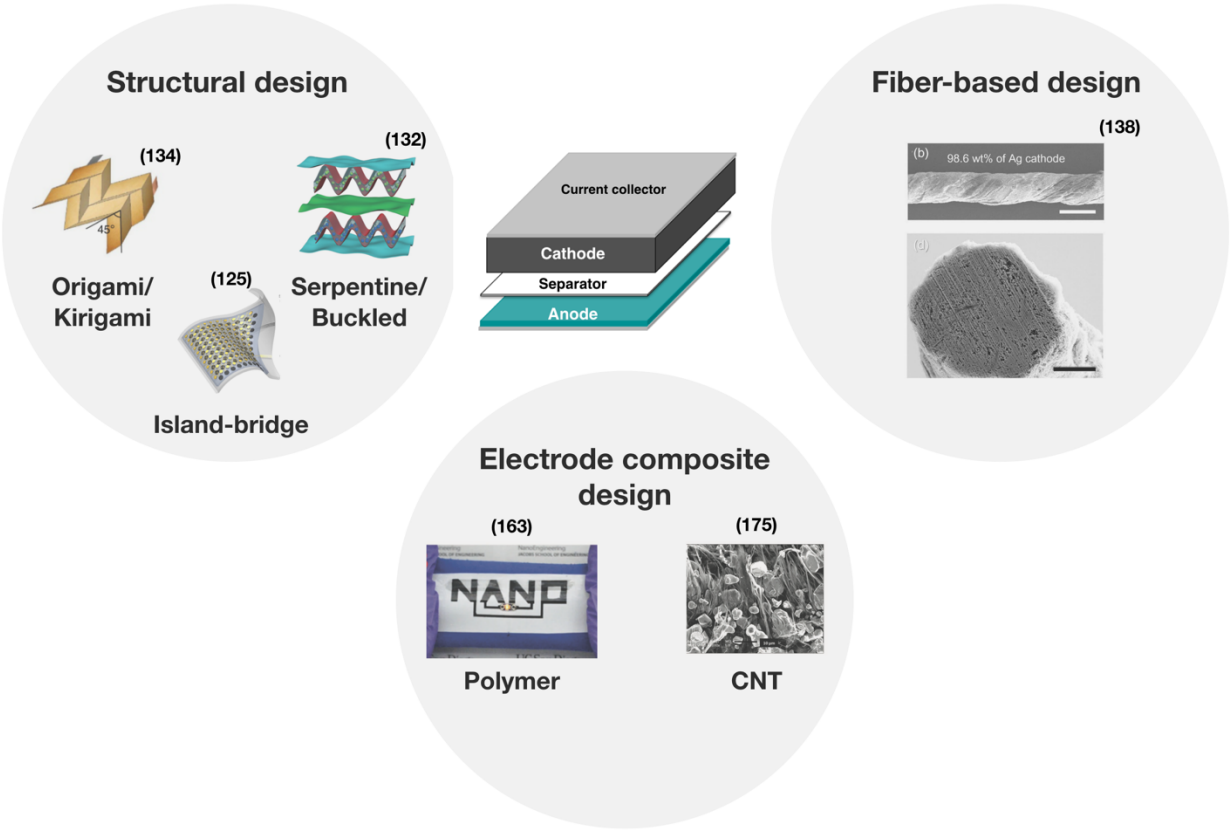

Figure 1.1 Categories for device/electrode composite design strategies: structural designs, fiber-based designs and electrode composite designs.

were developed to accommodate the applied deformation on the device level, leaving the constituent materials minimally strained.

Island-bridge structure

Island-bridge configurations comprise rigid island materials connected with highly deformable interconnects (bridges). The bridges are designed to withstand significant deformations without effecting the integrity of the constituent material. Bridges in the shape of serpentine ribbons were extensively studied for applications in compliant electronics (*119–124*). When the serpentine ribbon is deformed, it can rotate and buckle to accommodate the applied strain, minimizing intrinsic strain in the materials. Rogers et al. have demonstrated stretchable Li-ion batteries by using an island-bridge architecture with self-similar serpentine interconnects (*125*). The rigid electrode discs were connected in parallel with photolithographically patterned serpentine-shaped interconnects **(Figure 1.2a)**. The batteries maintained areal capacity of 1.1 mAh cm^{-2} for up to 20 charge/discharge cycles (Fig. 1.2b) and maintained stable power output under up to 300% biaxial strain. Qu et al. used a similar approach to fabricate Zn-air batteries with stretchability up to 100% (*126*). Yin et al. developed a methodology for screen-printed serpentine interconnects and combined them with coin cells as island regions into the stretchable battery pack (*127*). The screen

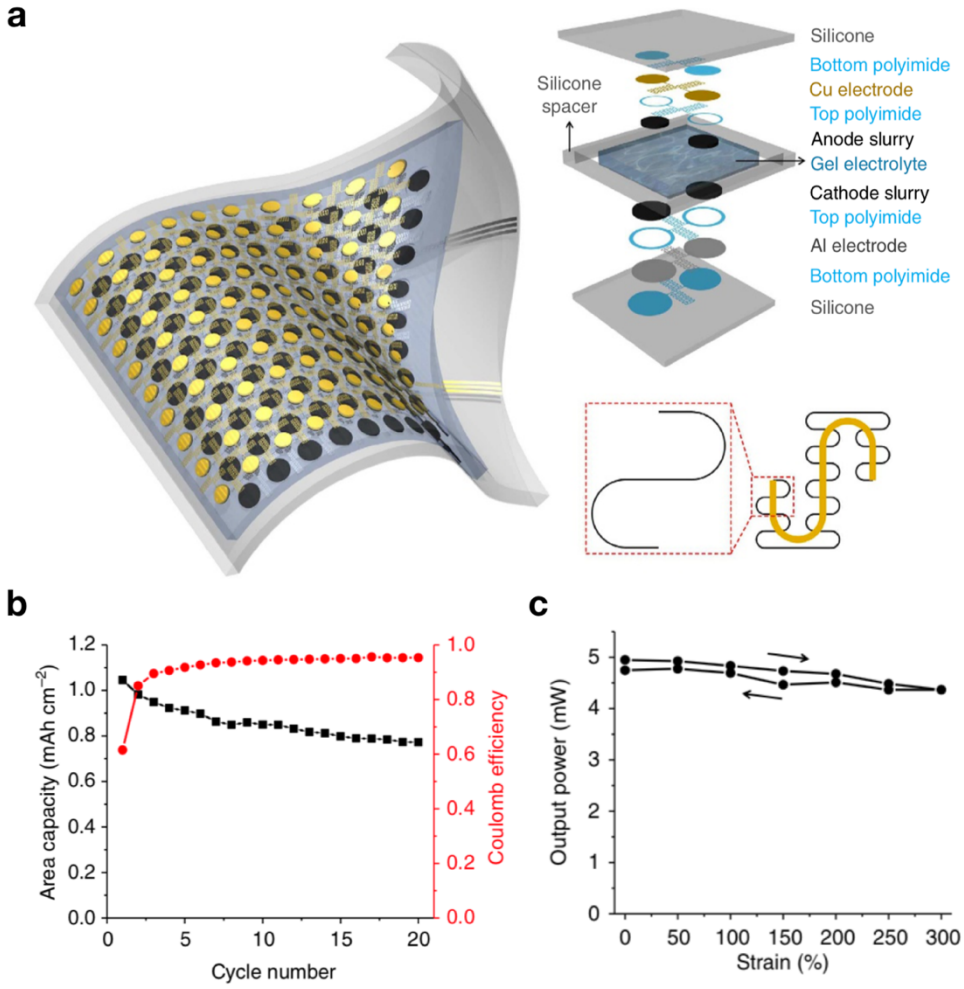

Figure 1.2: (a) Illustration of the fully assembled flexible battery fabricated via island-bridge approach and various layers in the battery structure. (b) Capacity retention (black) and coulombic efficiency (red) over 20 cycles. (c) Output power as a function of applied biaxial strain. Reproduced from (*125*) with permission of Nature Publishing Group.

printing route is an attractive solution for low-cost mass manufacturing. Similar to batteries, wearable electrochemical sensors had been achieved through island-bridge design. Lee et al. used serpentine gold traces and graphene islands to fabricate a stretchable electrochemical device with thermoresponsive microneedles for diabetes monitoring and therapy (*128*).

Buckled/Serpentine structure

Serpentine ribbon architecture can be utilized not only to achieve stretchability of the interconnects used in the island-bridge architectures discussed above, but also to attain deformability of the entire

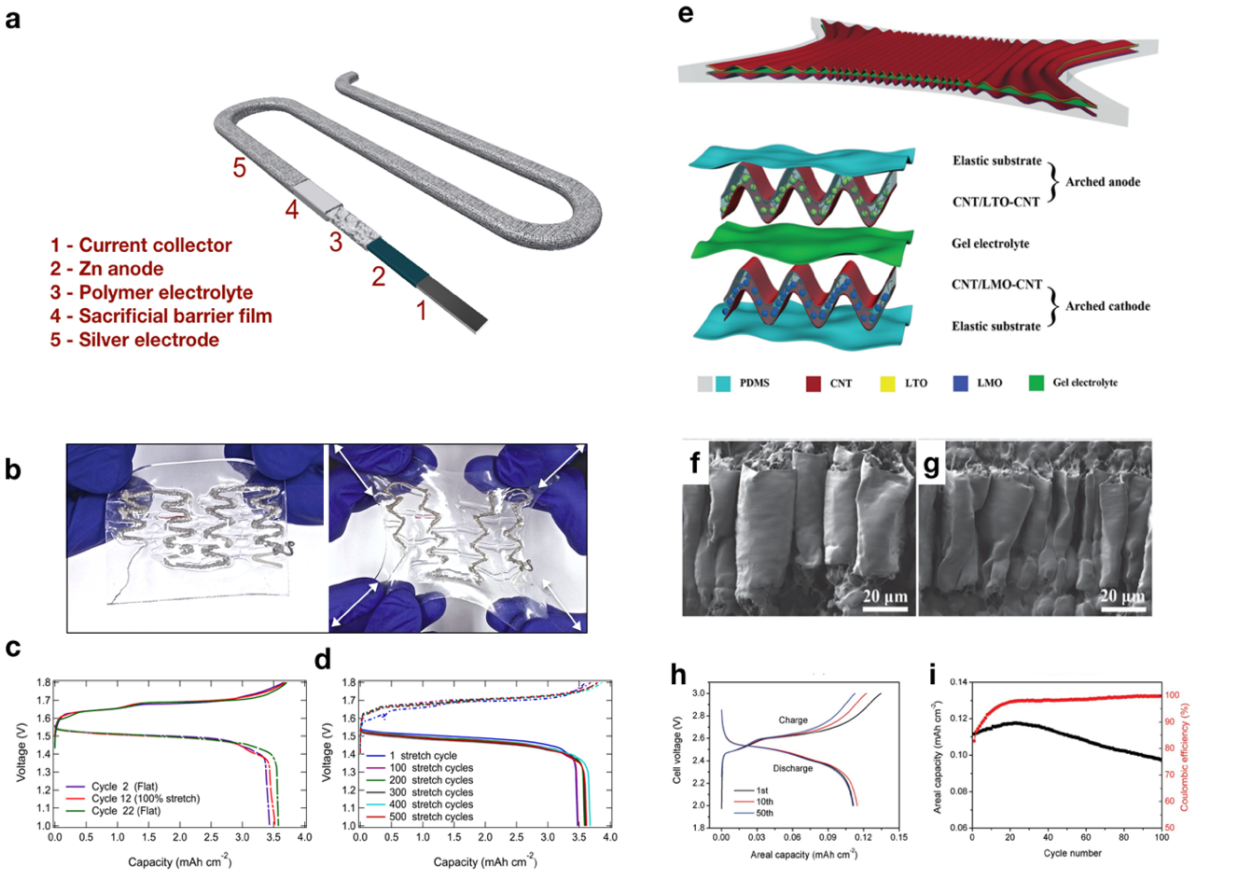

Figure 1.3: (a) The assembly flow diagram for the stretchable serpentine-shaped batteries fabricated using the current collector of serpentine ribbon geometry. (b) Images of the full battery assembled around self-similar serpentine current collector. Geometry of the battery facilitates biaxial stretching. (c) The galvanostatic charge-discharge curves for the 2nd (relaxed configuration), 12th (stretched configuration) and 22nd (relaxed configuration) electrochemical cycles of the battery. (d) Galvanostatic charge-discharge curves for the electrochemical cycles following 1st, 100th, 200th, 300th, 400th, 500th stretch cycles of the battery (*128*). (e) Schematic illustration of the battery with arched stretchable electrodes and its multilayered structure. SEM of the arched electrode structure before (f) and after (g) 1000 stretching cycles at a strain of 400%. Galvanostatic charge/discharge curves (h) and cycling performance (i) of the battery after 200 stretching cycles. Reproduced from (*132*) with permission from John Wiley and Sons.

battery structure. We have shown the serpentine-shaped zinc-silver oxide batteries that can be stretched with tunable degree and directionality while maintaining their specific capacity (*129*). Our approach utilizes serpentine current collectors as a structural support and backbone for all battery components **(Figure 1.3a)**. Figure 1.3b shows photographs of a battery assembled around self-similar serpentine current collector. Serpentine geometry of the battery facilitates biaxial stretching (Figure 1.3c). Figure 1.3d and e shows the galvanostatic charge-discharge curves for the 2nd (relaxed), 12th (stretched to 100%) and 22nd (relaxed) electrochemical cycles of the battery; and

galvanostatic charge-discharge curves for the electrochemical cycles following 1st, 100th, 200th, 300th, 400th, 500th stretch cycles of the battery. The internal resistance drop is not observed from the plateaus of the charge-discharge curves after the battery is stretched, indicating that active materials are not delaminating from the current collectors. Overall the battery exhibits stable performance in both flat and 100% stretched configurations with minor fluctuations in the capacity in both cases. The details on the battery optimization are discussed in Chapter 3 of this thesis.

Structures similar to serpentine ones inspired development of deformable battery designs with out-of-plane waviness in the undeformed state. When the structure is stretched the waves flatten in the plane resulting in the small strain experienced by the structure. Metal conductors (*119*), carbon nanotubes (*130*) and graphene have been assembled into stretchable wavy

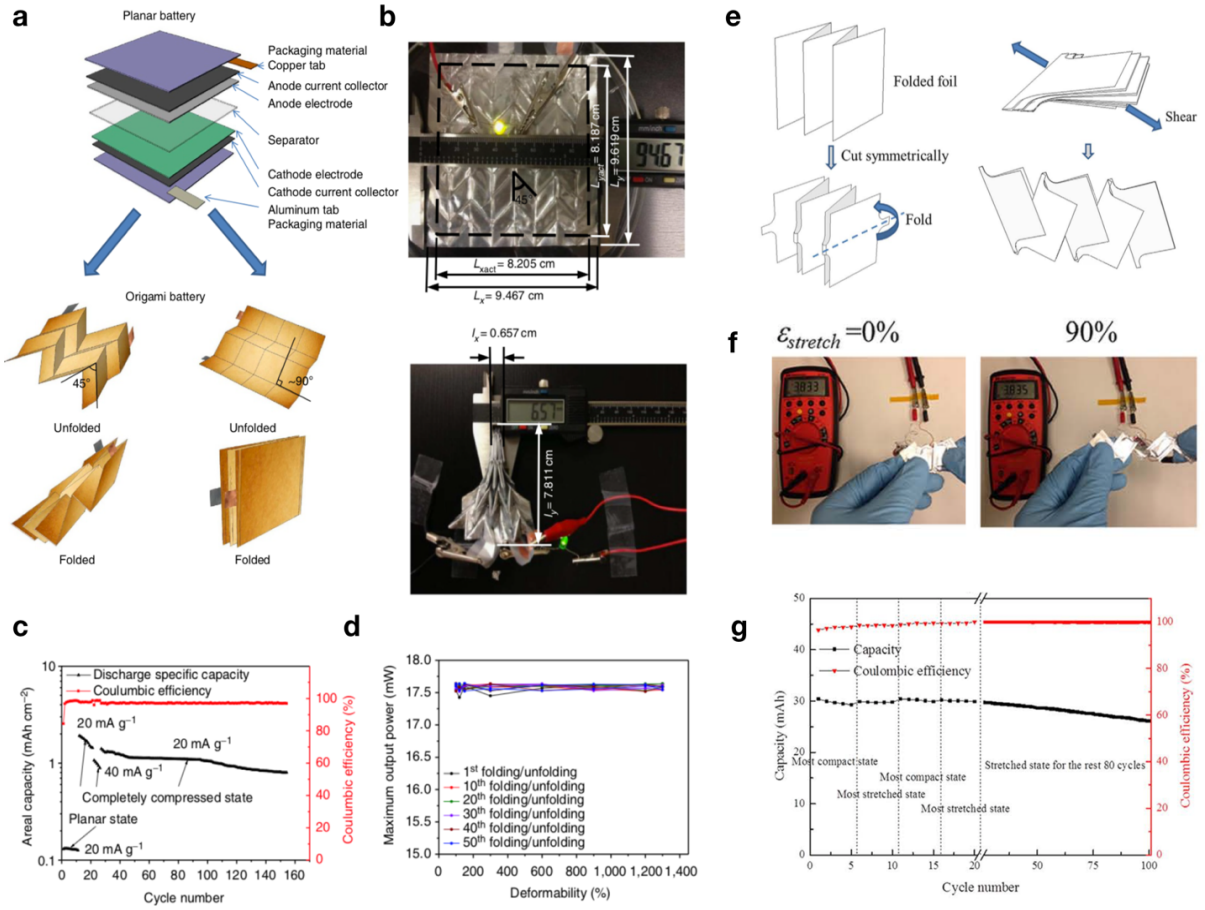

Figure 1.4: (a) multilayer structure of conventional battery in the planar state and schematic of the origami folding. (b) Photograph of the origami battery in the unfolded and the folded states (c) Capacity retention and coulombic efficiency as a function of the cycle number. (d) Power output of the origami battery as a function of linear deformability. Reproduced from (*134*) with permission of Nature Publishing Group. (e) Illustration of the fabrication process of the kirigami pattern. (f) Photograph of stretching a kirigami battery (g) Cyclic stability of the kirigami battery at compact and stretched states. Reproduced from (*135*).

conductors (*131*). Building on these works, Weng et al. developed a Li-ion battery with arched electrodes that can withstand a 400% strain (*132*). Figure 1.3e shows components of the stretchable battery: arched anode and cathode, formed by sandwiching electroactive material in-between two arched CNT sheets; gel electrolyte; elastic polymer packaging. SEM of the arched electrode structure before and after 1000 stretching cycles at a strain of 400%, can be seen in Figure 1.3f and g respectively. The structure preserves morphology after stretching. Galvanostatic charge/discharge curves and cycling performance of the battery after 200 stretching cycles are shown in Figure 1.3h and i respectively. The battery retained 87% of its capacity after 100 charge/discharge cycles, attesting to the stable cycling performance of the device after mechanical deformation. Therefore, various design strategies based on the properties of serpentine ribbons can be applied to enable compliance of the electrochemical systems. Investigating the fatigue resistance of the batteries more extensively would make a stronger case for these methodologies. Researchers commonly evaluate battery performance after several hundred deformation cycles, with arbitrary speed and extent of the deformation. At the same time, a wearable battery is likely to experience tens of thousands of deformations throughout its lifetime. The diversity of battery designs hindered the establishment of standard mechanical testing procedures, making it difficult to adequately evaluate and compare mechanical performance of different battery systems. Absence of a commercially available automated testing apparatus might be also contributing to the lack of more rigorous characterization, as some of the systems have to be repeatedly deformed manually. In addition, custom apparatus would have to be built in house for each specific project due to the vast diversity in the battery dimensions and architectures. It is necessary to demonstrate flexible and stretchable batteries with mechanical endurance that is on par with commercial requirements (withstanding >10000 deformation cycles with the extent and speed of the deformation defined by the target application).

Kirigami/Origami designs

Several methods for achieving deformability of electronics were based on the kirigami and origami techniques. For example, the potential of kirigami and origami to assemble complex deformable 3D electronic structures was demonstrated by Zhang et al. (*133*). Song et al. applied the kirigami and origami principles to achieve stretchability of Li-ion batteries (*134*, *135*). The process for fabrication of kirigami and origami batteries started with fabricating a planar battery consisting of current collectors, anode and cathode, separator and packaging. Then the planar battery was folded into geometrical shapes (faces) that are connected by predefined creases. The folding and unfolding imposes strain at the creases but does not strain the faces, thus allowing to achieve structure deformability while keeping faces undeformed. **Figure 1.4** illustrates the origami (a) and kirigami (e) patterns. To create origami structure, the planar battery was folded into parallelograms (Fig. 1.4a). When the two parallel sides of the resulting structure are pulled together, the battery is folded. Figure 1.4b depicts photograph of the origami battery in the unfolded and the folded states, demonstrating up to 1,340% linear deformability from the completely compressed state to the planar state. Figure 1.4c shows the areal capacity for the planar and completely compressed states. At a current rate of 20 mA g^{-1}, the areal capacity was about 0.2 mAh cm^{-2} for when the origami battery was in its planar unfolded state and increased to 1.4–2.0 mAh cm^{-2} when the origami battery was completely compressed. The battery was cycled for up to 160 cycles. Figure 1.4d shows the power output of the origami battery as a function of linear deformability. The output

power was stable over 50 linear deformation cycles up to a linear deformability of 1,340%. Kirigami comprises combination of cutting and folding. Figure 1.4e illustrates the folding and cutting sequence to fabricate a kirigami lithium ion battery. When two ends of the final structure are stretched, rotation occurs at the cuts to accommodate stretching. Stretching the battery does not affect the output voltage of the battery, as seen from the photograph of stretching a kirigami battery that is connected to a voltmeter in Figure 1.4f. Figure 1.4g shows cyclic stability of the

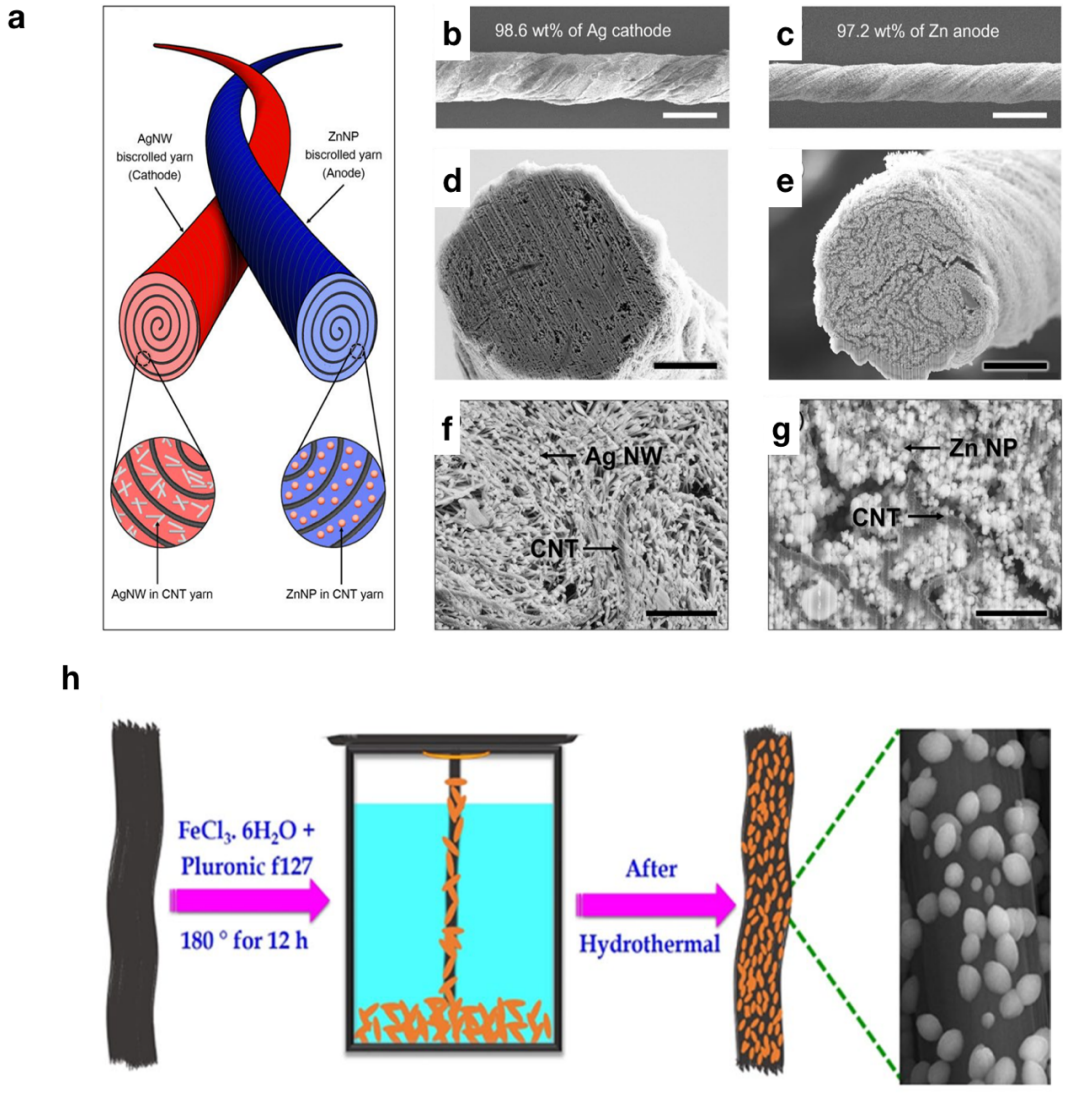

Figure 1.5: (a) Schematic of the yarn-based aqueous silver-zinc battery fabricated by embedding active materials into inner structure of CNT yarn. SEM images for surface of the biscrolled (b) Ag nanowires/CNT cathode yarn and (c) Zn nanoparticles/CNY anode yarn. SEM micrographs of the cross-sectional area of the (d) Ag/CNT and (e) Zn/CNT yarns. Magnified SEM images of the (f) Ag nanowires embedded in CNT and (g) Zn nanoparticles embedded in CNT. Reproduced from (*138*) (h) Schematic of the preparation of the conductive carbon fiber functionalized with Fe_2O_3 to construct a flexible biosensing platform. Reproduced from (*157*).

battery at compact and stretched states. Battery shows good stability with over 85% capacity retention after 100 cycles.

Thus, kirigami and origami techniques can be used to achieve significant levels of deformability, without exposing most of the battery to stress. However, creases experience extensive stress during the stretching cycles. Therefore, reliable performance of the kirigami and origami batteries is determined by the endurance of the material comprising creases. In the above works, authors implemented CNT-coated paper conductor as a fatigue resistant current collector. However, more rigorous optimization and mechanical testing of the crease materials should be done in the future.

Fiber - based designs

Developing fiber-based wearable electrochemical systems are of high interest, due to ease of integrating/weaving them into a cloth (*40*, *131*, *136*, *137*). Additionally, fiber-based assemblies are excellent in maintaining integrity under mechanical deformation, like bending, stretching, twisting. Fiber bundles minimize strain, and thus extend fatigue life of the fibers. They are also less susceptible to catastrophic rupture than solid films. Flexible fiber electrodes for electrochemical devices are mainly fabricated by either embedding active materials within a compliant conductive fiber, or by growing them onto its surface. Most demonstrations use carbon-based fibers (*34*, *37*, *138–153*) due to desired features of carbon for fabricating electrochemical electrodes, such as high surface area, chemical inertness and high conductivity. Although conductivity is highly variable depending on the manufacturing approach and can vary from <10 to >5000 S cm^{-1} for CNT fibers (*154*). Light weight and adoptability to low-cost high-volume manufacturing contribute additional value to this class of materials. A range of techniques have been used to create carbon scaffolds with incorporated electroactive materials, for example electrochemical or chemical deposition on carbon fibers, dip-coating fibers in the electroactive material, scrolling carbon composites with electroactive materials into yarns.

The representative example of the fiber-based battery has been shown by Lee et al. (*138*). The authors fabricated a yarn-based aqueous silver-zinc battery by embedding active materials into inner structure of CNT yarn **(Figure 1.5a)**. Such approach can ensure high mass loading of active materials without compromising the mechanical performance of the composite electrodes. The biscrolling method (*155*) was used to achieve 99 $_{wt}$% loading of silver and zinc in yarn electrodes. Figure 1.5b,c shows SEM images for surface of the biscrolled Ag nanowires cathode yarn and Zn nanoparticles anode yarn respectively. SEM micrographs of the cross-sectional area of the Ag/CNT and Zn/CNT yarn shows a porous structure (Figure 1.5d,e) desirable to ensure permeability of the battery electrodes with electrolyte. The active metal nanoparticles are in a close contact with adjacent CNT bundles, forming efficient constructing network (Fig. 1.5f,g). The battery has high linear capacity of 0.285 mAh cm^{-1} – adequate for the energy source of wearable electronics.

The fiber-based approach is less typical for electrochemical sensors than for batteries. The sensing components has to be in the immediate contact with the skin, which might be challenging to achieve with fibrous structure. Additionally, it could be difficult to control sweat supply and

removal rate at the fiber electrode surface, due to absorptive nature of the fibers. Fabricating sensors on textiles also introduces requirement for prolonged stable performance, in contrast, sensor printed on the low-cost plastic can be disposed after single use. Nevertheless, several examples of fiber-based electrode architectures were successfully implemented for electrochemical sensing (*143*, *145*, *156–162*). Recently, Sekar et al. used a conductive carbon fiber functionalized with Fe_2O_3 to construct a flexible biosensing platform for monitoring biomarkers in sweat and used cortisol as a model analyte (*157*). Fe_2O_3 was coated on the conductive carbon fiber using hydrothermal method (Figure 1.5h), and served as the mediator for the electrochemical detection of cortisol. Monoclonal cortisol antibodies served as a detection mechanism and were immobilized via electrostatic interaction. The sensor exhibited a good linearity ($r^2 = 0.998$) for a linear range from 1 fg to 1 μg with a detection limit of 0.005 fg mL^{-1}. Sensor was also used to measure cortisol levels in human sweat and the results were confirmed with the commercial chemiluminescence immunoassay method.

Therefore, fiber-based electrochemical systems are anticipated to find a broad range of applications for fabrication of wearable batteries. To enable incorporation into the cloth, it is important that such systems are fabricated from safe materials, as they would be in close proximity to the skin. Additionally, encapsulation techniques that preserve advantages of the fiber architecture, such as chemically resistive elastomeric coatings impermeable to moisture and air need to be developed.

Electrode composite designs

In addition to achieving compliance via structural and fiber-based designs, electrochemical electrodes can be designed to be intrinsically compliant. Numerous composite electrode materials have been developed for applications in both batteries and electrochemical sensors. They commonly consist of an active component, nanostructured rigid filler with good conductivity and a polymer that ensures electrode flexibility/stretchability. In case of electrochemical sensors polymers often perform additional function of immobilizing enzymes or ionophore reagents. High aspect ratio conductive materials such as CNTs or carbon fibers, have been commonly used as conducting fillers. They can slide along each other and maintain percolation network under strain (*144*). Importantly, the compliant electrode formulations described above are compatible with scalable, well established, low-cost printing techniques, enabling mass production of these devices.

Kumar et al. demonstrated all-printed stretchable zinc- silver oxide battery through design of the electrode formulation (*163*). **Figure 1.6** shows battery in relaxed (a) and twisted (b) configurations. The novelty of the work was in using polystyrene-*block*-polyisoprene-*block*-polystyrene (SIS) elastomer as the binder for the battery electrodes. SIS can achieve ~1300% elongation and is simple to process, compared to other elastomers such as exoflex, that require an additional curing step. Through optimizing the composition of the electrode, the authors were able to achieve a battery design that maintained a high areal capacity of 2.5 mAh cm^{-2} after multiple stretching cycles to 100% (Figure 1.6c). Simple, low-cost manufacturing route adds further value to this approach. From our experience, using elastomers as a binder for batteries with aqueous electrolyte, like zinc-silver oxide, leads to incomplete utilization of the active material. The elastomer blocks the surface of the active particles, preventing electrolyte from reaching the them,

thus precluding their participation in the electrochemical reaction. Therefore, the percent utilization of the active materials has to be calculated and factored in, when evaluating the overall economics of the process. Particularly, when expensive materials, such as silver oxide, are used.

Wearable electrochemical sensors commonly have planar architecture with intrinsically compliant electrodes printed from solution. Planar architecture ensures chemical sensing directly on the skin, which is challenging to achieve with fiber-based sensors described in the previous section. The printable inks for the flexible counter and reference electrodes are widely available commercially. The working electrode optimization constitutes majority of the research efforts. Recently inks for printing working electrode components appeared on the market and were used in several demonstrations. For example, Lin et al. used commercially available Prussian blue ink to print the mediating layer for the wearable glucose sensor (*17*). The group of J. Wang produced a significant body of the work in the field of flexible printed electrochemical sensors. Among other innovations they pioneered the concept of temporary-transfer tattoo electrochemical biosensors (*13*, *14*, *16*, *18*). Figure 1.6d-f shows a representative example of the printed flexible tattoo sensor for monitoring lactate in sweat (*13*). To fabricate the sensor silver/silver chloride- and carbon-inks were screen-printed onto the temporary tattoo paper to form the reference and transducer electrodes (Figure 1.6b). Prior to printing, inks were modified by dispersing the carbon fibers. Adding carbon fibers increased the tensile strength and conductivity of the electrodes. The working electrode was then functionalized with electrochemically active components (Fig. 1.6c) by sequentially drop-casting TTF mediator and enzyme solutions. Finally, biocompatible polymer chitosan solution was cast on top to form the barrier film that prevents the enzyme diffusion. The enzymatic biosensor exhibited selectivity toward lactate with linearity up to 20 mM (Figure 1.6d) and could be stored for 5 months while preserving 90% of signal. Undoubtedly, screen printed tattoo sensors represent an attractive platform for fabricating wearable electrochemical sensors. This study showed the great potential of the platform to continuously monitor lactate. Measuring several additional key parameters would help to further evaluate the commercial readiness of the platform. Particularly, it is important to measure reproducibility, performance under prolonged continuous operation, effect of the analyte flow rate on the sensor response, and insensitivity to the salts present in sweat. In our recent study we concurrently measured enzyme activity and response of the TTF-based lactate sensor in five different salts individually (*164*). We found that while NH_4Cl and $MgCl_2$ do not affect enzyme activity or sensor performance in physiologically relevant ranges of salt concentration, increasing NaCl or KCl concentration decreases enzyme activity and sensor current. On the other hand, change in $CaCl_2$ concentration induced a nonlinear change in the sensor performance and enzyme activity. Additionally, reproducibility is particularly

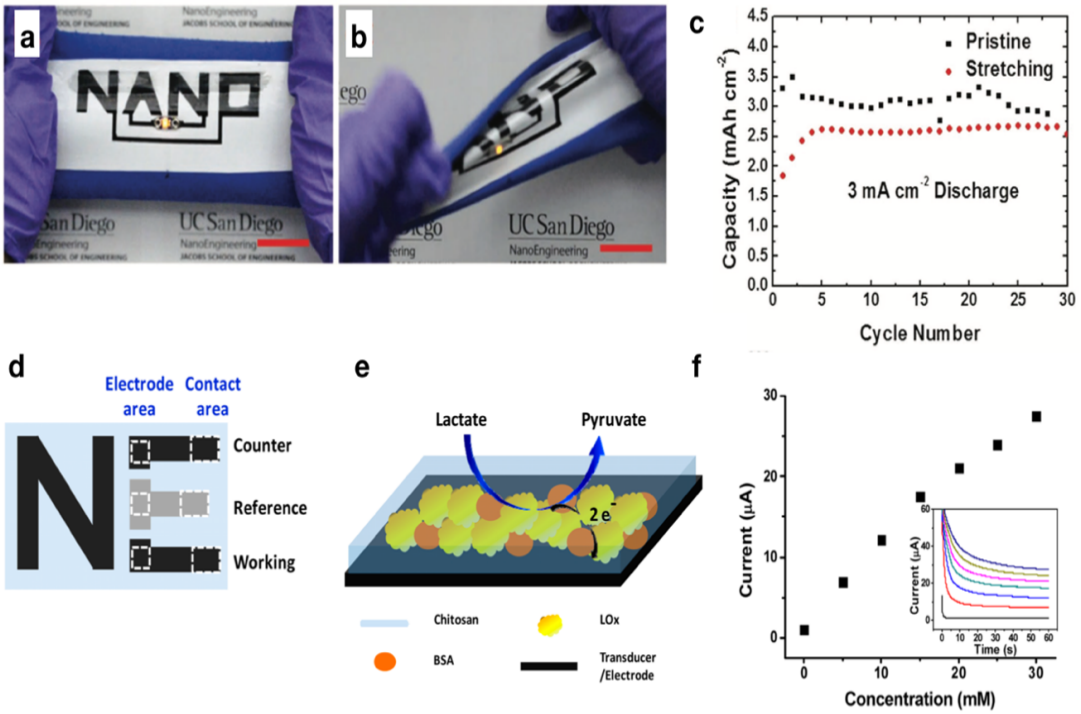

Figure 1.6: Printed stretchable battery in relaxed (a) and twisted (b) configurations. (c) The discharge capacity during 30 cycles, cycled with 3 mA h cm^{-2}. Stretching battery has been 100% stretched ten times before the electrochemical cycling. Reproduced from (*163*) with permission of John Wiley and Sons (d) Schematic illustration of a three-electrode tattoo lactate electrochemical sensor. (e) Constituents of the reagent layer of the working electrode (f) In vitro calibration curve of tattoo biosensor; inset, amperometric response to different lactate concentrations up to 30 mM with 5 mM increments. Reproduced from (*13*) with the permission of American Chemical Society.

important to confirm for this sensor chemistry. After deposition from the solution, TTF forms crystals of random sizes and distribution throughout electrode. This might result in variability of chitosan membrane throughout the electrode, leading to differences in membrane properties from device to device. Variability in membrane morphology between devices might lead to variability in transport characteristics of the membrane and, consequently, variability in sensor performance. Furthermore, change in the analyte flow rate at the electrode surface might have a profound effect on the sensor response, if the chitosan layer is not effectively limiting lactate diffusion. Thus, a change in the perspiration rate might produce false sensor response. We discuss these arguments in more detail in chapter 5 of the thesis.

Composite electrodes for batteries were also designed withbinder-free polymer, with a CNT or carbon microfiber network maintaining mechanical integrity of the electrode, as well as serving the function of conductive additive and current collector. Numerous binder-free composites for flexible Na-ion and Li-ion battery electrodes have been developed using carbon

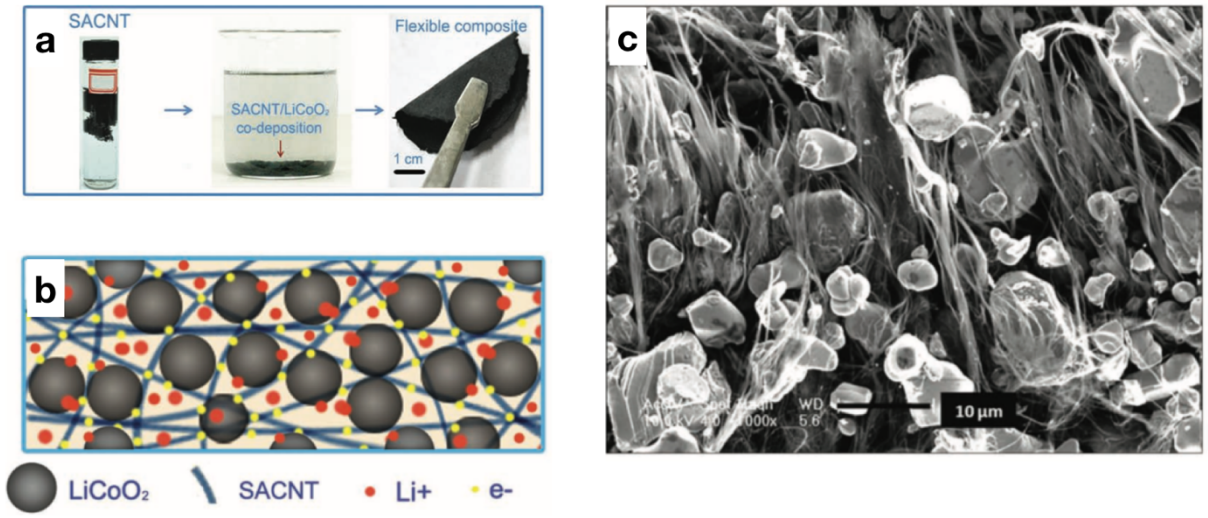

Figure 1.7: (a) $LiCoO_2$-SACNT co-deposition process (b) Schematic of the structures of the binder-free $LiCoO_2$-SACNT electrode. (c) Cross-sectional SEM image of a $LiCoO_2$-SACNT composite. Reprinted from (175) with permission of John Wiley and Sons.

materials (*165–175*). For example, Luo et al. used a simple method of ultra-sonication and co-deposition to produce flexible electrode with commercially available material ($LiCoO_2$) embedded in a supper-aligned carbon nanotube (SACNT) network **(Figure 1.7a,b)** (*167*). Active particles and SACNTs were dispersed in ethanol and ultrasonicated to form an interpenetrated network of $LiCoO_2$ particles and SACNTs. Following the completion of the ultrasonication the resulting composite would co-deposit to the bottom of the container. The composite was lightweight, with high contact area between active materials and SACNTs (Figure 1.7c). High intrinsic strength and flexibility of the SACNT bundles ensured flexibility of the electrode. Furthermore, such binder-free configurations allow to eliminate metal current collectors that commonly add >10% to the electrode weight (*118*), and thus, to increase the gravimetric energy density of the electrode. It is of critical importance to develop a roadmap for low-cost and large-scale manufacturing of such electrodes in order to achieve commercially competitive products.

1.4 Thesis outline

Previous sections point out to some of the existing shortcomings in the development of the wearable electrochemical devices:

- Reports of flexible and stretchable batteries commonly characterize mechanical performance by subjecting a battery to several hundred deformation cycles (the battery is deformed to an arbitrary extent) followed by electrochemical cycling. At the same time, the battery is likely to experience tens of thousands of deformations of various degrees throughout its lifetime as a

part of a wearable system. Thus, the characterization results neither inform about the utility of the battery for real life applications, nor about its mechanical limits. It is necessary to demonstrate flexible and stretchable batteries with mechanical endurance that is on par with commercial requirements (withstanding >10000 deformation cycles with the extent and speed of the deformation defined by the target application).

- Bulk of the wearable battery demonstrations are based on Li-ion ion battery chemistry, which often relies on toxic and/or flammable components. More attention should be devoted to non-toxic systems, preferably comprising more abundant and disposable materials.
- Incorporating additional functionalities commonly introduces additional inactive components to the battery structure. This reduces the amount of energy that can be stored per unit volume or per unit area of the battery. At the same time, it is important to maximize energy density, since dimensions of a battery are often limited with the size of the device being powered. An optimum system would match the commercial product in terms of energy density while having a flexible form factor.
- Despite the development of several attractive platforms for wearable electrochemical sensors, the publications commonly investigate only a subset of parameters required for commercial use. Fast response, sensitivity to physiologically relevant concentrations of analyte, batch to batch reproducibility, stable long-term performance under continuous operation, specificity, long-term storage and mechanical resilience have to be evaluated before a system can be claimed to be commercially viable.

These are important limitations of the wearable electrochemical systems and are addressed in this thesis. Chapter 2 discusses design and fabrication of the flexible wire battery based on intrinsically safe Zn/Ag_2O battery chemistry. We use learnings from the battery fabrication process optimized in Chapter 2, to develop a new compliant battery design concept, described in Chapter 3. The new approach is in the utilization of metal current collectors with enhanced mechanical design, such as helical springs, serpentines and spirals, as a structural support and backbone for the rest of the battery components. Depending on the choice of current collector geometry, batteries can be fabricated with flexible or stretchable form factors to match the mechanical properties of wearable electronic systems. As an example, we show the stretchable battery mentioned in the previous section of this chapter and, importantly, a flexible wire battery that is resilient to repetitive dynamic mechanical load and can withstand >17,000 bending cycles. In Chapter 4 we describe a flexible Zn/MnO_2 battery that is safe, environmentally sustainable and has a volumetric energy density of 320 mWh cm^{-3}, approaching that of the commercial AA alkaline battery. The battery was enabled by the new MnO_2 electrode composite fabricated through in-situ polymerization of the polymer hydrogel. Chapter 5 discusses the development of the flexible sensing platform to monitor lactate, sodium ion and ammonium ion in sweat, fabricated via low-cost printing methods. We used commercially available materials that have been previously implemented for engineering wearable sweat sensors. We outline optimization steps to achieve sensor performance for continuous monitoring of given metabolites, and importantly, we point out aspects that remain to be studied or addressed before such system can become a commercially viable product. Conclusions and future work are presented in Chapter 6.

CHAPTER 2

Fabrication of high-performance flexible silver-zinc wire battery

Portions of this chapter have been submitted for publication in (*102*).

2.1 Introduction

Conformable electronic wearable systems will enable improvements in human health monitoring (*176–179*). The development of a high energy density flexible wearable battery that maintains safe and stable operation under mechanical deformation is crucial for the autonomous operation of optimal wearable devices. The ideal wearable battery would not change the aesthetic features of the garment nor cause discomfort to the user. To date, most flexible batteries have been planar systems assembled by the consecutive stacking of electrodes and separators. This planar architecture can be flexed only in certain directions and could eventually fail due to delamination caused by shear forces imposed by flexing (*180*) . This poses limitations of integration with wearable technologies. As an alternative, architecture wire batteries offer omnidirectional flexibility; they can be folded into arbitrary shapes, wrapped around body parts like the neck or the wrist as well as weaved or sewn into fabrics (*137*, *181–183*).

In recent studies new electrode composites were created in order to replace rigid components of conventional batteries with robust and compliant substitutes that enable such wire battery architectures (*32*, *33*, *37–40*, *42*, *44*, *45*, *146*, *182*, *184–186*). Lithium-ion (Li-ion) chemistries have received special attention due to their well-engineered stability and high energy density (*34*, *44*, *45*, *182*, *185*). However, simultaneously achieving high specific capacity and long cycle life of the wire batteries remains a challenge. Kwon et al. reported first Li-ion wire battery with linear capacity of 1 mAh cm^{-1} at a discharge rate of 0.1C over 8 cycles (*39*). Weng et al. reported a Li-ion battery based on carbon nanotube-lithium oxide composite yarns with improved cycle life of 100 cycles, but with a lower linear capacity of 0.22 mAh cm^{-1} (*33*). In addition, risk of exothermic decomposition reactions between organic electrolyte and active materials (*187*) imposes a hazard associated with most Li-ion battery materials for wearable applications. Battery chemistries that rely on aqueous electrolytes are inherently safer and thus, are more suitable for powering wearable technologies. Wire structured zinc-air and zinc-carbon aqueous batteries with

capacities of 0.9 and 0.18 mAh cm^{-1} respectively have been recently demonstrated (*32*, *37*). However, the primary nature of these batteries is a limitation for garments and jewelry. Silver-zinc battery chemistry is another alternative based on an aqueous electrolyte. In addition to being non-volatile and rechargeable, the silver-zinc chemistry provides energy density comparable to that of commercially available Li-ion batteries. Nevertheless, its widespread use is hindered by such shortcomings as high cost of silver, lower operating voltage and limited cycle life compared to its Li-ion counterparts. Despite of these limitations, it can be a good energy storage alternative for integration with smart garments, where safety and energy density are of the primary importance and the lifetime of the battery is comparable with the lifetime of the garment. To date, there are few reports on wearable primary (*31*, *102*, *188*) and secondary (*186*, *189*) silver-zinc batteries with planar configuration. Rechargeable systems show cycling (*186*) or areal capacity (*189*) limitations despite of innovative manufacturing approaches. The stretchable silver-zinc battery (*189*) has a low areal capacity of 0.11 mAh cm^{-2} while the epidermal tattoo battery with areal capacity of 1.3–2.1 mAh cm^{-2} (*186*) is stable only over 13 cycles.

Here we report on the fabrication and the electro-mechanical performance characterization of rechargeable silver-zinc wire batteries. We implement a cathode architecture with silver

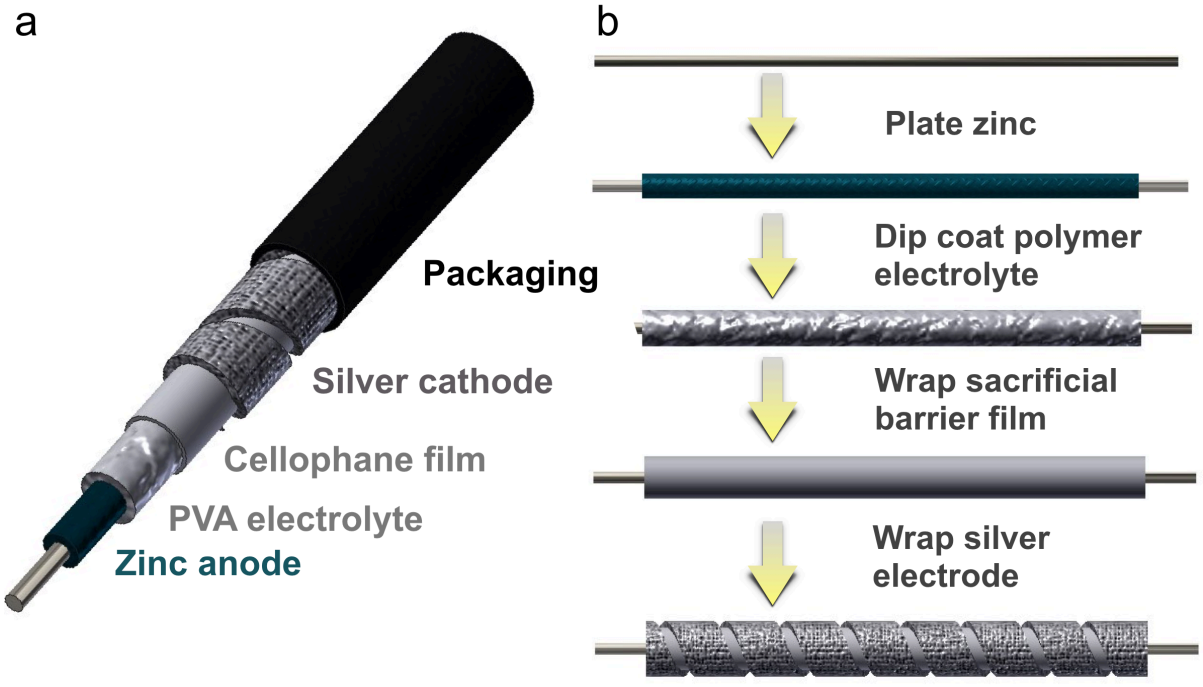

Figure 2.1: (a) Schematic of the silver-zinc wire battery showing cell components. (b) Schematic illustrating step-by-step wire battery assembly process. Schematics was drawn by Michael Wang (*102*).

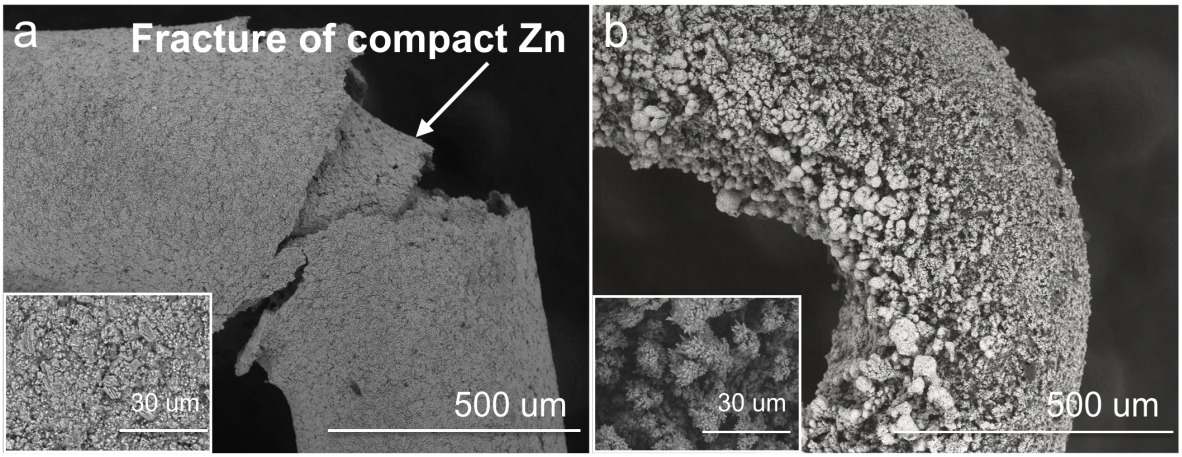

Figure 2.2: SEM micrograph of the zinc deposited on the tin-coated copper wire and subjected to mechanical deformation. Zinc was plated in the galvanostatic mode at the current density of (a) 10 mA cm^{-2} and (b) 30 mA cm^{-2} (*102*).

nanoparticle ink embedded into the conductive thread. The battery has a specific discharge capacity of 1.4 mAh cm^{-1} at 0.5C discharge rate, with a capacity retention of above 98% after 170 cycles. We demonstrate that the wire battery maintains this capacity after repeated flexing to a bending radius of 5 mm.

Migration of silver ions to the counter electrode and subsequent poisoning of the electrode is a major impediment to long cycle life in silver-zinc batteries (*118*), limiting battery life to 50-100 cycles depending on cycling parameters (*190*). Silver migration also causes growth of fine silver metal crystals inside the separator leading to short circuits. We mitigate this limitation and improve the lifetime of the battery by reducing the dissolution of silver ions with an optimized potassium hydroxide (KOH) concentration of 2M in the electrolyte. In addition, 20 μm cellophane film was embedded between cathode and anode to form a sacrificial barrier. Cellophane mitigates the migration of silver ions to the separator and counter electrode by reducing them to insoluble silver metal and gets oxidized during this process (*118*). The optimum battery operation parameters were reached by studying the effect of cycling rate on the silver electrode morphology and electrochemical performance of zinc-silver battery. These modifications improved the performance to over 170 stable cycles. This high specific capacity and long cycle life silver-zinc wire battery create new possibilities in implementing wearable garments such as activewear with integrated performance trackers and continuous health monitoring systems, fashion wear and jewelry with integrated electronics like LEDs or solar modules etc.

2.2 Optimization of the battery components

The schematic of the wire battery and the fabrication process is illustrated in **Figure 2.1a** and 2.1b respectively. The anode is composed of electrodeposited Zn on tin-coated copper wire. Subsequently the anode was dip-coated into the polyvinyl alcohol (PVA)-KOH polymer electrolyte, which served as a separator. A thin cellophane film was wrapped around the PVA separator to further reduce migration of silver ions towards the zinc electrode. The silver electrode was fabricated by dip coating a conductive stainless steel thread into a silver nanoparticle solution; subsequently, cathode was electrochemically oxidized to Ag_2O or AgO after the battery was fabricated. The electrode was then wrapped around the anode-electrolyte assembly resulting in a wire battery with a 2.5 mm diameter.

Optimum morphology of electrodeposited Zn

The mechanical flex stability of the wire battery anode depends critically on the morphology of electrodeposited Zn which can be controlled by adjusting the plating current (*191*, *192*). **Figure 2.2**a shows an anode with the compact boulder Zn morphology, obtained at lower (10 mA cm^{-2}) current density. Figure 2.2b shows dendritic Zn deposit, plated at higher (30 mA cm^{-2}) current density. The compact Zn fractured after flexing while dendritic Zn was able to maintain mechanical integrity. Void spaces in the dendritic Zn deposit make it more flexible than compact Zn. Subsequently, all Zn anodes were plated at the current density of 30 mA cm^{-2} to achieve dendritic Zn morphology that withstands mechanical stresses. In addition, Chamoun et. al. (*193*) showed that using dendritic and hyper dendritic zinc preforms can stabilize cycle life by altering ramification process.

Properties of polymer electrolyte

To simplify the fabrication process, the electrolyte/separator for the battery was constructed by dip-coating Zn anode into the PVA-KOH polymer gel. Using this approach, we benefit from chemical stability of PVA in alkaline media, its high ionic conductivity and ability to sustain mechanical stress (*194–196*), while utilizing simplicity of dip-coating technique. To inhibit undesired hydrogen evolution on the thermodynamically unstable Zn electrode KOH was saturated with zinc oxide (ZnO) and bismuth oxide (Bi_2O_3) (*29*, *197*, *198*). Conductivity of the PVA-KOH film used in the wire battery is 10^{-2} S cm^{-1}, as determined by impedance spectroscopy measurement **(Figure 2.3)**.

Effect of imbedding cellophane sacrificial film

Silver-zinc batteries require additional separator-membrane on the positive side to protect the PVA separator and zinc anode from the oxidative attacks of silver ions.[29] Ideal membrane should be permeable to hydroxyl species and impermeable to silver ions. However, designing ideal

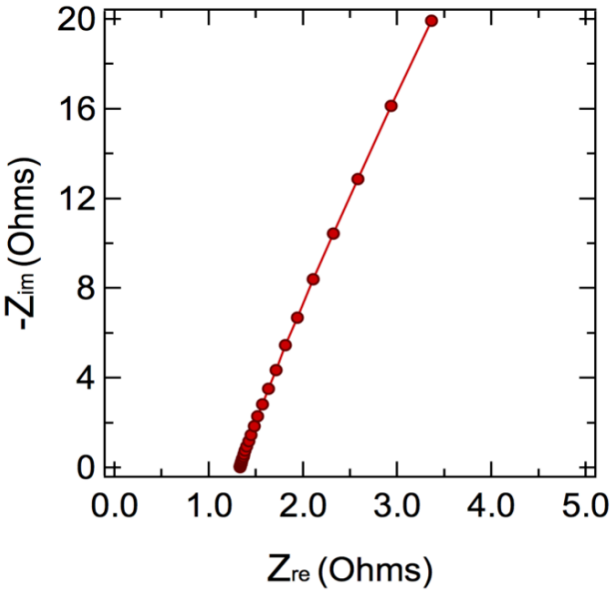

Figure 2.3: High frequency region of the Nyquist plot of the PVA-KOH polymer electrolyte. Impedance measurement was performed at frequencies ranging from 10^6 to 0.1 Hz at amplitude of 10 mV. The ionic conductivity, $\boldsymbol{\sigma}$, of the polymer electrolyte was calculated according to the formula $\boldsymbol{\sigma} = \frac{\boldsymbol{l}}{\boldsymbol{RA}}$, where l is the film thickness, R is the bulk resistance and A is the area of the film. The bulk resistance was determined from the high-frequency intercept of the impedance curve with the real axis (*102*).

membrane remains a challenge due to synergic effect of several parameters that aid adsorption and migration of ionic species thought the polymeric matrix, such as pore size, electrostatic and steric factors. The cellophane membrane has been widely used as a barrier for silver migration in conjunction with different separators (*118*, *199*). Cellulose – constituent component of cellophane – reduces silver ions to metallic silver, thus mitigating further migration of these species (*118*, *190*). The major drawback of cellophane is its gradual destruction as a consequence of oxidative silver attacks. We utilized 20 μm cellophane film wrapped around PVA coating to serve as a sacrificial barrier for decelerating silver migration. To prolong the lifetime of the barrier we used the double layer of the film.

To investigate the effect of embedding cellophane film on the impedance of the wire battery we performed EIS measurements of the batteries with and without cellophane membrane and correlated them with electrochemical data. EIS measurements were performed at frequencies ranging from 10^6 to 0.1 Hz at amplitude of 10 mV at open circuit condition. The battery was tested after assembly and equilibration for 2 hours. The resulting Nyquist plots are shown in the **Figure 2.4**a. They consist of depressed semicircle in high to medium frequency range (in the lower range of abscissa axes) and sloping tale in the low frequency range (in the higher range of abscissa axes). Inductive data obtained at high frequencies do not influence the rest of the spectra (*200*) and do not bear interest to the discussion, therefore, they were excluded from the plot. The high frequency intercept with abscissa corresponds to the Ohmic resistance of the battery and is dominated by the electrolyte resistance (*31*, *200*, *201*). The depressed semicircle can be attributed to the kinetic impedance due to charge transfer interfaces within the battery, such as particle to particle interface, current collector to particle interface and particle to electrolyte interface (*31*, *201*). The depressed shape results from the variations in capacitance and resistance throughout the electrodes caused by non-uniform morphology. Kinetic response combines contribution from both electrodes but is

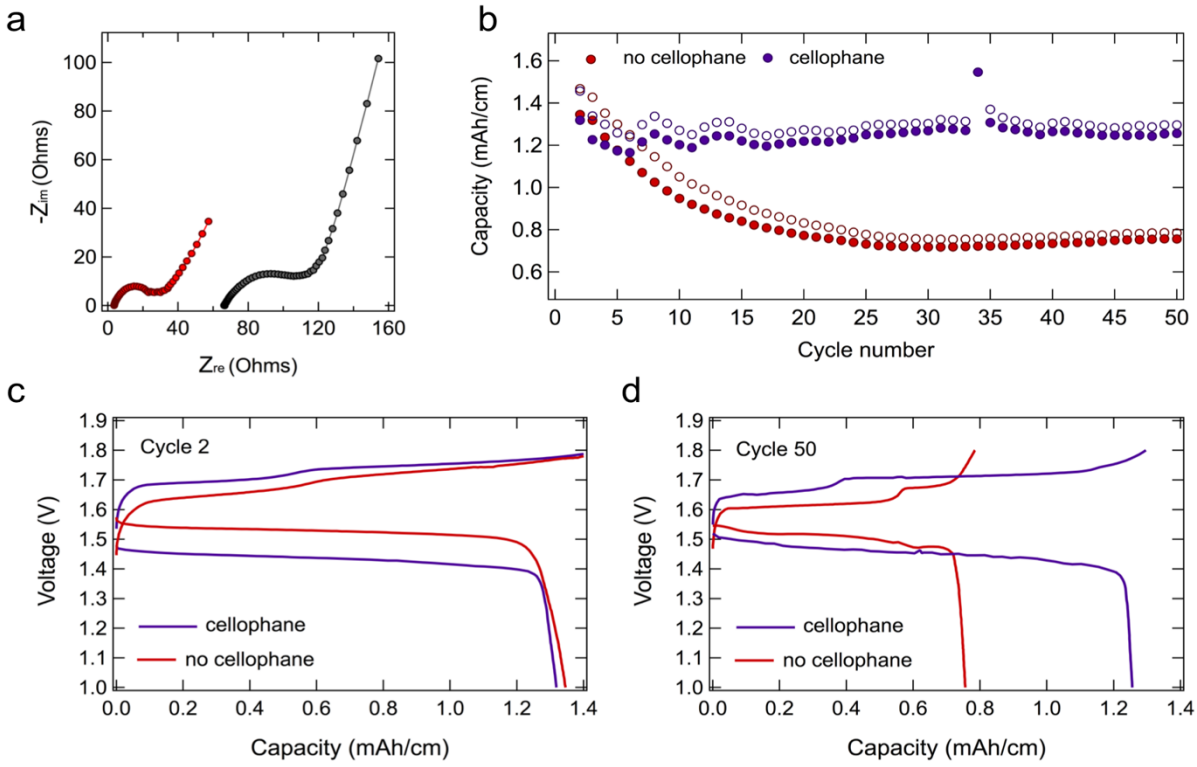

Figure 2.4: (a) Nyquist plots and (b) cycling performance of the wire batteries with and without embedded cellophane film. Charge-discharge curves for the (c) 2nd and (d) 50th electrochemical cycles of the battery in (b) (*102*).

dominated by the impedance of limiting silver electrode (*31*, *200*, *201*). The low frequency range is attributed to the solution diffusion Warburg process at the cathode (*102*, *201*). As seen from the Nyquist plots in Figure 2.4a, the intercept with abscissa increased by 62 Ohms and the radius of the semicircle increased by 17 Ohms as a result of embedding the cellophane barrier. Increase in the abscissa intercept indicates that the film hindered ionic transport of electrolyte ions and resulted in the increased PVA-KOH-cellophane composite resistance if compared to PVA-KOH and, thus, increased Ohmic resistance of the battery. Increase in the radius of the semicircle must be due to changes in particle-to- electrolyte interface, since current collector-to-particle and particle-to-particle interface remain unchanged. Since silver electrode is in direct contact with the cellophane film, such response could be an indicator of poorer wetting of the film, if compared to PVA electrolyte.

Cycling performance and charge-discharge curves of the 2nd and 50th electrochemical cycles of the batteries with and without cellophane film are shown in Figure 2.4b-d. Battery with cellophane maintains stable performance, while battery without cellophane looses 47% of its capacity after 30 cycles (Figure 2.4b). Discharge potential of the battery decreases by 0.09 V after

embedding the cellophane film (Figure 2.4c), however, this difference reduces to 0.06 V by the 50th electrochemical cycle (Figure 2.4d). Lowering of the battery discharge potential is a reflection of increase in the Ohmic resistance of the battery with embedding of the cellophane film. As cycling progresses, the polymer electrolyte in the battery without cellophane deteriorates, resulting in the increase of the Ohmic resistance of this battery. As a result, the difference between discharge potentials of two devices reduces, making the Ohmic contributions from the cellophane less profound. Therefore, cellophane film contributed to increase in Ohmic and charge transfer resistances of the battery. Nevertheless, second separator is a necessary component to achieve long cycle life of the battery. The battery without this modification looses capacity as a result of gradual poisoning of the PVA electrolyte and zinc electrode. Even after integration of the cellophane film, the total resistance of the device was in the same range or smaller than have been previously reported for the wire batteries (*32*, *39*). It is important to note that structural and transport parameters of cellophane strongly depend on the film fabrication process (*202*). Therefore, for higher rate applications, where resistance losses should be further minimized, different film alternatives can be considered.

Effect of KOH concentration

To further decelerate silver ions migration and extend lifetime of the battery we adjusted the concentration of silver ions in the electrolyte by varying KOH concentration. The effect of KOH concentration in the electrolyte on the cycling performance of the silver-zinc wire battery operated at 0.25C charge and 0.5C discharge rates between 1 V and 1.8 V is shown in **Figure 2.5**. Change in specific capacity with cycle number was investigated for 25 wt.% (5.6M), 20 wt.% (4M) and 10 wt.% (2M) KOH content in the electrolyte (Figure 2.5 a,d, b,e and c,f respectively). Initially, charge-discharge capacity is higher in the batteries containing more concentrated KOH solution, while the columbic efficiency is lower (2.7 mAh cm^{-1} charge and 1.65 mAh cm^{-1} discharge capacity for the battery with 25 wt.% KOH content; 2.3 mAh cm^{-1} charge and 1.55 mAh cm^{-1} discharge capacity for the battery with 20 wt.% KOH content; 1.3 mAh cm^{-1} charge and 1.2 mAh cm^{-1} discharge capacity for the battery with 10 wt.% KOH content). As cycling progresses capacity of the batteries with 20 wt.% and 25 wt.% KOH content continuously decays and then abruptly falls below 20 wt.% of its original value after 17 and 20 cycles respectively. In contrast, batteries with 10 wt.% KOH demonstrate stable capacity throughout the cycle range. Both lower columbic efficiency and premature failure of the batteries with higher KOH content can be attributed to increased solubility of silver in more concentrated KOH solutions (*203*, *204*). Firstly, higher concentration of silver ions in the electrolyte of these batteries leads to accelerated silver migration, poisoning of Zn electrode and destruction of cellophane barrier, thus, expediting battery failure. Secondly, higher solubility of silver results in greater capacity losses on dissolution that do not recover in the consecutive cycles resulting in lower efficiencies. Additionally, Zn corrosion processes occurring on an anode are more thermodynamically favorable in higher concentrated KOH solutions. Therefore, part of the energy supplied on charge is consumed by Zn dissolution, further contributing to decrease in columbic efficiency. Figure 2.5d-f shows galvanostatic charge/discharge curves for the 4th, 10th and 18th cycles of the batteries with 25 wt.%, 20 wt.% and

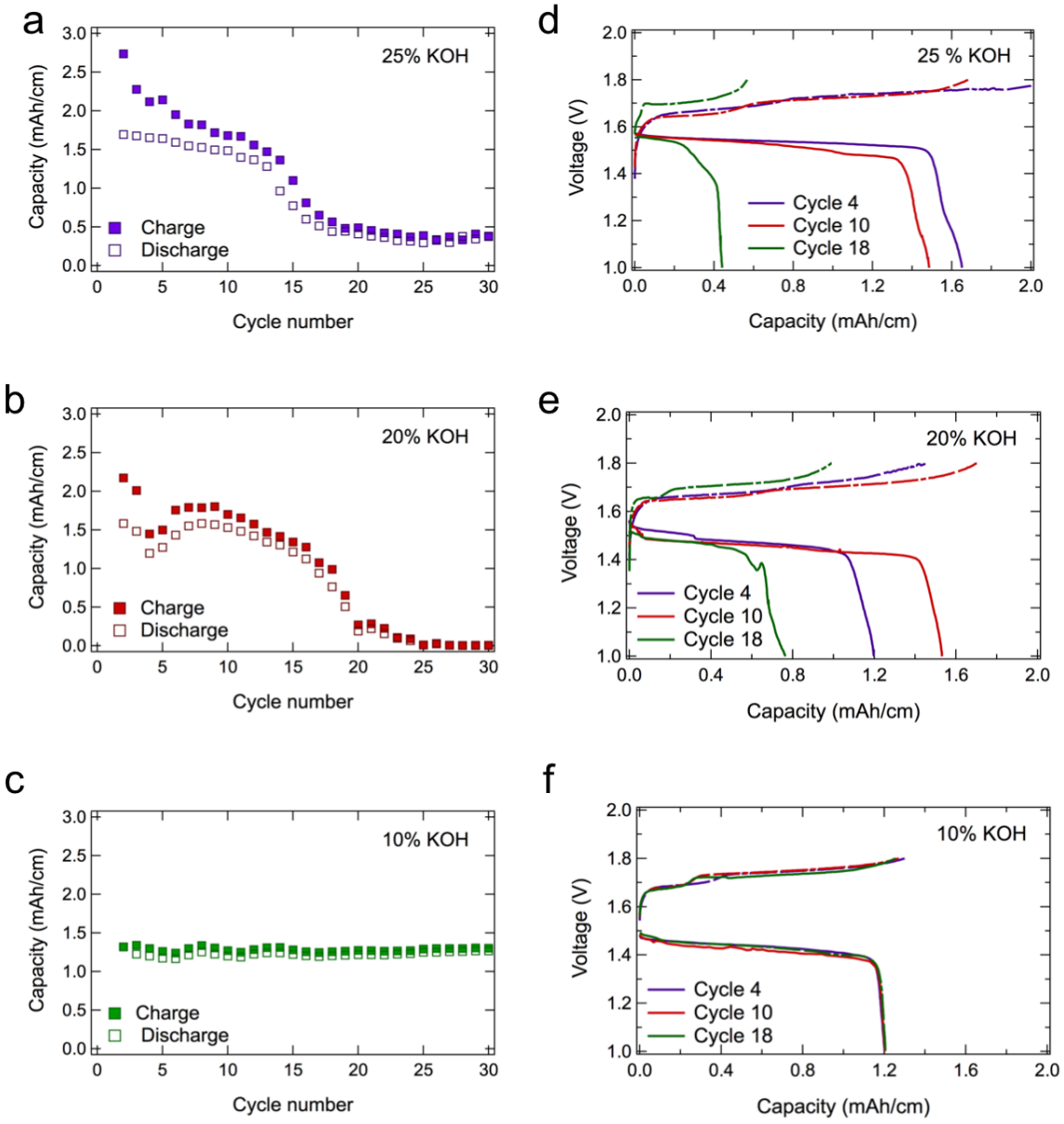

Figure 2.5: Effect of potassium hydroxide concentration in the electrolyte on the cycling performance of silver-zinc wire battery operated at 0.25C charge and 0.5C discharge rates between 1 V and 1.8 V with electrolyte containing (a) 25 wt.%, (b) 20 wt.% and (c) 10 wt.% potassium hydroxide. (d) – (f) Galvanostatic charge/discharge curves for cycles 4, 10, 18 of the batteries in (a) – (c) (*102*).

10 wt.% KOH content. As seen from the voltage values of charge-discharge curves, lowering

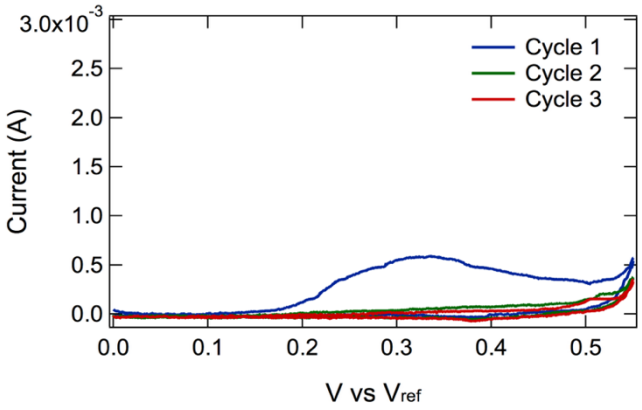

Figure 2.6: Cyclic voltammogram for the silver electrode current collector (stainless steel thread) in 2M KOH 0.2M ZnO saturated with Bi_2O_3 vs. Hg/HgO at 0.1 mV s^{-1}. The oxidation peak is seen only in the fist cycle, indicating that the thread is oxidized during the fist cycle and remains electrochemically inert during the consecutive cycles (*102*).

KOH concentration from 25 wt.% to 10 wt.% results in the potential drop of ~0.05 V. Decreasing of the electrolyte conductivity as the KOH content is reduced from 25 wt.% to 10 wt.% causes this drop. Consequently, energy efficiency of the batteries with lower KOH content is reduced. However, this compromise is compensated by the prolonged cycle life of the battery.

Fabrication of the silver cathode

Current collector for the flexible electrode should provide mechanical support and conductive network to the electrode. Commonly, carbon based current collectors such as carbon nanotube threads and carbon fibers have been used in the wire batteries due to electrochemical stability over the potential window of the battery (*33*, *34*, *146*, *184*, *185*). However, the low electronic conductivity of carbon based materials leads to high Ohmic potential drops when the battery is operated at high C-rates. In order to reduce potential drops we chose stainless steel (SS) threads as the current collector for silver electrodes. SS threads are highly conductive and have porous architecture. The cyclic voltammetry (CV) shows that threads oxidize during the first charge cycle (**Figure 2.6)** and remain stable over subsequent cycles. As a result, their resistance increases from 7 ohms to 15 ohms. Even with initial increase in resistance, the conductivity of the SS threads is an order of magnitude higher than that of the carbon based fibers, making SS threads a reasonable choice for the current collector.

To reduce fabrication costs and improve shelf life of the battery, we constructed cathode by dip coating stainless steel thread in the silver nanoparticle ink. The deposition results in uniform silver coating, as shown in the **Figure 2.7**. The assembled silver electrode can be oxidized to Ag_2O or AgO and the battery can be formed when needed (*205*).Thus, battery components are subjected to the oxidative attack of silver oxide for a shorter period of time. Therefore, by using silver nanoparticle ink, we achieved good printability and simple fabrication of the cathode as well as extended shelf life of the battery.

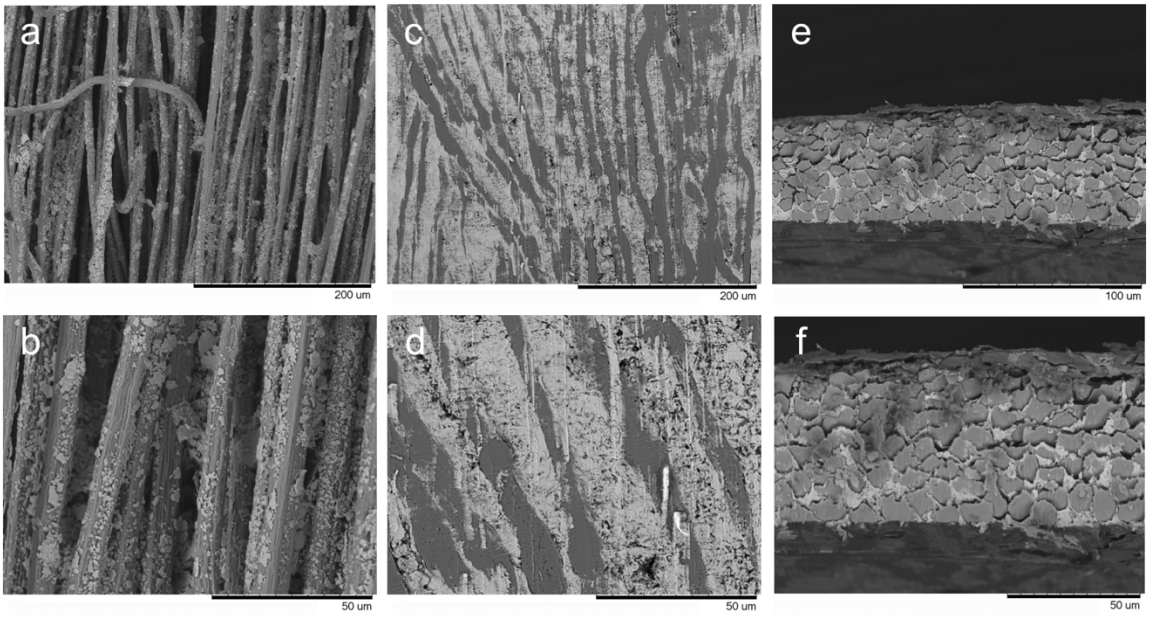

Figure 2.7: SEM of the (a) – (d) top view and (e) – (f) cross section of the silver electrode constructed by dip coating of the stainless steel thread into the silver nanoparticle ink (a) – (b) before and (e) – (f) after calendaring. Silver ink coating has good uniformity throughout the thread (*102*).

2.3 Electrochemical performance of the silver-zinc wire battery

The percent utilization of electrodes is one of the factors determining cycle life of silver zinc batteries. Utilization of silver on the order of 57% of the theoretical capacity has been used to design long-life cells (*118*). The utilization of silver electrode in the wire battery ranged between 47% and 60.5% of the theoretical capacity of Ag_2O, at 0.5C rate of discharge, resulting in the 109 mAh g^{-1} to 140 mAh g^{-1} designed capacity based on silver cathode, which was a limiting electrode in the battery. Variations in the capacity utilization of silver are caused by differences in morphology of thread-embedded electrodes originated from random distribution of thread fibers and manual dip-coating process. Automating dip-coating process can minimize the range of silver utilization fraction. The capacity ratio of anode to cathode in the wire battery is 2.75 to 1. Therefore, cycling of Zn was limited to a range of 17% to 22% of anode theoretical capacity at 0.5C discharge rate. The utilization of Zn to the fraction of its theoretical capacity is crucial for preventing failure of the battery through occlusion of mass transport of Zn electrode. Mass transport is hindered by formation of ZnO during discharge, which commences at the separator

and moves toward the current collector (*206–208*). It has been shown that cycling of pre-formed dendritic zinc to a fraction of its total capacity mitigates the aforementioned failure mechanism for many cycles (*193*).

Improving cyclability through particle size maintenance during AgO/Ag_2O to Ag conversion on discharge

The Ag/Ag_2O cathode is both the capacity limiting electrode as well as the cycling critical electrode. Electro-oxidation of silver in alkaline solutions is a two-step process and can be represented in the simplified form by the following equations:

$$2Ag + 2OH^- \Leftrightarrow Ag_2O + H_2O + 2e^- \quad (2.1)$$

$$Ag_2O + 2OH^- \Leftrightarrow Ag_2O_2 + H_2O + 2e^- \quad (2.2)$$

However, other processes such as nucleation overvoltages, solid-state diffusion, and dissolution of silver complicate this scheme. Ag_2O formation proceeds through dissolution precipitation mechanism (*200*) . This process starts with dissolution of silver species in KOH forming $Ag(OH)^-$. When saturation of the KOH solution with $Ag(OH)^-$ approaches two times the solubility limit, Ag_2O precipitates out on the electrode forming an oxide film on the Ag surface. While Ag_2O film grows, ionic transport though the oxide layer is gradually hindered until it reaches the value of dissolution rate. In the sintered silver electrodes, the Ag_2O layer can grow up to 2 micron in thickness before the formation of AgO begins (*31*, *201*). The growth of AgO phase takes place throughout the Ag_2O layer. The potential of the electrode further increases to oxygen generation regime when growth of AgO stops. CV data for the silver electrode is presented in the **Figure 2.8a**. CV measurement was conducted from 0 to 0.6 V against Hg/HgO reference electrode at rate of 0.1 mV s^{-1}. Anodic peaks are associated with formation of Ag_2O and AgO, as well as possible formation of higher level oxides (*31*, *32*) and dissolution of silver to form $Ag(OH)^-$ species; cathodic peaks represent their counterparts. Peaks for the oxidation and reduction reactions are fused together - indication of incomplete conversion of Ag to Ag_2O before the reaction of Ag_2O to AgO starts, and the same is true for the reduction reactions. It can be attributed to the size of silver particles. The height of the peaks increases with scan number indicating increasing oxidation of the silver electrode. Beyond 0.6 V oxygen is generated at the electrode.

Particle size maintenance during AgO/Ag_2O to Ag conversion on discharge is critical to maintain cyclability. The particle size is determined by the rate at which battery is discharged with smaller particles formed at faster discharge rates (*209*, *210*). Smaller particles are desirable as they can be fully oxidized on the consequent charge, while oxidation in the larger particles will stop at the thickness determined by ionic transport limitations (Figure 2.8 b) (*209*, *211*). In order to determine the optimum discharge rate, silver-zinc batteries were discharged at slow (0.05C and 0.1C) and fast (0.5C and 0.25C) rates between 1.8 V and 1 V (Figure 2.8 c,d). Capacity gradualy fades with cycle number when the batteries are discharged at 0.05C and 0.1C rates. The decline is more pronounced in the cells discharged at rate 0.05C than in those discharged at 0.1C. Capacity

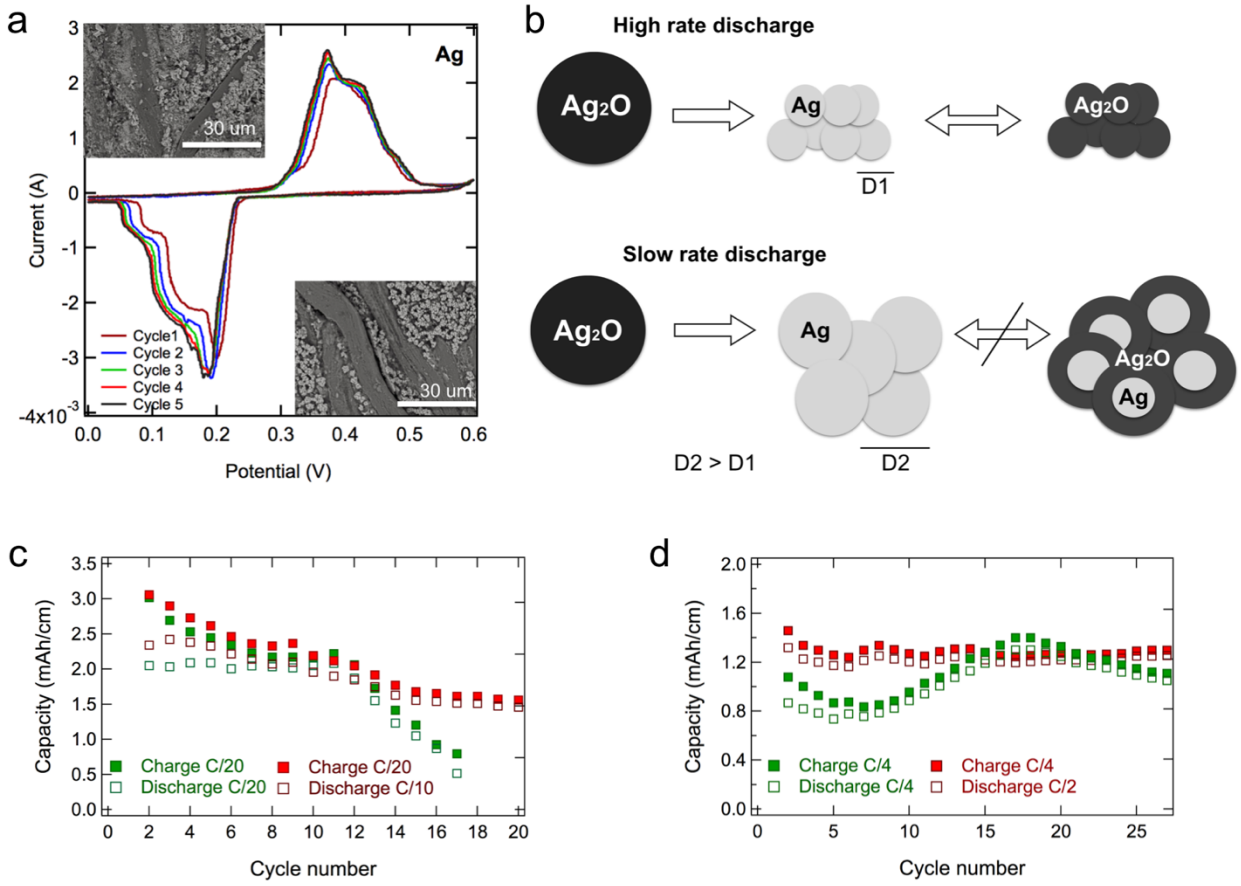

Figure 2.8: (a) Cyclic voltammogram for the silver electrode in 2M KOH 0.2M ZnO saturated with Bi_2O_3 vs. Hg/HgO at 0.1 mV s^{-1}. (b) Diagram illustrating morphological changes in silver electrode operated at slow vs. fast charge/discharge rate. Comparison of the cycling performance of silver-zinc batteries charged at the same rate to 1.8 V and discharged at different rates to 1 V. Specific capacity (mAh cm^{-1}) and columbic efficiency (%) of two batteries (c) charged at rate 0.05C, discharged at rates 0.1C and 0.05C (d) charged at rate 0.25C, discharged at rates 0.25C and 0.5C (*102*).

fluctuates when the battery is discharged at 0.25C and is stable when the battery is discharged at the 0.5C rate. Therefore, the corresponding cycling profiles show that optimum discharge rate is >0.5 C. Consequently, in order to maintain stable capacity, batteries presented in this work were discharged at the rates 0.5C and above.

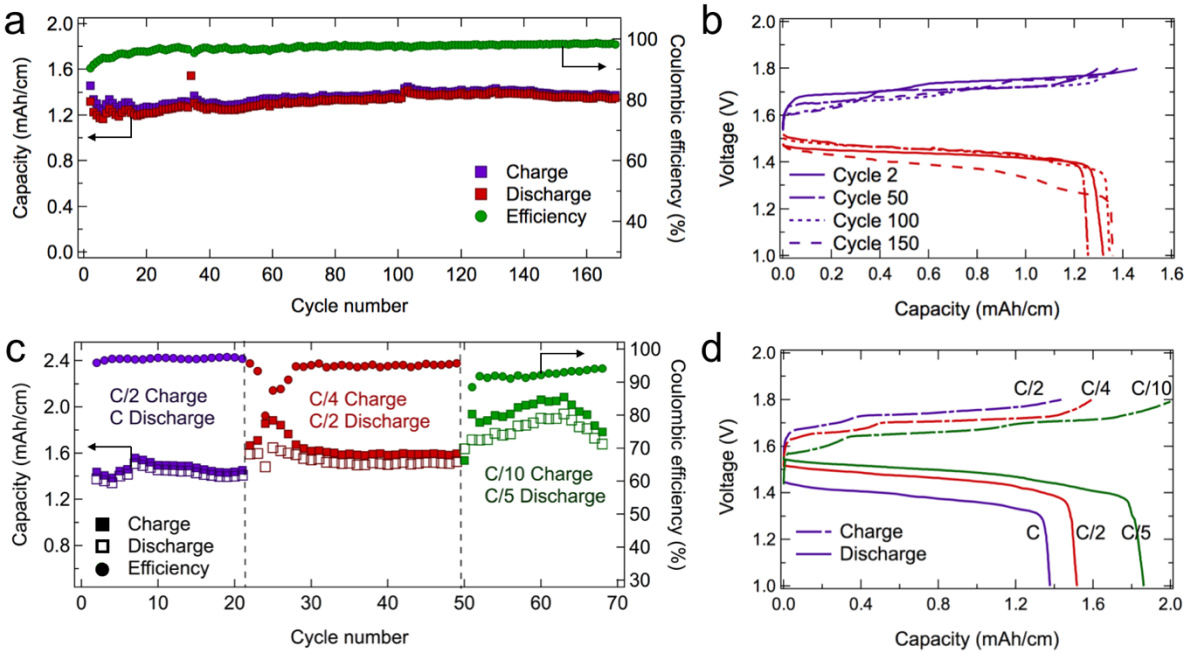

Figure 2.9 (a) Capacity per unit length (mAh cm^{-1}) and columbic efficiency (%) of silver-zinc wire battery cycled at 0.25C charge and 0.5C discharge rates between 1 V and 1.8 V. (b) Galvanostatic charge/discharge curves for cycles 2, 50, 100 and 150 of the battery in (a). C)Specific capacity (mAh cm^{-1}) and columbic efficiency (%) of silver-zinc wire battery cycled between 1 V and 1.8 V at charge rates 0.5C, 0.25C, 0.1C and discharge rates C, 0.5C, 0.25C respectively. (d) Galvanostatic charge/discharge curves of the battery in (c) for charge rates 0.5C, 0.25C, 0.1C and discharge rates C, 0.5C, 0.2C respectively (*102*).

Efficiency and cycle stability of the batteries operated between 1V and 1.8V and between 1V and 2V

In general, a silver-zinc battery can be charged to 1.8 V or 2 V to form monovalent zinc-silver oxide (Zn-A_2O) or divalent zinc-silver oxide (Zn-AgO), respectively.
The full cell reaction between zinc with AgO proceeds via two-step mechanism:

$$Zn + 2AgO \Leftrightarrow Ag_2O + ZnO \quad (1.86\ V) \tag{2.3}$$

$$Zn + Ag_2O \Leftrightarrow 2Ag + ZnO \quad (1.59\ V) \tag{2.4}$$

While the Ag_2O vs. Zn proceeds with reaction 2 alone.

By utilizing the full valence range of silver the Zn-AgO system delivers higher energy density than Zn-A_2O. However, other parameters such as efficiency and cycle stability of the battery are important. We investigated the performance of both systems by operating the batteries between 1 V and 1.8 V (to form Ag_2O) as well as between 1 V and 2 V (to form AgO) at 0.5C discharge and 0.25C charge rates. **Figure 2.9a** shows the cycling performance of the battery charged to 1.8V. Figure 2.9b shows charge-discharge curves for 2nd, 50th, 100th and 150th cycles of the battery. The capacity of the battery gradually increases up to 131st electrochemical cycle (from 1.22 mAh cm^{-1} to 1.41 mAh cm^{-1}) and then decreases to 1.22 mAh cm^{-1} by 170th cycle. The increase in capacity can be attributed to higher silver electrode utilization as cycling proceeds. Since morphology of silver electrode changes with each electrochemical cycle, minor variations in capacity are expected. The higher electrode utilization could be caused by increase in porosity of the electrode as a result of cycling and, thus, higher electro-active surface area exposed to electrolyte. The increase in electrode porosity is confirmed by the SEM characterization of morphology of the silver electrode that had undergone 180 electrochemical cycles versus as prepared silver electrode. The decrease in capacity after 131st cycle could occur due to multiple factors associated with battery aging, such as deterioration of cellophane barrier and PVA separator, corrosion of current collectors and loss of electrolyte due to its migration through plastic seals. The aging process is also accompanied by increase in internal resistance of the battery. It is represented by the potential drop of 0.1 V observed from the plateau of the discharge curve for 150th electrochemical cycle in Figure 4B. The battery was charged at 0.1C, 0.25C, 0.5C and discharged at 0.2C, 0.5C, 1C rates respectively (the discharge to charge rate ratio was kept as two to one for consistency). Specific discharge capacity decreased from ~1.85 mAh cm^{-1} at 0.2C to ~1.45 mAh cm^{-1} at 1C, resulting in ~20% capacity loss. Decrease in capacity is related to higher ohmic potential drop when the cell is cycled at higher rates. Efficiency increased from ~93% at 0.2C to ~95% at 0.5C and ~97% at 1C, due to variation in silver morphology, as discussed previously. Thus, operating the wire battery at higher rates resulted in better stability and higher columbic efficiencies.

To investigate the performance of AgO-Zn system, the wire battery was cycled between 1 V and 2 V. The discharge capacity increased by ~15% as compared to the battery charged to 1.8 V **(Figure 2.10)**. However, the cell cycled with only 80% efficiency. Using AgO the capacity started to decrease after 60 cycles, leading to ~40% capacity loss after 100 cycles. Accelerated failure of the battery operated to 2 V occurs due to increased concentration of silver ions in the electrolyte and thus faster silver diffusion through cellophane barrier, as well as undesired oxygen evolution. Both phenomena are caused by spontaneous AgO to Ag_2O decomposition via reaction $2AgO \rightarrow Ag_2O + ½\ O_2$, which is thermodynamically favorable in the basic environment.[1] From the galvanostatic discharge curve in Figure 2.10b we observe only one discharge plateau, instead of expected two plateaus. Potential values of the observed plateau correspond to those of Ag_2O-Ag couple, while plateau corresponding to AgO-Ag_2O couple is absent. Single plateau indicates that Ag_2O to AgO transition that occurs in a bulk of the electrode (*31*) does not proceed to an end leaving the Ag_2O-Ag film on the surface. This film insulates AgO layer from being in contact with

current collector. Since the potential of an electrode is determined only by the compounds that are in contact with the current collector (*202*), the higher voltage step is given up, while additional capacity is gained. The single discharge plateau is a favorable phenomenon, since such discharge profile is highly desirable for practical applications. Thus, without careful control of the formation of AgO from Ag_2O, batteries charged to 2 V exhibit lower efficiencies and shorter cycle life than batteries cycle limited to 1.8 V. Therefore, despite higher capacities achieved by cycling battery 2 V, it is advantageous to operate the battery between 1 V and 1.8 V as documented well (*118*).

2.4 Mechanical performance of the wire battery

Stable electrochemical performance under mechanical deformation is another key requirement for a wearable battery. **Figure 2.11**a and 2.11b shows the cycling performance and galvanostatic charge-discharge curves of Ag-Zn wire battery cycled at 0.25C charge and 0.5C discharge rates between 1 V and 2 V while being subjected to 100 flexing cycles to a specified bending radius under quasi-static (i.e. slow) conditions. To control flexing diameter, the battery was wrapped around cylinder of 2.54 cm, 1.60 cm, 1.27 cm, 1 cm diameter as shown in Figure 2.11c. The diameter of the control cylinder was decreased after each set of 100 bending cycles. Figure 2.11a shows that the capacity remains stable even after repeated flexing up to a bending radius of 5 mm. As seen from Figure 2.11b, resistive overpotential does not seem to be a function of flex to different diameters, indicating that no delamination or significant cracking of active layers occurs. These results confirm that the wire battery can successfully withstand mechanical perturbations that are expected to occur during wearing.

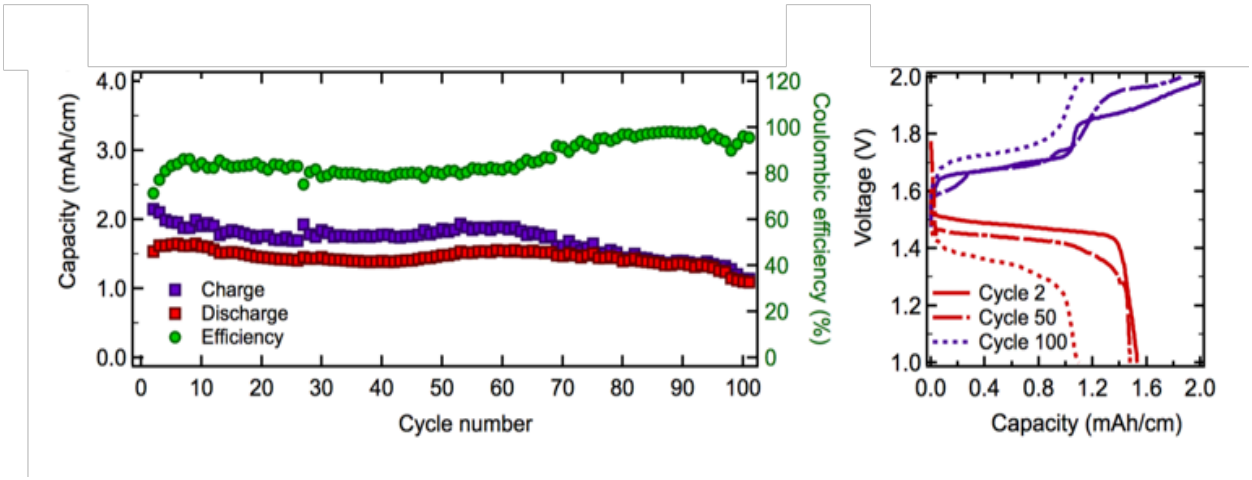

Figure 2.10: (a) Capacity per unit length (mAh cm^{-1}) and columbic efficiency (%) of silver-zinc wire battery cycled at 0.25C charge and 0.5C discharge rates between 1V and 2V. (b) Galvanostatic charge-discharge curves for 2nd, 50th and 100th cycles of the battery (*102*).

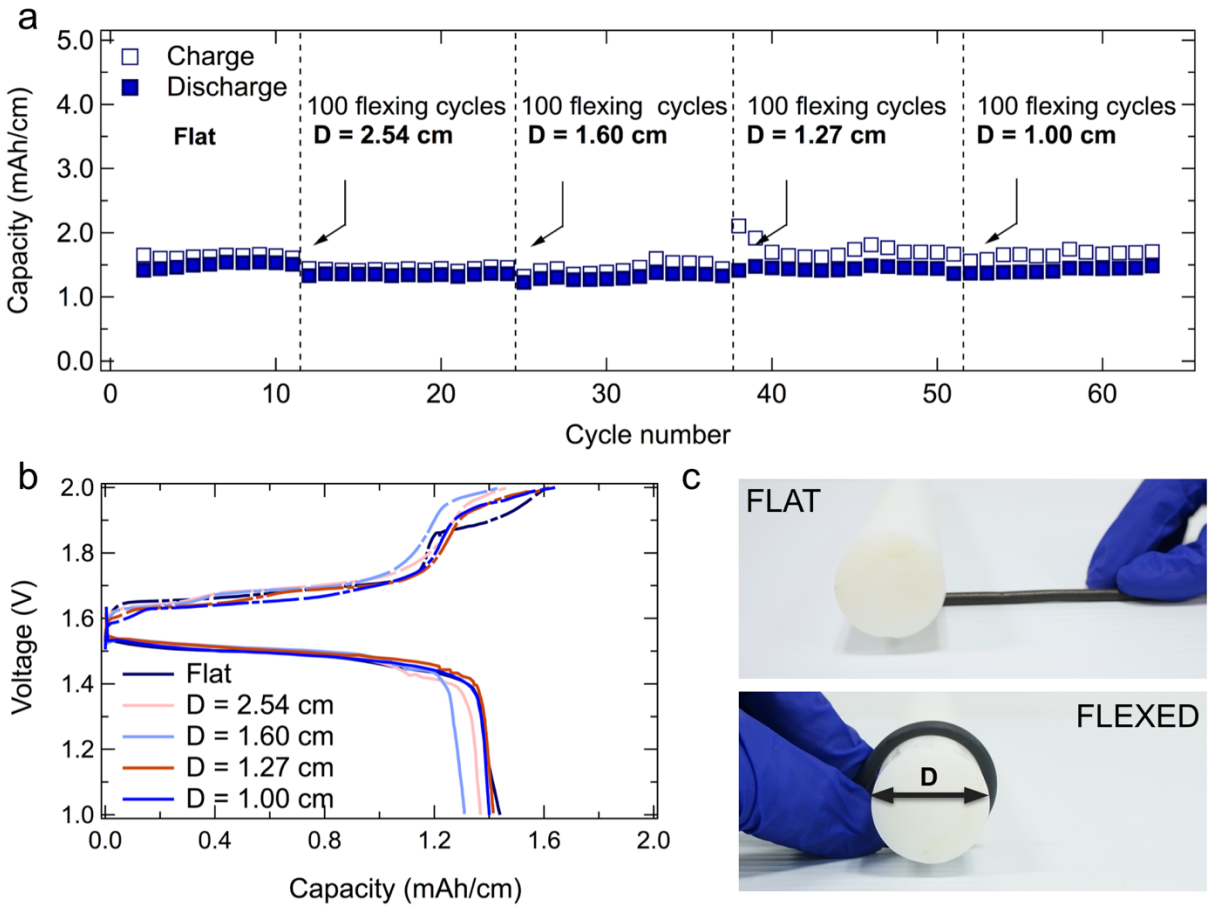

Figure 2.11: Capacity per unit length (mAh cm^{-1}) and columbic efficiency (%) (a), galvanostatic charge discharge curves (b) of silver-zinc wire battery cycled at 0.25C charge and 0.5C discharge rates between 1 V and 2 V. Battery was periodically subjected to 100 flexing cycles by being wrapped around a cylinder of 2.54 cm, 1.60 cm, 1.27 cm, 1 cm diameter, as shown in (c). Radius of the cylinder was decreased after each set of 100 bending cycles (*102*).

We further arranged multiple batteries in series to form modules with high output voltage. **Figure 12** shows three batteries connected in series and sealed within heat shrinkage plastic tube. The battery module was able to continuously power a red LED display while being deformed.

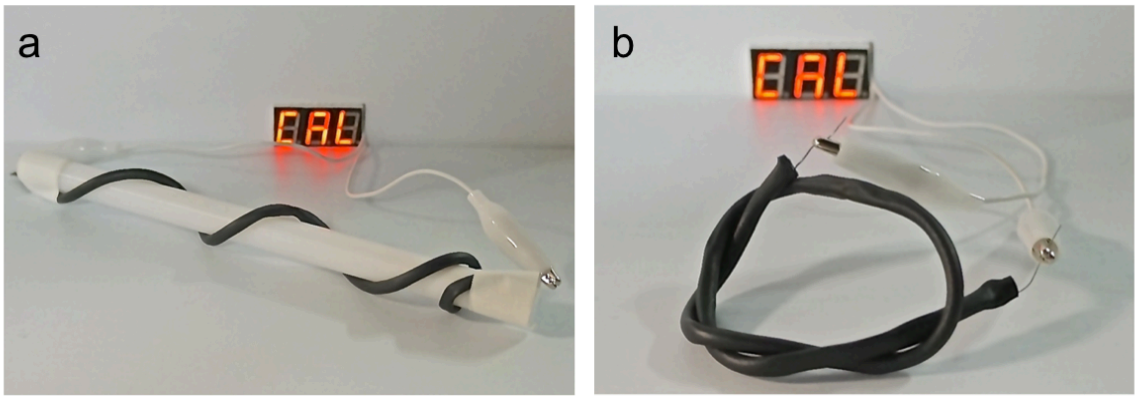

Figure 2.12: Three batteries in series sealed in chemically resistive tubing powering LED screen while (a) being wrapped around the cylinder of 0.85 cm radius and (b) tied in a nod (*102*).

2.5 Conclusion

In conclusion, we demonstrated a new design and fabrication approach of the wire battery, with linear capacities between 1.2 to 1.8 mAh cm^{-1} at a 0.5C discharge rate, by utilizing low cost fabrication processes and the silver-zinc battery chemistry. The volumetric and gravimetric energy densities of the wire battery reach 53.4 Wh L^{-1} and 18.35 Wh kg^{-1} respectively at 0.5C discharge rate. We show that the lifetime of the battery can be improved to over 170 stable cycles by optimizing potassium hydroxide (KOH) concentration in the electrolyte to reduce the dissolution of silver ions and by embedding a cellophane membrane between the anode and cathode to inhibit migration of silver ions towards the zinc electrode. The wire battery can withstand multiple bending cycles without change in electrochemical performance. It has versatile form factor that can be tuned towards specific applications.

Several milestones have to be overcome to further improve compliant technologies based on silver zinc chemistry and alkaline systems in general. One of the unresolved issues is a lack of binders that are stable in alkaline media, provide good adhesion of an active material to the substrates and at the same time have a rheology suitable to printing. Another drawback of silver-zinc technology is relatively short cycle life. Development of a separator/electrolyte that inhibits silver migration can prolong cycle life of silver-zinc batteries. Polymer electrolyte for primary printed silver zinc battery was recently reported, however similar electrolyte for rechargeable system is still to be developed. For wire or fiber shaped devices, electrochemically stable current collector with high conductivity is another important constituent required to scale such battery to arbitrary length.

2.6 Experimental section

Zinc electrodeposition

Corresponding amounts of KOH (Sigma Aldrich 85% anhydrous pellet) and ZnO (Sigma Aldrich 99.9%) were dissolved in deionized (DI) water to produce 5.6M KOH 0.37M ZnO solution. 0.1 g of Bi_2O_3 (Sigma Aldrich 99.999%) was added to the solution and mixed overnight. Solution was decanted to remove bismuth oxide that remained as a solid precipitate. Zn was electrodeposited on a tin coated copper wire (Belden) from prepared electrolyte in the galvanostatic mode at the current density of 30 mA cm^{-2} for 5000 seconds using a Gamry Potentiostat.

Silver electrode preparation

Stainless steel coated conductive thread (Sparkfun, conductive thread #60) was dipped into silver nanoparticle ink (DuPont 5064H). The composition of the ink is as follows: Dimethyl Glutarate (5 - 10%), Dimethyl Succinate (1 - 5%), Vinyl Polymer (5 - 10%), Silver (Metallic) (60 -100%), Ketone Solvent (10 - 30%). Silver nanoparticles are in the shape of flakes with the size distribution varying from nanometer range to ~5 μm. Excess ink was thoroughly removed. Silver coated thread was sintered for 30 min at 140 C° in the vacuum oven. Resulting silver electrode was approximately 250 μm thick. The electrode was calendared to 20% of its original thickness using a calendar press.

Polymer electrolyte preparation and characterization

PVA (Sigma Aldrich, MW 85000-124000, 99% hydrolyzed) was mixed with DI water in the 1:10 ratio and left to dissolve overnight in the oven at 80 C°. The liquid electrolyte was added to the mixture drop by drop to achieve 1:1.3 PVA:KOH ratio (by dry weight). The mixture was stirred for at least two hours. The resulting gel electrolyte was used for dip coating of Zn electrode or casted in the petri dish to obtain polymer film that was used in electrochemical impedance spectroscopy (EIS) measurements. To perform EIS measurements the film of 1 square inch area and approximate thickness of 0.5 mm was sandwiched between two stainless steel electrodes. The measurement was done using Gamry Potentiostat at frequencies ranging from 10^6 to 0.1 Hz at amplitude of 10 mV.

Silver–zinc wire battery assembly

Zn electrode was dip coated with PVA polymer electrolyte. The procedure was repeated 5 times letting the gel coating to dry in between in order to prevent short circuits. The cellophane film (McMaster Carr) was cut into stripes and then wrapped around anode-electrolyte assembly followed by wrapping silver electrode. To perform electrochemical characterization the device was sealed within transparent elastomeric adhesive pouch (3M 4910). It consists of three adhesive

elastomeric sheets, with a well cut in the middle sheet. The bottom and the middle sheet were first adhered together; the battery was then placed into the well and covered with the top sheet, leaving the current collectors exposed. Liquid electrolyte containing 2M KOH 0.2M ZnO saturated with Bi_2O_3 was added before sealing the battery in the amount of 50 μL per centimeter of battery length. The transparent seal allowed for the visual observation of the devises during electrochemical cycling.

To encapsulate the battery, the battery assembly was placed in the tubing followed by continuous moving of a heat gun along the length of the device, thus exposing the tubing to ~120 C° shrinking temperature. The inner radius of the tubing in a shrunk configuration exceeds the radius of the wire battery by 0.25 mm. This allows addition of the liquid electrolyte (in the quantity and composition mentioned above) before sealing the ends of the tube with chemically resistive Epoxy (3M) as well as minimizes exposure of the battery to the heat. It is necessary to note that we did not conduct studies on the effect of heat exposure on the electrochemical performance of the device. Different chemically resistive tubing can be used as an alternative to avoid the undesirable effects of heat exposure, such as damage of polymer electrolyte or cellophane barrier.

Cyclic voltammetry measurements were carried out using Gamry Potentiostat. Full cells were tested using MTI battery analyzer. SEM microscopy was carried out on TM-1000 (Hitachi).

CHAPTER 3

Utilization of current collector geometry to design flexible and stretchable batteries for wearable electronics

Portions of this chapter have been submitted for publication in (*128*).

3.1 Introduction

There is currently a great deal of interest in incorporating electronic functions into clothing and wearable devices, for applications such as sensing and healthcare (*212*). Flexible and stretchable batteries play an important role on achieving the vision of wearable and conforming electronics. In recent years several approaches have been developed in order to achieve compliant batteries. The initial demonstrations were flexible batteries based on conventional planar structures, assembled though stacking of the battery components (*28*, *29*). These designs evolved into more advanced form factors that enabled omnidirectional flexibility. Batteries in the shape of a fiber or wire (*32–45*), for example, can be twisted, tied and weaved into fabrics, allowing integration with wearable garments. In addition, several approaches to design stretchable batteries have been proposed, particularly using concepts of kirigami (*213*), origami (*214*), bridge-island battery design (*215*), arched electrode architecture (*132*), winding fibers around elastic support (*34*), embedding battery active materials within stretchable fabrics (*99*) and embedded nanowire elastic conductors (*189*). Despite innovative design strategies, there are no reports of wire batteries that exhibit fatigue resistance sufficient for applications in wearable systems that are likely to undergo thousands of flex cycles throughout their lifetime. In the case of stretchable batteries, none of the systems offer safety, compliance along multiple axes and flexibility of electrode components simultaneously.

The compliant battery design concept introduced here addresses the aforementioned limitations of existing stretchable and wire-shaped battery systems. This strategy could be applied to a number of material composites and is demonstrated here on the silver–zinc (Ag-Zn) system, which has the advantage of high energy density combined with intrinsic safety. The core of the approach is in the utilization of metal current collectors with enhanced mechanical design, such as helical springs, serpentines and spirals, as a structural support and backbone for the rest of the battery components. These architectures effectively accommodate stress imposed by mechanical

deformation, thus minimizing strain experienced by the electrodes without compromising their surface area. Depending on the choice of current collector geometry, batteries can be fabricated with flexible or stretchable form factors to match the mechanical properties of wearable electronic systems, while utilizing same battery chemistry, cell components and fabrication steps.

We demonstrate the concept through fabrication and electrochemical-mechanical characterization of batteries with two form factors – flexible wire and stretchable serpentine. We achieve flexible wire batteries by shaping the current collector-electrode as a helical band spring. The wire batteries show linear capacity of 1.2 mAh cm^{-1}, are resilient to repetitive dynamic mechanical load and can withstand >17,000 bending cycles to the bending radius of 0.5 cm under continuous operation mode without a decrease in electrochemical performance. While utilizing a current collector in the form of a helical band spring enabled omnidirectional flexibility of the battery; its elongation remained limited. Therefore, in order to achieve batteries that can be readily stretched, we utilized a current collector with serpentine ribbon geometry. In this structure, stretchability is facilitated by the out-of-plane rotations of serpentine ribbons and batteries can operate under 100% stretch. The degree and direction of stretching can be modified through changing the serpentine geometry. In addition to stretching, the battery based on serpentine ribbon can accommodate flexible motions in one plane. Thus, the omnidirectional, fatigue-resistant flexibility of the wire-shaped battery based on helical band spring makes it the preferred geometry for flexible applications. On the other hand, the serpentine-shaped battery that can be readily stretched along two axes is preferred for integration with stretchable electronics.

Integrating compliant batteries with energy harvesting devices is crucial for widespread realization of autonomous wearable power sources. Therefore, it is not only important to design batteries with compliant form factors but also to study their performance as a part of practical wearable systems. We explore jewelry-integrated power source design in the form of a bracelet that includes a compliant battery and a photovoltaic module. The battery comprises part of the wristband that is expected to undergo flexing motions throughout the lifetime of the accessory. The battery with wire geometry is chosen due its omnidirectional flexibility and resilience to flexing motions. However, if stretchability is one of the design considerations, an accessory with the same energy harvesting and storage capabilities can be achieved using a battery with serpentine architecture. The photovoltaic module charges the battery under multiple lighting conditions, including time-varying illumination that mimics the light conditions a wearable device may be exposed to during a typical daily routine. Such an accessory is able to harvest and store energy and provide power ranging from microwatts to milliwatts, depending on the illumination.

3.2 Design and fabrication of compliant batteries

The fabrication process for the compliant batteries is presented in **Figure 3.1**a. It starts with the fabrication a metal current collector of a specific geometry (ribbon or serpentine), followed by sequential deposition of the battery components. The mechanical properties of the final battery structure, wire (Fig. 3.1b) or serpentine (Fig. 3.1c) architecture, is determined by the current collector geometry. In order to scale the fabrication of wire or stretchable batteries to larger areas, the current collector must have good mechanical properties in addition to high conductivity. In our process, we use metal current collectors to achieve efficient current transport and use geometry to achieve flexibility. Typically, metal current collectors withstand elastic strains in a range of only 1% before plastic deformation and eventual fatigue. The geometry used here allows extending the range of elastic strain that the current collector can withstand during battery deformation. This contributes to an increase in fatigue resistance and battery lifetime. The extent of such increase is highly dependent on the current collector geometry. For example, in case of the serpentine current collector described in this work, the optically detectable plastic deformation does not occur till ~ 100% strain (**Figure 3.2**). The helical band spring served as a current collector for the flexible wire-shaped batteries. To fabricate the helical band, we first cold-rolled the tin-coated copper wire by passing it between two rollers that compressed the cylindrical wire into 30 μm thick and 400 μm-wide bands. Cold rolling served a dual function of fabricating bands with desired dimensions and increasing the yield point of the material. The resulting bands were winded into a

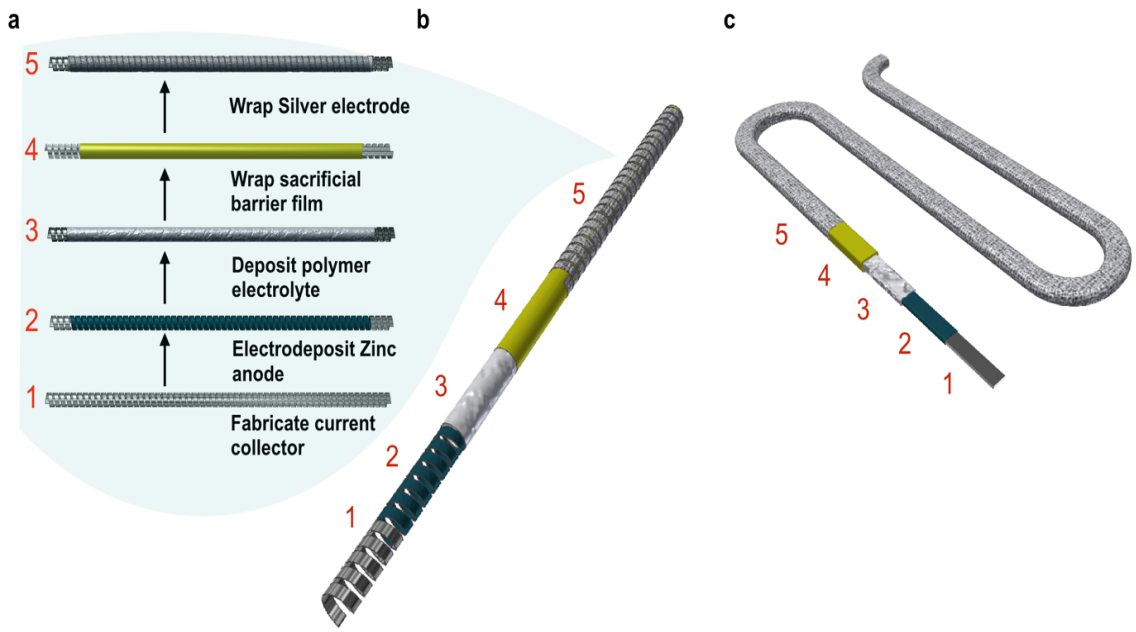

Fig. 3.1: (a) The assembly flow diagram for the (b) flexible wire-shaped batteries achieved by shaping the current collector-electrode as a helical band spring and (c) stretchable serpentine-shaped batteries fabricated using the current collector of serpentine ribbon geometry. Schematics drawn by Michael Wang (*128*).

helical spring shape with inner diameter of 1 mm **(Figure 3.3a,b)**. Adjustments to geometric parameters such as

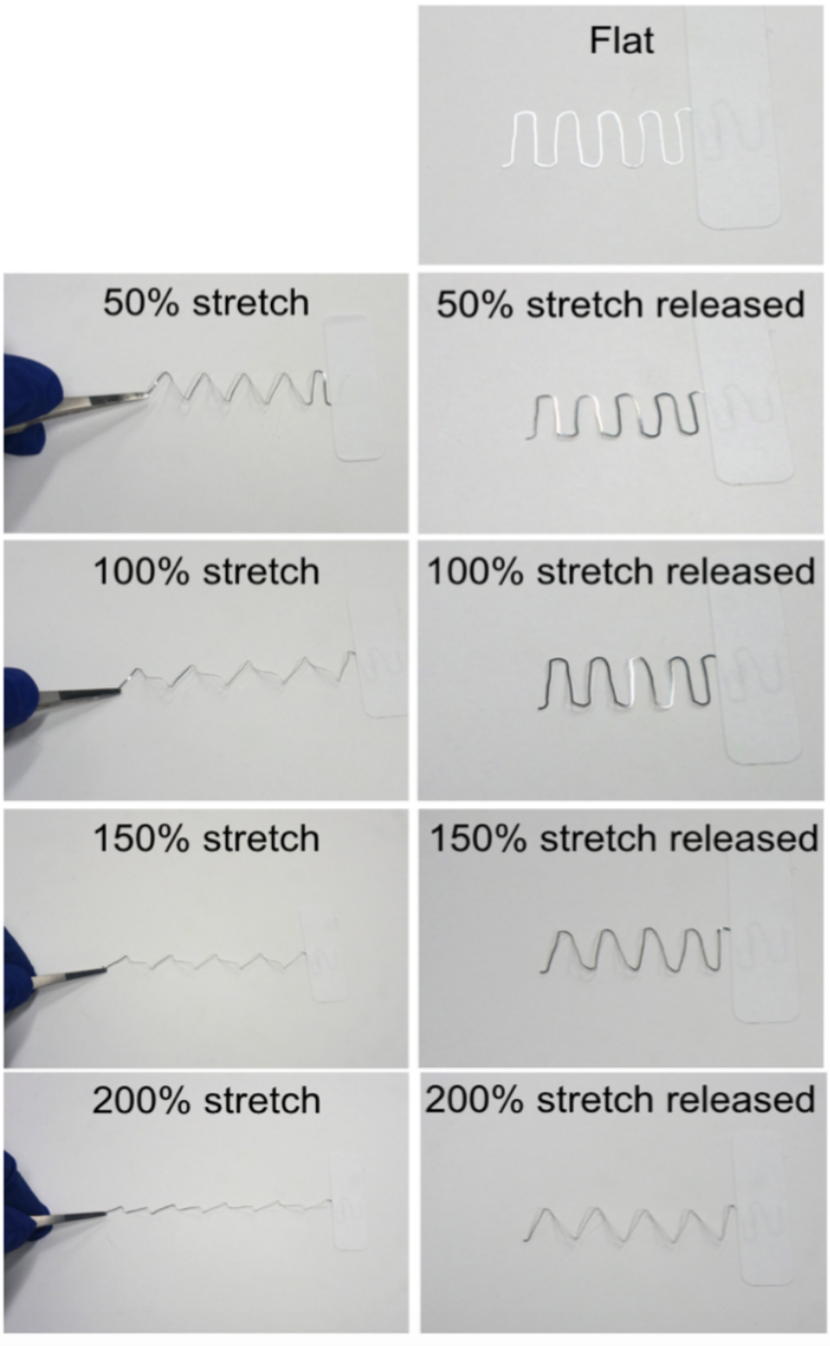

Figure 3.2: The images for the serpentine ribbon current collectors stretched to 50%, 100%, 150% and 200% before and after releasing the stretch (*128*).

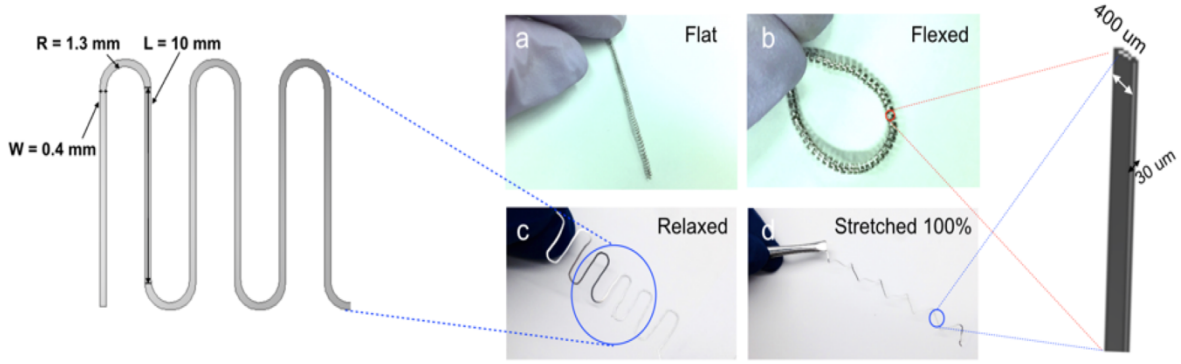

Figure 3.3: Optical images of the (a,b) helical band spring and (c,d) serpentine ribbon current collectors in a relaxed (a,c) and deformed (b,d) state. The schematics illustrate dimensions of the serpentine as well as thickness and width of the serpentine and helical band spring (*128*).

band width to spring diameter ratio, inter-coil distance, and band thickness can further decrease the stress: these parameters can be optimized to meet the geometric needs of the application, the energy density of the battery, and the flexibility requirement of the application. Analogously, the serpentine current collector for stretchable batteries was fabricated by bending the wire into the serpentine conformation and cold-rolling it into ribbons (Fig. 3.3c,d). The serpentine ribbon current collector accommodates mechanical strain through out-of-plane rotations, thus reducing the stress placed on materials when the structure is stretched (*119*, *120*, *216*, *217*). Similarly to the spring, the dimensions of the serpentine can be tuned according to the deformability requirements of the application.

In our process, Zn was electroplated on the tin-coated copper current collector to form the battery anode. Copper was used as a current collector material due to its high ductility and resistance to corrosion in alkaline environment. The ductility of copper allows the current collector to be cold- rolled into the desired shape and is not leveraged after that. Zn was plated at high current densities that resulted in hyper-dendritic morphology. This morphology can accommodate mechanical stress more effectively than dense Zn due to the presence of void spaces between dendrites and has been shown recently to cycle at higher rates and with better consistency than standard particulate paste zinc anodes (*193*, *218*). The Zn-current collector composite was dip-coated in the polyvinyl alcohol (PVA) based polymer electrolyte and wrapped with a cellophane layer. Cellophane protects the PVA separator and zinc anode from the oxidation by silver ions. Cellophane membrane is an effective a barrier for silver migration (*118*, *199*, *219*, *220*) due to

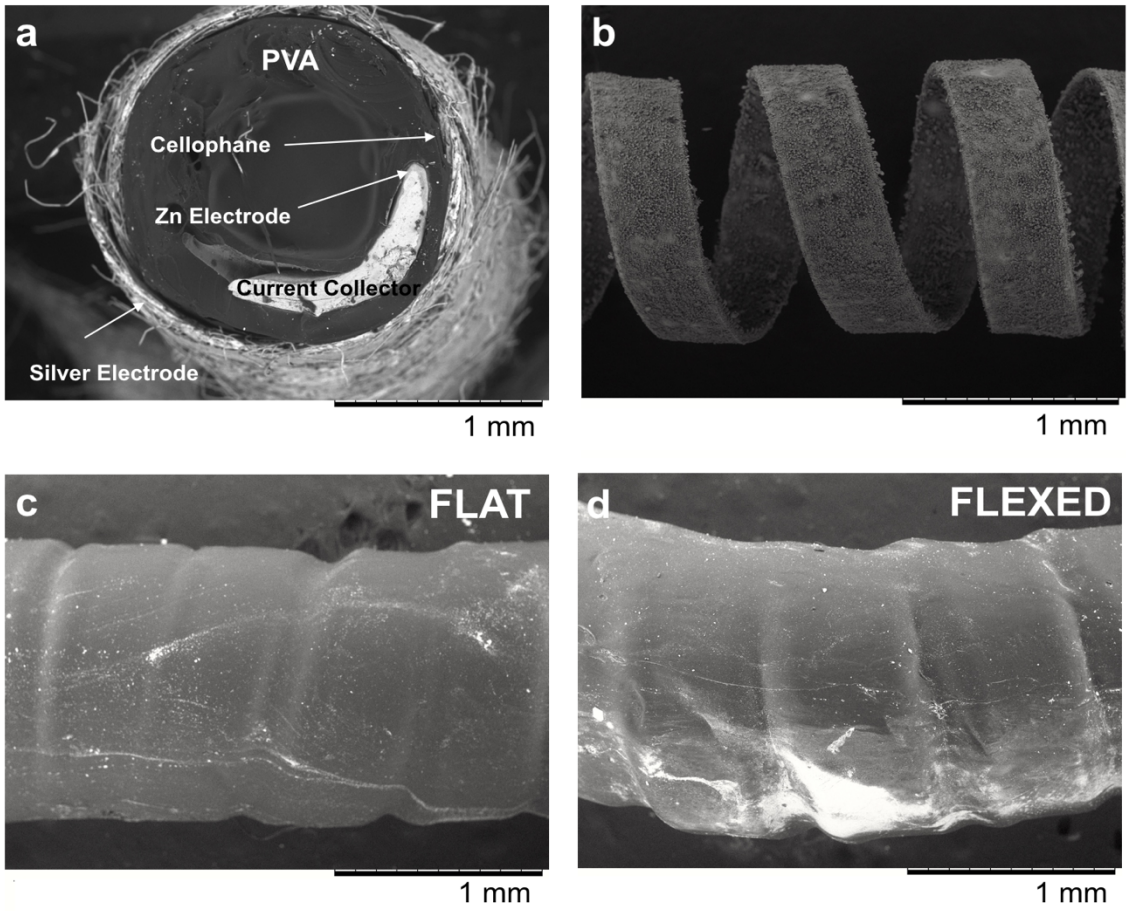

Figure 3.4: SEM image of the wire battery cross-section illustrating battery components (a). Helical spring current collector with electrodeposited Zn anode (b). Zn electrode coated with PVA polymer electrolyte in the flat configuration (c) and flexed to 1cm inner diameter (d) (*128*).

reducing properties of its constituent component – cellulose, which reduces silver ions to metallic silver, mitigating their further migration (*118*, *221*). The PVA polymer electrolyte further enhances the mechanical properties of the battery by providing flexible support to the Zn electrode and delocalizing the stress experienced by the electrode (*124*). Lastly, the Ag electrode was wrapped around the structure to finish the battery. The details of the battery components are demonstrated via SEM characterization of the wire battery architecture **(Fig. 3.4)**. The silver electrode was constructed by embedding silver nanoparticle ink into a conductive thread and cold-rolling the resulting composite to obtain a 30 μm-thick band **(Fig. 3.5)**. The thread embedded electrode used

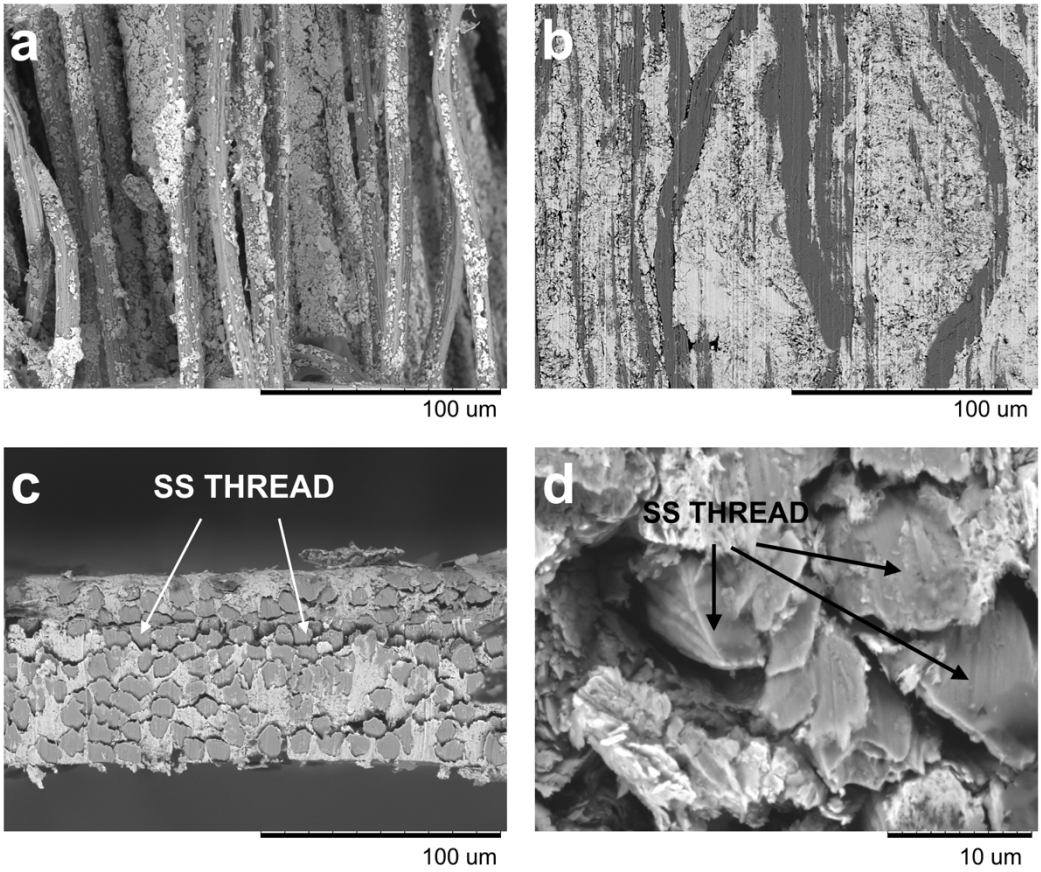

Figure 3.5: SEM micrograph of the top view (a,b) and cross section (c,d) of the silver electrode constructed by dip coating of the stainless steel (ss) thread into the silver nanoparticle ink before (a) and after (b-d) calendaring (*128*).

here can be easily wrapped around an electrode-electrolyte assembly of any shape, contributing to a simpler device manufacturing process. 2M KOH 0.2M ZnO liquid electrolyte saturated with Bi_2O_3 was added in the amount of 50 μL per centimeter of battery length before sealing the battery. The Ag_2O cathode was electrochemically formed after the battery is fully assembled by a slow (0.05C) charging cycle to 1.8 V.

3.3 Electrochemical and mechanical performance of the flexible wire batteries

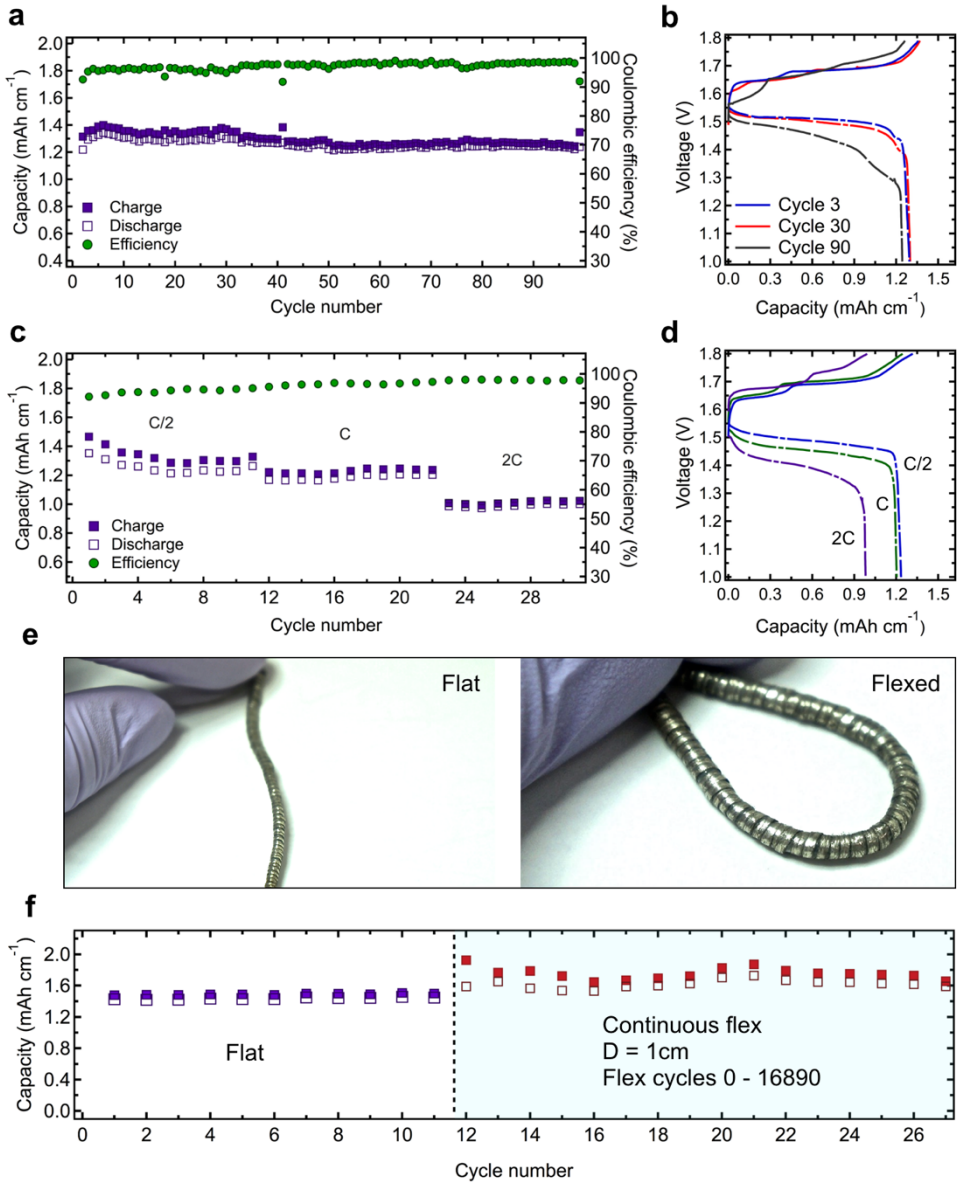

Fig. 3.6: (a) Capacity per unit length (mAh cm^{-1}) and coulombic efficiency (%) of silver-zinc wire battery cycled at 0.25C charge and 0.5C discharge rates between 1 V and 1.8 V. (b) Galvanostatic charge-discharge curves for cycles 3, 30, 90 of the battery in a. (c) Specific capacity (mAh cm^{-1}) and coulombic efficiency (%) of silver-zinc wire battery cycled between 1 V and 1.8 V at charge rates C, 0.5C, 0.25C and discharge rates 2C, C, 0.5C respectively. (d) Galvanostatic charge-discharge curves of the battery in c. (e) Optical images of the flexible wire battery in a relaxed and deformed state. (f) Cycling performance of the battery operated in a flat configuration and while being continuously flexed to a bending diameter of 1 cm (*128*).

The cycling performance of the wire battery based on the helical band current collector, operated between 1.8V and 1.0V, and corresponding charge-discharge curves are presented in **Fig. 3.6**a and Fig. 3.6b. The initial specific discharge capacity was approximately 1.33 mAh cm^{-1}, which fluctuated in the range of ~0.03 mAh cm^{-1} and stabilized after 33 electrochemical cycles. After 100 electrochemical cycles the magnitude of the discharge capacity incrementally decreased and reached 1.25 mAh cm^{-1}. The reduction in the capacity was accompanied by a decrease of the voltage values of the discharge curve plateaus. The mid-point voltage of the discharge plateau decreased from ~1.52 V for the 3rd electrochemical cycle to ~1.51 V and ~1.48 V for the 30th and 90th electrochemical cycles respectively, as shown in Fig. 2b. Such behavior is anticipated in silver-zinc batteries and usually attributed to an increase in the impedance of the battery with cycling. This increase in impedance is caused by the deterioration of the polymer electrolyte and cellophane barrier by oxidative attacks of silver ions; loss of electrolyte through plastic encapsulation; and corrosion of the current collectors and electrodes (*118*). Overall, the battery charged at 0.25C and discharged at 0.5C rates has high specific capacity (~1.25 mAh cm^{-1} at 0.5C discharge rate) and exhibits stable performance with capacity retention of 94% over 100 electrochemical cycles. This is on the high end of performance of silver zinc battery systems, which have typically had cycle life limited to 50-100 electrochemical cycles (*190*).

Cycling performance of the battery at different rates (0.25C, 0.5C, C charge and 0.5C, C, 2C discharge respectively) and corresponding charge-discharge curves are presented in Fig. 3.6c and Fig. 3.6d respectively. The 2:1 ratio of discharge rate to charge rate was previously shown to be optimal because of the effects of cycling rate on the morphology of silver and on material utilization during cycling (*103*). The battery retained 96.5% and 82% of its capacity when the discharge rate was increased from 0.5C to C and from C to 2C respectively. The specific capacity fluctuated in a range of ~0.025 mAh cm^{-1} when the battery was discharged at 0.5C and remained stable when the battery was discharged at C and 2C rates. The coulombic efficiency increased from ~95% at 0.5C to ~97% and ~98% at C and 2C rates respectively. Typically, smaller Ag particles are formed when the battery is discharged at higher rates. Smaller particles are oxidized fully on the subsequent charge resulting in more efficient material utilization, while material in larger particles (which form during slow discharge) can remain partially unutilized due to ionic transport limitations (*103*). Thus, the battery operates with higher efficiencies and improved stability when cycled at rates of 0.5C and above, and retains 79% of its capacity when discharge rate is increased from 0.5C to 2C.

Since power consumption of wearable electronic systems is application dependent, the battery is likely to operate at varying discharge rates that are contingent on the load duty cycle of the system. We expect battery to exhibit stable cycling profile if the load currents fall within the range of 0.5C and above of the battery discharge rates. On the other hand, capacity might fluctuate or gradually fade with cycle number, if the battery is discharged at slower rates (*103*). However, among other factors, the period of time for which the slow discharge takes place determines if such decrease or fluctuation in the battery capacity will actually occur. Since numerous wearable

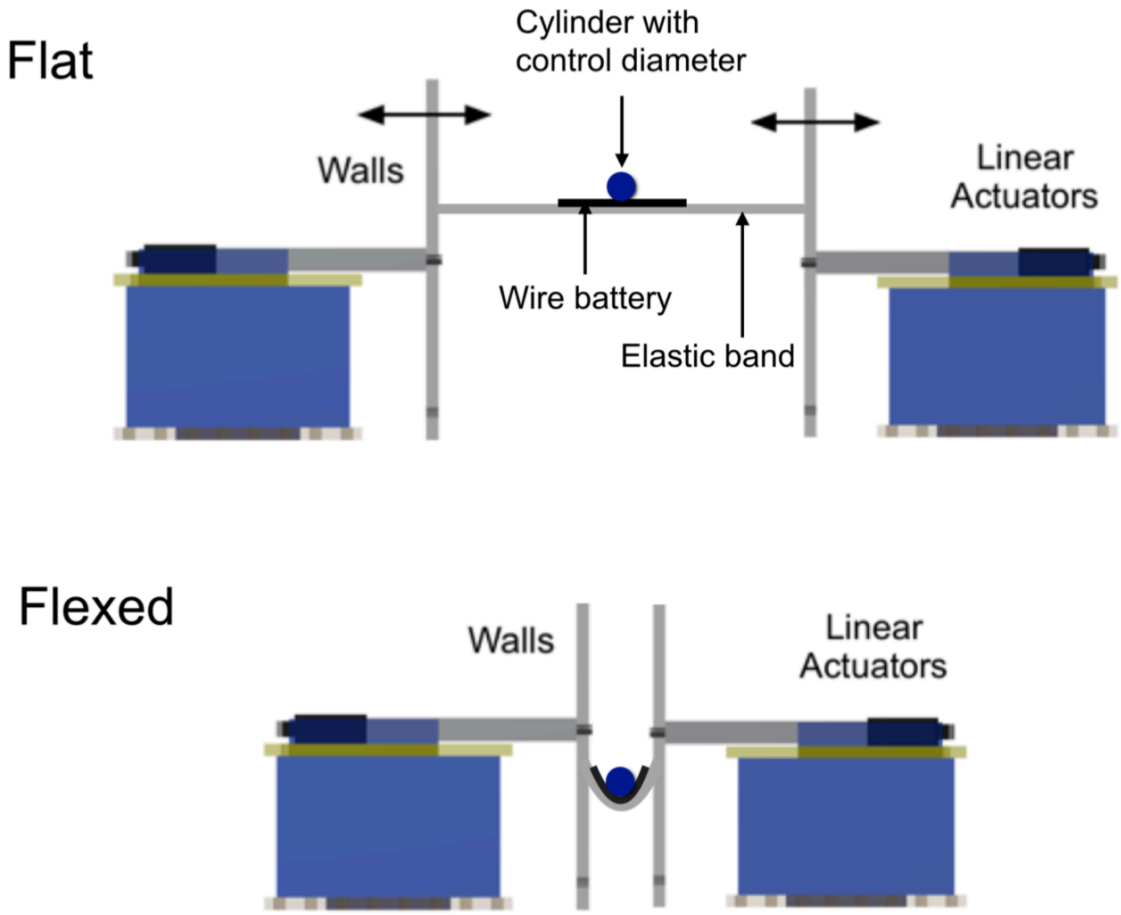

Figure 3.7: The schematic of the custom-made flexing apparatus. The battery is placed on the elastic band attached on both ends to the two linear actuators that control the flexing speed. Motion of linear actuators towards each other causes the elastic band to relax and bend. Schematics drawn by Michael Wang.

electronic systems operate in the high current regime during data collection or transmission (*222*, *223*), the bulk of the battery's capacity is expected to discharge at high rates. Therefore, we do not expect decrease in cycling stability when these batteries are utilized as part of wearable systems. The effect of combination of charge/discharge rates on the capacity utilization of these batteries should be studied more rigorously with respect to specific application.

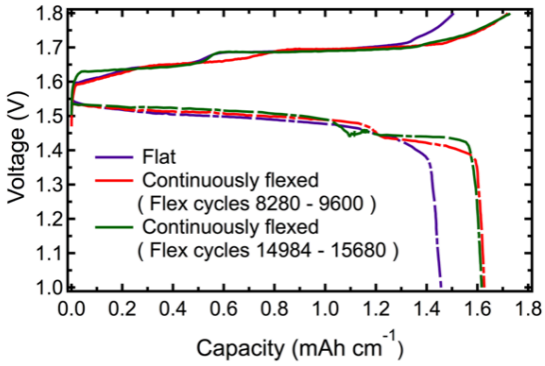

Figure 3.8: Galvanostatic charge-discharge curves for the 10th, 19th and 26th electrochemical cycle of the battery presented in Figure 2f. The charge-discharge curves for the 19th and 26th cycle were obtained while operating the battery under continuous flexing regime, when the curves for the 10th cycle were obtained while cycling the battery in a flat configuration. The overall capacity of the battery increases by over 10% as a result of flexing. The increase in capacity can be attributed to increase in the active surface area of the limiting Ag electrode and thus higher material utilization (*128*).

Wire-shaped batteries for wearable applications are likely to undergo thousands of flex cycles of various combinations throughout their lifetime. Therefore, excellent mechanical endurance under repetitive load is a major design consideration for such a battery. The optical images of the flexible wire battery in flat and flexed configurations are presented in Fig. 3.6e and show high flexibility. The effect of repetitive dynamic mechanical load on the electrochemical performance was studied by monitoring the performance of the battery when the device is operated under continuous flexing conditions. The flexing was performed using a custom-made stage, shown in **Fig. 3.7**, at the rate of 2 flexing cycles per minute. The length of the battery used for this study was 1.5 cm. By keeping the length of the battery comparable with the bending diameter, we ensured that the device was subjected to mechanical stress throughout its whole length. Fig. 2f compares the cycling performance of the battery operated in a flat configuration and while being continuously flexed to a bending diameter of 1 cm. Minor fluctuations in capacity and decrease in efficiency are observed when the battery is operated in the continuous flexing regime versus when operated in a flat configuration. The capacity fluctuations were more pronounced during the first five electrochemical cycles; after that the system stabilizes, as indicated by the constant capacity and the increased efficiency of consecutive cycles. The overall capacity of the battery increased by over 10% as a result of flexing (**Figure 3.8**).

3.4 EIS analysis of the processes occurring in the wire battery as a result of flexing

The specific capacity of as-fabricated flexible wire batteries based on spring current collector varies in the range 0.8 mAh cm^{-1} to 1.4 mAh cm^{-1} (caused by the manual assembly process of the limiting silver electrode) and increases after flexing up to 1.6 mAh cm^{-1}. To analyze processes occurring in the wire battery as a result of flexing that lead to the capacity increase, we performed electrochemical cycling, while periodically stopping and flexing the battery 1500 times in-between the electrochemical cycles. EIS measurements were carried out before and after flexing while keeping the battery in a flat position. The flexing diameter was decreased from 2.54 cm to 1.60 cm and finally to 1 cm after each set of flexing cycles. **Figure 3.9** shows electrochemical cycling performance of the battery. The capacity first increases gradually from 0.8 mAh to 1.4 mAh following the first set of 1500 flexing cycles and then stabilizes with only minor increase immediately following each consecutive flexing cycle to a smaller radius. We speculate that increase in capacity after flexing was caused by increase in the active surface area between the limiting silver electrode and electrolyte. It is very likely to occur through formation of flexing-induced micro cracks in the thread-embedded silver electrode. Since electrolyte transport to the additional areas of the electrode does not occur instantaneously; the capacity increases gradually for the seven electrochemical cycles following the first set of flexing cycles. Minor increase in capacity immediately following second and third set of flexing cycles can be attributed to the formation of additional electro-active surfaces when battery is flexed to the smaller bending radii. To confirm our speculation we conducted analysis of the Nyquist plots from the EIS data.

The Nyquist plots consist of two depressed semicircles in the high to medium and medium to low frequency ranges and the sloping tail in the low frequency range. Inductive data obtained at high frequencies are not included in the plot, since they are irrelevant to the discussion and do not influence the rest of the impedance spectra (*200*). The high frequency intercept with abscissa is attributed to the Ohmic resistance of the battery with the highest contribution from the electrolyte resistance (*31*, *200*, *201*). The two depressed semicircles represent kinetic impedance from both electrodes, dominated by the impedance of limiting silver electrode (*31*, *200*, *201*). The semicircles are depressed due to non-uniformity of the electrodes and thus varying capacitance and resistance contributions throughout the electrodes (*200*). The first semicircle was attributed to the charge transfer interfaces within the battery. The EIS response is dominated by the second semicircle, which was attributed to the Ag_2O surface coverage resistance (*200*). The low frequency spectrum of the battery impedance is influenced predominantly by solution diffusion Warburg process at Ag_2O cathode (*201*). Generally, increase in active surface area of an electrode results in the decrease of the kinetic impedance response due to increased area available for charge transfer (*224*, *225*). However, in zinc-silver system the response is overweighed by the contribution from Ag_2O coverage resistance. It is known that both Ag and Ag_2O are present in the electrode when the battery is discharged (*209*, *210*, *226*) and that Ag_2O is mechanically weaker then Ag (*205*).

Therefore, when battery is flexed micro cracks are likely to occur at the areas of the electrode with high Ag_2O content, resulting in exposing more of the Ag_2O surface and increasing overall surface resistance of the electrode-electrolyte interface. If our speculations about the increase in capacity of the battery being caused by increase in the active surface area of silver electrode are correct, then increase in capacity would be reflected in the increase of the radius of the second semicircle of the Nyquist plot.

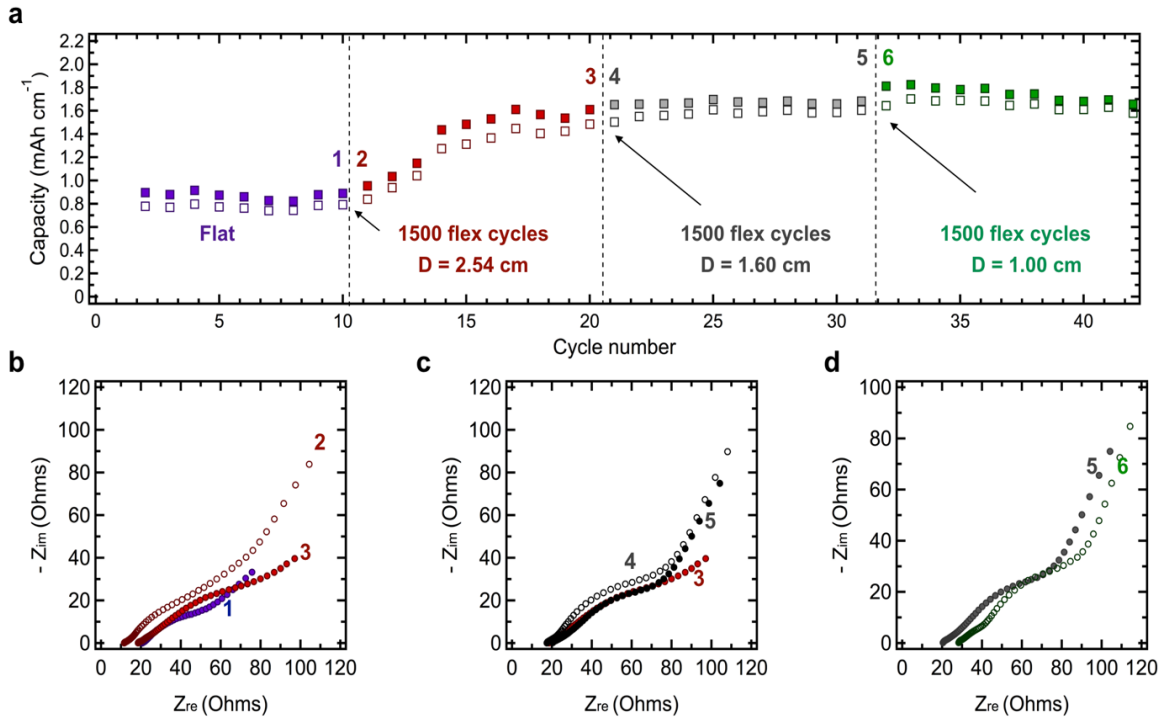

Figure 3.9: (a) Cycling profile of the wire battery subjected to periodic flexing of 1500 flex cycles. The flexing diameter was decreased from 2.54 cm to 1.60 cm and to 1 cm after each set of flexing cycles. (b-d) The Nyquist plots of the EIS measurements taken before and after flexing to 2.54 cm, 1.60 cm and 1 cm respectively. EIS measurements were performed at frequencies ranging from 10^6 to 0.1 Hz at amplitude of 10 mV and were carried out while keeping the battery in a flat position (*128*).

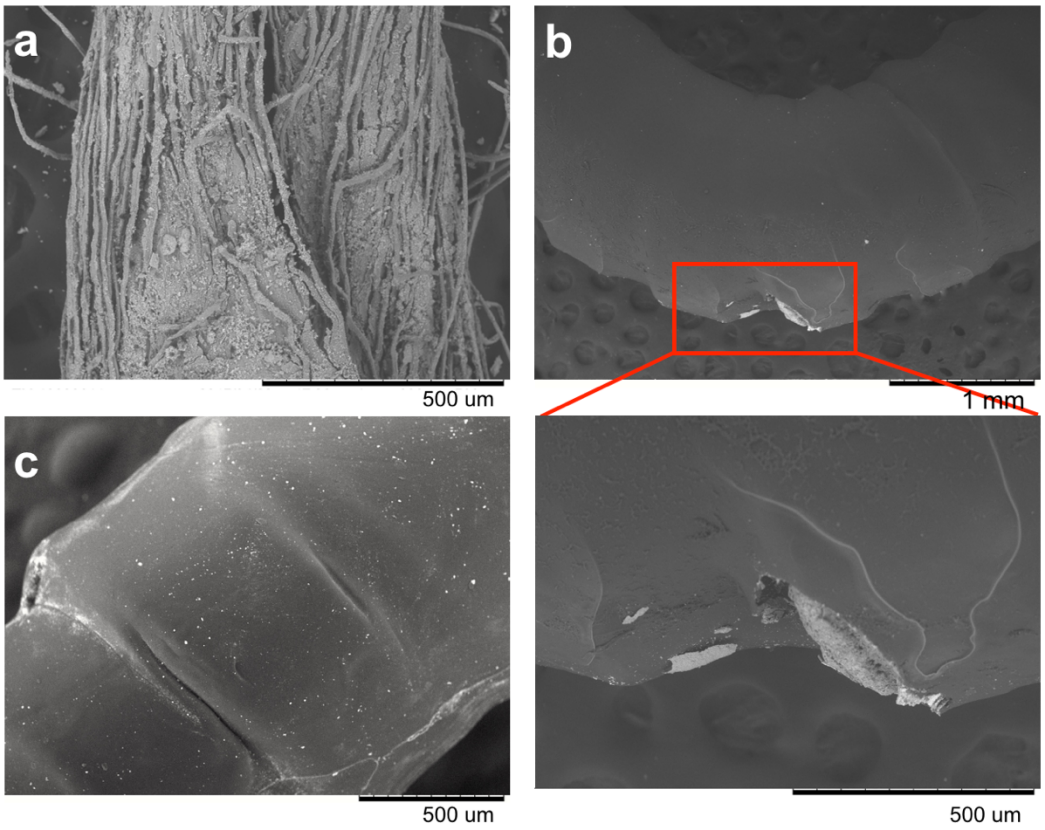

Figure 3.10: SEM micrograph of cycled 180 times (in a charged state) silver electrode (a). Silver ink remains adhered to the thread after cycling. SEM images of the Copper-Zn-PVA composite after subjecting to 20 000 flexing cycles to the radius of 0.5 cm (b,c). Localized tear of the PVA polymer electrolyte caused by flexing (b). Plastic deformation of the polymer electrolyte layer in the regions in-between the coils, represented by wrinkling of the PVA (c). Since tears in the PVA layer lead to short circuits and consequent failure of the battery, the mechanical properties of the electrolyte-separator are the limiting factor to the mechanical performance of this system (*128*).

The Nyquist plots of the EIS measurements taken before and after flexing are presented in Figure 3.9 b-d. Curves 1 and 2 in Figure 3.9b correspond to Nyquist plots of the EIS measurements taken immediately before and after the first set of 1500 flexing cycles respectively. Curve 3 corresponds to the measurement taken after ten electrochemical cycles following the flexing. The increase in the radii of the second semicircle of the 2nd and 3rd curves corresponds to increase in capacity following the flexing and consecutive electrochemical cycling. Figures 3.9c and 3.9d show Nyquist plots of the EIS measurements taken before and after second and third sets of flexing cycles. The second semicircle radii of these plots remain relatively constant. Thus, increase in capacity coincides closely with the increase in the radii of the second semicircle in the EIS spectra, supporting our speculations that the increase in capacity of the battery is caused by increase in the

active surface area of silver electrode. Therefore, EIS measurements support the speculation that the increase in capacity is attributed to an increase in the active surface area of the limiting Ag electrode, leading to higher material utilization as a result of flexing. Thus, the electromechanical characterization demonstrated that constructing the battery around the helical band spring current collector resulted in a device resilient to repetitive dynamic mechanical load. The post-mortem SEM characterization **(Fig. 3.10)** invokes that further increase of sustainability of the wire batteries should be focused on polymer electrolyte.

3.5 Electrochemical and mechanical performance of stretchable batteries

The elongation of the battery based on the helical spring current collector is limited by the mechanical properties of the polymer electrolyte, cellophane layer and silver electrode. Replacing the helical spring current collector with serpentine ribbon geometry overcomes this limitation and improves the effective macroscale elasticity of the battery.

The electromechanical characterization of serpentine-based batteries was performed using a simple structure. Prior to electrochemical characterization of the battery, the stretching and elastic deformation limits were determined empirically. The optical images for the serpentine ribbon current collectors stretched to various degrees as well as after releasing the stretch are presented in Fig. 3.1. The serpentines had a stretching limit close to 200%. Optically detectable plastic deformation occurred after 100% stretch. Although the current collectors are likely to deform plastically prior to reaching 100% stretch limit (*217*), the deformation must have occurred locally, since the structure was able to return to its original shape. Therefore 100% stretch was chosen as the experimental limit for electromechanical testing of the battery.

The electromechanical performance of the serpentine battery was then evaluated by operating the battery flat, 100% stretched, as well as under periodic stretch conditions at 0.25C charge and 0.5C discharge rates between 1 V and 1.8 V. The specific capacity was normalized by the active area of the battery, i.e. excluding the area occupied by the elastomer, and is in the range of 3.5 mAh cm^{-2} when discharged at 0.5C rate, as can be seen in **Fig. 3.11** a-c. Fig. 3.11a shows electrochemical cycling performance of the battery that was first operated in a relaxed configuration (region I), then stretched to 100% (region II) followed by cycling in a relaxed configuration (region III). Subsequently the battery was subjected to five sets of 100 stretch cycles. Every set of 100 stretch cycles was alternated with one electrochemical cycle (region IV) followed by cycling in a relaxed configuration (region V). This set of experiments allowed characterization of the electromechanical performance of the battery after periodic stretching as well as under the strain of 100%.

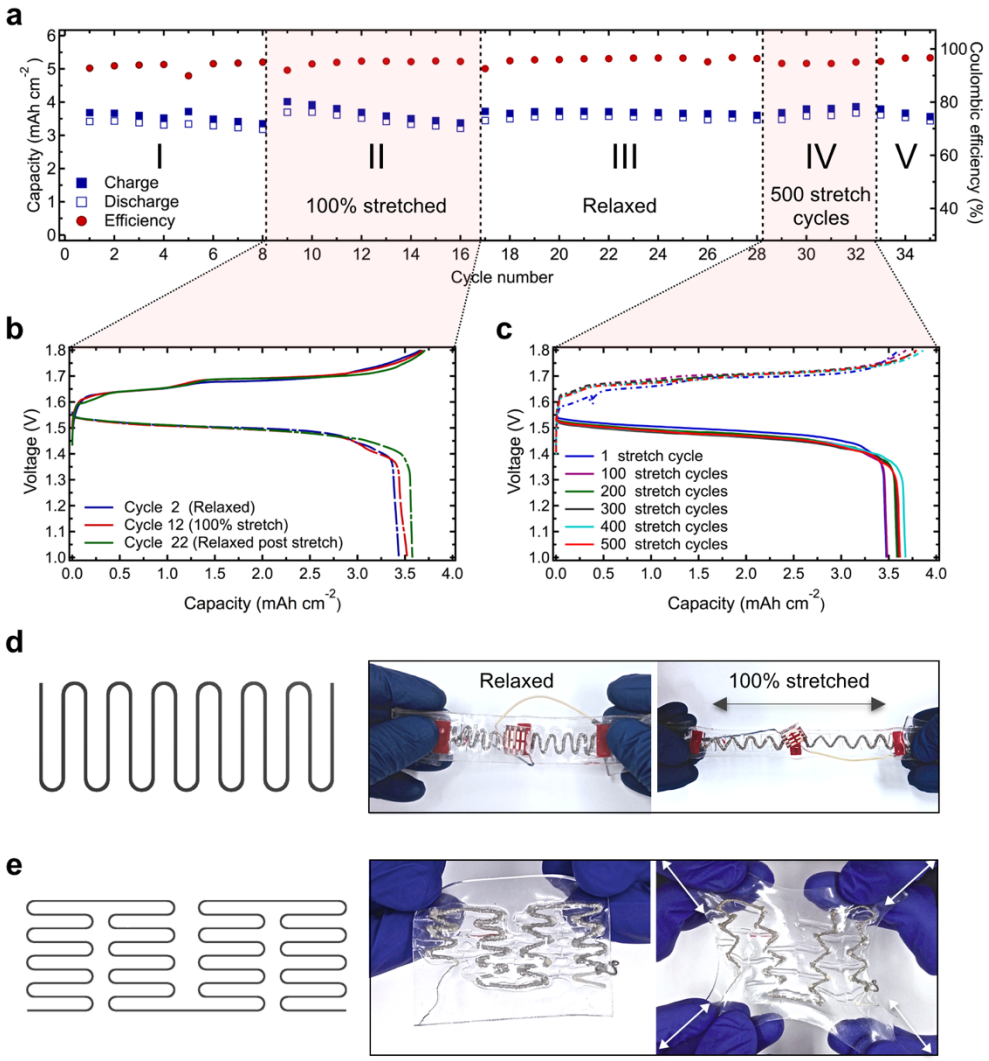

Figure 3.11: (a) Specific capacity (mAh cm^{-1}) and coulombic efficiency (%) of the battery that was first operated in a relaxed configuration (region I), then stretched to 100% (region II) followed by cycling in a relaxed configuration (region III), then subjected to five sets of 100 stretch cycles. Each set of 100 stretch cycles was alternated with one electrochemical cycle (region IV) followed by cycling in a relaxed configuration (region V). (b) The galvanostatic charge-discharge curves for the 2^{nd} (flat configuration), 12^{th} (stretched configuration) and 22^{nd} (flat configuration) electrochemical cycles of the battery in a. (c) Galvanostatic charge-discharge curves for the electrochemical cycles following 1^{st}, 100^{th}, 200^{th}, 300^{th}, 400^{th}, 500^{th} stretch cycles of the battery in a. (d) Schematics of simple serpentine current collector and optical images of four serpentine-shaped batteries connected in series. (e) Schematics of self-similar serpentine current collector and optical images of the full battery assembled around such current collector. Geometry of the battery facilitates biaxial stretching (*128*).

Electrochemical cycling performance of the battery in a flat and 100% stretched configurations is presented in Fig. 3.11a as regions I, II and III. The initial value of capacity is ~3.5 mAh cm^{-2}. The capacity increases during the electrochemical cycle immediately following the change in mechanical configuration of the battery, i.e. after the battery is stretched (region II) and after it is released to its original state (region III), and then gradually stabilizes to its initial value during five consecutive cycles. The galvanostatic charge-discharge curves for the 2^{nd} (flat configuration), 12^{th} (stretched configuration) and 22^{nd} (flat configuration) electrochemical cycles are presented in Fig. 3.11b. The internal resistance (IR) drop is not observed from the plateaus of the charge-discharge curves after the battery was stretched, indicating that active materials are not delaminating from the current collectors. Overall the battery exhibits stable performance in both flat and 100% stretched configurations with minor fluctuations in the capacity in both cases.

Figure 3.11a region IV shows electrochemical cycling performance of the battery under the periodic stretch condition. The data demonstrates that the overall capacity of the battery increases by >3% after 200 stretch cycles and remains unaffected by 300 consecutive stretch cycles. This minor change in capacity can also be observed in the corresponding galvanostatic charge-discharge curves (for the electrochemical cycles following 1^{st}, 100^{th}, 200^{th}, 300^{th}, 400^{th}, 500^{th} stretch cycles) presented in Fig. 3.11c. The specific discharge capacity of the battery increased from ~3.5 mAh cm^{-2} to ~3.6 mAh cm^{-2} after 200 stretch cycles and remained stable on subsequent cycles. Thus, these results clearly demonstrate that the stretchable battery based on serpentine current collector exhibits stable cycling profile when tested under both periodic mechanical load conditions and in a stretched configuration.

The simple serpentine configuration is suitable for systems intended for uniaxial stretching. The configuration allows easy connection of several batteries in series to produce higher output voltage, if such is required. Four serpentine-shaped batteries are connected in series continuously to power an organic light emitting diode (OLED) (with the current demand of 4.17 mA at ~ 6 V) while being stretched to 100%, as shown in Fig. 3.11d. Electronic systems designed for biaxial in-plane stretching cannot be effectively integrated with a battery having serpentine configuration due to the unidirectional stretchability of the serpentine system. This drawback can be overcome by changing the current collector geometry to a self-similar serpentine ribbon. Fig. 3.11e shows schematics of the self-similar serpentine and optical images of the full battery assembled around such a current collector in relaxed and stretched configurations. The Figure demonstrates that the geometry of the battery facilitates its biaxial stretching. This makes a battery with self-similar serpentine configuration a promising candidate for integration with devices that stretch along two axes.

3.6 Integration into wearable energy harvesting and storage accessory

We have developed a wearable energy harvesting and storage bracelet based on organic photovoltaic modules and the wire-shaped batteries described above. A power source in the form

of a bracelet is ideal to power wearable sensors on the wrist, a location in which a number of vital biosignals can be measured (*212*). For this application, the battery dimensions are selected to provide sufficient capacity to power wearable low-power electronics, and the voltage of the photovoltaic module is selected in order to charge the battery directly without the addition of circuitry such as maximum power point tracking. The battery charging profiles through typical workday lighting conditions are studied.

The design of a battery for integration into a wearable system is guided by such considerations as safety, mechanical properties, and the amount of energy required to satisfy the application requirements. Wire architecture, whose design allows seamless integration into accessories, was chosen for this system. We used a low duty cycle resistive sensor system (*222*) as a target electronic system that could be powered by the battery. The battery was designed to meet the energy requirement of such a system, which was estimated to be ~6 mWh day^{-1}. The capacity of the wire battery can be readily adjusted through varying its length and was tuned to be 4 mAh, which is sufficient for powering the sensor system during the course of one day.

Design of the battery for integration into wearable energy harvesting and storage accessory

Since increasing the length of the wire battery can lead to increased internal resistance, causing the battery to discharge at lower voltage, we investigated the magnitude of the voltage drop to ensure that the battery of the chosen length is able to meet the energy requirements of the target system and studied the cycling performance of the battery to ensure that it retains its capacity during cycling. We compared galvanostatic charge-discharge curves of 1-cm and 4-cm batteries to estimate the magnitude of the potential drop associated with increased battery length. **Figure 3.12**a shows that the discharge plateau of the 4-cm battery exhibits ~0.049 V lower voltage values compared to the 1-cm battery, as estimated by midpoint voltage. On average, the observed potential drop was ~0.03 V and never exceeded ~0.05 V. The variations in voltage drop were caused by the manual assembly of the battery components and could be minimized by automating the assembly process. The 4-cm battery therefore provided the target discharge voltage of ~1.5 V despite increasing the length by 4 times. Since the increase in internal resistance of the device was small, the 4-cm battery was able to meet the energy requirement of >6 mWh.

Since the battery was sized for daily cycling, we investigated the cycling stability of the battery to ensure that it retains its capacity during cycling. The cycling profile of the battery is shown in Figure 3.12b. The battery exhibited good performance, with an average capacity of 1.1

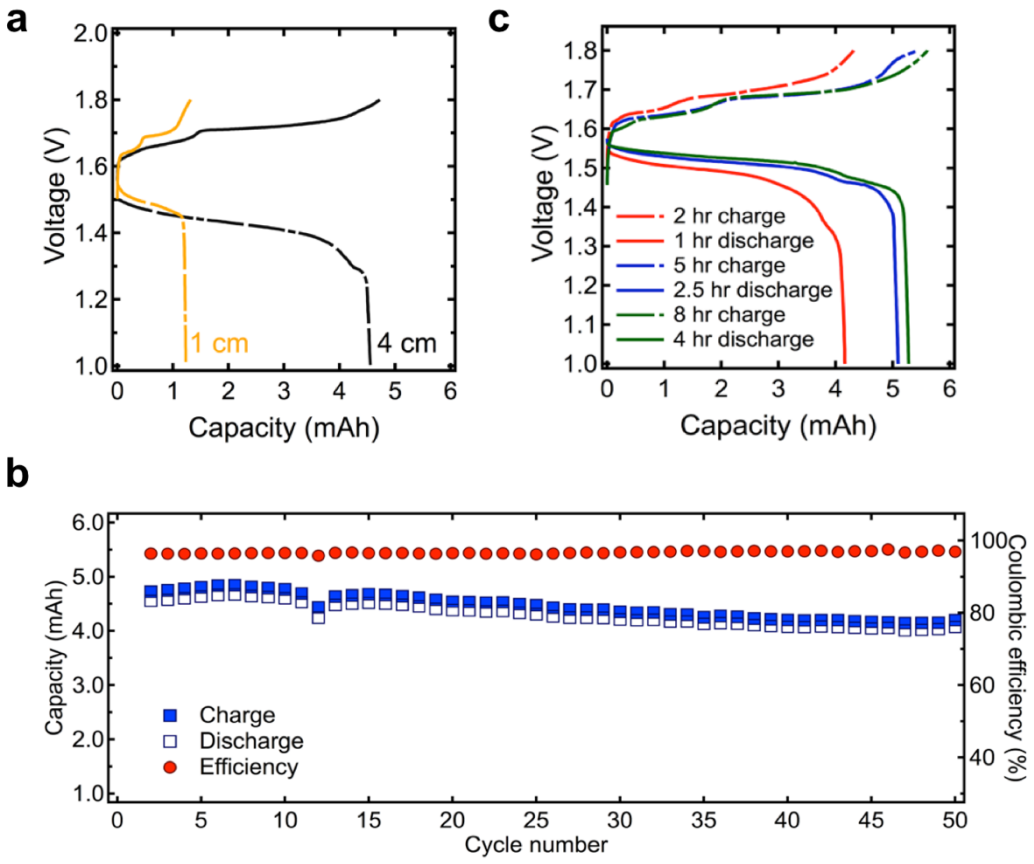

Figure 3.12 (a) Galvanostatic charge-discharge curves of 1-cm (yellow) and 4-cm (black) silver-zinc wire battery operated at 0.25C charge and 0.5C discharge rates. (b) Capacity (mAh) and coulombic efficiency (%) of 4-cm battery cycled at 0.25C charge and 0.5C discharge rates between 1 V and 1.8 V. (c) Galvanostatic charge-discharge curves of 4-cm battery for charge rates 0.125C, 0.2C, 0.5C and discharge rates 0.25C, 0.4C, 1C respectively *(128)*.

mAh, coulombic efficiency of ~96.5 %, and capacity retention of 88% after 50 electrochemical cycles. The minor decrease in capacity can be attributed to the migration of silver ions through the plastic seals towards the zinc electrode and subsequent poisoning of the electrode, coupled with factors associated with battery aging such as deterioration of the cellophane barrier and PVA separator and corrosion of the current collectors. Therefore, the battery maintained the capacity set by the wearable accessory design parameters after 50 electrochemical cycles.

Because the rate of charge depends on the lighting conditions as well as the efficiency of the solar module, it is important to evaluate the performance of the 4-cm-long wire battery cycled at different charge-discharge rates in a range relevant to solar charging. The galvanostatic charge-discharge curves for the battery operated at different rates (0.125C, 0.2C, 0.5C charge and 0.25C, 0.4C, 1C discharge respectively) between 1 V and 1.8 V are shown in Figure 3.12c. Although the charge to discharge rate ratio will vary under real life conditions, the analysis of its effects on the battery performance is beyond the scope of the paper. Figure 3.12 c shows that the range of charge voltage falls between 1.6 V and 1.8 V for all charge rates, which is within the window acceptable for the solar module. In addition, the battery retained capacity above 4 mAh over the range of discharge conditions. Thus, the battery maintained the capacity set by the wearable accessory design parameters after 50 electrochemical cycles, provided the target discharge voltage of ~1.5 V, and could be cycled at different charge-discharge rates in a range relevant to solar charging.

Wearable accessory design and performance

Although flexibility is frequently mentioned as a strict requirement for wearable electronics, jewelry is an exception as it often contains a combination of rigid and flexible structures. Thus, a wide range of potential jewelry-integrated power source designs can be explored that include both rigid and flexible devices. Here, rigid OPV modules were designed as discussed elsewhere (*129*) , based on a bulk heterojunction active layer of poly[N-9'-heptadecanyl-2,7-carbazole-alt-5,5-(4,7-di-2-thienyl-2',1',3'-benzothiadiazole)] (PCDTBT) and [6,6]-phenyl C_{71}-butyric acid methyl ester ($PC_{71}BM$). The modules used indium tin oxide (ITO) coated glass substrates, a hole transport layer of poly(3,4-ethylenedioxythiophene):polystyrene sulfonate (PEDOT:PSS), and the cathode was aluminum with a dipole interlayer of polyethyleneimine ethoxylated (PEIE). A module with 4 cells was selected because it provides a constant and high charging current over the battery voltage range.

The OPV modules and battery were then connected together to characterize the solar charging process in a wearable energy harvesting and storage system. **Figure 3.13** shows photographs of a bracelet consisting of a 4-cell OPV module with a wire battery integrated into the wristband, an example design of an energy harvesting and storage accessory. The OPV module was connected directly to the battery, maintaining it at the same voltage as the battery throughout charging. The voltage across and current flowing into the battery during 12 hours of charging under the 3000 lux CFL are given in Figure 3.13b, showing the increase in battery voltage as it charged as well as the stability of the OPV module current. Figure 3.13c shows the voltage and current as the battery was charged completely under simulated sunlight. The duration of the charge, 4 hours,

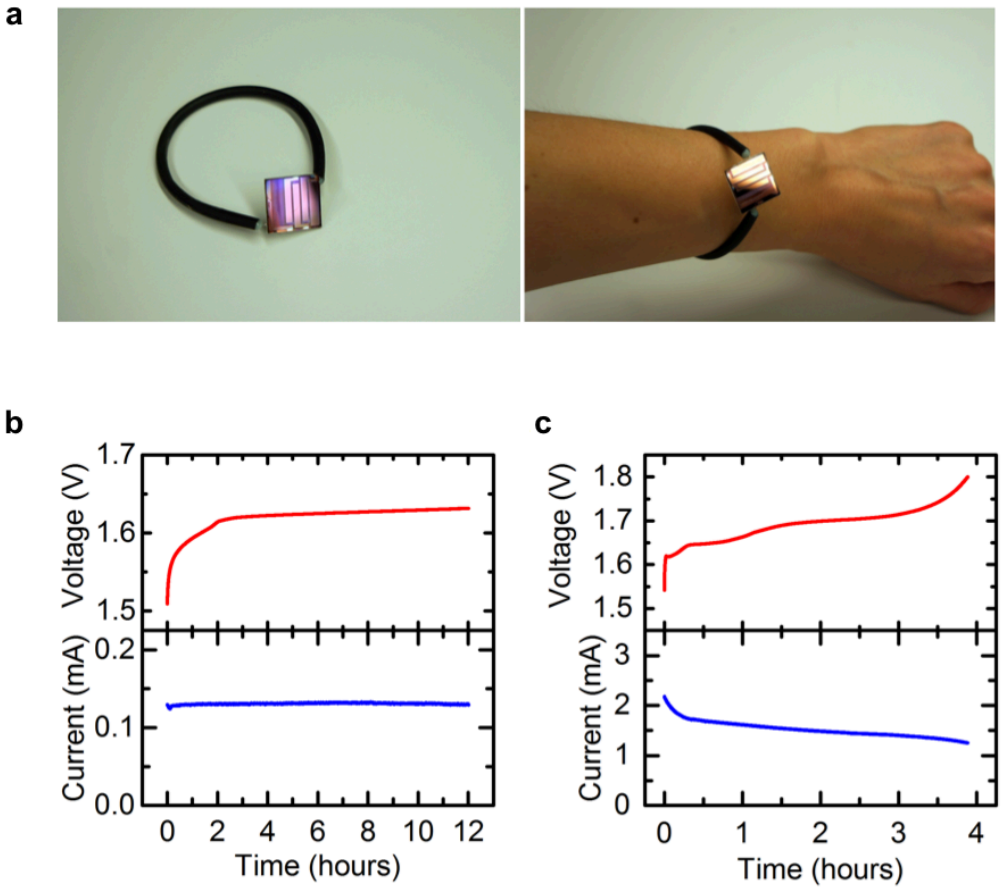

Fig. 3.13: (a) Images of photovoltaic module and wire battery integrated into a wearable bracelet. (e-f) Voltage and current during battery charging. OPV module is exposed to either CFL lighting with illuminance of 3000 lux (b) or sunlight (c). Data collected by A. Ostfeld (*128*).

with an average current of 1.4 mA, is consistent with the measured capacity of the battery operated at this rate.

3.7 Conclusion

We demonstrate a new design concept to fabricate stretchable and flexible batteries. This strategy relies on utilizing mechanically robust current collector geometries such as serpentines, or helical springs to serve as a structural support for the rest of the battery components. The choice of current collector geometry determines the mechanical properties of the battery. To demonstrate the concept we explored two different current collector geometries – helical band spring and serpentine ribbon. The battery fabricated around the helical band spring current collector has the form factor of a flexible wire. Such geometry ensured omnidirectional flexibility and fatigue resistance to flexing motions. Electrochemical-mechanical characterization of flexible wire-shaped batteries based on the helical band spring current collector showed that they can withstand flexing >17,000 times to the bending radius of 0.5 cm. The elongation of the wire battery is limited by the mechanical properties of the polymer electrolyte, cellophane layer and silver electrode. In order to achieve devices that can be readily stretched we fabricated batteries around serpentine ribbon current collectors. Serpentine-shaped batteries retained their electrochemical performance while being stretched to 100% and can accommodate flexible motions in one plane. Furthermore, we have shown that biaxial stretching can be realized by utilization of a self-similar serpentine current collector. Therefore, using current collectors with spring and serpentine geometries as a backbone for the battery components represents a promising fabrication approach for compliant batteries with a range of mechanical properties. Integration with the organic solar module into a wearable energy bracelet demonstrates the suitability of these batteries for real-life applications.

3.8 Experimental section

Fabrication of the battery components

To fabricate the helical band spring current collector we used a 125 μm diameter tin coated copper wire (Alpha Wire, Tinned Copper, ASTMB-33, CID-A-A-59551). Commercially pure Tin (Sn), 40 micro-inches thick, is plated on copper by the manufacturer as a corrosion inhibitor. The wire was cold-rolled using calendar press to the thickness of 30 μm and winded around a 1 mm diameter rod to form a helical band spring. To fabricate the serpentine current collector, the same wire was first bent into a serpentine structure of the desired configuration and then cold-rolled to the thickness of 30 μm.

The zinc electrode was electrodeposited on a tin coated copper current collector (Alpha Aesar) in the galvanostatic mode at the current density of 40 mA cm^{-2} for 3000 seconds using a Gamry Potentiostat. To prepare the electrolyte, corresponding amounts of KOH (Sigma Aldrich

Figure 3.14: The schematic of the encapsulation of serpentine battery (*128*).

85% anhydrous pellet) and ZnO (Sigma Aldrich 99.9%) were dissolved in deionized (DI) water to produce 5.6M KOH 0.37M ZnO solution. 0.1 g of Bi_2O_3 (Sigma Aldrich 99.999%) was added to the solution and mixed overnight.

The silver electrode was prepared by dipping stainless steel conductive thread (Sparkfun, conductive thread #60) into silver nanoparticle ink (DuPont 5064H). Excess ink was thoroughly removed. The silver coated thread was sintered for 30 min at 140°C in the vacuum oven. Resulting silver electrode was approximately 250 μm thick. The electrode was calendared to 20% of its original thickness using a calendar press.

Polymer electrolyte was prepared by mixing PVA (Sigma Aldrich, MW 85 000 – 124 000, 99% hydrolyzed) with DI water in the 1:10 ratio and left to dissolve overnight in the oven at 80°C. The liquid electrolyte was added to the mixture drop by drop to achieve 1:1.3 PVA:KOH ratio (by dry weight). The mixture was stirred for at least two hours.

Battery assembly

Zn electrode was either dip coated (in the case of the wire battery) or spray coated (in the case of the serpentine battery) with PVA polymer electrolyte. The cellophane film (McMaster Carr) was cut into stripes and then wrapped around the anode-electrolyte assembly followed by wrapping the silver electrode. The batteries were sealed into stretchable elastomer (3M 4910). 2M KOH 0.2M ZnO liquid electrolyte saturated with Bi_2O_3 was added before sealing the battery in the amount of 50 μL per centimeter of battery length. The serpentine battery was encapsulated within the elastomer matrix and sandwiched between two elastomeric sheets. The matrix serves a dual function. Firstly, it provides the spacing required for the out-of-plane rotation while the battery is being stretched. Secondly, it ensures that the battery deforms uniformly throughout the whole length. The schematic of the encapsulation is presented on the example of simple serpentine battery in **Figure 3.14**. The wire battery was encapsulated in a similar manner, with a well cut in the middle elastomer sheet replacing the matrix.

Battery characterization

EIS measurements were performed at frequencies ranging from 10^6 to 0.1 Hz at amplitude of 10 mV at open circuit condition using Gamry Reference 600 electrochemical analyzer. The battery was fully discharged and allowed to equilibrate for at least three hours before each measurement**.** Full cells were tested using MTI battery analyzer. SEM microscopy was carried out on TM-1000 (Hitachi).

OPV-battery system characterization

Battery current collectors were connected to the corresponding OPV module terminals using conductive epoxy (Circuit Works TDS#CW 2400). Simulated air mass 1.5 solar illumination was provided using an Oriel Sol1A solar simulator. Indoor illumination was provided using either a CFL (GE Energy Smart Daylight CFL 6500K) or LED (Feit Electric Dimmable A19 LED 3000 K) bulb. The height of the bulbs above the solar module was adjusted to produce either 300 lux or 3000 lux, using a Hamamatsu S2387-66R silicon photodiode to measure the power and a Thorlabs CCS200 spectrophotometer to measure the lamp spectra. A Keithley 2400 source-meter was used to measure the current-voltage characteristics of the OPV modules and to record the current and voltage during solar battery charging.

CHAPTER 4

Electrode composite for flexible printed zinc-manganese dioxide batteries through in-situ polymerization of polymer hydrogel

Portions of this chapter have been submitted for publication in Energy Technology.

4.1 Introduction

Fabricating electronics in a flexible wearable format has significant advantages for health monitoring and sensing (*136*, *227–230*). High-fidelity sensor-skin interfaces improve signal to noise ratio through the intimate contact of the device and body (*227*, *231*, *232*). In addition, ability to wear the devices directly on the skin can enable continuous monitoring of metabolites in bodily fluids like sweat (*3*, *12*, *24*, *164*). Standalone operation of such electronic systems cannot be realized without power source, such as a battery (*129*, *180*, *223*, *233*). If the battery is not equally compliant, it will negate the advantages of these flexible devices. Thus, flexible batteries play an important role in achieving the vision of wearable and conforming electronics.

In addition to being compliant, such a battery has to meet the energy and power requirements of the wearable systems, to be safe and environmentally sustainable. Among mainstream battery chemistries zinc-manganese dioxide (Zn/MnO_2) is well suited for the purpose. Due to its characteristics such as low material costs, high energy density and exceptional safety, it has been widely commercialized in the rigid cylindrical format by Duracell®, for example. In a commercial system Zn paste and MnO_2 paste are tightly packed in the can, which serves a dual function of casing and a current collector. Once removed from the rigid can, such paste-like electrodes disintegrate. Thus, achieving flexibility of Zn/MnO_2 system requires new engineering approaches.

To date, there have been few demonstrations of flexible Zn/MnO_2 batteries (*29*, *99*, *180*, *198*, *234–240*). Several used commercially available materials with innovative component revolving around device design (*29*, *99*, *180*, *198*, *234*, *235*, *239*, *240*), while other relied on the novel materials' synthesis, where materials are intrinsically flexible (*236–238*). In this work we use commercially available materials. Gaikwad et al. previously achieved high flexibility and

energy density Zn/MnO_2 batteries through dip-coating battery slurry with commercially available components into the supporting membrane that served as a mechanical support for the resulting electrode (*29*, *99*, *180*, *198*, *235*), Kaltenbruner et al. embedded electrode paste into an elastomeric matrix (*240*). While the above approaches ensured flexibility, inactive components significantly reducedthe amount of energy that can be stored per unit volume or per unit area of the battery. At the same time, it is important to maximize energy density, since dimensions of the battery are often limited with the size of the device being powered. An optimum system would match the commercial product in terms of energy density and at the same time have a flexible form factor. It is not reasonable to compare energy per unit area of the thin film flexible device to the cylindrical commercial can. Therefore, we targeted matching the energy per unit volume of AA alkaline battery, which is in a range of 350 mWh/cm^3 (*118*).

We fabricated compliant Zn/MnO_2 battery stack, where flexible Zn and MnO_2 electrodes were sandwiched with a commercially available separator. The electrodes were fabricated by printing electrode composites on the flexible substrate using doctor blade. Since the capacity of the battery was limited by the mass of MnO_2 in the cathode, the thickness of MnO_2 electrode was increased to ~4 times that of Zn electrode. Therefore, cracking and delamination of thicker MnO_2 cathode were limiting mechanical performance of the flexible batteries. One of the main challenges for realizing flexibility of MnO_2 electrode is the absence of a commercially available binder that would ensure mechanical integrity of the electrode composite. Binders available on the market are developed primarily for Li-ion battery chemistry. When utilized in the Zn/MnO_2 battery such binders either disintegrate in alkaline media; or block the surface area of the active particles in a way that prevents electrolyte contact with the particle and thus prohibits electrochemical reaction between active material and electrolyte; or simply do not provide sufficient adhesion. In order to realize printed, flexible Zn/MnO_2 batteries with high specific energy density, alternative solution had to be found to replace conventional binder.

An effective binder for the flexible electrode would accommodate mechanical deformation of the electrode and have strong adhesion to the electroactive particles and the conductive additive. The binder should also be chemically compatible with electrolyte and permeable to it. In this work we utilized PVA *in situ* cross-linked with polyacrylic acid PAA as a gel polymer binder for MnO_2 electrode. PVA/PAA membranes have been previously explored as solid polymer electrolytes for alkaline batteries (*241–243*) . The results from these studies indicate good stability of PVA/PAA in alkaline media and good conductivity (up to10^{-2} S/cm) of aqueous hydroxide species, which are the important electrode design considerations. In addition, PVA cross-linked with PAA has been previously studied for applications as a separation membrane material (*244*). The studies reveal that membranes obtained via crosslinking of PVA with 15%-20% PAA exhibit high tensile strength (900 kg/cm^2) without brittleness. These mechanical properties make cross-linked PVA/PAA a good candidate as a binder for flexible batteries. Song et al., used in-situ thermal crosslinking of PAA and PVA as a polymer binder for Si anodes in Li ion batteries (*245*). However, it has never been implemented in alkaline batteries. In this work,

PVA/PAA gel was *mixed* with the rest of the electrode components and crosslinked *in situ* via thermal treatment. The binder formed three-dimensional interpenetrated polymer network throughout the electrode, confining active material and conductive additive. Furthermore, to improve the energy density and rate capability of the printed battery electrodes, we replaced graphite with Single Walled CNTs. Due to their unique structure, CNTs have high aspect ratio and surface area, which allows them to form efficient conductive networks with smaller wait fraction in the electrode.

We compared the performance of flexible Zn/MnO_2 batteries with MnO_2 electrode of conventional and modified compositions, while keeping a commercial composition of Zn electrode. When the discharge rate was increased from C/10 to C/3, a battery with conventional electrode composition retained 60% capacity, while battery with modified electrode retained 93% capacity for the same discharge rates. This indicates that, despite lower fraction of conductive additive, CNTs form a more efficient conductive network that facilitates rapid kinetics of electrochemical reaction. Importantly, the modified electrode showed profound improvement in mechanical properties. It retained 97% of its capacity after being subjected to repetitive mechanical deformation. Finally, the battery with the modified electrode had high areal energy density of 4.8 mWh cm^{-2} and volumetric energy density of 320 mWh cm^{-3} , approaching that of the commercial AA alkaline battery.

4.2 Electrochemical and mechanical performance of the flexible battery with standard electrode composition

In Zn/MnO_2 battery system, Zn serves as an anode and has a gravimetric specific capacity of 820 mAh/g. MnO_2 serves as a cathode, with capacity of 308 mAh/g. Consequently, the capacity of the battery is limited by the mass of MnO_2 electrode. Therefore, the processes occurring at MnO2 electrode largely determine discharge profile of Zn/MnO2 batteries. Since Zn has significantly higher capacity per gram of material than MnO2, the discharge profile of Zn/MnO_2 batteries is largely determined by the processes occurring at MnO_2 electrode. The most accepted model describes it as shown in **Figure 4.1**. Discharge proceeds via two-electron reaction. The starting material is γ-MnO_2, which is build up from oxygen octahedral with Mn atom in the middle and contains 2x1 tunnel structures (*208*, *246*). The first reduction step involves reducing the Mn^{4+} ion to Mn^{3+} by introducing electron into the lattice (*247*, *248*) (Fig. 4.1a). Electrons can move in the lattice, therefore the position of Mn^{3+} (not the manganese ion itself) moves around in the entire lattice (Fig. 4.1b). At the same time, H_2O molecules (an abundant source of protons under this condition) may be decomposed at the solid-solution interface, and protons are introduced into the lattice forming OH^-. OH- also moves around in the entire lattice by means of the proton jumping

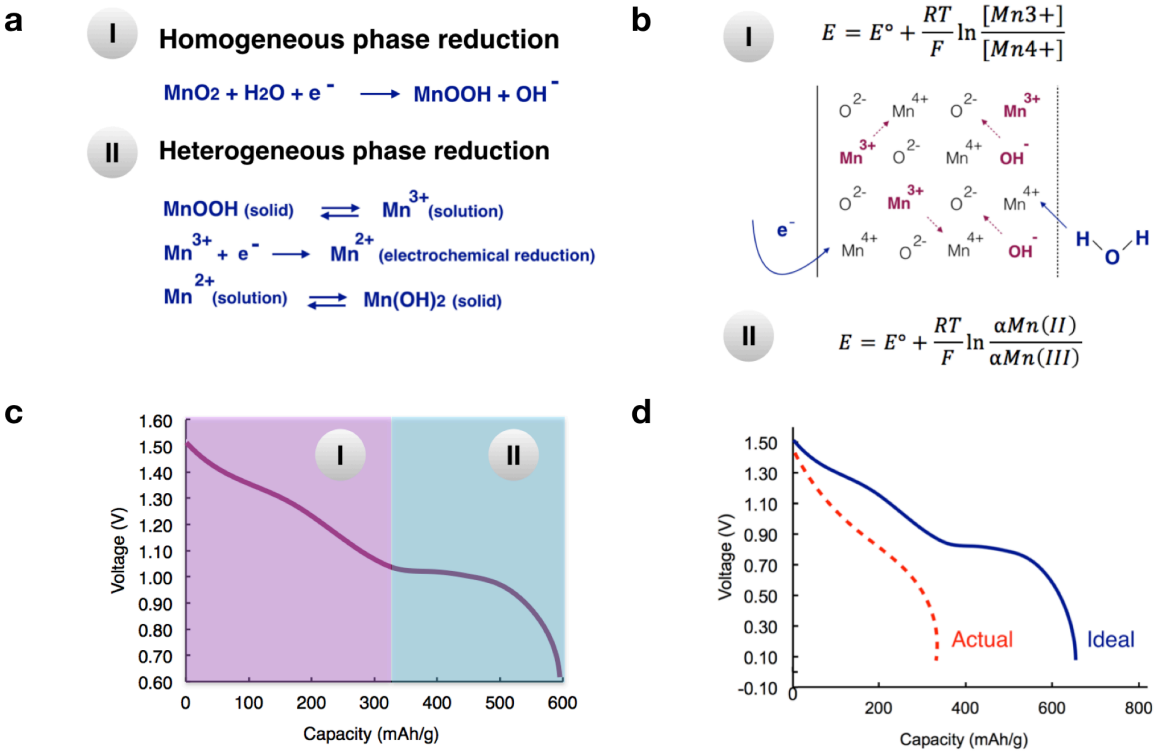

Figure 4.1: (a) Electrochemical reactions describing two reduction steps of the Mn^{4+} ion. (b) Equations determining potential of the electrode during the two reduction steps and corresponding schematics of the homogeneous phase reduction mechanism. (c) Schematic of the shape of the ideal discharge curve of Zn/MnO_2 battery as determined by reduction mechanism. (d) Schematic demonstrating extent of deviation of the discharge curve from ideal case due to losses associated with the current flow.

from one $O^{=}$ site to another. As the discharge proceeds, the concentrations of Mn^{3+} and OH^- in the lattice increases, both of these species become distributed homogeneously throughout the oxide lattice. This discharge mechanism is referred to as homogeneous phase reduction. The electrode potential of the oxide having a homogeneous phase may be determined by the activity of the electron in the lattice, or by the ratio of $[Mn^{3+}]/[Mn^{4+}]$ in the solid (Fig. 4.1b). Since the ratio gradually changes, we observe the sloppy discharge curve (Fig. 4.1b,c). However, as the discharge proceeds the original MnO_2 lattice expands, because the ionic radius of OH^- (1.53A) is greater than that of $O^{=}$ (1.40A), and Mn^{3+} (0.62A) is greater than Mn^{4+} (0.52A) (*247*). Therefore, at a certain point, the crystal structure is transformed to a new, more energetically favorable form in which such a free movement of the electron and proton may not be possible. As a result, alpha-MnOOH or gamma-MnOOH is formed. The second reduction step proceeds via different mechanism (*249*,

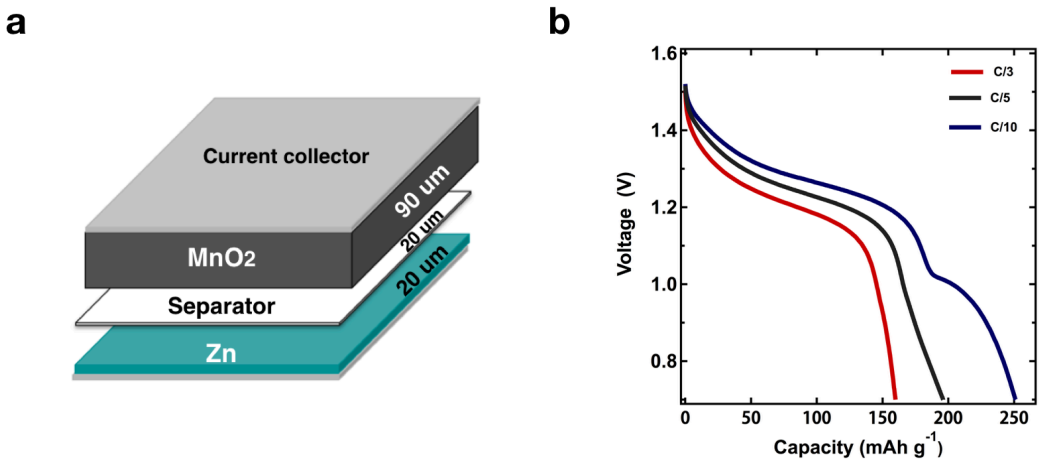

Figure 4.2: (a) Schematic of the flexible battery stack. (b) Galvanostatic discharge curves for the battery operated at C/10, C/5 and C/3 rates. Two discharge regions defined by plateaus on the curves correspond to two MnO_2 reduction reactions. Electrode shows 60% capacity retention when discharge rate is increased from C/10 to C/3. Data collected by Cheryl Chang.

250). Mn^{3+} species are soluble in electrolyte. They are reduced to Mn^{2+} when they come in contact with any conductive surface. Since the solubility of Mn^{2+} is much lower than that of Mn^{3+}, any Mn^{2+} species generated will precipitate almost immediately as $Mn(OH)_2$ on the surface of the electronic conductor. Concentrations of dissolved Mn (II) and Mn (III) are equal to their solubility values as long as the two solid phases exist. Consequently, the potential will remain constant during the discharge (Fig. 4.1a-c). Under certain experimental conditions formation of spinel is observed (*251*). The above processes explain the shape of the ideal discharge curve of Zn/MnO_2 battery. The actual shape of the discharge curve deviates from ideal case due to losses associated with the current flow (Fig. 1d). Losses are different in nature. Looses associated with ionic resistance of the electrolyte and the electronic resistances of the electrodes, and the current collectors result in the Ohmic potential drop. In most cases Ohmic potential drop is dominated by the conductivity of electrolyte. In this case the battery will reach its discharge voltage limit faster and drop in capacity of the battery will occur. Sluggish charge transfer at different interfaces, like interface between active material and electrolyte or active material and conductive additive result in charge transfer polarization. In addition, there can be looses due to concentration polarization, i.e. depletion of the reactants at the electrode surface (*118*).

To fabricate flexible battery electrodes, we printed current collector onto the flexible plastic substrate, followed by printing electrode composite on top. We used doctor blade to print the electrodes, as it allows rapid deposition of inks with high solid loading. We used the AA alkaline battery electrode compositions (*29*, *198*) . Zn ink consisted of Zn, as an active material, ZnO and Bi_2O_3, as corrosion inhibitors, commercially available PSBR binder and ethylene glycol as a solvent. Since Zn is highly conductive, no conductive additive is needed for Zn ink. The MnO_2 ink consisted of gamma-MnO_2 as an active material, KS6 graphite as a conductive additive, PSBR binder and water as a solvent. The electrodes were sandwiched into a flexible battery stack shown in **Figure 4.2a**. Figure 4.2b shows galvanostatic discharge curves for the battery operated at C/10, C/5 and C/3 rates. We observe two discharge regions, defined by plateaus on the curves, corresponding to two MnO_2 reduction reactions. We access considerably more capacity during the first electron reaction than during the second. This is expected, because the product of the second reaction - $Mn(OH)_2$ precipitates on the surface of the graphite. $Mn(OH)_2$ and is a poor electronic conductor, therefore, as the layer builds up, the resistance increases to the point where no more reduction of species can occur, thus causing electrode failure (*248*, *249*, *251–253*). As the discharge rate increases losses due to polarization increase for both reactions. Specific discharge capacity decreased from 265 mAh g^{-1} at C/10 to ~210 mAh g^{-1} at C/5 to 165 mAh g^{-1} at C/3 resulting in ~38% capacity loss, which compromises utilization of this battery in high rate

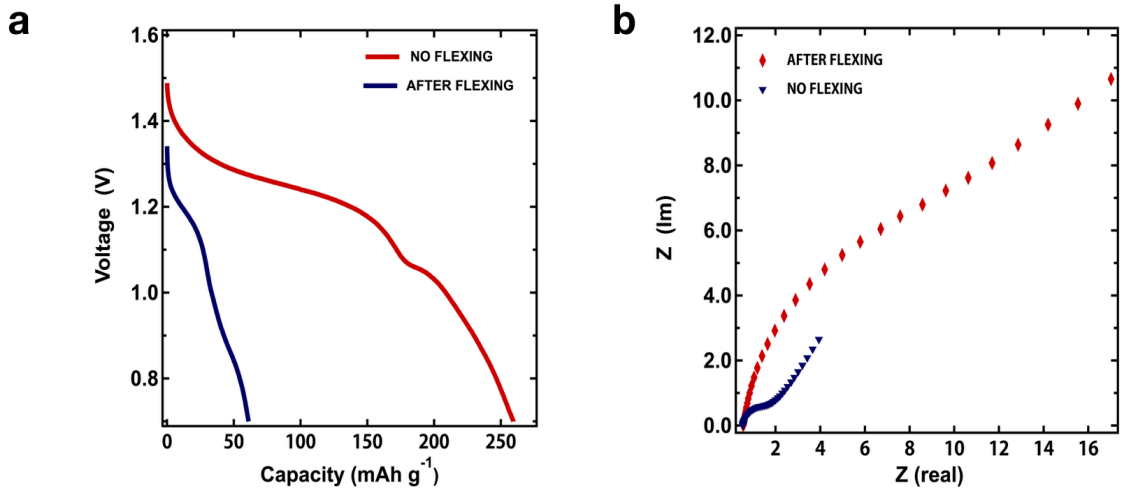

Figure 4.3: (a) Galvanostatic discharge curves of the battery discharged without flexing compared to the battery discharged after being wrapped around 0.5-inch radius cylinder 100 times while keeping MnO_2 electrode in tension. Capacity decreases to 23% of its original value as a result of flexing. (b) Data for EIS measurements on the flat battery and the battery that has undergone flexing.

applications. We will further demonstrate how the rate capability can be improved by replacing the graphite with a more efficient conductive additive – CNTs.

The thickness of the MnO_2 electrode is ~4 times higher than that of the Zn electrode, making it more prone to failure. Therefore, the MnO2 electrode limits the mechanical performance of the battery. When the battery is flexed, the electrode experiences tensile and compressive stresses. The possible structural failures caused by these stresses are delamination of the active layer from the current collector and formation of cracks in the layer. Delamination takes place when the shear stress at the interface exceeds a critical value; cracking occurs when tensile stress exceeds the tensile strength of the electrode composite. Electrochemical and mechanical performance in a battery are coupled. The delamination or cracking of the active layers leads to an Ohmic potential drop at the start of discharge. Flexing can also lead to increase in charge transfer resistance due to loss of contact between conductive additive and active material; as well as to formation of inactive phases like spinel, due to non-uniform potential distribution in the electrode.

To evaluate the effect of mechanical load on the electrochemical performance of the battery, we subjected it to the series of flexing cycles before discharge. The battery was wrapped around 0.5-inch radius cylinder 100 times while keeping MnO_2 electrode in tension. **Figure 4.3a** shows the galvanostatic discharge curves of the battery that was discharged without flexing compared to that of the battery discharged after being flexed. As a result of flexing capacity decreases to 23% of its original value. To elucidate the cause of failure we carried out EIS measurements on the flat battery and battery that has undergone flexing. Figure 4.3b shows EIS curves for two cases. The shape of the EIS curves is consistent with the typical impedance plot for Zn/MnO2 battery (*254*). It resembles a semicircle in the high frequency region, dominated by kinetics and a tail in a low frequency region, dominated by mass transfer. The first interception of the semicircle corresponds to Ohmic potential drop and the second – to charge transfer polarization, and the low frequency region – to diffusion controlled processes. EIS data show the significant increase in charge transfer resistance of the battery, indicated by the increase in the radius of the semicircle. This is the evidence of loss of contact between particles, which leads to loss of electrical pathways within the electrode. This indicates that the commercial binder has poor adhesion properties and is not maintaining the mechanical integrity of the electrode.

Thus, analysis of the electrochemical performance of the battery operated at different conditions showed that the battery looses 40% of its capacity when the discharge rate increased from C/10 to C/3, and 77% - as a result of mechanical stress. This served as a motivation for design of the alternative electrode composition that addresses these limitations.

4.3 MnO_2 electrode composite through situ polymerization of polymer hydrogel: design considerations

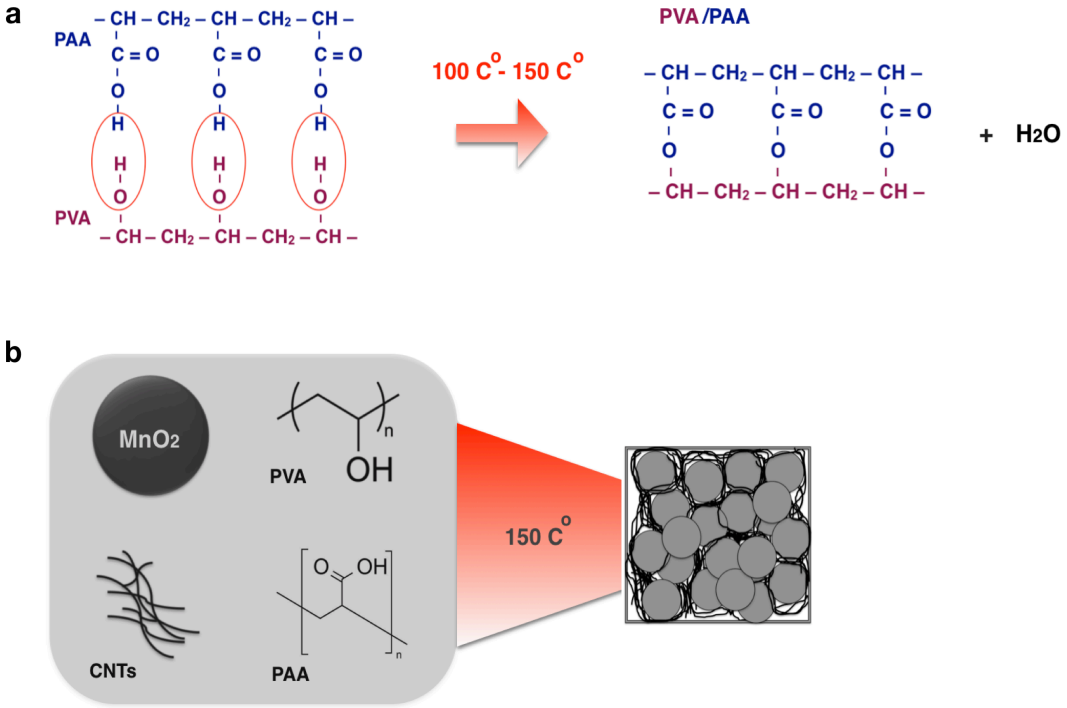

Figure 4.4: (a) Schematics of the condensation reaction between PVA and PAA. - COOH groups of PAA react with - OH groups of PVA forming interpenetrated polymer network. (b) Components and process parameters of the modified electrode: PVA is dissolved in water, CNTs are added to the mixture and ultrasonicated, followed by addition of MnO_2 and PAA. The slurry is printed onto the current collector and baked at 150 °C for 1 hour.

As previously discussed, cracking and delamination of the MnO_2 cathode limit the mechanical performance of flexible batteries based on the Zn/MnO_2 chemistry. The conventional MnO_2 electrode composite comprises gamma-MnO2 as an active material, graphite conductive additive, PSBR binder and water as a solvent. Binder that can accommodate mechanical deformation of the electrode and has strong adhesion to the electroactive particles and the conductive additive is a critical component of the composite. PSBR binder film disintegrates in the electrolyte. This results in the poor mechanical performance of the MnO_2 electrode with conventional composition.

As an alternative to PSBR, we designed the polymer gel binder that forms a three-dimensional interpenetrated polymer network throughout the electrode, confining active material and conductive additive particles. Particularly, we used PVA/PAA polymer gel that was cross-linked *in situ* with the rest of the electrode components via thermal treatment. It has been shown

that when exposed to temperatures ranging from 150 °C to 180 °C solution of PVA and PAA undergoes condensation reaction where –COOH groups PAA react with OH groups of PVA (*244*) forming interpenetrated polymer network **(Fig. 4.4a).** A low molecular weight PAA (2000) was used to facilitate chain mobility of PAA within PVA. The mechanical properties of the resulting PVA/PAA films can be controlled by varying heat treatment conditions and the ratio of the polymers. The PAA ratio of 15-20% was determined as optimum by Rhim et al. (*244*) by measuring the glass transition temperature (Tg) of the cross-linked PVA/PAA membranes. The Tg value increases with increasing PAA content until the PAA fraction reaches 15%, remaining nearly constant beyond 15%. This indicates that addition of PAA beyond 15% has minimal effect on the crosslinking reaction. The same authors used measurement of changes in Tg to show that the amount of time required to complete reaction at 150 °C to 180 °C is 45 min – 1 hour. Additionally, the content of PAA impacted mechanical properties of the PVA/PAA membranes. The higher tensile modulus was observed for higher PAA fraction. At the same time, the tensile strength increased with increasing PAA fraction up to 15% of PAA content and then gradually decreased due to brittleness of the samples. Thus, the optimum conditions for preparing PVA/PAA membranes were achieved by treating PVA and 2000 molecular weight PAA in the ratio 85:15 at 150 °C to 180 °C for 45 min – 1 hour. We used the above information to define the polymer content and processing conditions of the electrode. The modified electrode composite contained PVA/PAA in the ratio 85:15 and was baked at 150 °C for 1 hour.

In order to improve rate capability of the electrode and decrease the fraction of conductive additive, we replaced graphite with CNTs. The fiber-like structure of carbon nanotubes, their high aspect ratio and conductivity allows establishing effective electrical percolation network at a lower weight loading than conventional carbons (*255*, *256*). We replaced 10% mass fraction of KS6 graphite with the 1% mass fraction of CNTs. This mass fraction has been shown to be optimum for Li ion battery systems (*255*). Due to the hydrophobic nature of CNT's, they are poorly dispersible in water - the solvent used to prepare the MnO_2 electrode. However, PVA and PAA binder components can serve as surfactants that facilitate the dispersion of CNTs. Alkyl chains act as hydrophobic component and absorb on the surface of carbon nanotubes, while hydrophilic segments stretch into the water (*257*). Polymer also increases the viscosity of the solution, and, thus, inhibits re-aggregation of CNTs after dispersion. Since PVA comprises the major part of the binder mixture (85%) and PAA serves primarily as a crosslinker, we used PVA dissolved in water as a base for CNT formulation.

Ultrasonication was used to separate nanotube clusters in the PVA/CNT suspension. Ultrasonication conditions are one of the defining parameters of the CNT/polymer formulation and final composite composition. Ultrasonication delivers shear stress to CNT's surface, through creation and imploding of bubbles in the vicinity of CNTs. Shear stress leads to separation of CNT aggregates, but at the same time can induce pulling effect on the nanotubes and can lead to fracture of the nanotubes (*258*). Improvement in dispersion has been shown to have the reverse effect on the conductivity. The composite morphology with phase separated clusters of CNTs has been

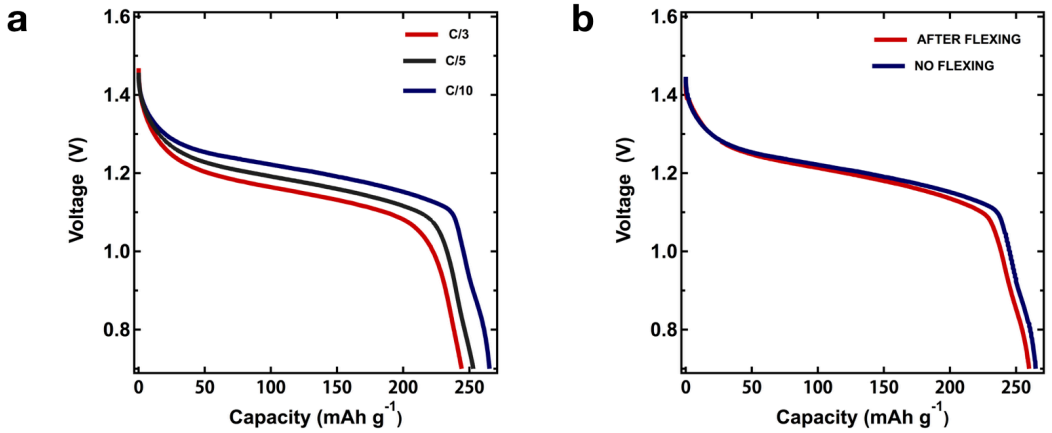

Figure 4.5: (a) Galvanostatic discharge curves for the battery operated at C/10, C/5 and C/3 rates. MnO_2 electrode fabricated using modified approach shows 93% capacity retention when discharge rate is increased from C/10 to C/3. (b) Galvanostatic discharge curves of the battery discharged without flexing compared to the battery discharged after being flexed. The battery shows capacity retention of 97% after being wrapped around 0.5-inch radius cylinder 100 times while keeping MnO_2 electrode in tension.

shown to have more effective electron transport than homogeneous CNT network (*259*). Thus, under strong shearing conditions composites mixed for less time are expected to have higher conductivity due to 1) avoiding damage of nanotubes 2) resulting in CNT aggregates that facilitate electron transport. We limited ultrasonication time of PVA/CNT solution to 20 min, at the mid-range amplitude of 40% using a Branson Digital Sonifier probe. No precipitation was observed in CNT/PVA mixture for at least 24 hours after dispersion. The above considerations were taken into account when preparing the electrode slurry. To facilitate the CNT dispersion, PVA was first dissolved in water, after which CNTs were added to the mixture and ultrasonicated, followed by addition of MnO_2 and PAA. The slurry was printed onto the current collector and baked at 150 °C for 1 hour (Fig. 4.4b). The resulting electrode was combined with the rest of the battery components to form the flexible battery.

4.4 Electrochemical and mechanical performance of the flexible battery with the MnO_2 composite comprising interpenetrated binder network and CNT conductive additive

The galvanostatic discharge curves of the battery with MnO_2 electrode composite comprising PVA/PAA binder and CNT conductive additive are shown in **Figure 4.5a**. The data for the battery

with standard electrode composition discharged under the same conditions is shown in Figure 2b. At C/10 both batteries show similar specific capacity of 270 mAh g^{-1} and 265 mAh g^{-1} respectively. However, the specific discharge capacity of the battery with the standard electron composition decreases from 265 mAh g^{-1} at C/10 to ~210 mAh g^{-1} at C/5 to 165 mAh g^{-1} at C/3 resulting in ~40% capacity loss. At the same time, the battery with the modified MnO_2 electrode retains 93% of capacity when the discharge rate is increased from C/10 to C/3, with slight decrease in capacity from 270 mAh g^{-1} at C/10 to ~260 mAh g^{-1} at C/5 to 250 mAh g^{-1} at C/3. Thus, MnO_2 electrode fabricated using modified approach shows 93% capacity retention when discharge rate is increased from C/10 to C/3, compared to ~60% capacity retention in the battery with the conventional electrode composition. This indicates that CNTs form more efficient conductive network than graphite facilitating high kinetics of electrochemical reaction. Replacing KS6 graphite with CNTs also allows reducing the weight fraction of conductive additive in the electrode from 10% to 1%.

Analyzing the shape of the discharge curves for both batteries we observe that the discharge curves of the battery with the modified electrode composition have flatter plateau with lower potential. Lower plateau potential confirms the formation of the MnOOH oxide on the surface of MnO_2 particles during thermal treatment (*250*, *260*). At C/10, 20% more capacity is accessed during the first electron reaction in the modified case, in comparison to the conventional case. The second electron reaction is almost absent in the modified case, while it constitutes ~20% of the overall capacity in the conventional case. The reason can be elucidated by revisiting the mechanism for the second MnO_2 reduction step. Reduction proceeds via dissolution-precipitation mechanism (*249*, *250*). Mn^{3+} species dissolve in the electrolyte and get reduced to Mn^{2+} when they come in contact with the conductive surface. Since the solubility of Mn^{2+} is much lower than that of Mn^{3+} any Mn^{2+} species generated will precipitate as $Mn(OH)_2$ on the surface of the electronic conductor forming a layer that eventually occludes the ion transport to the conductor and, thus, terminates the reaction. If PVA/PAA binder coats MnO2 particles, then Mn^{3+} and Mn^{2+} ions are trapped in the vicinity of the particles and reach the solubility limit significantly faster. Thus, we can expect Mn^{2+} to precipitate almost immediately on the surface on CNTs in the vicinity of the particles, hindering further reaction.

The modified electrode shows significant improvement in mechanical properties. Figure 4.5b compares galvanostatic discharge curve of the flat battery to the curve of the battery that was subjected to the series of flexing cycles before discharge. The battery shows capacity retention of 97% after being wrapped around 0.5-inch radius cylinder 100 times while keeping the MnO_2 electrode in tension. In contrast, the battery with standard electrode composition (Figure) looses 77% of its capacity after being flexed at the same conditions.

To further optimize the fraction of the conductive additive in the MnO_2 electrode, we varied the CNT fraction in the composite. The effect of CNT weight fraction on the performance of the battery discharged at C/3, C/5 and C/10 rates is shown in **Figure 4.6** a, b and c respectively. For all rates, discharge capacity of the battery decreases when the CNT weight fraction is decreased

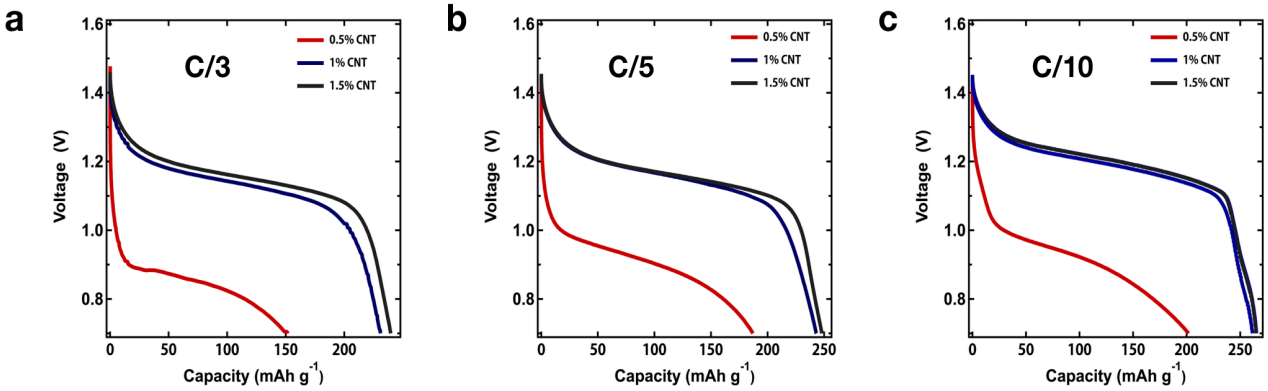

Figure 4.6: Galvanostatic discharge curves for the batteries with 0.5%, 1% and 1.5% CNTs operated at (a) C/3, (b) C/5, (c) C/10 rates.

from 1% to 0.5% (175 mAh g^{-1}, 200 mAh g^{-1} and 225 mAh g^{-1} discharge capacity for the battery with 0.5% CNT content for C/3,C/5 and C/10 respectively; 240 mAh g^{-1}, 253 mAh g^{-1} and 270 mAh g^{-1} discharge capacity for the battery with 1% CNT for the same rates). When the CNT fraction is increased from 1% to 1.5% the discharge capacity increases from 240 mAh g^{-1} to 250 mAh g^{-1} for C/3 discharge rate, and remains nearly unchanged at ~253 mAh g^{-1} and ~270 mAh g^{-1} at C/5 and C/10 rates respectively. As seen from the voltage values of the discharge curves, lowering CNT concentration from 1 wt.% to 0.5 wt.% results in the potential drop of 0.3V, 0.22V and 0.18V for C/3, C/5 and C/10 respectively. Consequently, energy efficiency of the batteries with lower CNT content is reduced. Decrease of the electrode conductivity as the CNT content is reduced causes this drop. Therefore, a weight fraction of 0.5% is not sufficient to create an effective conductive network in the MnO2 electrode composite and the higher fraction of CNT is desirable for optimum battery performance. On the other hand, increasing CNT weight fraction from 1% to 1.5% does not result in energy efficiency increase for slower operating rates of C/5 and C/10; 4% capacity gain is observed at C/3. Thus, if the battery is expected to operate at low rates, increasing CNT fraction beyond 1% does not add value in terms of energy efficiency.

Figure 4.7 shows SEM images of the cross-sectional (a,d) and top (b,c,e,f,) view of the electrodes with conventional (a-c) and modified (d-f) compositions. The image of the conventional electrode shows that graphite particles are homogeneously dispersed throughout the composite. However, the particles are neither connected between themselves, nor do they seem to adhere to MnO particles. The images of the modified electrode show that PVA/PAA/CNT composite homogeneously coats MnO_2 particles. CNTs are incorporated into the polymer. Additionally, we can clearly see the polymer bridges between the particles – holding the structure together. Thus, analysis of the SEM images supports the hypothesis regarding the mechanical failure mechanism

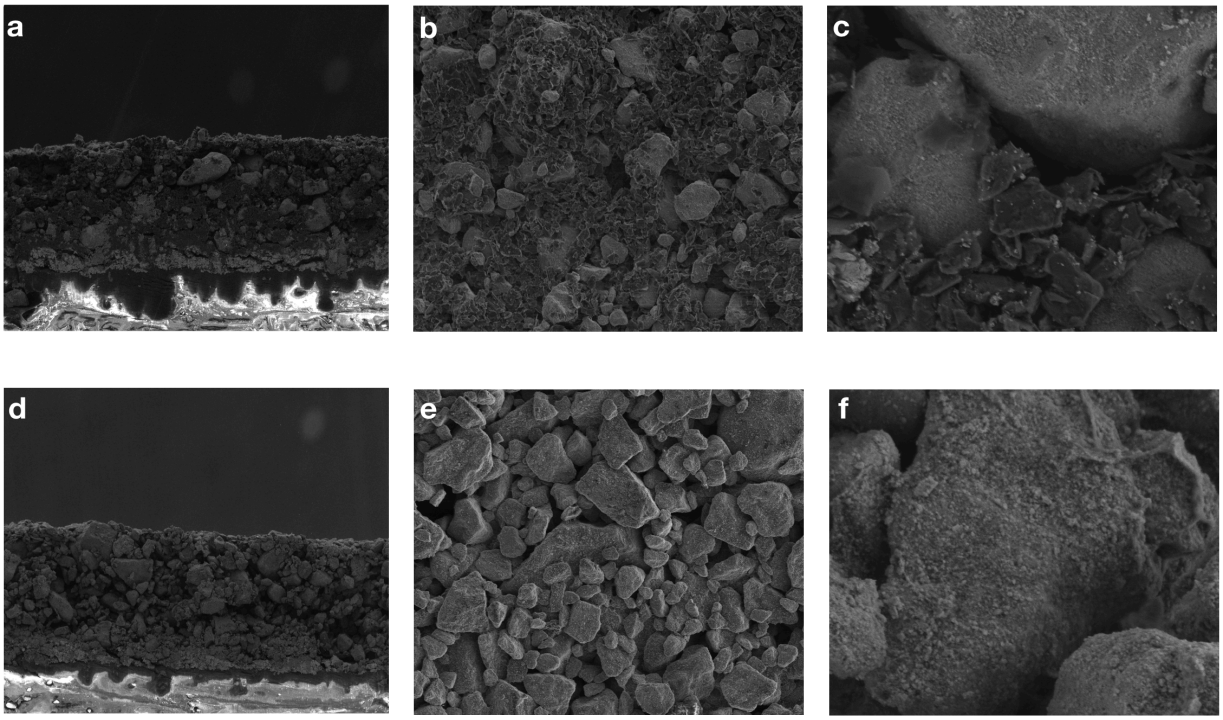

Figure 4.7: Crossectional (a,d) and top (b,c,e,f,) view of the conventional (a-c) and modified (d-f) electrodes.

of the electrode with conventional electrode composition: due to loss of contact between particles, which leads to loss of electrical pathways within the electrode. It also confirms that PVA/PAA/CNT forms three-dimensional interpenetrated polymer network throughout the electrode, confining the active material.

4.5 Conclusion

This work elaborates on design of the electrode composite for flexible printed Zn/MnO_2 batteries, with the goal of improving mechanical and electrochemical performance, as well as specific energy density of the battery. In order to improve flexibility we chose PVA *in situ* cross-linked with PAA as a polymer binder for the MnO_2 electrode. PAA/PVA composite is chemically compatible with KOH electrolyte used in $ZnMnO_2$ chemistry and permeable to it. It also exhibits high tensile strength without brittleness, which are desired mechanical properties for the binder. In order to improve rate capability of the electrode and decrease the fraction of conductive additive, we replaced graphite with CNTs. Resulting electrode comprised polymer network with enclosed

MnO_2 particles and conductive network of CNTs. Battery fabricated with MnO_2 electrode based on CNT/PVA/PAA composite showed improved capacity retention when discharged at high rates, and profound improvement in mechanical properties compared to the batteries with conventional electrode composition. It retained 93% capacity when the discharge rate was increased from C/10 to C/3, as well as 97% of its capacity after being flexed. In contrast, batteries based on conventional composition retained 60% and 23% respectively. The battery with the modified electrode had a high areal energy density of 4.8 mWh cm^{-2}. The volumetric energy density of 320 mWh cm^{-3} approached that of the commercial device (350 mWh cm^{-3}).

4.6 Experimental section

To prepare a current collector a doctor blade was used to print a 10 mm Ag ink layer (Creative Materials 118-09) on the PEN substrate (DuPont). The substrate was then baked at 125°C for 30 min. The thickness of the Ag layer after the baking step was approximately 5μm. The MnO_2 ink of conventional composition was prepared as previously described elsewhere (*29*). Briefly, ink consisted of a mixture (by dry weight) of 80% MnO_2 (Tronox), 10% graphite (KS6, Timcal) and 10% polystyrene binder (LICO Technology Corp.). DI water was used as a solvent. The Zn ink was a mixture (by weight) of 69.3% Zn (Sigma–Aldrich), 7.3% ZnO nanopowder (Inframat), 10.9% Bi_2O_3 (Alfa Aesar), 10.9% ethylene glycol, and 1.6% polystyrene binder. The inks were printed on the silver current collector and baked in an oven at 100°C for 60 min to remove the solvent. The MnO_2 ink of modified composition was prepared as follows: 0.1g of PVA (31000-50000MW Sigma Aldrich) was dissolved in 2.4g DI water, after that 0.04g of CNTs from Carbon Solutions, Inc in the form of iP-Single Walled Carbon Nanotubes were added to the mixture and ultrasonicated for 20 min at the amplitude 40%. 3.98g of MnO_2 and 0.019g of PAA were added to the mixture and mixed using Vortex mixer for 5 min at 3000 rpm. The slurry was printed onto the current collector and baked at 150 °C for 60 min. A solution of KOH (5.6M) and ZnO (0.37M) was used as the electrolyte, which was prepared by mixing KOH pellets and ZnO powder in DI water. The mixture was stirred until a clear solution formed. A polyvinyl alcohol/cellulose wet-laid nonwoven material soaked in the electrolyte was used as a separator (Freudenberg Vliesstoffe KG, Germany). The electrodes and the separator were cut to a size of 1 $inch^2$ with extended tabs to connect to the battery. The separator was sandwiched between the two electrodes and the cell was heat sealed between two layers of PVC (75mm, McMaster). The contact between the tab and the PVC sheet was sealed with double-sided tape (3M). The tape was stable in high-pH solutions. The assembled battery was discharged by using a battery tester (MTI Corp). The EIS measurements were performed by using a Gamry potentiostat. SEM was performed by using a TM3000 (Hitachi).

CHAPTER 5

Printed electrochemical sensors for continuous sweat monitoring: satisfying prerequisites for commercial use

Portions of this chapter have been submitted for publication in Scientific Reports.

5.1 Introduction

Non-invasive detection of biomarkers in bodily fluids is of great interest for assessing the body's response to physical activity, as well as for clinical diagnostics. Sweat has many advantages compared to other non-invasive biofluids (tears, saliva), as was comprehensively reviewed by Heikenfield et al. (*3*). Attempts to use sweat for diagnostics in clinics date back to the 1940s, but up until recently they were significantly hindered by difficulty in sweat sample collection and storage. This issue is now being resolved through development of flexible wearable sensors that can be placed in close contact with the skin. This allows for sampling of the sweat as it is secreted onto the skin, addressing impediments around the collection of the sweat sample and degradation of the analytes in sweat. It also allows for the continuous monitoring of biomarkers, enabling the vision of personalized, point-of-care health monitoring.

Major developments in sweat sensing field have to be realized in order to implement the vision of using sweat for individualized health monitoring. Algorithms for processing vast amounts of data from multiple sensors need to be developed before we can build a representative picture of an individual's health. Additionally, there is an added complexity from not completely understood secretion mechanisms of the eccrine gland and blood-to sweat biomarker partition pathways. For example, as comprehensively described by Sonner et al. (*261*), transport mechanism of biomarker from blood plasma into the sweat (diffusion) differ from the transport mechanism from sweat duct to the skin surface (advection). As a result, the biomarker dilution ratio is unknown. Additionally, for example, metabolite lactate can be produced by the sweat grand itself, potentially dominating the diffusion of lactate from plasma (*262*). Therefore, models for biomarker partitioning and transport mechanisms have to be developed for each species of interest.

In addition to developments around data processing, a significant effort has to be directed towards fabrication of reliable sensing components for multiple sweat analytes. The prerequisites

for developing commercially viable sweat sensors are fast response, sensitivity to physiologically relevant concentrations of analyte, batch to batch reproducibility, stable performance under continuous operation, specificity, i.e. insensitivity to other analytes present in sweat, long-term storage, and ideally, no calibration requirement. Sensor design should also be adapted to fit large scale manufacturing approaches.

To date, different sensing methods have been used to build wearable sweat sensors and their components. Impedance-based sensors have been shown to be effective in monitoring sweat rate (*4*, *5*) and could be integrated with sensing components for biomarker monitoring to correct for the effect of sweat rate on the concentration of biomarker. Sensors based on colorimetric readouts were coupled with microfluidic sweat supply and removal systems (*6*, *7*). Optical sweat sensing was also investigated (*8*, *9*). Electrochemical sensors gained the most traction due to their high specificity, low cost and commercially available material systems (*10–12*). Compliant wearable sensors for monitoring single (*13–21*) and multiple (*4*, *8*, *22–27*) analytes in sweat were developed using electrochemical sensing mechanisms. While these works advance the important aspects of sensor development, sensors that meet all the requisites of the commercially viable system have not been shown.

In this chapter we describe the flexible sensing platform to monitor lactate, sodium ion (Na^+) and ammonium ion (NH_4^+) in sweat **(Fig. 5.1)**. Tracking the change in the concentration of these species during the exercise can provide important information for optimizing individual's sport/fitness routine, as well as for prevention of complications that could be dangerous to the overall health. Sodium deficit, for instance, is a primary cause of heat cramps (*263*) and in extreme cases can result in a severe medical condition – hyponatremia. Although concentration of sodium in sweat is not directly correlated to its plasma concentration, monitoring sodium concentration

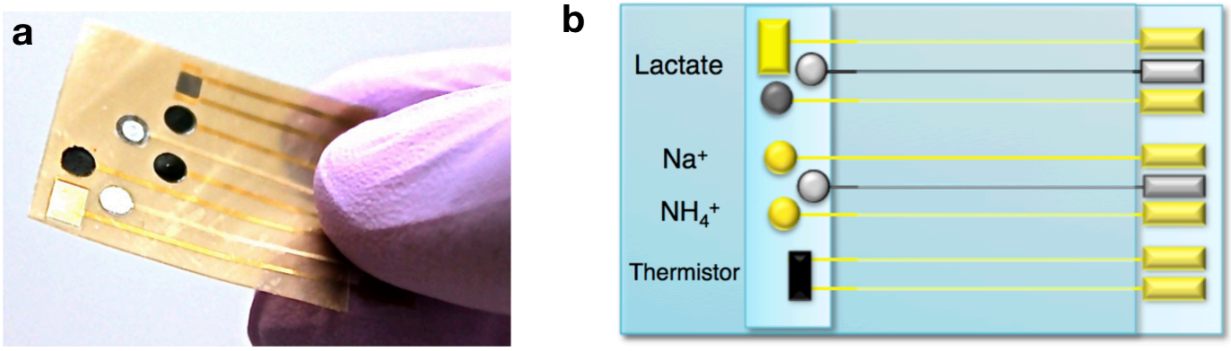

Figure 5.1: (a) Image and (b) schematic of the sweat sensing platform.

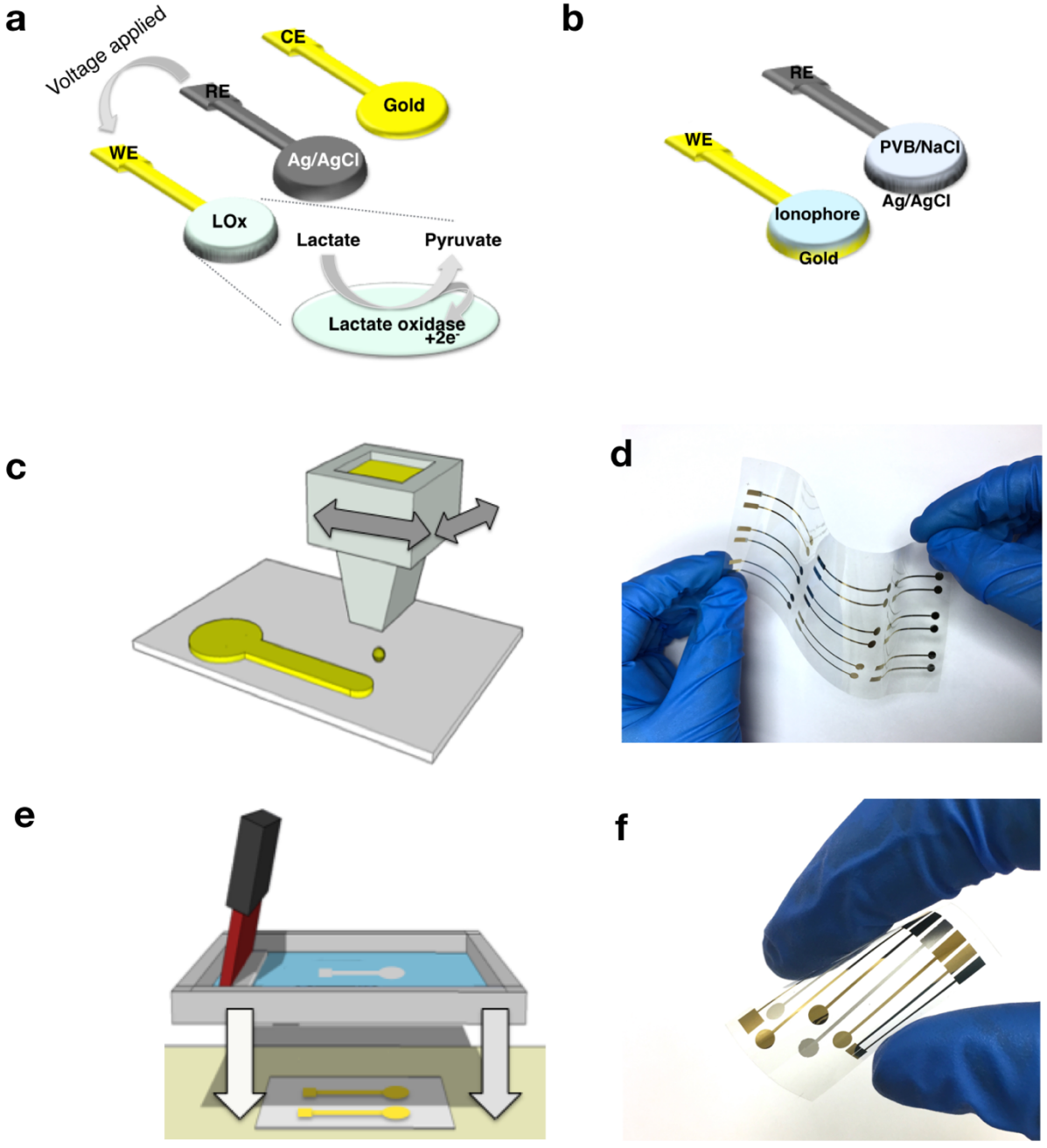

Figure 5.2: Schematic of the (a) amperometric and (b) potentiometric sensor configurations. (c) Inkjet printing of the commercially available gold nanoparticle ink onto PEN substrates and (d) image of the resulting substrate with gold traces. (e) screen printing of the Ag/AgCl traces for reference electrodes for potentiometric and amperometric sensors and (f) image of the substrate with printed gold transducer and Ag/AgCl reference electrodes. Schematics drawn by Joe Corea

in sweat can act as a good guide for estimating loss of this ion in blood and provide guidance regarding the amount of sodium that needs to be replenished. It's been shown that the increased concentration of lactate in sweat is a good indicator of the metabolic acidosis which can develop during prolonged exercise (*8,9*). Although, high exertion exercises might lead to increase in lactate concentration due to activity of sweat gland itself and might not correlate with blood lactate. High concentration of ammonia is an indicator of low levels of carbohydrates (*265*) and can also be an indicator of other metabolic conditions associated with the intense physical performance (*266*). Thus, monitoring concentrations of lactate, ammonium and sodium ions in sweat can have benefits, especially for the monitoring of effects of prolonged or intense physical activity.

Lactate is monitored through amperometric measurements, which require three electrode setup. Potential is set between working and reference electrode to facilitate electrochemical reaction between enzyme lactate oxidase present in the working electrode and lactate in sweat. The resulting current is then detected **(Figure 5.2a)**. Potentiometric measurements of sodium ion and ammonium ion are performed by measuring potential difference between reference and ion selective electrodes, thus requiring two-electrode design (Figure 5.2b). Ion selective electrodes comprise of ionophores that reversibly bind Na^+ or NH_4^+ ions, ideally resulting in Nerstian response to the change in ion concentration.

Scalable manufacturing is an important consideration in sensor design. We used inkjet printing, screen printing and drop casting to deposit sensor components on a flexible substrate. Working transducer electrodes for both potentiometric and amperometric sensors, as well as the counter electrode for the amperometric sensor were fabricated by inkjet printing, using commercially available gold nanoparticle ink onto 25 μm thick polyethylene naphtalate (PEN) substrates (Figure 5.2c). Figure 5.2d shows the resulting substrate with gold traces. The reference electrodes for potentiometric and amperometric sensors consisted of commercial Ag/AgCl ink, screen printed onto the same substrate (Figure 5.2 e,f). In the case of the potentiometric sensors, an additional layer of carbon nanotubes (CNT) dispersed in tetrahydrofuran (THF), followed by Polyvinyl butyral (PVB)/NaCl membrane were drop casted on top of the Ag/AgCl layer. The sensing membranes for the sodium and ammonium sensors consisted of the sensing ionophores that were drop casted onto the gold working electrodes. The working electrode for the lactate sensor consists of the mediating layer, fabricated by drop casting CNT/tetrathiafulvalene (TTF) suspension onto the gold trace, followed by lactate oxidase enzyme immobilized in the chitosan/CNT suspension.

We used commercially available materials that have been previously implemented for fabrication of the wearable sweat sensors. We outline optimization steps to achieve printed sensors for continuous monitoring of the lactate, Na^+ or NH_4^+ ions and show how different optimization

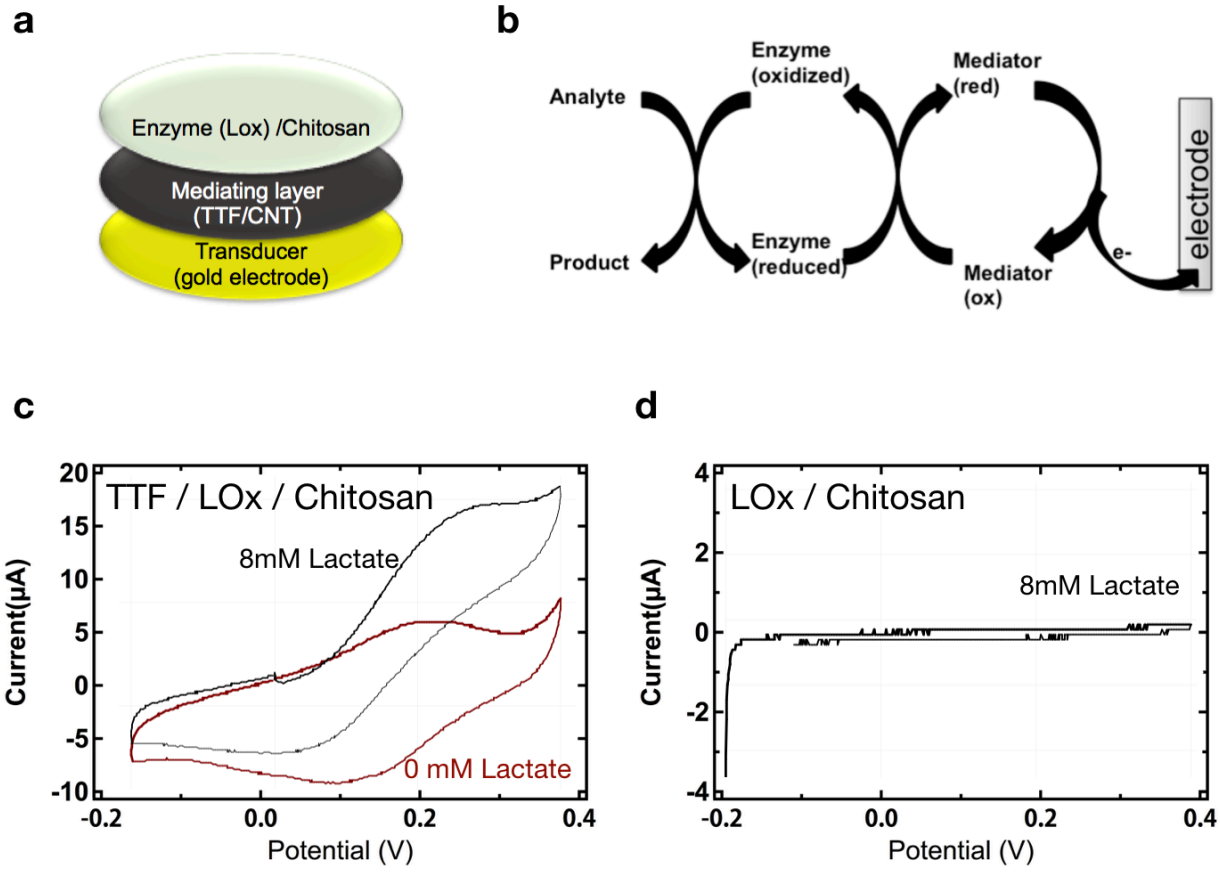

Figure 5.3: (a) Schematics of the working electrode. (b) Schematicts of the mediated reaction. The mediating layer shuttles electrons from the enzyme to the electrode, improving charge distribution to catalytic enzymatic sites within the sensing layer. (c) CV plots for the mediated working electrodes tested with and without presence of lactate. (d) CV plot of the unmediated electrode.

parameters affect the sensor performance. We point out aspects that remain to be studied and/or addressed before such system can become a commercially viable product.

5.2 Optimization of the printed flexible lactate sensor

Design of the working electrode

Designing and optimizing fabrication flow for the working electrode constitutes the most significant effort in the lactate sensor development. **Figure 5.3a** shows schematics of the working

electrode. It consists of three layers sequentially deposited onto the flexible substrate. The top layer comprises sensing component – LOx, immobilized in the polysaccharide chitosan to prevent its efflux into the sweat. The bottom layer is a gold transducer electrode. The mediating layer, composed of a tetrathiafulvalene (TTF) mediator and CNTs, is incorporated between LOx and transducer. The mediating layer shuttles electrons from the enzyme to the electrode, improving charge distribution to catalytic enzymatic sites within the sensing layer (Fig. 5.3b). This results in lowering the operation voltage of the sensor and decreasing the likelihood of oxidation of other analytes present in sweat, thus reducing interference. For example, LOx without mediator has an oxidation voltage around 0.6V, which corresponds to that of Uric Acid and Ascorbic Acid, also present in sweat (*267*). We chose TTF due to its well-characterized performance in enzymatic sensors (*267–269*) and compatibility with dermal applications (*13*).

When lactate from sweat comes in contact with enzyme on the electrode, the flavin adenine dinucleotide (FAD) of enzyme oxidizes it to pyruvate, while the dinucleotide itself gets reduced. The enzyme is then oxidized back to its original form by TTF+, at the same time TTF+ is reduced to TTF. Then it is converted back to TTF+ on the electrode. Two electrons are produced as a result of this reaction, as shown in the Equations (5.1-5.3) below. Thus, the detected current is directly proportional to the concentration of lactate.

(5.1) $\text{Lactate} + \text{LOx (FAD)} \Leftrightarrow \text{Pyruvate} + \text{LOx (FADH}_2\text{)}$

(5.2) $\text{LOx (FADH}_2\text{)} + 2\text{TTF}^+ \Leftrightarrow \text{LOx (FAD)} + 2\text{TTF} + 2\text{H}^+$

(5.3) $2\text{TTF} \Leftrightarrow 2\text{TTF}^+ + 2\text{e}^-$

The system's redox potentials vary depending on the composition of the electrode. Overall, in order to avoid interference from electroactive species in sweat, applied positive potential should not exceed 0.45 V (*268*). We determine the operating potential of working electrode through cyclic voltammetry (CV). To reduce the number of variables, we used a commercially available silver/silver chloride (Ag/AgCl) electrode as a reference and platinum wire as a counter electrode.

Figure 5.3c shows the CV plots for the mediated working electrodes tested with and without the presence of lactate. The curve without lactate (red) has one oxidation (top) and one reduction (bottom) peak corresponding to the oxidation and reduction of TTF. On the addition of lactate, the oxidation peak increases in size, while reduction peak decreases. The oxidation peak increases because the lactate in the solution is oxidized in addition to TTF contributing to the higher current. The reduction peak is reduced because reaction 5.3 (right to left) is inhibited by larger amounts of TTF which are present, because 5.2 is also inhibited by large amounts of Lox(FADH_2) caused by reaction 5.1. The maximum current is achieved at ~ 0.2 V, which is significantly lower than the theoretical 0.6V required to operate the sensor without TTF. Figure 5.3d. confirms that the electrode fabricated without TTF and operated in the same potential range

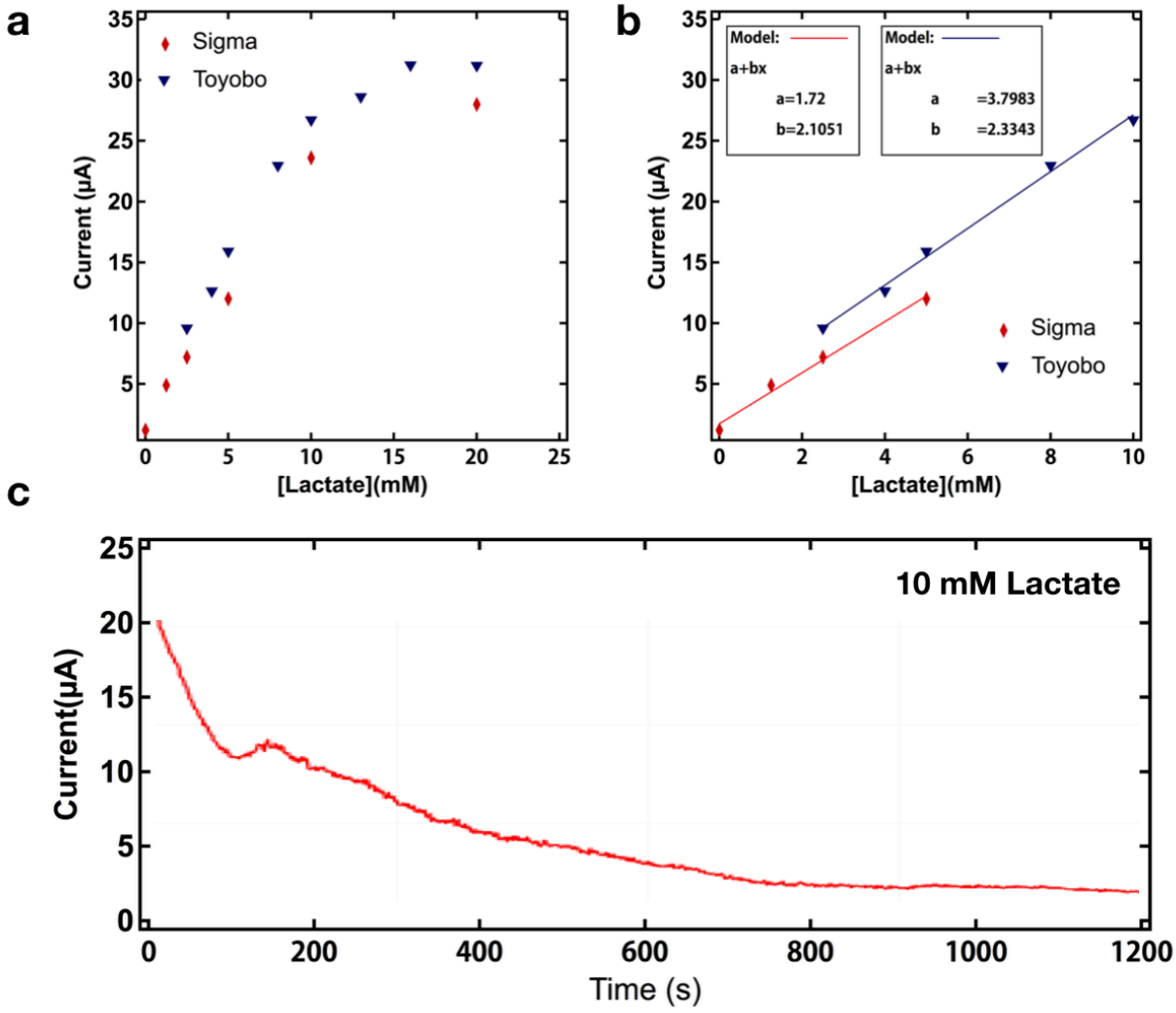

Figure 5.4: (a) Calibration curves and (b) slopes of the trendline fit in the linear range for the sensors fabricated with enzymes from two different manufactures – Toyobo and Sigma Aldrich. The concentration of lactate was varied between 0 and 25mM, the value of current readout for each concentration of lactate was recorded after 60s. (c) Current readout of the sensor operated continuously for 20 minutes in 10mM of lactate.

is unresponsive to the addition of lactate. Therefore, in the consequent studies, all electrodes were fabricated with TTF mediator and 0.2 V potential step (vs. Ag/AgCl commercial reference) was used for measurements of sensor sensitivity.

The composition of the mediated lactate sensors has been well documented (*13*, *26*, *27*, *270*, *271*). We used previous reports of highly sensitive lactate sensors as a guidance in determining the original sensor composition (*13*). We fabricated sensors with enzymes from two different manufactures – Toyobo and Sigma Aldrich, keeping the rest of the electrode components and dimensions fixed, and evaluated results keeping in mind performance benchmarks for wearable sweat sensors, i.e. high sensitivity, linear range up to 25 mM, and stable performance under continuous operation. **Figure 5.4a** shows calibration curves for the sensors. The concentration of lactate was varied between 0 and 25mM, the value of current readout for each concentration of lactate was recorded after 60s at 0.2V versus the reference electrode. Both sensors were sensitive up to 10mM of lactate. The corresponding sensitivities are shown in Figure 5.4b as a slope of the trendline fit in the linear range. Sensors with Toyobo and Sigma enzymes showed sensitivity of 2.33 μA/mM and 2.1 μA/mM respectively. Thus, enzymes from both manufacturers show comparable performance. In the consequent studies we used Toyobo. Although the sensitivity values are sufficient for wearable sweat monitoring, the detection limit has to be expanded from 10mM to 25mM. Sensors with linear range of 25mM can sense the transition from aerobic to anaerobic metabolism during exercise. In the following discussion we will show how the linear range can be expanded to 25mM through the optimization of the mediating and enzyme layers of the working electrode.

To continuously monitor lactate concentration during an exercise session the sensor needs to maintain the stable operation for the whole duration of an exercise. Figure 5.4c shows current readout of the sensor operated continuously for 20 minutes in 10mM of lactate. The sensor did not maintain stable performance, losing 80% of its signal within 10 minutes. We hypothesize that this effect was caused by efflux of poorly immobilized enzyme and soluble TTF+ from the electrode. This issue was successfully addressed through the optimization of sensor components.

Optimization of the working electrode components

In order improve the sensitivity and long-term stability, as well as to increase the linear range of the sensor to 25mM lactate, we optimized the mediating layer and enzyme layers of the working electrode.

The mediating layer is formed by drop casting a suspension of TTF/CNT in acetone and ethanol on the surface of gold transducer. TTF is a small molecule, that crystallizes when solvent evaporates. Changing the concentration of TTF/CNT in the suspension will affect the size of resulting TTF crystals. Particularly, lowering the concentration leads to formation of smaller TTF crystals resulting in larger contact area between enzyme and mediator layers. We varied the concentration of the TTF/CNT suspension deposited on the working electrode surface from 25mg/ml to 100mg/ml TTF. For each of the concentrations the total solid content and the TTF/CNT ratio were held constant, while the deposited volume was changed. For TTF concentrations of 100mg/mL, 50mg/mL and 25mg/mL the concentration of CNTs was 5mg/mL, 2.5mg/mL and 1.25mg/mL respectively. The deposited volume varied from 3μL, to 6μL, to 12μL respectively and was deposited in 3μL aliquots. **Figure 5.5a-c** shows the effect of TTF/CNT

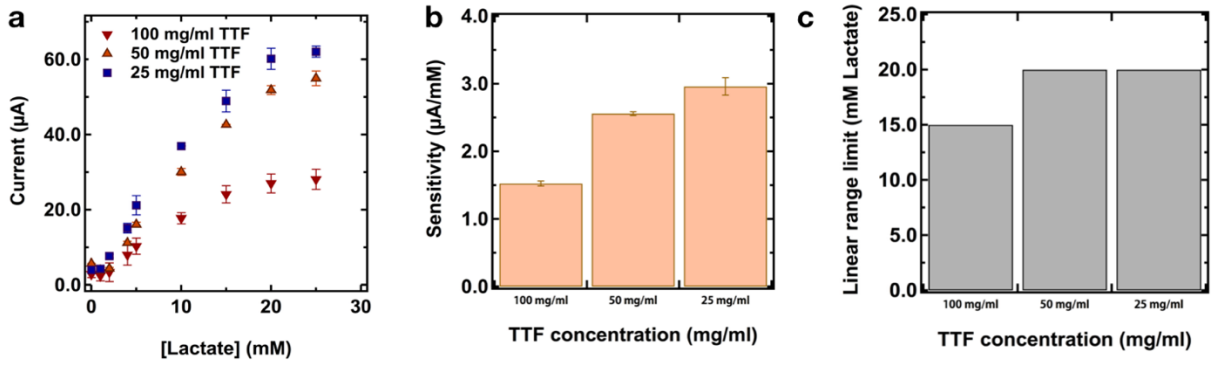

Figure 5.5: The effect of TTF/CNT concentration on the linear range (a,c) and sensitivity (b) of the lactate sensor. The concentration of the TTF/CNT suspension deposited on the working electrode surface was varied from 25mg/ml to 100mg/ml TTF. For each of the concentrations the total solid content and the TTF/CNT ratio were held constant, while the deposited volume was changed. Data partially collected by Maggie Payne.

concentration on the linear range (a,c) and sensitivity (b) of the sensor. The linear range and sensitivity increase from up to 10mM to up to 15 or 20mM lactate and from 1.5 µA/mM to 2.7 µA/mM respectively when TTF/CNT concentration decreases from 100mg/mL to 25mg/mL. Decreasing concentration from 50mg/mL and 25mg/mL resulted in marginal improvement. Therefore, we did not investigate further dilution and used 25mg/mL TTF in the mediating layer.

To improve sensor performance, we optimized three parameters in the enzyme layer: chitosan weight percent, CNT weight percent, and enzyme loading. Chitosan is a polysaccharide that acts as an immobilizer to stabilize the enzyme and prevent efflux of enzyme into the surrounding environment. LOx exhibits strong electrostatic interactions between with protonated amino groups on the chitosan chains. In addition, chitosan has been shown to have film-forming ability, permeability toward water, good adhesion, and biocompatibility, making it an excellent immobilizer for wearable printed sensor. Optimum concentration of chitosan in the enzyme layer is critical for proper enzyme immobilization. Insufficient chitosan content in the electrode will lead to suboptimal immobilization of enzyme; while excessive chitosan loading can result in blockage on LOx active sites and contribute to resistive losses. **Figure 5.6a-c** shows the effect of chitosan content in the enzyme layer on the sensor response to different concentrations of lactate. Increasing chitosan concentration from 0.1 wt.% to 0.6 wt.% results in increase of the linear range from 5mM to 20mM, and increase of sensitivity from 2 µA/mM to 4.2 µA/mM. Further increase in chitosan content shows decrease in sensitivity to 3.2 µA/mM and no further expansion of the linear range. Initial increase in linear range can be explained by the increase in the density of the

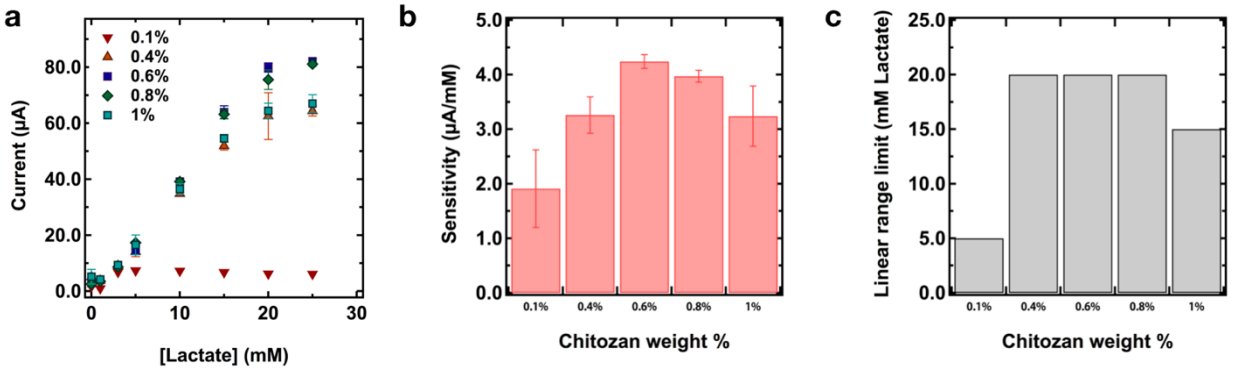

Figure 5.6: The effect of chitosan content in the enzyme layer on the sensor response to different concentrations of lactate. Data partially collected by Maggie Payne.

enzyme film, thus the expansion of the diffusion-limited region. Increase in sensitivity can be attributed to the enzyme retention and stabilization in the chitosan matrix; and is in agreement with previous reports of high LOx activity in the chitosan matrix. Therefore, 0.6 wt.% chitosan in the enzyme layer resulted in the highest sensitivity and linear range and was used for the further optimization.

In order to improve the charge transfer efficiency between enzyme and solution we added CNTs in the enzyme layer. While unmodified carbon nanotubes are hydrophobic and segregate in the aqueous solutions, chitosan has been proven to be an effective dispersing agent (*272*). CNT-chitosan nanocomposites were previously implemented to detect bio-molecules such as lactate, ethanol or cholesterol (*142*). **Figure 5.7a-c** shows calibration curves for the sensors with different CNT content in the enzyme layer, ranging from 0 wt.% to 1.5 wt.%. Increasing CNT content from 0 wt.% to 1 wt.% results in an increase of the linear range from 5mM to 20mM, and an increase of sensitivity from 2 µA/mM to 4 µA/mM. Further increase in chitosan content shows diminishing

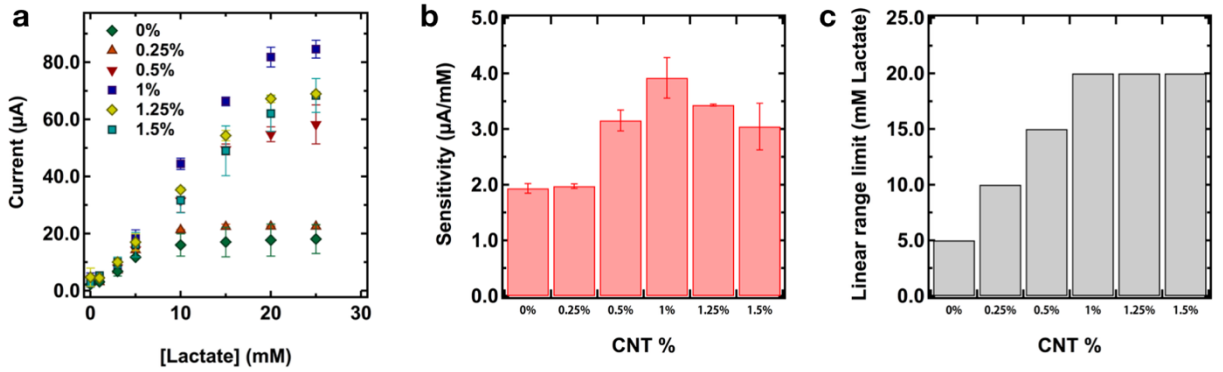

Figure 5.7: (a) Calibration curves (b) sensitivities and (c) linear ranges for the sensors with different CNT content in the enzyme layer, ranging from 0 wt.% to 1.5 wt.%. Data partially collected by Maggie Payne.

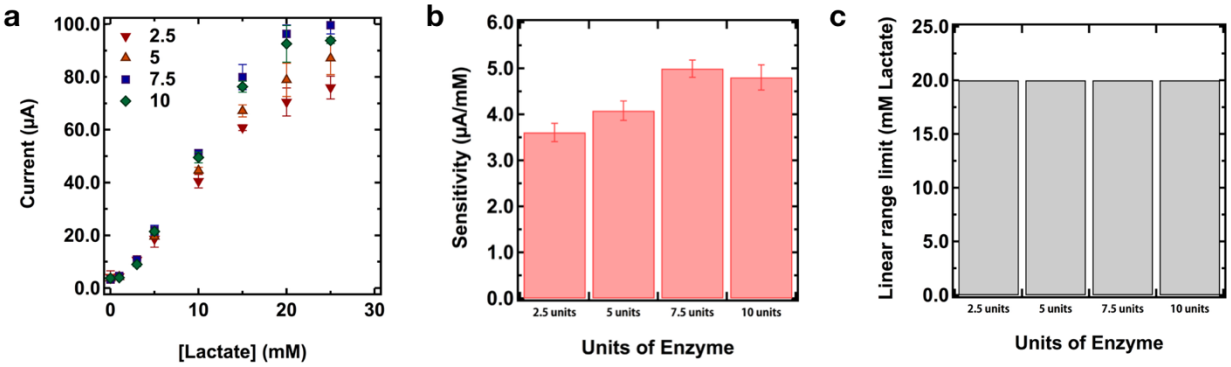

Figure 5.8: The effect of changing enzyme content from 2.5 to 20 units on the sensor response to different concentrations of lactate. Data partially collected by Maggie Payne.

return, with sensitivity decreasing to 3 μA/mM when the concentration of CNTs is increased from 1 wt.% to 1.5 wt.%. Including more than 1 wt.% of CNTs in the sensor can potentially hinder transport of lactate to LOx active sites, resulting in lower sensitivity of the sensor. Thus, the addition of up to 1 wt.% CNTs improves the conductivity of the composite.

The enzyme loading was optimized by varying the units of enzyme in the enzyme layer of the 3mm diameter electrode. **Figure 5.8a-c** shows the effect of changing enzyme content from 2.5 to 20 units on the sensor response to different concentrations of lactate. Sensitivity increases from 3.5 μA/mM to 5 μA/mM, when enzyme content is increased from 2.5 units to 7 units. Sensitivity decreases to 4.7 μA/mM when the enzyme content is further increased to 10 units. Linear range is unaffected by the enzyme content. Thus, enzyme loading of 7.5 units per 3mm diameter electrode area gives the highest sensitivity of 5 μA/mM. Enzyme content in the enzyme layer had less profound impact on sensor performance, compared with chitosan or CNT loading.

Performance of the fully printed sensor

To achieve a fully printed sensor, the optimized working electrode was integrated with printed reference and counter electrodes. Reference electrodes were fabricated via screen printing of commercially available Ag/AgCl paste. Counter electrodes were inkjet-printed from commercially available gold ink. The image of the printed lactate sensor is shown in **Figure 5.9a**. Because there is a difference in potential between commercially available and printed reference electrodes, we ran CV to determine the operating potential of working electrode against printed reference. Figure 5.9b shows the CV plot for the fully printed lactate sensor. The maximum current is achieved at ~ 0V, therefore, potential was held at 0V when operating the fully printed sensor. Figure 5.9c shows

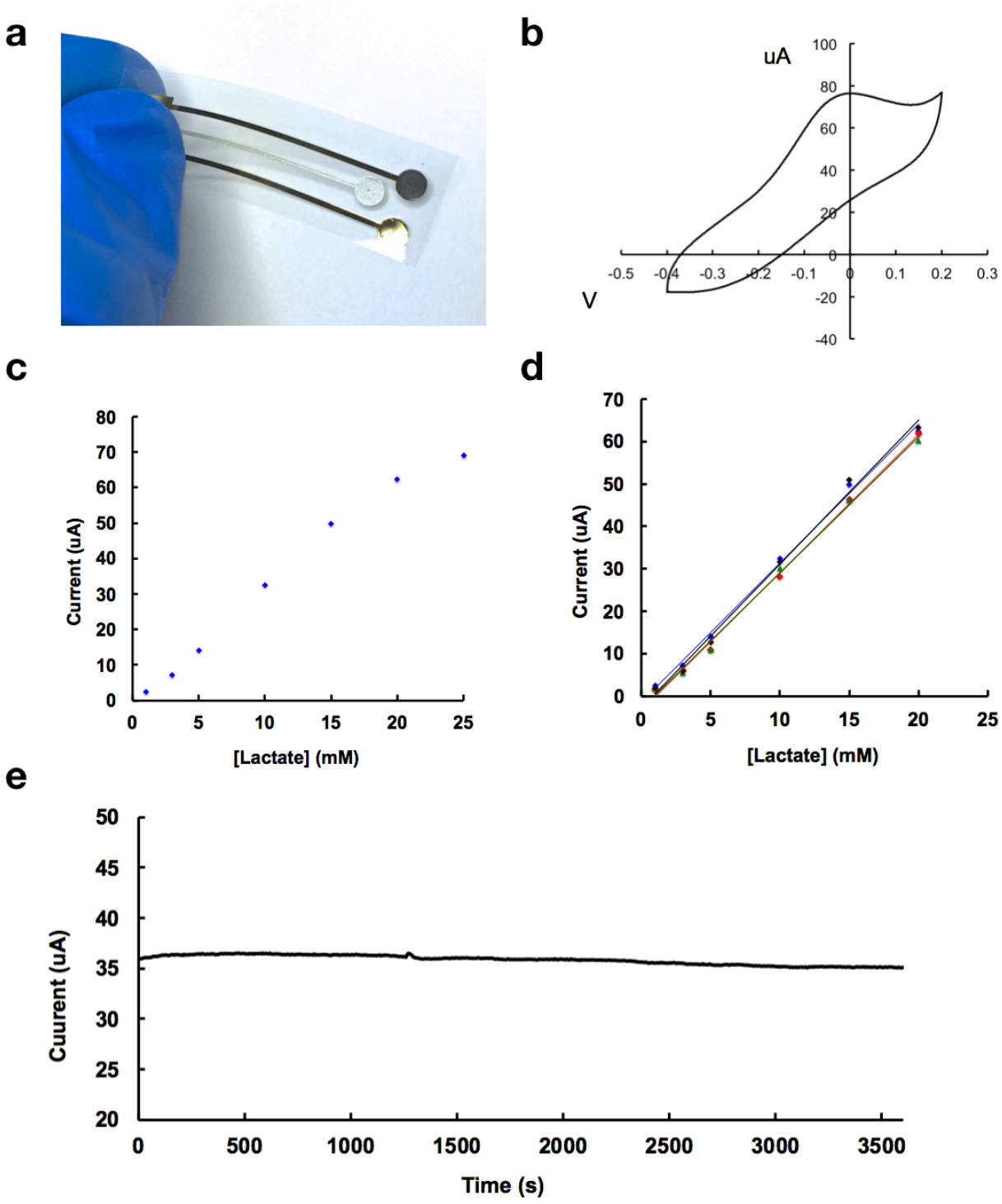

Figure 5.9: (a) The image of the fully printed lactate sensor. (b) CV, (c) calibration plots, (e) reproducibility and (e) long term stability of the fully printed lactate sensor.

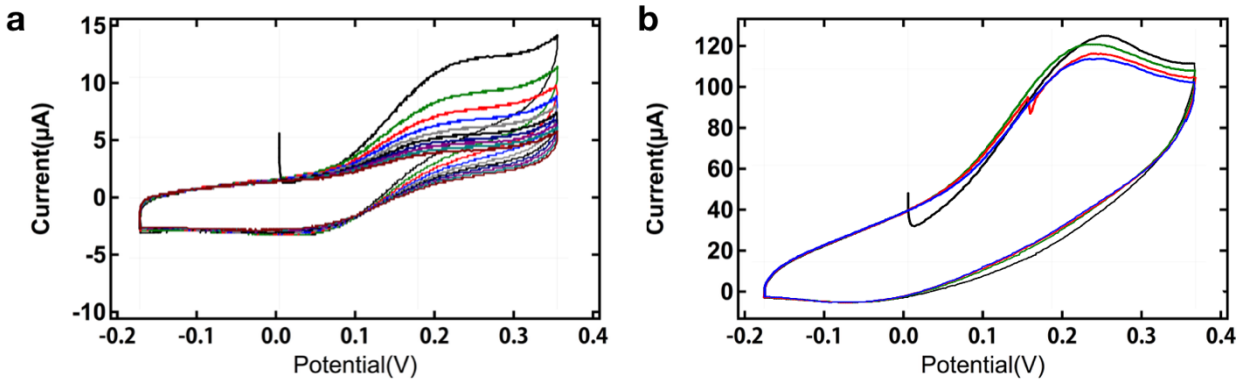

Figure 5.10: CVs of the working electrodes(a) before and (b) after optimization. Both working electrodes were tested against commercial Ag/AgCl reference and platinum counter.

calibration plot of the sensor. Device is sensitive up to 25 mM of lactate. The reproducibility and sensitivity in the linear range is shown in Figure 9d. Sensor is highly reproducible with sensitivity ~5 μA/mM or ~25 μA/mM cm^2. Furthermore, to ensure that the sensor can continuously monitor during an exercise session, we operated it for an hour in 10 mM lactate. Figure 9e shows the corresponding sensor response. It retains 97% of current, indicating usability for continuous monitoring during exercise.

Figure 5.10 further highlights the improvement in performance of the working electrodes as a result of optimization. Cyclic voltammograms of the working electrodes before and after optimization are shown in Figure 5.10a and b respectively. Both working electrodes were tested against commercial Ag/AgCl reference and platinum counter. As seen from Figure 5.10a, the oxidation peak of the non-optimized electrode decreases with each consecutive cycle. This effect was likely caused by efflux of poorly immobilized enzyme and soluble TTF+ from the electrode, leading to less current generated at electrode. As previously discussed, to effectively immobilize enzyme we optimized the weight fraction of chitosan and CNTs in the enzyme layer. This also resulted in the increased density of the enzyme layer leading to more effective entrapment of TTF+ at the electrode. As a result, the height of the oxidation peak remains constant when cyclic voltammetry is repetitively performed on the working electrode (Figure 5.10b). Additionally, we optimized suspension of TTF/CNT to facilitate formation of smaller TTF crystals. This resulted in larger contact area between enzyme and mediator layers, facilitated electron transfer to more enzyme sited and thus, led to an increase in the maximum current generated at the working electrode from 12 μA to 120 μA.

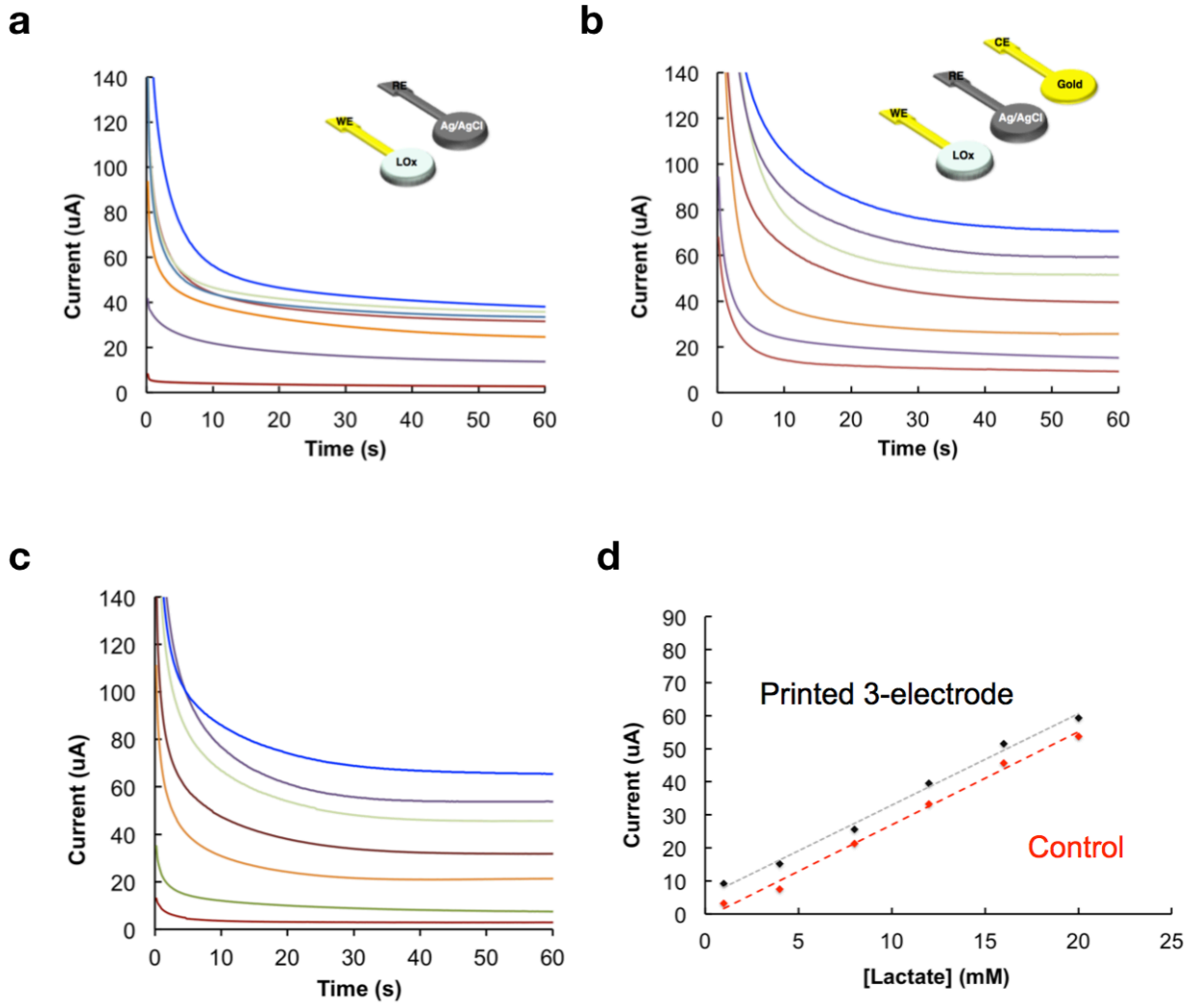

Figure 5.11: Chronoamperometric response to increasing lactate concentrations of (a) fully-printed two-electrode and (b) fully-printed three-electrode sensor and (c) sensor tested with commercially available reference and counter electrodes under the same conditions. (d) Calibration curves of the fully printed sensor with three-electrode configuration and the sensor tested with commercially available reference and counter electrodes.

In previous literature reports of printed sensors, a two-electrode configuration consisting of working and reference electrodes was occasionally used. This simplifies the circuit design and reduces the number of manufacturing steps. To identify the optimum configuration, we compared the performance of three-electrode and two-electrode sensors. **Figure 5.11** shows the

chronoamperometric response to increasing lactate concentrations of printed two-electrode (a) and printed three-electrode (b) sensors, as well as the sensor tested with commercially available reference and counter electrodes under the same conditions (c). The fully printed sensor with a three-electrode configuration matches the performance of the counterpart with commercial reference and counter electrodes, showing the same sensitivity and linear range with minor constant offset in current (Figure 5.11d). The two-electrode configuration showed lower sensitivity and linear range. In three-electrode setup the reference electrode maintains a stable potential in varying ionic environments, since the counter electrode works to counter the redox reactions that occur on the surface of the working electrode by allowing current to pass between the counter and working electrodes. In two-electrode configuration Ag/AgCl electrode performs the function of both reference and counter electrodes, resulting in poor control of the interfacial potential across the electrochemical interfaces.

In summary, fabricating the working electrode using a conventional approach resulted in the linear range that did not match physiological levels of lactate in sweat, as well as poor long-term stability of the device. We optimized each layer of the electrode to achieve good long-term stability as well as extend the linear range up to 20 mM (the device is sensitive up to 25 mM with slight curvature in response after 20 mM), with high sensitivity of ~5 μA/mM for a 3mm diameter electrode. Particularly, we used an optimal weight fraction of chitosan and CNTs in the enzyme layer to effectively immobilize enzyme and optimized suspension of TTF/CNT that is deposited on gold transducer electrode to serve as a mediating layer. Furthermore, performance of the fully printed sensor is in good agreement with that of the sensor tested with commercially available counter and reference electrode.

5.3 Incorporation of the diffusion-limiting membrane into the lactate working electrode

Rationale

If the enzymatic reaction is fast, then the rate at which lactate is reduced to pyruvate at the working electrode and, thus, the sensor response is limited by mass transfer of lactate to the electrode surface (linear region of the sensor response curve). Mass transfer, in turn, is determined by the bulk concentration of lactate, area of the electrode, diffusion and convection (*273*). For the applications considered in this work, the wearable sensor needs to be placed directly on the skin and continuously measure lactate concentration under variable sweat flow rate. Therefore, the transport of lactate to the electrode surface would be challenging to control. We observed

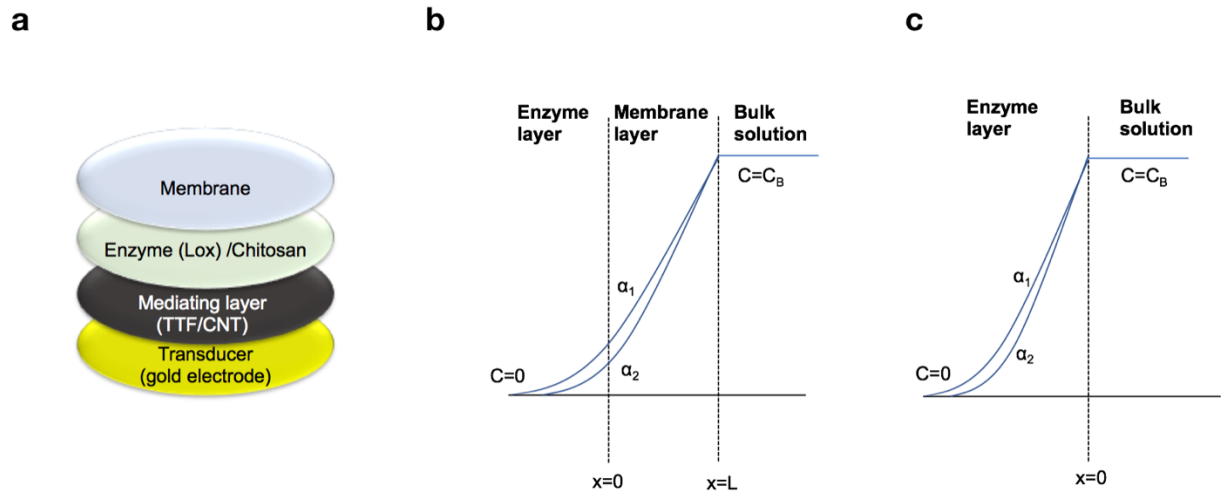

Figure 5.12: (a) Schematics of the working electrode with the diffusion limiting membrane. Analyte diffusion profiles in the sensors (b) with and (c) without diffusion limiting membranes.

significant fluctuations in current when sensors were tested in the solution that was continuously mixed, versus solution that was stagnant. Additionally, to enable future mass production of such sensors, it is important to achieve reproducibility in performance from batch to batch. Variation in sensitivity from batch to batch can occur due to the effect of the environmental conditions such as pH, temperature, time in storage on the activity of enzyme. Additionally, Payne et al. showed that biologically relevant concentrations of sodium, potassium, and calcium ions present in sweat affect enzyme activity and sensitivity of the lactate sensors (*164*). Both of the above limitations can be mitigated by incorporation of a diffusion limiting membrane on top of the electrode **(Fig. 5.12a).** M. Alvarez-Icaza et. al. outlined the model for change in sensitivity with respect to enzyme kinetics for the sensors with and without diffusion-limiting membrane (*274*) (Fig. 5.12b,c). The variation in sensitivity was represented by the derivative of the sensitivity with respect to the parameter α, which represents the enzyme kinetics. Equations (5.4) and (5.5) show expressions for the sensors with and without membrane respectively.

$$\frac{\partial Sm}{\partial \alpha} = \left(\frac{D_S^2}{2}\right) * \left(\frac{\sqrt{\frac{De}{\alpha}}}{\left(Ds + L\sqrt{De\alpha}\right)^2}\right) \quad (5.4)$$

$$\frac{\partial S}{\partial \alpha} = \frac{1}{2} * \sqrt{\frac{De}{\alpha}} \quad (5.5)$$

Here Sm and S are sensitivities of sensors with and without membrane, De - diffusivity in the enzyme layer and D_S - in the area surrounding the enzyme layer. L is the thickness of the membrane. α= Vmax/Km, where Vmax is the maximum reaction rate and Michaelis- Menten constant.

To account for the difference in the sensitivity of the two types of sensors, the change in sensitivity was divided by the sensitivity to obtain the relative sensitivity. The resulting equations were as follows:

$$\frac{\partial Sm/\partial \alpha}{Sm} = \frac{1}{2\alpha} * \frac{1}{1+\frac{L}{Ds}*\sqrt{De\alpha}} \quad (5.6)$$

$$\frac{\partial S/\partial \alpha}{S} = \frac{1}{2\alpha} \quad (5.7)$$

The equation for the sensor with incorporated membrane contains an extra term $\frac{1}{1+\frac{L}{Ds}*\sqrt{De\alpha}}$. Since all the variables must be positive, the term should be less than or equal to one. This leads to the conclusion that the use of a membrane on top of the sensor reduces the relative variation of the sensor's sensitivity with respect to variations of the enzyme activity. An additional benefit of diffusion limiting membrane is increased linearity of the sensor response. Increasing linear detection range to above 40mM can extend the range of applications of the sensor. Chronic clinical conditions such as pressure ischemia, panic disorder, and cystic fibrosis are characterized by increased lactate in sweat. The lactate levels of such patients reach 40mM. Therefore, being able to detect high concentrations of lactate would enable potential utilization of such sensors for clinical monitoring, in addition to exercise/performance monitoring.

Evaluation of polymers for the diffusion limiting membrane

Membranes should have uniform thickness, porosity and hydrophilicity. Up to date polyurethane (PU) (*275*, *276*) and Nafion (*277–280*) membranes have been widely used due to their biocompatibility and presence of polar groups in the chain. Similarly, use of hydrogels, such as (hydroxyethyl methacrylate)-based (pHEMA) hydrogel (*270*) or its derivatives (*281*) were reported. Polyvinyl chloride (PVC) membrane was used to fabricate printed lactate sensor (*16*).

Fabrication method plays a critical role in the membrane performance. Certain casting and drying conditions can lead to uneven membrane thickness or porosity (*282*), resulting in uneven membrane properties, which , in turn, can negatively affect reproducibility in sensor performance. Since this work focuses on printed sensors, it was important to investigate the performance of the sensors with membranes that were printed from the solution.

We first tested the performance of the sensors with Nafion and PU membranes, since PU and Nafion have been widely used in the literature. **Figure 5.13a** shows calibration curves for the sensors with Nafion membranes deposited from 3% and 5% solution of Nafion in lower aliphatic alcohols and water. The concentration of lactate was varied between 0 and 45mM, the value of current readout for each concentration of lactate was recorded after 60s. Interestingly, both sensors were sensitive only up to 10mM of lactate, compared to 25mM for sensors without membrane. Additionally, the maximum current decreased from 80 μA to 2.4 μA, if compared to that of sensors

without membrane. This is indicative of the negative effect of Nafion solution on the rate of enzymatic reaction for the given chemistry. Therefore, we did not investigate membrane deposited from the Nafion solution further. Figure 5.13b shows the calibration curves for the sensors with PU membranes. In previous reports sensors with PU membranes were conditioned before testing. Therefore, we tested sensors with PU membranes deposited from two different concentrations of PU (10% in red, 5% in blue) before (circles) and after (diamonds) two hours of conditioning in pH 7 buffer. Sensors with both 10% and 5% PU membranes change their response after conditioning. Although performance improves in both cases, we did not consider PU as a candidate material. Sensor should maintain stable performance with minimum conditioning time, while sensors with PU membranes continued changing performance even after two hours.

As an alternative to PU and Nafion, we tested copolymer of polystyrene and poly (methyl methacrylate) (PMMA). Figure 5.13c shows the response of the sensors with membranes deposited from 1% and 3% polymer solution. The linear ranges of sensors are 20mM and 50mM lactate respectively. Although the sensitivity of the sensor with 3% polymer membrane is adequate for wearable sweat monitoring, we observed the same issue as with PU membrane, i.e. the sensor requires long conditioning time.

Next, we evaluated the performance of sensors with polyvinylidene fluoride (PVDF) membranes, due to previously reported uniform porosity and good film forming ability of the PVDF based membranes (*282*). Figure 5.13d shows the calibration curves of the sensors with PVDF membranes of three different thicknesses. Membrane thicknesses are expressed in terms of volume of the deposited polymer solution – 1.5 µL, 2 µL and 3 µL, with area of the working electrode being fixed to 3mm diameter circle. Sensors with membranes from both 2 µL and 3 µL polymer solutions result in 45mM detection range, sensors with membrane from the 1.5 µL solution have linear range up to 35mM. Despite of the hydrophobicity of PVDF, sensors with membranes formed from 3 µL, 2 µL and 1.5 µL polymer solutions showed good sensitivities of 0.05 µA/mM, 0.15 µA/mM and 0.2 µA/mM respectively. Additionally, sensors with PVDF membranes did not require conditioning of more than 15min. Furthermore, the sensitivity can be further increased by making polymer solution of PVDF with a hydrophilic polymer, like PMMA. Figure 5.13e shows the calibration curves for sensors with PVDF and PVDF/PMMA membranes. Addition of hydrophilic PMMA resulted in the increase of sensitivity from 0.05 µA/mM to 0.1 µA/mM without compromising linear detection range of 45mM. However, using membranes deposited from two-component polymer solution has its drawback of introducing variability in membrane structure. Therefore, in hope to achieve sensitivity and linear range similar to PVDF/PMMA, but without variability in membrane composition, we tested the performance of

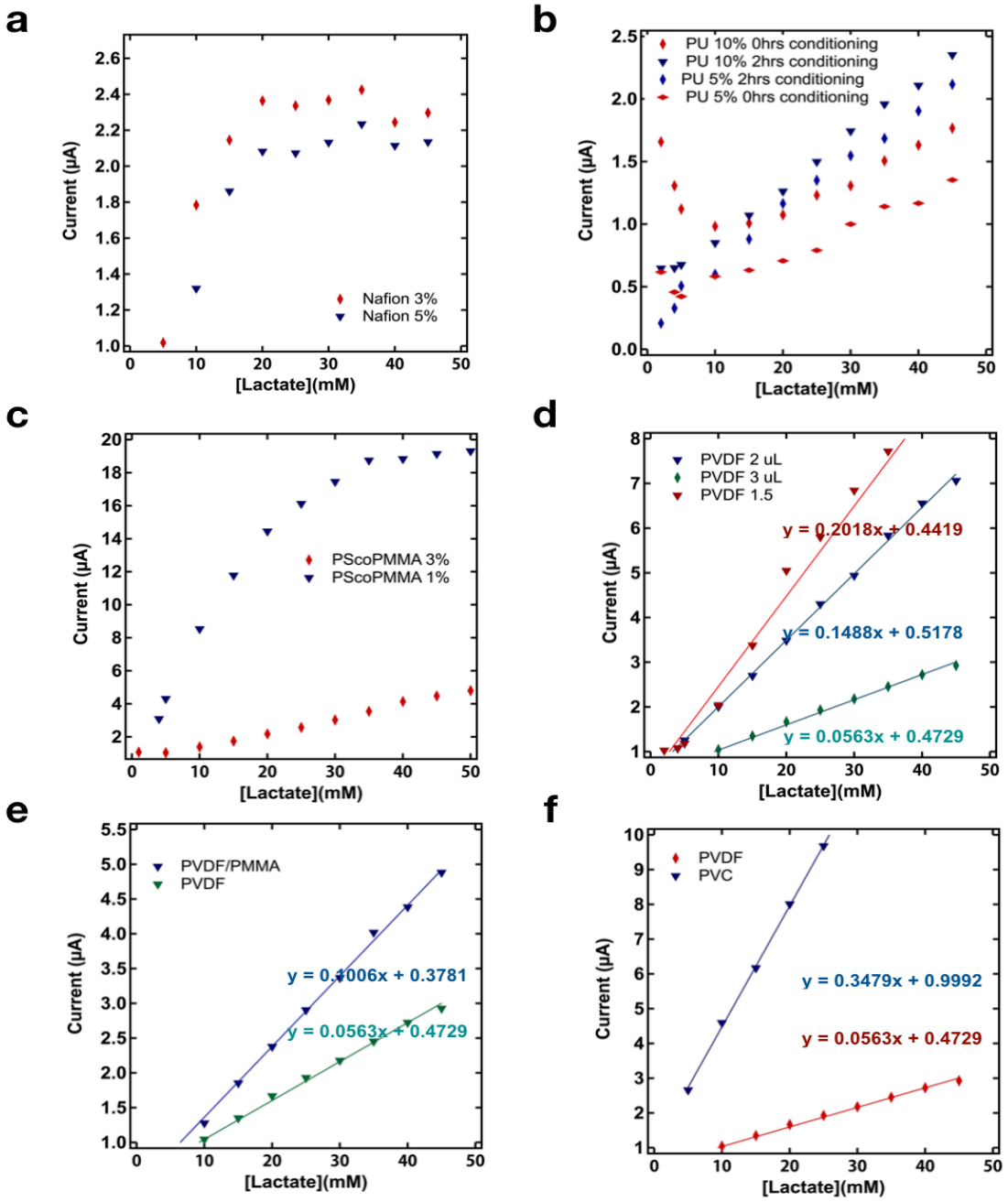

Figure 5.13: Calibration curves for the sensors with (a) Nafion, (b) PU, (c) PScoPMMA membranes. (d) Calibration curves of the sensors with PVDF membranes of three different thicknesses. Membrane thicknesses are expressed in terms of volume of the deposited polymer solution – 1.5 µL, 2 µL and 3 µL. (e) Calibration curves for sensors with PVDF and PVDF/PMMA membranes with the same mass fraction of polymer. Data partially collected by Veronika Pister.

sensors with polyvinylchloride (PVC) membranes. PVC has similar chain composition to that of

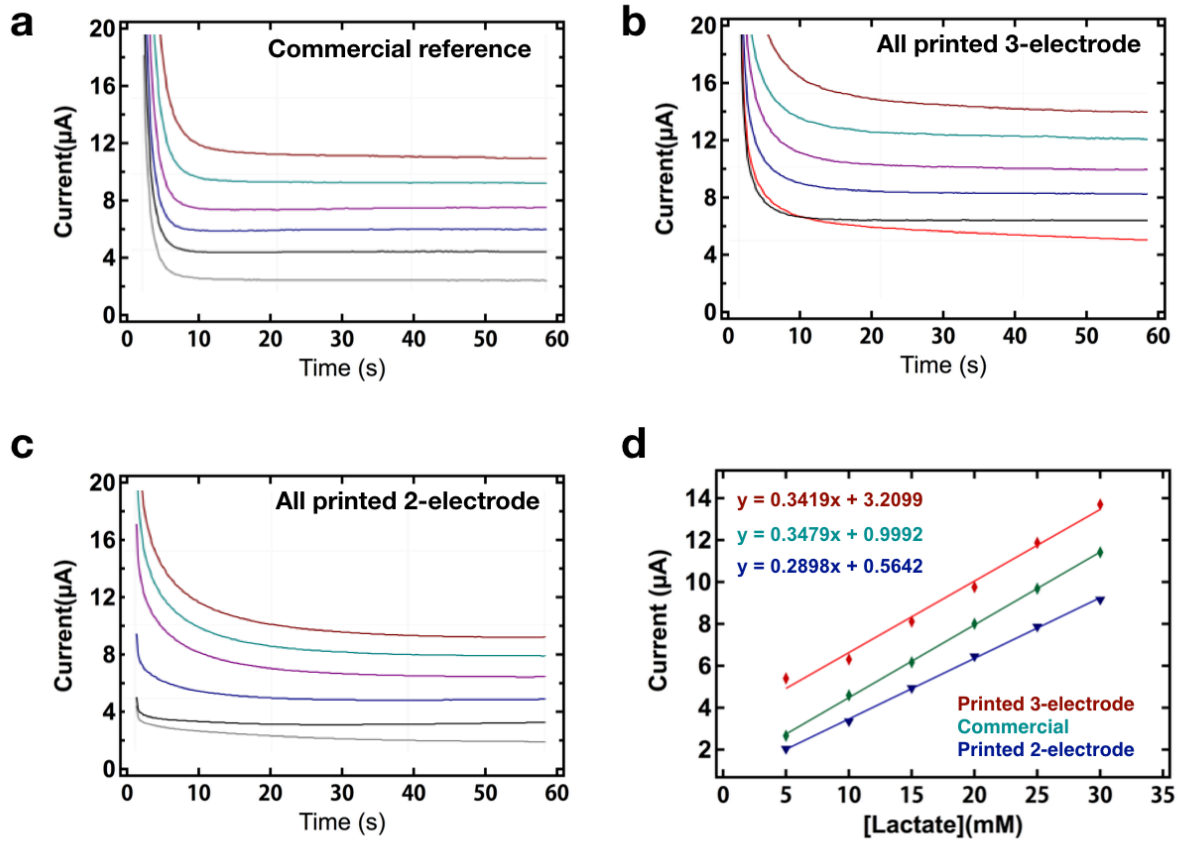

Figure 5.14: Chronoamperometric response to the increase in lactate concentrations of the (a) sensors with commercial reference and counter electrodes, (b) fully-printed sensors with three-electrode and (c) fully-printed sensors with two-electrode configuration with diffusion limiting membrane. (d) Calibration plots for sensor with commercial reference and counter electrodes, printed sensors with three-electrode and two-electrode configurations.

PVDF, but is more hydrophilic. Sensors with PVC membranes showed high sensitivity of ~0.35 μA/mM (Figure 5.13f), three times higher than the PVDF/PMMA membrane with the same polymer content, but with linear range of at least 30mM. Similarly to sensors with PVDF membranes, sensors with PVC membranes did not require conditioning of more than 15min. Because this particular platform was designed for sport monitoring, 30mM range satisfies design parameters. Therefore, PVC was chosen as a polymer for preparation of the diffusion limiting membrane.

Performance of the sensors with the diffusion limiting membrane

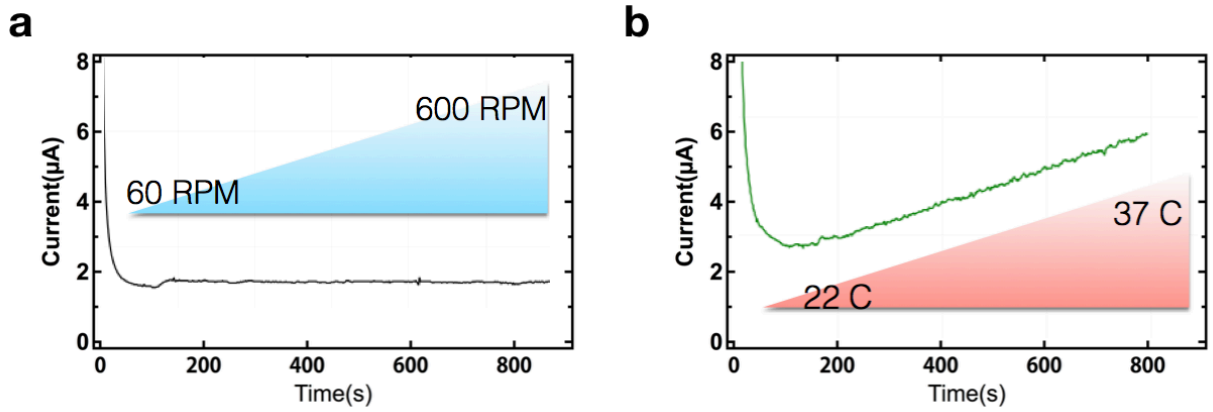

Figure 5.15: (a) Readout of the sensor placed in a beaker with the solution stirred at RMP changing from 0 to 600. (b) Sensor readout upon elevation of temperature from 22 °C to 37 °C

Figure 5.14 compares performance of the sensors with diffusion limiting membrane in a printed two-electrode (c) and printed three-electrode (b) configurations, as well as sensor tested with commercially available reference and counter electrodes (a) under the same conditions. We used the same working electrode to compare the sensor performance in three configurations mentioned above. We first tested the electrode against commercial Ag/AgCl reference and platinum counter. After that the same electrode was attached to the substrate with printed reference and counter. As done previously, for the printed configuration – the reference electrodes were fabricated via screen printing of commercially available Ag/AgCl paste. Counter electrodes were inkjet-printed from commercially available gold ink. Chronoamperometric response to increasing lactate concentrations of the sensors with diffusion limiting membrane in three different configurations is shown in Figure 5.14a-c. The concentration of lactate was varied between 5 and 30mM, the current for each concentration of lactate was recorded for 60s. The corresponding sensitivities are shown in Figure 5.14d as a slope of the trendline fit in the linear range. The trend of difference in performance between sensors with membrane in three configurations mimics the previously observed results of the sensors without membrane. Particularly, sensor with three-electrode configuration matches the performance of its counterpart tested with commercial reference and counter electrodes, showing the same sensitivity and linear range with minor constant offset in current (Figure 5.14d). Two-electrode configuration showed lower sensitivity and slower response (i.e. taking longer to achieve steady state response). The difference in sensitivity was less profound than that of sensors without membrane, likely due to the lower overall current readout.

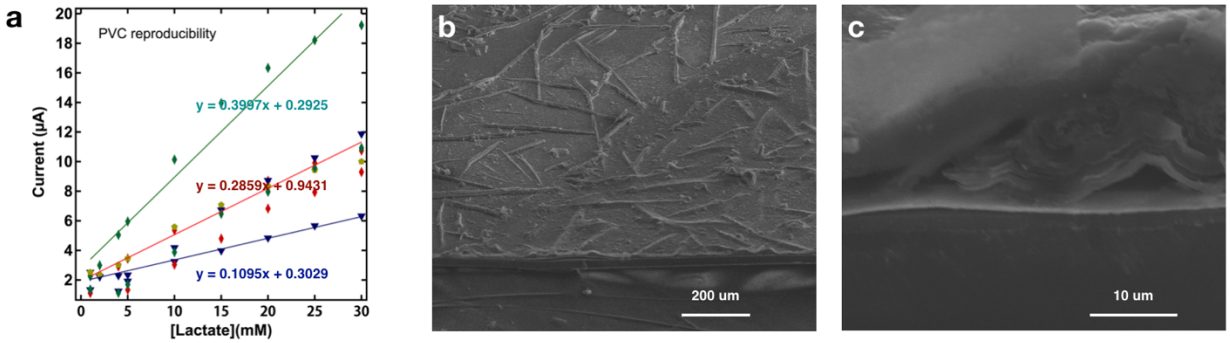

Figure 5.16: (a) Calibration curves of sensors from three different batches. (b) Top and (c) cross-section SEM images of the working electrode for sensing of lactate.

As previously mentioned, wearable sensor needs to be placed directly onto the skin and has to continuously measure lactate concentration under variable sweat flow rate. To test if diffusion limiting membrane mitigated the effect of change in flow rate on sensor readout, we placed the sensor in a beaker of 5 mM lactate solution that was stirred at RMP from 0 to 600, while continuously measuring the sensor readout. Figure 5.15a shows that sensor response remains stable when the RPM is increased. This observation confirms that the diffusion limiting membrane can be used in situations where transport of lactate to the electrode surface is challenging to control. Additionally, since skin/environment temperature variations can affect enzyme reaction kinetics, we investigated the effect of temperature elevation on the sensor response. Figure 5.15b shows the sensor readout upon elevation of temperature from 22 °C to 37 °C. As a result of temperature increase, the sensor response increases from 3 µA to 6 µA. Therefore, real time calibration of sensor response with respect to temperature variation is required for wearable sensing applications.

To test batch- to-batch variability, we compared the performance of different batches of sensors fabricated with PVC membrane. **Figure 5.16a** shows calibration curves of sensors from three batches. The sensitivity ranges from 0.1 µA/mM to 0.4 µA/mM, with 70% of the devices showing sensitivity of ~0.3 µA/mM. This is a significant variability, compared to the same sensors without membrane, that consistently performed within experimental error. To elucidate the reason for the variability in sensor performance, we conducted SEM of the working electrode. Figure 5.16b,c shows the top (b) and cross-section (c) images of the electrode. From Figure 5.16b, surface of the sensor appears rough, with randomly distributed needle-like structures. Zoomed-in cross-section image in Figure 5.16c, reveals that needle-like structures are crystals of TTF. The fact that TTF crystals have random size and distribution throughout electrode results in membrane thickness variability throughout the electrode, leading to differences in membrane properties from device to device. Variability in membrane morphology between devices leads to variability in transport characteristics of membrane and, consequently variability in sensor performance.

In summary, in the scenario where wearable sweat sensor should be placed directly onto the skin to perform continuous measurements of lactate, the variations in sweat rate can lead to

variations in the transport rate of lactate to the electrode surface, causing variations in the sensor readout. This limitation was addressed by the incorporation of the diffusion limiting membrane on the electrode surface. Because diffusion within the membrane is significantly lower than the external diffusion, the sensor response is unaffected by the motion of sweat. We evaluated the performance of sensors with Nafion, PU, PVDF, PVDF/PMMA and PVC membranes. All membranes were drop-casted from the solution. PVC membranes showed the best sensitivity of ~0.35 μA/mM in the relevant linear range of 0-30 mM lactate. Additionally, sensors with PVC membranes did not require extensive conditioning and were showing stable response after 15min. PVC diffusion limiting membrane mitigated the effect of change in flow rate on the sensor readout, as confirmed by stable sensor response under varying transport conditions. However, incorporating the membrane led to variability in sensor performance. SEM characterization revealed that crystalline nature of the TTF mediator led to random structure of the electrode surface. This, in turn, resulted in the variable morphology of the diffusion limiting membrane that was deposited on top of the sensor surface, and led to poor reproducibility of the devices. Therefore, in fabrication of printed sensors with diffusion-limiting membrane, careful consideration should be given to the morphology of the sensor components.

5.4 Achieving stability of the reference electrode

Potentiometric sensors rely on determination of the potential between ion selective and reference electrodes when there is no current flowing in-between. The reliable performance of these sensors highly depends on the stability of the reference electrode in different ionic environments. The reference electrode is conventionally achieved by depositing polymeric membrane saturated with chloride salt on top of the printed Ag/AgCl layer.

The morphology and thickness of Ag/AgCl layer should be optimized to achieve fast and reversible response. We compared performance of screen printed **(Figure 5.17a,b)** and stencil printed (Figure 5.17c,d) Ag/AgCl layers with two thicknesses – 25 μM and 50 μM. Figure 5.17a,c shows the emf response of the screen printed (a) and stencil printed (c) layers tested against single junction commercial Ag/AgCl reference in concentrations of NaCl solution ranging from 10^{-4} M to 10^{-1} M (physiologically relevant range). The linear fit for the response of the corresponding stencil and screen-printed electrodes is shown in Figure 5.17 d and b respectively. All conditions result in close to the ideal Nerstian behavior (59 mV/decade), although screen-printed electrodes show better linear fit. Thickness, at the given range of 25 μm-50 μm, did not play a role in the electrode performance regardless of the deposition technique. All Ag/AgCl layers showed faster

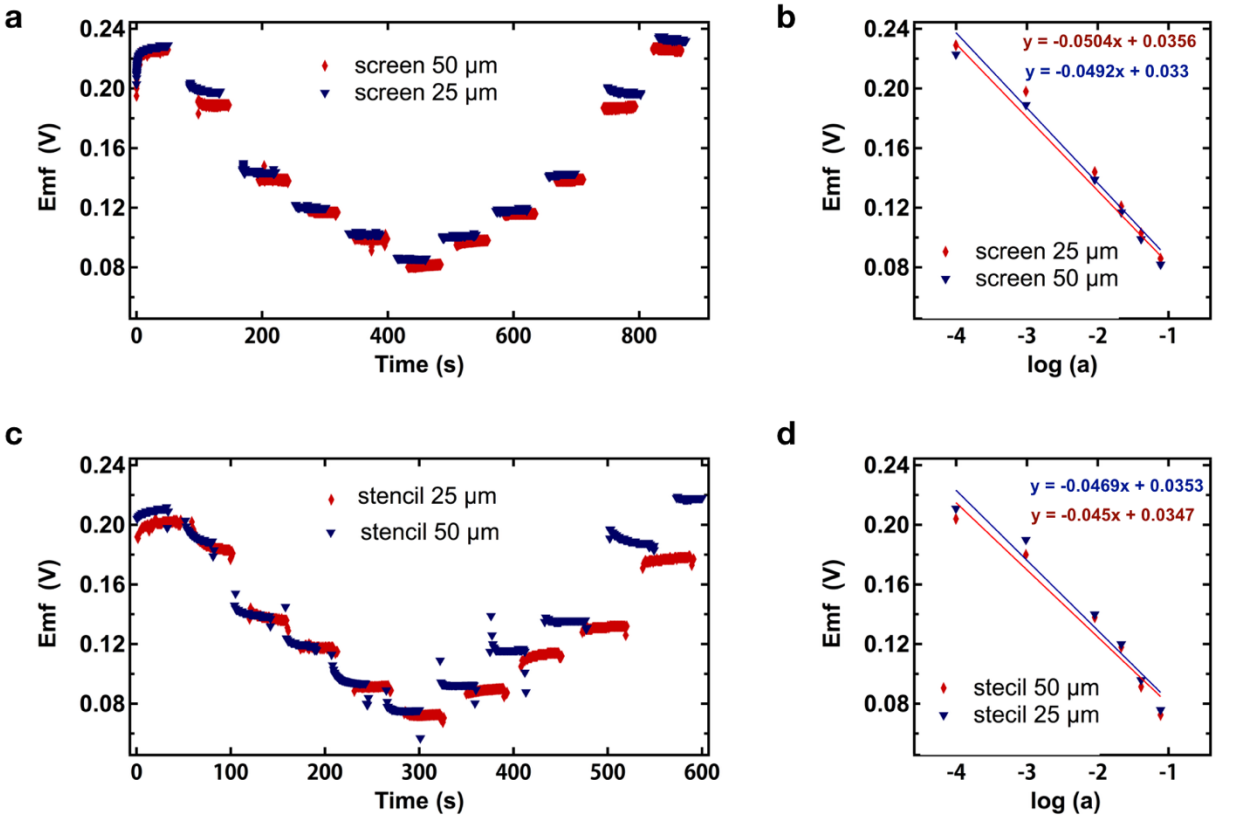

Figure 5.17: Emf response of the (a) screen printed and (c) stencil printed electrodes tested against single junction commercial Ag/AgCl reference in concentrations of NaCl solution ranging from 10^{-4} M to 10^{-1} M. Linear fit for the response of the corresponding (d) stencil and (b) screen-printed electrodes.

response in higher concentrated analyte solutions. However, screen-printed layers showed faster response over the range of NaCl concentrations. Therefore, we used screen-printing to deposit the Ag/AgCl layer for the reference electrode.

To elucidate the reason for the difference in electrode response we examined the morphology of the printed Ag/AgCl patterns. **Figure 5.18** shows the top view SEM of the 25µm and 50 µm screen printed (a-d) and 50 µm stencil printed (e-f) Ag/AgCl electrodes. Screen printed electrodes have higher roughness than the stencil printed electrodes, irrespective of the thickness. Rougher electrodes have higher surface area leading to faster equilibration upon immersion in the solution and, thus, faster response to the change in NaCl concentration.

In order to eliminate sensitivity of the electrode to the change in Cl^- concentration, we combined the Ag/AgCl layer with a PVB membrane (*283*). The thickness of the membrane is an

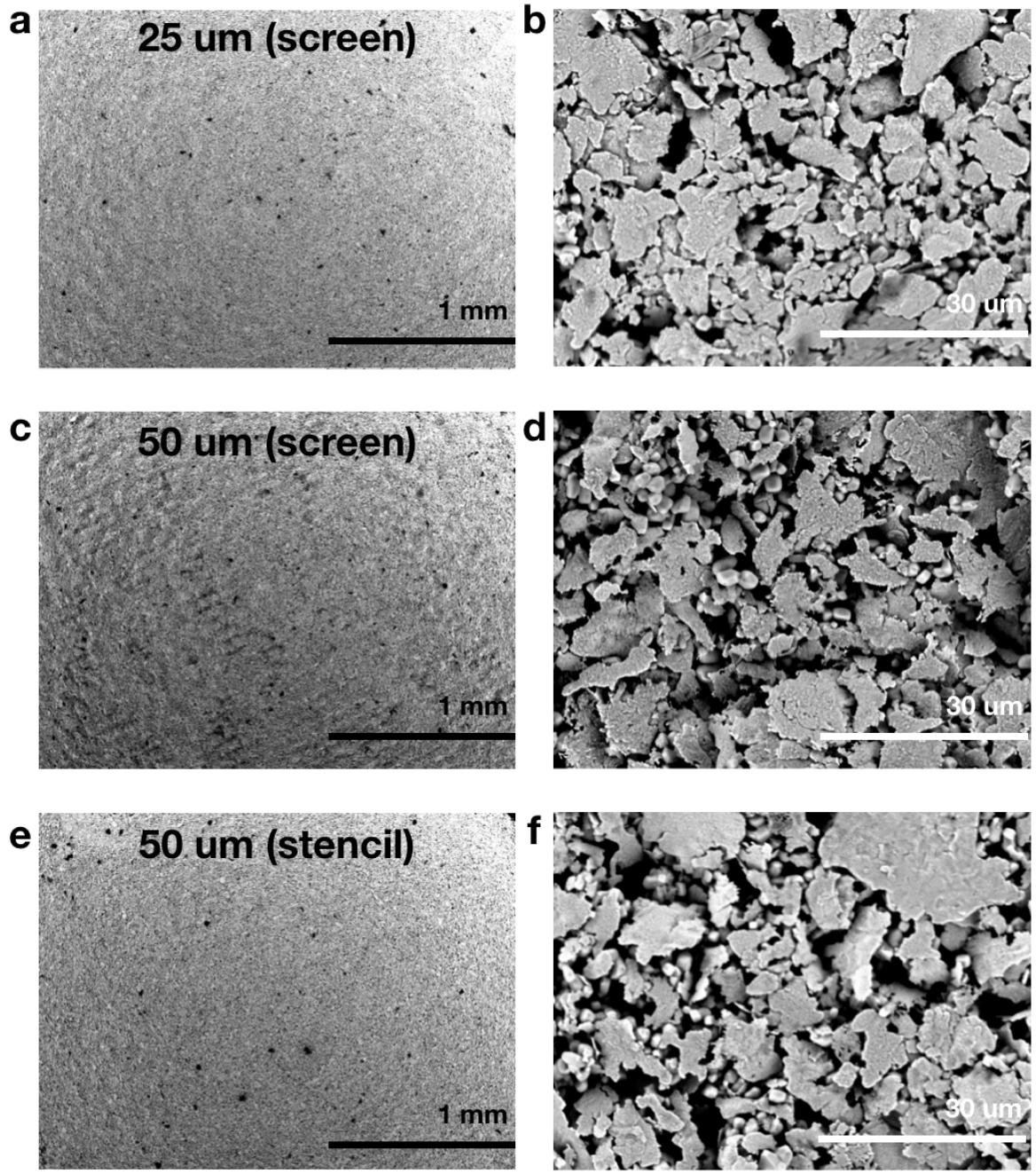

Figure 5.18: Top view SEM of the 25μm and 50 μm (a-d) screen printed and (e-f) 50 μm stencil printed Ag/AgCl electrodes.

important parameter in the electrode architecture. The membrane should be thick enough to

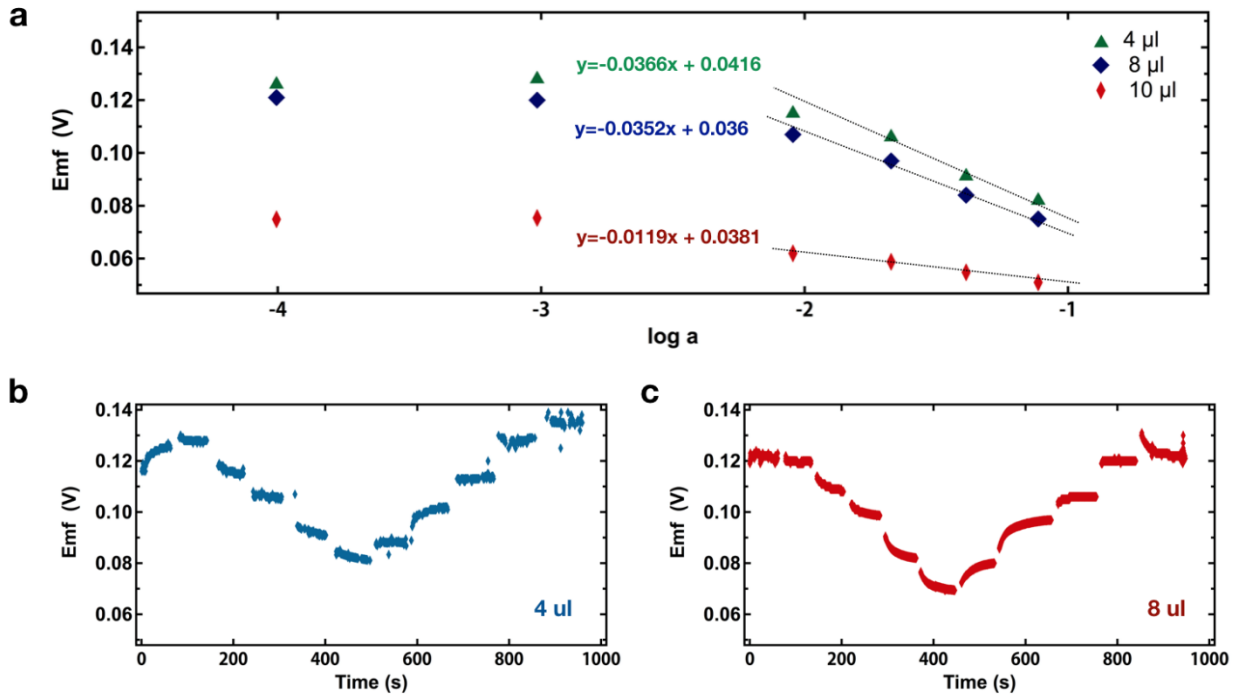

Figure 5.19: (a) Potential response of the reference electrodes with different membrane thicknesses to change in activity of NaCl solution. Membrane thickness is presented in terms of volume of the deposited solution – 4 µL, 8 µL, 10 µL. (b-c) Potential readouts for the electrodes with 4 µL and 8 µL membranes.

maintain high concentration of chloride ions at the electrode surface and prevent the efflux of the ions into the external solution. At the same time, electrode with thick membrane might require extensive conditioning in order to achieve stable response. Potential response of the reference electrodes with different membrane thicknesses to change in activity of NaCl solution is presented in **Figure 5.19**. Membrane thickness is presented in terms of volume of the deposited solution – 4 µL, 8 µL, 10 µL. Reference electrodes are not sensitive to changes in concentrations below ionic activity values of 10 E-3 M. The electrodes exhibited linear response in the region of higher activity values with a slope of -11, -35 and -37 mV/decade for the membranes formed from 10 µL, 8 µL and 4 µL of the polymer solution respectively. Thicker electrodes were less sensitive to the change of salt activity, but stability was not achieved for the electrodes with the given range of membrane thickness. Additionally increasing thickness of the membrane resulted in longer equilibration time, as confirmed by Figure 5.19b,c showing the corresponding potential readouts for the electrodes with 4 µL and 8 µL membranes. The electrodes were immersed in the solutions of different NaCl concentrations and response was recorded for 10 seconds following the immersion. Electrodes with 8 µL membranes show poor reversibility and delayed response. Therefore, incorporating thin PVB membrane at the electrode was ineffective for achieving

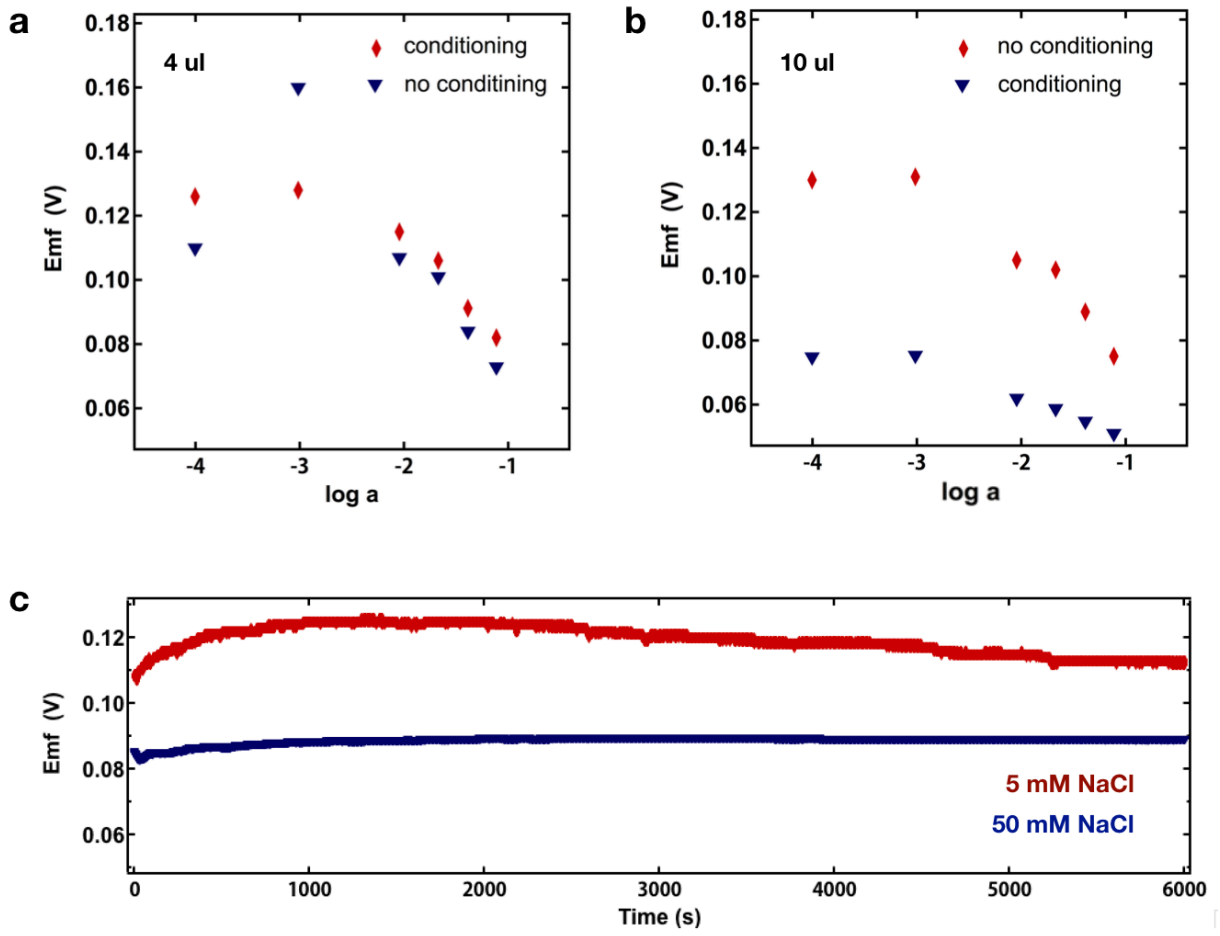

Figure 5.20: response to the change in ionic activity of NaCl of the electrode with membranes deposited from (a) 4 µL and (b) 10 µL polymer solution. (c) Continuous potential response of the electrode immersed in the 50 mM and 5 mM NaCl solutions.

electrode stability, likely due to diffusion of chloride ions from the membrane into the solution. Increasing membrane thickness is not an optimum approach for mitigating this issue, since electrodes with thicker membranes require longer equilibration time. We developed an alternative approach for improving stability of the reference electrode, that will be discussed further.

The effect of conditioning time on the sensitivity of the electrode to changes in salt concentration is shown in **Figure 5.20**. Electrodes with membranes deposited from 4 µL and 10 µL polymer solution were conditioned for 12 hours in 50 mM NaCl and then subjected to solutions with different ionic activity of NaCl. Figure 5.20a shows that response on the electrode with

thinner membrane before and after conditioning remains unchanged, i.e. both conditioned and not conditioned electrodes are not sensitive to changes in concentrations below ionic activity values of 10 E-3 M and exhibit linear response in the region of higher activity values with a slope of ~ -37 mV/decade of NaCl concentration. Figure 5.20b shows the response to the change in ionic activity of NaCl of the electrode with thicker membrane. The sensitivity of the electrode reduces from ~ -37 mV/decade to -11 mV/decade as a result of conditioning.

While conditioning has a favorable influence on the stability of the electrode in different electrolyte concentrations, requirement for prolonged conditioning complicates manufacturing/usability of the sensors for wearable applications. Under ideal scenario, the reference electrode would require short term or no conditioning. In order to determine the minimum amount of time required for conditioning of the electrode, we continuously measured potential response of the electrode immersed into the 50 mM and 5 mM NaCl solutions. Figure 5.20c shows that the electrode immersed into 5 mM and 50 mM solutions reach stable potential after 5000sec and ~600 seconds respectively. Since the average concentration of NaCl in sweat is around 50 mM, we expect that the reference electrode would not require conditioning exceeding 10 min.

To improve reference electrode stability we explored modifications to the PVB membrane using carbon nanotubes (CNTs). CNTs have been previously incorporated into membrane of the reference electrode in order achieve stable response (*26*). CNTs can provide surface area for Cl^- ion adsorption and, thus, facilitate retention of the ions at the electrode surface. We explored two approaches: in the first case we incorporated CNTs into the membrane; in the second case, CNT layer was created between the membrane and Ag/AgCl to act as a surface for adsorption and retention of chloride ions. Homogeneous CNT/THF suspension was first achieved using the block copolymer PEO-PPO-PEO (F127) as a surfactant and then deposited via drop-casting to form the

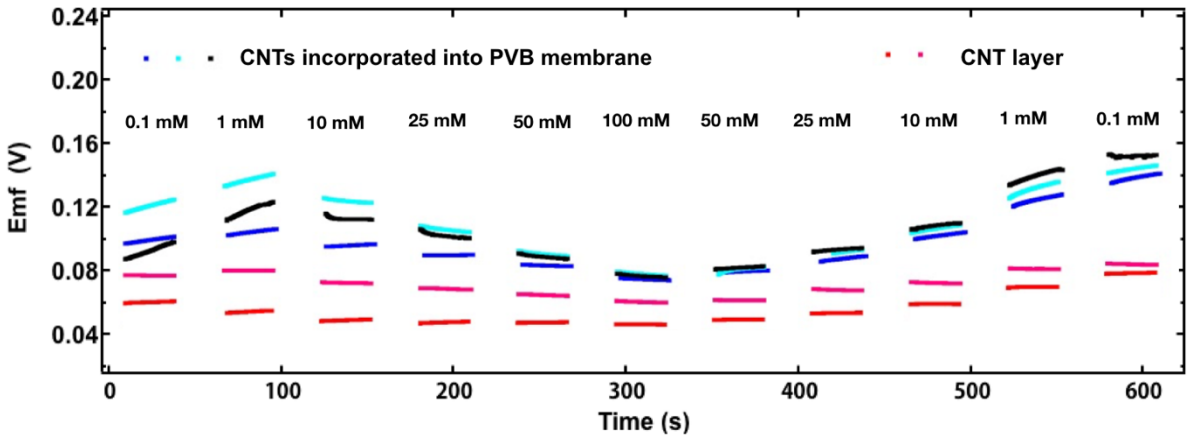

Figure 5.21: Sensitivity to changes in NaCl concentration of the reference electrodes fabricated with CNTs dispersed in the membrane (blue, dark blue, black) and the electrodes with CNT layer (purple, red). Data collected by Caleb Woods.

layer. Figure 5.21 compares sensitivity to changes in NaCl concentration of the reference electrodes fabricated with CNTs dispersed in the membrane (blue, dark blue, black) to the

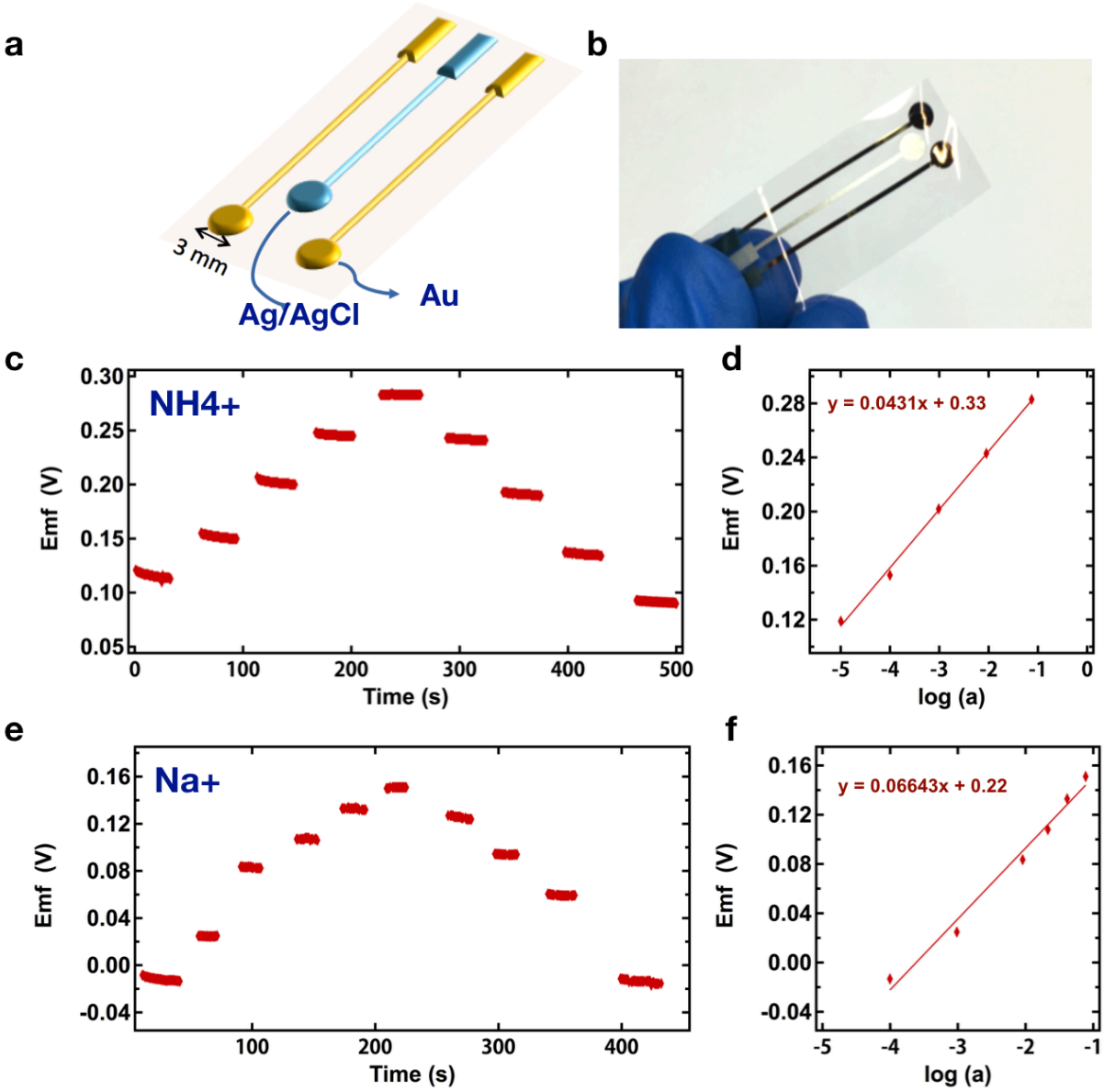

Figure 5.22: (a) Schematic (b) image of the printed potentiometric sensors for Na^+ and NH_4^+. Open circuit potentials of (c,d) Na^+ and (d,e) NH_4^+ sensors in the electrolyte solutions with physiologically relevant concentrations of the corresponding ions.

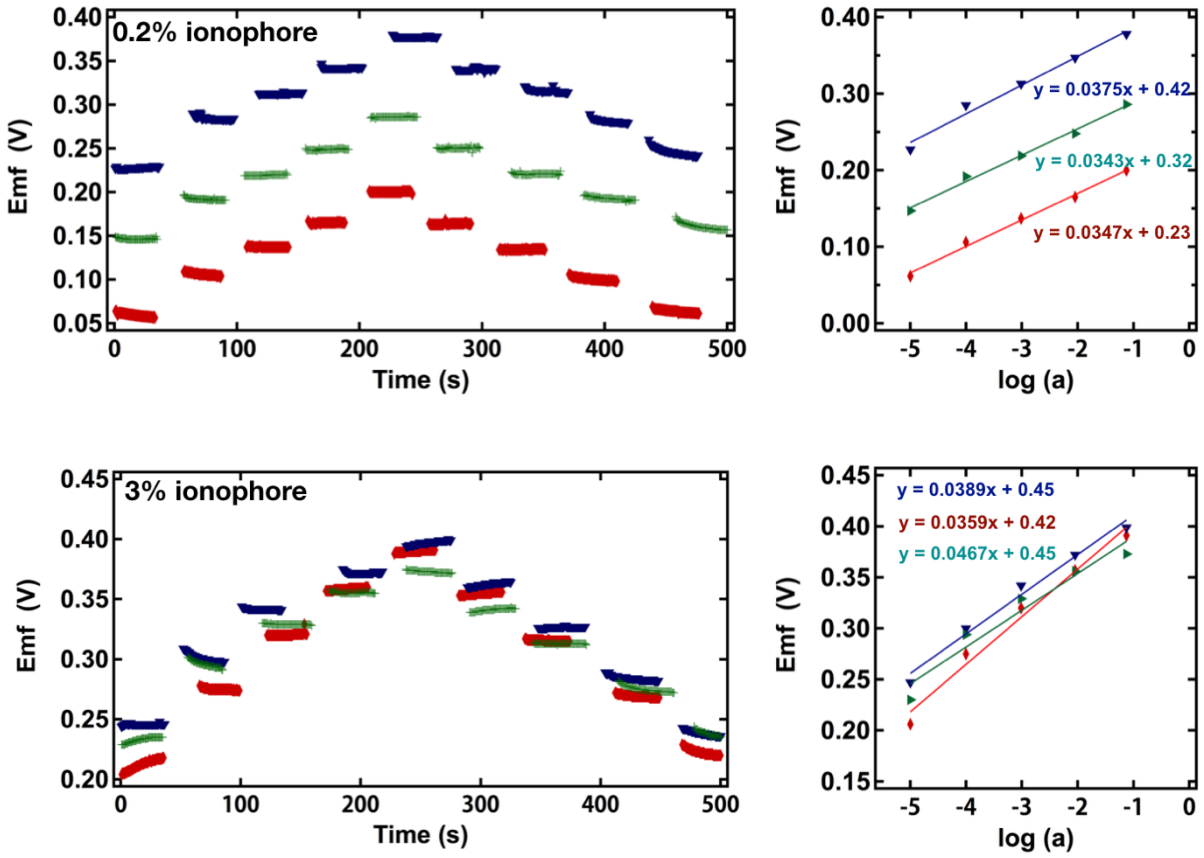

Figure 5.23: Open circuit potentials of the NH_4^+ sensing electrodes with (a,b) 0.2% and (c,d) 3% ionophore tested against commercial reference and counter electrodes.

electrodes with CNT layer (purple, red). Reference electrodes fabricated with CNTs dispersed in the membrane exhibit unstable response in the region of lower (0.1mM 1mM) NaCl concentrations and show linear response in the region of higher (10mM – 100mM) salt concentrations, with overall variations in potential ranging from 0.08 to 0.13 mV. The electrodes with CNT layer show significantly improved constancy with overall potential variation ranging between 0.075 and 0.08 mV. Thus, by introducing CNT layer between the PVB membrane and Ag/AgCl layer we obtained reference electrode with minimal sensitivity to variations in the concentration of NaCl solution.

5.5 Performance of the potentiometric sensors

Potentiometric measurements for Na^+ and NH_4^+ were enabled by coupling the reference electrode described in the section 5.4 with ISEs (Figure 5.22a,b). ISEs were prepared by first combining ion-selective ionophores with PVC as a polymer additive, and then drop-casting ionophore-polymer

solutions onto the gold transducer electrodes to form an ion-selective membranes. Ionophores reversibly bind Na^+ or NH_4^+ ions, ideally resulting in Nerstian response to the change in ion concentration. Figure 6c-f shows the open circuit potentials of Na^+ and NH_4^+ sensors in the electrolyte solutions with physiologically relevant concentrations of the corresponding ions. Both ion-selective sensors show a near-Nerstian behavior with sensitivities of 43 mV and 66 mV/decade of concentration for NH_4^+ and Na^+ sensors respectively.

While sensing electrodes for potentiometric sensors require minimum optimization, beyond previously reported protocols for sensor fabrication. Certain parameters, like ionophore concentration, did play a role in the sensor performance. Figure 5.23 shows the open circuit potentials of the NH_4^+ sensing electrodes with 0.2% (Figure 5.23a,b) and 3% (Figure 5.23c,d) ionophore tested against commercial reference and counter electrodes. Both types of the ion-selective electrodes show a near-Nerstian response with sensitivities of ~40 mV/decade of NH_4^+ concentration. However, unlike electrodes with 3% ionophore, electrodes with 0.2% ionophore show the potential readout with an offset of 0.1V. This can be potentially addressed by calibrating sensors before use, but is overall undesirable for the wearable sensor devices.

In summary, potentiometric measurements require a stable reference electrode that is insensitive to the changes in Cl^- concentration. Such printed reference electrodes were previously realized by depositing polymeric membrane saturated with chloride salt on top of Ag/AgCl layer. However, we did not achieve stable reference electrode through this method, likely due to diffusion of chloride ions from the membrane into the solution. We addressed this issue by incorporating CNT layer between the membrane and Ag/AgCl layer to act as a surface for adsorption and retention of chloride ions. Coupling the reference electrode with ISEs for Na^+ and NH_4^+ enabled printed wearable potentiometric sensors with near-Nerstian response.

5.6 Conclusion

We described optimization of the flexible platform to monitor lactate, Na^+ and NH_4^+ ions in a sweat based on the electrochemical sensing. We used commercially available materials and scalable fabrication methods. Optimization of the working electrode constitutes the most significant effort for realizing an amperomentic lactate sensor, while a stable reference electrode is a challenge for achieving reliable Na^+ and NH_4^+ potentiometric sensors.

The working electrode for lactate sensor consists of the mediating layer, fabricated by drop casting CNT/TTF suspension onto the gold trace, followed by lactate oxidase enzyme immobilized in the chitozan/CNT suspension. We optimized each layer of the electrode to achieve good long-term stability and reproducibility, as well as high sensitivity of ~5 μA/mM in the linear range of up to 25mM lactate (the biologically relevant concentration range). However, in the scenario where the wearable sweat sensor is placed directly on the skin to perform continuous measurements of lactate, the variations in sweat rate led to variations in the transport rate of lactate to the electrode

surface, causing variations in sensor readout. We observed significant fluctuations in a current when sensors were tested in the solution that was continuously mixed, versus solution that was stagnant. Incorporation of the PVC diffusion limiting membrane on the electrode surface addressed this limitation, but at the same time led to poor reproducibility of the devices. SEM characterization revealed that crystalline nature of the TTF mediator led to random structure of the electrode surface. This, in turn, resulted in the variable morphology of the diffusion limiting membrane that was deposited on top of the sensor surface, and led to variability in sensor response. Therefore, methods to planarize electrode surface before depositing the membrane should be adopted to improve reproducibility of the sensors with this particular composition. Additionally, future work should include the selectivity studies. Payne et al. showed that biologically relevant concentrations of sodium, potassium, and calcium ions present in sweat affect enzyme activity and sensitivity of the lactate sensors (*164*). This suggests that in order to achieve accurate measurements of lactate these species might need to be included in a multiplexed sensor configuration (in addition to pH and temperature) where their effects are back-calculated to determine an accurate numerical value for lactate in sweat. Another solution might revolve around developing a membrane preventing diffusion of the above species to the electrode. A membrane can also mitigate variation in sensitivity by limiting lactate diffusion, according to the model described in the introduction to this section. From our preliminary experiments, PVC membrane was not effective in mitigating the variations in sensitivity to a significant extent. Developing such membrane represents considerable effort of its own. Furthermore, mediated sensors historically suffer from degradation of enzymatic activity over time and, therefore, long-term storage studies should be performed before the enzymatic sensor chemistry can be used for commercial product.

From our experience, the sensing component (ISE) of potentiometric sensors could be reliably fabricated from previously reported methods, however achieving stable reference electrode was a challenge. Potentiometric sensors rely on a reference electrode that is insensitive to the changes in Cl^- concentration. Such printed reference electrodes were previously realized by depositing polymeric membrane saturated with chloride salt on top of Ag/AgCl layer. However, we did not achieve stable sensor performance through this method, likely due to diffusion of chloride ions from the membrane into the solution. We addressed this issue by incorporating CNT layer between the membrane and Ag/AgCl layer to act as a surface for adsorption and retention of chloride ions. This effective modification led to a stable, reproducible reference electrode. Coupling the reference electrode with ISEs for Na^+ and NH_4^+ enabled printed wearable potentiometric sensors with near-Nerstian response. The sensors showed good selectivity and long-term stability (data not presented in this thesis).

Based on the above discussion - potentiometric sweat sensors could satisfy prerequisites for the commercial production in the near future, while enzymatic sweat sensors require significant development.

5.7 Experimental section

SelectophoreTM grade sodium ionophore X, bis(2-ethylhexyl) sebacate (DOS), sodium tetrakis[3,5-bis(trifluoromethyl)phenyl] borate (Na-TFPB), polyvinyl chloride (PVC), tetrahydrofuran (THF), Polyvinyl butyral, analytical grade salts of ammonium chloride and sodium chloride (99.5%), nonactin (ammonium ionophore I), 2-nitro- phenyl-octyl ether (o-NPOE) with >99% purity, chitosan, acetone, ethanol, and acetic acid were obtained from Sigma Aldrich. Lactate Oxidase was obtained from Toyobo. Carbon nanotubes were obtained from Carbon Solutions, Inc in the form of iP-Single Walled Carbon Nanotubes. pH 7.0 buffer was obtained from Fisher Scientific.

Gold electrodes were inkjet-printed using Harima gold ink. Ag/AgCl was screen-printed using Engineered Materials Systems, Inc. ink. Electrodes were printed on PQA2 PEN 25μm thick. In the case of the potentiometric sensors, an additional layer of carbon nanotubes (CNT) dispersed in THF, followed by PVB/NaCl membrane were drop casted on top of the Ag/AgCl layer. Homogeneous CNT/THF suspension was achieved using the block copolymer PEO-PPO-PEO (F127) as a surfactant. Printed electrodes were encapsulated using laser-cut Teflon tape.

To make the mediating layer for the lactate sensor, carbon nanotubes were dispersed in ethanol and sonicated for 20 minutes at 40% amplitude using a Branson Digital Sonifier probe. 400μL of TTF was added to 2mL CNT dispersion, and the resulting solution was sonicated for 20 minutes at 40% amplitude. The TTF/CNT dispersion was then deposited on the working electrode surface. To make the enzyme layer, chitosan was dissolved in 1% acetic acid in water (0.6% chitosan by weight for optimized sensors), and CNTs were added (1% by weight for optimized sensors). This mixture was sonicated for 20 minutes at 40% amplitude. In a separate vial, lactate oxidase was measured out and dissolved in Fisher pH 7.0 buffer (for optimized sensors, 1500 U/mL). The lactate oxidase mixture was mixed 1:1 with the chitosan and CNT mixture and deposited on top of the mediating layer (1 drop of 10μL for optimized sensors). The sensors were then dried overnight in an Environmental Chamber at 35C.

The ammonium-selective membrane solution consisted of 0.2 wt% of nonactin, 69.0 wt% of o-NPOE and 30.8 wt% of PVC, as described elsewhere (*14*). The sodium-selective membrane solution consisted of 1 mg sodium ionophore X, 0.55 mg Na-TFPB, 33 mg PVC, and 65.45 mg DOS dissolved in 660 mL of THF

CHAPTER 6

Conclusion and future work

This thesis advances the development of wearable electrochemical systems: batteries and electrochemical sensors. In the domain of wearable battery technology, we demonstrate flexible and stretchable batteries with mechanical endurance that is on par with commercial requirements (withstanding >10000 deformation cycles with the extent and speed of the deformation defined by the target application). Additionally, we develop flexible battery that matches the commercial product in terms of energy density and at the same time has a flexible form factor. Moreover, we focused on intrinsically safe, non-toxic silver-zinc (Ag/Zn) and zinc-manganese dioxide (Zn/MnO_2) battery chemistries, which are highly desirable for wearable applications. For electrochemical sensors, we outlined optimization steps to achieve printed flexible sensors for continuous monitoring of the Lactate, Na^+ or NH_4^+ ions and showed how different optimization parameters affect the sensor performance. The outcomes of the research and suggestions for future work are summarized here.

Chapter 2 discussed design and fabrication of the flexible wire battery based on intrinsically safe Zn/Ag_2O battery chemistry. We achieved over 170 stable cycles by optimizing potassium hydroxide (KOH) concentration in the electrolyte to reduce the dissolution of silver ions and by embedding a cellophane membrane between the anode and cathode to inhibit migration of silver ions towards the zinc electrode. We used learnings from the battery fabrication process optimized in Chapter 2, to develop new compliant battery design concept, described in Chapter 3. The new approach used the metal current collectors with enhanced mechanical design, such as helical springs, serpentines and spirals, as a structural support and backbone for the rest of the battery components. Depending on the choice of current collector geometry, batteries were fabricated with flexible or stretchable form factors to match the mechanical properties of wearable electronic systems. As an example, we showed stretchable battery and flexible wire battery that is resilient to repetitive dynamic mechanical load and can withstand >17,000 bending cycles. These results represented significant progress towards achieving wearable batteries. One drawback of silver-zinc technology is relatively short cycle life (compared to Li-ion) due to migration of silver

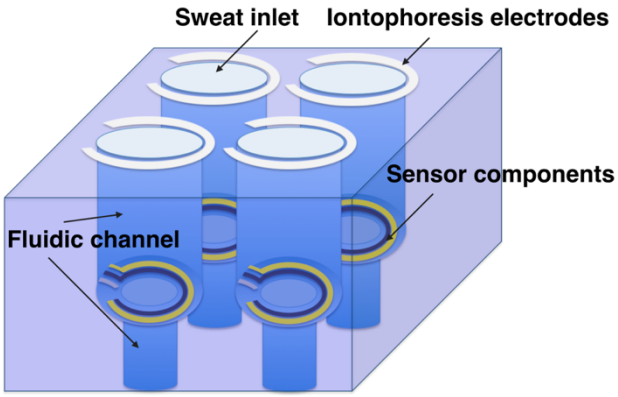

Figure 6.1. Conceptual design of the wearable sweat sensor with fluidic sweat supply and removal system.

to Zn electrode and subsequent poisoning of the electrode. Development of a separator/electrolyte that inhibits silver migration can prolong cycle life of silver-zinc batteries. Furthermore, encapsulation techniques that preserve advantages of the fiber/wire architecture, such as chemically resistive elastomeric coatings impermeable to moisture and air need to be developed.

In chapter 4 we reported a unique approach to fabricate mechanically robust MnO_2 electrode with volumetric energy density matching that of a commercial AA alkaline battery. Our approach used polyvinyl alcohol /polyacrylic acid gel crosslinked *in situ* via thermal treatment as a binder for the electrode. The batteries had high volumetric energy density of 320 mWh cm^{-3} and retained 97% of capacity after being flexed. Similar battery electrode fabrication approach could be explored to achieve flexible MnO_2 electrodes in rechargeable Zn/MnO_2 battery systems, which have been receiving a great deal of attention (*104*, *284*) . MnO_2 electrodes in these systems are subject to volume change due to Zn intercalation (*104*). This causes structural disintegration of the electrodes during cycling. Fabricating electrodes through in situ crosslinking of PVA and PAA, results in formation of the polymer coating on the surface of the particles. This coating might potentially prevent structural collapse of the particles during cycling. Additionally, based on the application requirements, increasing the battery energy density could be explored further through increasing the thickness of the electrodes. To maximize the mechanical flexibility of the thicker electrodes, their composition has to be fine-tuned to achieve optimum cohesion strength of the electrode and its adhesion to the current collector. Overall, protocols to measure the adhesion and cohesion strength of composite battery electrodes are not standardized. As a result, researches adopted and modified various mechanical testing methods (*285–288*). For example, Gaikwad et al. used the modified peel test and drag test, as tools to investigate the effect of the electrode formulation on the mechanical strength of the electrodes (*287*). These testing methods could be used to further study the effect of changing the electrode composition on the mechanical strength of the electrodes fabricated through in-situ polymerization of PVA/PAA.

In chapter 5 we described optimization of the flexible platform to monitor Lactate, Na^+ and NH_4^+ ions in sweat based on electrochemical sensing. Optimization of the working electrode constitutes the most significant effort for realizing amperometric lactate sensor, while stable reference electrode is a challenge for achieving reliable Na^+ and NH_4^+ potentiometric sensors. For potentiomentric sensors, we achieved stable, reproducible reference electrode by incorporating CNT layer between the membrane and Ag/AgCl layer to act as a surface for adsorption and retention of chloride ions. From our experience, the resulting potentiometric sensors could be

considered for commercial applications, if proven to satisfy long term storage requirements. For the lactate sensor, we optimized working rlrctrode to achieve good long-term stability, reproducibility, as well as high sensitivity of ~5 μA/mM in the linear range of up to 25mM lactate (biologically relevant concentration range). Future work should include the selectivity studies. Payne et al. showed that biologically relevant concentrations of sodium, potassium, and calcium ions present in sweat effect enzyme activity and sensitivity of the lactate sensors (*164*). This suggests that in order to achieve accurate measurements of lactate these species might need to be included in a multiplexed sensor configuration (in addition to pH and temperature) where their effects are back-calculated to determine an accurate numerical value for lactate in sweat. Another solution might revolve around developing membrane preventing diffusion of the above species to the electrode. Membrane can also mitigate variation in sensitivity due to variations in the sweat rate in the scenario where wearable sweat sensor should be placed directly on skin to perform continuous measurements of lactate. Developing such membrane represents significant effort of its own. Furthermore, efficient sweat supply and removal system has to be implemented for prolonged continuous sweat monitoring. The conceptual design of such system is shown in **Figure 6.1**. Sweat sensing components are integrated within fluidic channels and combined with iontophoretic electrodes that facilitate sweat secretion. Flexible silicone elastomeric pouch with fluidic channels can be fabricated using continuous liquid interface 3D printing. After that, dispenser printing can be used to print active components. Silicone surface has to be modified in order to facilitate adhesion of the sensing components to the walls of the fluidic channel, as well as made hydrophilic to ensure sweat flow.

Bibliography

1. Y. Khan, A. E. Ostfeld, C. M. Lochner, A. Pierre, A. C. Arias, Monitoring of Vital Signs with Flexible and Wearable Medical Devices. *Adv. Mater.* **28**, 4373–4395 (2016).
2. J. Heikenfeld *et al.*, Wearable sensors: modalities, challenges, and prospects. *Lab Chip*. **18**, 217–248 (2018).
3. J. Heikenfeld, Non-invasive Analyte Access and Sensing through Eccrine Sweat: Challenges and Outlook circa 2016. *Electroanalysis*. **28**, 1242–1249 (2016).
4. X. Huang *et al.*, Stretchable, Wireless Sensors and Functional Substrates for Epidermal Characterization of Sweat. *Small*. **10**, 3083–3090 (2014).
5. G. Liu *et al.*, A wearable conductivity sensor for wireless real-time sweat monitoring. *Sensors Actuators B Chem.* **227**, 35–42 (2016).
6. J. Choi, D. Kang, S. Han, S. B. Kim, J. A. Rogers, Thin, Soft, Skin-Mounted Microfluidic Networks with Capillary Bursting Valves for Chrono-Sampling of Sweat. *Adv. Healthc. Mater.* **6**, 1601355 (2017).
7. A. Koh *et al.*, A soft, wearable microfluidic device for the capture, storage, and colorimetric sensing of sweat. *Sci. Transl. Med.* **8**, 366ra165 (2016).
8. D. Morris *et al.*, Bio-sensing textile based patch with integrated optical detection system for sweat monitoring. *Sensors Actuators B Chem.* **139**, 231–236 (2009).
9. M. Singh, J. Truong, W. B. Reeves, J.-I. Hahm, Emerging Cytokine Biosensors with Optical Detection Modalities and Nanomaterial-Enabled Signal Enhancement. *Sensors (Basel).* **17** (2017), doi:10.3390/s17020428.
10. A. J. Bandodkar, J. Wang, Non-invasive wearable electrochemical sensors: A review. *Trends Biotechnol.* **32**, 363–371 (2014).
11. M. M. Raiszadeh *et al.*, Proteomic analysis of eccrine sweat: implications for the discovery of schizophrenia biomarker proteins. *J. Proteome Res.* **11**, 2127–39 (2012).
12. M. Bariya, H. Y. Y. Nyein, A. Javey, Wearable sweat sensors. *Nat. Electron.* **1**, 160–171 (2018).

13. W. Jia *et al.*, Electrochemical tattoo biosensors for real-time noninvasive lactate monitoring in human perspiration. *Anal. Chem.* **85**, 6553–6560 (2013).

14. T. Guinovart, A. J. Bandodkar, J. R. Windmiller, F. J. Andrade, J. Wang, A potentiometric tattoo sensor for monitoring ammonium in sweat. *Analyst*. **138**, 7031–8 (2013).

15. B. Schazmann *et al.*, A wearable electrochemical sensor for the real-time measurement of sweat sodium concentration. *Anal. Methods*. **2**, 342 (2010).

16. J. Kim *et al.*, Noninvasive Alcohol Monitoring Using a Wearable Tattoo-Based Iontophoretic-Biosensing System. *ACS Sensors*. **1** (2016), doi:10.1021/acssensors.6b00356.

17. Y. Lin *et al.*, Porous Enzymatic Membrane for Nanotextured Glucose Sweat Sensors with High Stability toward Reliable Noninvasive Health Monitoring. *Adv. Funct. Mater.* **29**, 1902521 (2019).

18. J. Kim *et al.*, Wearable temporary tattoo sensor for real-time trace metal monitoring in human sweat. *Electrochem. commun.* **51**, 41–45 (2015).

19. M. Barbadillo *et al.*, Gold nanoparticles-induced enhancement of the analytical response of an electrochemical biosensor based on an organic-inorganic hybrid composite material. *Talanta*. **80**, 797–802 (2009).

20. J. M. Goran, J. L. Lyon, K. J. Stevenson, Amperometric Detection of l -Lactate Using Nitrogen-Doped Carbon Nanotubes Modified with Lactate Oxidase. *Anal. Chem.* **83**, 8123–8129 (2011).

21. A. J. Bandodkar *et al.*, Epidermal tattoo potentiometric sodium sensors with wireless signal transduction for continuous non-invasive sweat monitoring. *Biosens. Bioelectron.* **54**, 603–9 (2014).

22. S. Anastasova *et al.*, A wearable multisensing patch for continuous sweat monitoring. *Biosens. Bioelectron.* **93**, 139–145 (2017).

23. D. Rose *et al.*, Adhesive RFID Sensor Patch for Monitoring of Sweat Electrolytes. *IEEE Trans. Biomed. Eng.* **9294**, 1–1 (2014).

24. S. Emaminejad *et al.*, Autonomous sweat extraction and analysis applied to cystic fibrosis and glucose monitoring using a fully integrated wearable platform. *Proc. Natl. Acad. Sci. U. S. A.* **114**, 4625–4630 (2017).

25. H. Y. Y. Nyein *et al.*, A Wearable Electrochemical Platform for Noninvasive Simultaneous Monitoring of Ca^{2+} and pH. *ACS Nano*. **10**, 7216–7224 (2016).

26. W. Gao *et al.*, Fully integrated wearable sensor arrays for multiplexed in situ perspiration analysis. *Nature*. **529**, 509–514 (2016).

27. S. Imani *et al.*, A wearable chemical–electrophysiological hybrid biosensing system for real-time health and fitness monitoring. *Nat. Commun.* **7**, 11650 (2016).

28. L. Hu, H. Wu, F. La Mantia, Y. Yang, Y. Cui, Thin, flexible secondary Li-ion paper batteries. *ACS Nano*. **4**, 5843–8 (2010).

29. A. M. Gaikwad, G. L. Whiting, D. A. Steingart, A. C. Arias, Highly flexible, printed

alkaline batteries based on mesh-embedded electrodes. *Adv. Mater.* **23**, 3251–5 (2011).

30. P. Hiralal *et al.*, Nanomaterial-Enhanced All-Solid Flexible Zinc - Carbon Batteries. *ACS Nano*. **4**, 2730–2734 (2010).
31. K. T. Braam, S. K. Volkman, V. Subramanian, Characterization and optimization of a printed, primary silver–zinc battery. *J. Power Sources*. **199**, 367–372 (2012).
32. J. Park, M. Park, G. Nam, J. Lee, J. Cho, All-Solid-State Cable-Type Flexible Zinc-Air Battery. *Adv. Mater.* **27**, 1396–1401 (2015).
33. W. Weng *et al.*, Winding aligned carbon nanotube composite yarns into coaxial fiber full batteries with high performances. *Nano Lett.* **14**, 3432–3438 (2014).
34. Y. Zhang *et al.*, Super-stretchy lithium-ion battery based on carbon nanotube fiber. *J. Mater. Chem. A*. **4**, 11054–11059 (2014).
35. Y. Xu, Y. Zhao, J. Ren, Y. Zhang, H. Peng, An All-Solid-State Fiber-Shaped Aluminum-Air Battery with Flexibility, Stretchability, and High Electrochemical Performance. *Angew. Chemie*. **55**, 7979–7982 (2016).
36. Y. Xu *et al.*, Flexible, Stretchable, and Rechargeable Fiber-Shaped Zinc-Air Battery Based on Cross-Stacked Carbon Nanotube Sheets. *Angew. Chem. Int. Ed. Engl.* **54**, 15390–15394 (2015).
37. X. Yu *et al.*, Flexible fiber-type zinc-carbon battery based on carbon fiber electrodes. *Nano Energy*. **2**, 1242–1248 (2013).
38. M. Peng *et al.*, Efficient fiber shaped zinc bromide batteries and dye sensitized solar cells for flexible power sources. *J. Mater. Chem. C*. **3**, 2157–2165 (2015).
39. Y. H. Kwon *et al.*, Cable-type flexible lithium ion battery based on hollow multi-helix electrodes. *Adv. Mater.* **24**, 5192–5197 (2012).
40. H. Qu *et al.*, Flexible fiber batteries for applications in smart textiles. *Smart Mater. Struct.* **24**, 25012 (2013).
41. T. Liu, Q.-C. Liu, J.-J. Xu, X.-B. Zhang, Cable-Type Water-Survivable Flexible Li-O2 Battery. *Small*. **12**, 3101–3105 (2016).
42. M. Park *et al.*, Organic-Catholyte-Containing Flexible Rechargeable Lithium Batteries. *Adv. Mater.* **27**, 5141–5146 (2015).
43. J. Ren *et al.*, Twisting carbon nanotube fibers for both wire-shaped micro-supercapacitor and micro-battery. *Adv. Mater.* **25**, 1155–1159 (2013).
44. J. Wang, C. Y. Wang, C. O. Too, G. G. Wallace, Highly-flexible fibre battery incorporating polypyrrole cathode and carbon nanotubes anode. *J. Power Sources*. **161**, 1458–1462 (2006).
45. J. Kim *et al.*, A layer-built rechargeable lithium ribbon-type battery for High Energy Density Textile Battery Applications. *J. Mater. Chem. A*. **2**, 1774–1780 (2014).
46. R. N. Adams, Carbon Paste Electrodes. *Anal. Chem.* **30**, 1576–1576 (1958).
47. L. S. Marcoux, K. B. Prater, B. G. Prater, R. N. Adams, A Nonaqueous Carbon Paste

Electrode. *Anal. Chem.* **37**, 1446–1447 (1965).

48. I. Švancara, K. Vytřas, K. Kalcher, A. Walcarius, J. Wang, Carbon Paste Electrodes in Facts, Numbers, and Notes: A Review on the Occasion of the 50-Years Jubilee of Carbon Paste in Electrochemistry and Electroanalysis. *Electroanalysis*. **21**, 7–28 (2009).
49. G. A. Rivas *et al.*, Carbon Nanotubes Paste Electrodes. A New Alternative for the Development of Electrochemical Sensors. *Electroanalysis*. **19**, 823–831 (2007).
50. G. Li, C. Wan, Z. Ji, K. Wu, An electrochemical sensor for Cd2+ based on the inducing adsorption ability of I−. *Sensors Actuators B Chem.* **124**, 1–5 (2007).
51. I. Švancara, M. Hvízdalová, K. Vytřas, K. Kalcher, R. Novotný, A microscopic study on carbon paste electrodes. *Electroanalysis*. **8**, 61–65 (1996).
52. J. Wang *et al.*, Glassy carbon paste electrodes. *Electrochem. commun.* **3**, 203–208 (2001).
53. Y. Liu, X. Dong, P. Chen, Biological and chemical sensors based on graphene materials. *Chem. Soc. Rev.* **41**, 2283–307 (2012).
54. E. Lindner, R. P. Buck, *Anal. Chem.*, in press, doi:10.1021/ac002805v.
55. *Inkjet-based Micromanufacturing* (John Wiley & Sons, 2012; https://books.google.com/books?hl=en&lr=&id=jLMqoirILhAC&pgis=1).
56. J. D. Newman, A. P. F. Turner, Home blood glucose biosensors: a commercial perspective. *Biosens. Bioelectron.* **20**, 2435–53 (2005).
57. J. Sutter, A. Radu, S. Peper, E. Bakker, E. Pretsch, Solid-contact polymeric membrane electrodes with detection limits in the subnanomolar range. *Anal. Chim. Acta*. **523**, 53–59 (2004).
58. K. Y. Chumbimuni-Torres, N. Rubinova, A. Radu, L. T. Kubota, E. Bakker, Solid contact potentiometric sensors for trace level measurements. *Anal. Chem.* **78**, 1318–22 (2006).
59. N. RUBINOVA, K. CHUMBIMUNITORRES, E. BAKKER, Solid-contact potentiometric polymer membrane microelectrodes for the detection of silver ions at the femtomole level. *Sensors Actuators B Chem.* **121**, 135–141 (2007).
60. L. Tymecki, S. Glab, R. Koncki, Miniaturized, Planar Ion-selective Electrodes Fabricated by Means of Thick-film Technology. *Sensors*. **6**, 390–396 (2006).
61. J. P. Wilburn, M. Ciobanu, N. I. Buss, D. R. Franceschetti, D. A. Lowy, Miniaturized reference electrodes with stainless steel internal reference elements. *Anal. Chim. Acta*. **511**, 83–89 (2004).
62. W. Vonau, U. Enseleit, F. Gerlach, S. Herrmann, Conceptions, materials, processing technologies and fields of application for miniaturized electrochemical sensors with planar membranes. *Electrochim. Acta*. **49**, 3745–3750 (2004).
63. T. Blaz, J. Migdalski, A. Lewenstam, Junction-less reference electrode for potentiometric measurements obtained by buffering pH in a conducting polymer matrix. *Analyst*. **130**, 637–43 (2005).
64. J. Ha *et al.*, A polymeric junction membrane for solid-state reference electrodes. *Anal. Chim. Acta*. **549**, 59–66 (2005).

65. R. Mamińska, A. Dybko, W. Wróblewski, All-solid-state miniaturised planar reference electrodes based on ionic liquids. *Sensors Actuators B Chem.* **115**, 552–557 (2006).

66. R. J. W. Lugtenberg, R. J. M. Egberink, A. van den Berg, J. F. J. Engbersen, D. N. Reinhoudt, The effects of covalent binding of the electroactive components in durable CHEMFET membranes—impedance spectroscopy and ion sensitivity studies. *J. Electroanal. Chem.* **452**, 69–86 (1998).

67. L. Y. Heng, E. A. H. Hall, Producing "Self-Plasticizing" Ion-Selective Membranes. *Anal. Chem.* **72**, 42–51 (2000).

68. L. Y. Heng, E. A. H. Hall, Methacrylic–acrylic polymers in ion-selective membranes: achieving the right polymer recipe. *Anal. Chim. Acta*. **403**, 77–89 (2000).

69. E. Malinowska, L. Gawart, P. Parzuchowski, G. Rokicki, Z. Brzózka, Novel approach of immobilization of calix[4]arene type ionophore in 'self-plasticized' polymeric membrane. *Anal. Chim. Acta*. **421**, 93–101 (2000).

70. L. v Heng, L. H. Chern, M. Ahmad, A Hydrogen Ion-Selective Sensor Based on Non-Plasticised Methacrylic-acrylic Membranes. *Sensors*. **2**, 339–346 (2002).

71. Y. Qin, S. Peper, E. Bakker, Plasticizer-Free Polymer Membrane Ion-Selective Electrodes Containing a Methacrylic Copolymer Matrix. *Electroanalysis*. **14**, 1375–1381 (2002).

72. K. Edelmann, A. Reiche, B. Sandner, J. Marstalerz, H. Müller, Copolymers from oligosiloxane methacrylates as a plasticizer-free membrane matrix for ion-selective sensors. *Polymer (Guildf).* **46**, 407–417 (2005).

73. S. Peper, A. Ceresa, Y. Qin, E. Bakker, Plasticizer-free microspheres for ionophore-based sensing and extraction based on a methyl methacrylate-decyl methacrylate copolymer matrix. *Anal. Chim. Acta*. **500**, 127–136 (2003).

74. Y. Qin, E. Bakker, Elimination of dimer formation in InIIIporphyrin-based anion-selective membranes by covalent attachment of the ionophore. *Anal. Chem.* **76**, 4379–86 (2004).

75. M. Püntener, T. Vigassy, E. Baier, A. Ceresa, E. Pretsch, Improving the lower detection limit of potentiometric sensors by covalently binding the ionophore to a polymer backbone. *Anal. Chim. Acta*. **503**, 187–194 (2004).

76. T. Le Goff, J. Braven, L. Ebdon, D. Scholefield, Phosphate-selective electrodes containing immobilised ionophores. *Anal. Chim. Acta*. **510**, 175–182 (2004).

77. R. Bereczki, R. E. Gyurcsányi, B. Agai, K. Tóth, Synthesis and characterization of covalently immobilized bis-crown ether based potassium ionophore. *Analyst*. **130**, 63–70 (2005).

78. J. H. Shin *et al.*, Characterization of epoxy resin-based anion-responsive polymers: applicability to chloride sensing in physiological samples. *Anal. Chem.* **76**, 4217–22 (2004).

79. A. Jiménez-Morales, J. C. Galván, P. Aranda, A new silver-ion selective sensor based on a polythiacrown-ether entrapped by sol–gel. *Electrochim. Acta*. **47**, 2281–2287 (2002).

80. Y.-Z. Long *et al.*, Recent advances in synthesis, physical properties and applications of conducting polymer nanotubes and nanofibers. *Prog. Polym. Sci.* **36**, 1415–1442 (2011).

81. S. Cosnier, A. Karyakin, Eds., *Electropolymerization* (Wiley-VCH Verlag GmbH & Co. KGaA, Weinheim, Germany, 2010).

82. L. Xia, Z. Wei, M. Wan, Conducting polymer nanostructures and their application in biosensors. *J. Colloid Interface Sci.* **341**, 1–11 (2010).

83. F. Faridbod, P. Norouzi, R. Dinarvand, M. R. Ganjali, Developments in the Field of Conducting and Non-conducting Polymer Based Potentiometric Membrane Sensors for Ions Over the Past Decade. *Sensors*. **8**, 2331–2412 (2008).

84. *Nanosensors for Chemical and Biological Applications: Sensing with Nanotubes, Nanowires and Nanoparticles* (Elsevier Science, 2014; https://books.google.com/books?hl=en&lr=&id=dQSjAgAAQBAJ&pgis=1).

85. A. Kisiel, H. Marcisz, A. Michalska, K. Maksymiuk, All-solid-state reference electrodes based on conducting polymers. *Analyst*. **130**, 1655–62 (2005).

86. J. Bobacka, A. Ivanska, A. Lewenstam, Potentiometric ion sensors. *Chem. Rev.* (2008), pp. 329–351.

87. E. Bakker, E. Pretsch, Nanoscale potentiometry. *Trends Analyt. Chem.* **27**, 612–618 (2008).

88. H. Chik, J. M. Xu, Nanometric superlattices: non-lithographic fabrication, materials, and prospects. *Mater. Sci. Eng. R Reports*. **43**, 103–138 (2004).

89. nature physics portal - looking back - Synthesis of carbon nanotubes, (available at http://www.nature.com/physics/looking-back/iijima/index.html).

90. R. Antiochia, I. Lavagnini, F. Magno, Electrocatalytic oxidation of NADH at single-wall carbon-nanotube-paste electrodes: kinetic considerations for use of a redox mediator in solution and dissolved in the paste. *Anal. Bioanal. Chem.* **381**, 1355–61 (2005).

91. S. Mao *et al.*, Ultrafast hydrogen sensing through hybrids of semiconducting single-walled carbon nanotubes and tin oxide nanocrystals. *Nanoscale*. **4**, 1275–9 (2012).

92. M. Rubianes, G. Rivas, Enzymatic Biosensors Based on Carbon Nanotubes Paste Electrodes. *Electroanalysis*. **17**, 73–78 (2005).

93. A. I. Gopalan, K. P. Lee, D. Ragupathy, S. H. Lee, J. W. Lee, An electrochemical glucose biosensor exploiting a polyaniline grafted multiwalled carbon nanotube/perfluorosulfonate ionomer-silica nanocomposite. *Biomaterials*. **30**, 5999–6005 (2009).

94. X. Yu, A. Manthiram, Electrode–electrolyte interfaces in lithium-based batteries. *Energy Environ. Sci.* **11**, 527–543 (2018).

95. L. Cheng *et al.*, Sparingly Solvating Electrolytes for High Energy Density Lithium–Sulfur Batteries. *ACS Energy Lett.* **1**, 503–509 (2016).

96. F. Wu, W. Fitzhugh, L. Ye, J. Ning, X. Li, Advanced sulfide solid electrolyte by core-shell structural design. *Nat. Commun.* **9**, 4037 (2018).

97. Y. Lu, L. Li, Q. Zhang, Z. Niu, J. Chen, Electrolyte and Interface Engineering for Solid-State Sodium Batteries. *Joule*. **2**, 1747–1770 (2018).

98. J. Pires *et al.*, Tris(2,2,2-trifluoroethyl) phosphite as an electrolyte additive for high-

voltage lithium-ion batteries using lithium-rich layered oxide cathode. *J. Power Sources*. **296**, 413–425 (2015).

99. A. M. Gaikwad *et al.*, Highly stretchable alkaline batteries based on an embedded conductive fabric. *Adv. Mater.* **24**, 5071–6 (2012).

100. R. Wang *et al.*, Nickel@Nickel Oxide Core-Shell Electrode with Significantly Boosted Reactivity for Ultrahigh-Energy and Stable Aqueous Ni-Zn Battery. *Adv. Funct. Mater.* **28**, 1802157 (2018).

101. W. Shi *et al.*, An ultra-dense NiS_2 /reduced graphene oxide composite cathode for high-volumetric/gravimetric energy density nickel–zinc batteries. *J. Mater. Chem. A*. **7**, 15654–15661 (2019).

102. K. Braam, V. Subramanian, Development of an air-stable , high energy density printed silver oxide battery for printed electronics. **27**, 689 (2015).

103. A. M. Zamarayeva *et al.*, Fabrication of a High-Performance Flexible Silver-Zinc Wire Battery. *Adv. Electron. Mater.* **2**, 1500296 (2016).

104. H. Li *et al.*, Advanced rechargeable zinc-based batteries: Recent progress and future perspectives. *Nano Energy*. **62**, 550–587 (2019).

105. P. Tan *et al.*, Flexible Zn– and Li–air batteries: recent advances, challenges, and future perspectives. *Energy Environ. Sci.* **10**, 2056–2080 (2017).

106. C. Guan *et al.*, Hollow Co_3O_4 Nanosphere Embedded in Carbon Arrays for Stable and Flexible Solid-State Zinc-Air Batteries. *Adv. Mater.* **29**, 1704117 (2017).

107. J. Fu *et al.*, Flexible Rechargeable Zinc-Air Batteries through Morphological Emulation of Human Hair Array. *Adv. Mater.* **28**, 6421–6428 (2016).

108. Z. Pei *et al.*, Enabling highly efficient, flexible and rechargeable quasi-solid-state zn-air batteries via catalyst engineering and electrolyte functionalization. *Energy Storage Mater.* **20**, 234–242 (2019).

109. K. Kordek *et al.*, Two-Step Activated Carbon Cloth with Oxygen-Rich Functional Groups as a High-Performance Additive-Free Air Electrode for Flexible Zinc-Air Batteries. *Adv. Energy Mater.* **9**, 1802936 (2019).

110. Q. Liu, Y. Wang, L. Dai, J. Yao, Scalable Fabrication of Nanoporous Carbon Fiber Films as Bifunctional Catalytic Electrodes for Flexible Zn-Air Batteries. *Adv. Mater.* **28**, 3000–3006 (2016).

111. F. Meng, H. Zhong, D. Bao, J. Yan, X. Zhang, In Situ Coupling of Strung Co_4N and Intertwined N–C Fibers toward Free-Standing Bifunctional Cathode for Robust, Efficient, and Flexible Zn–Air Batteries. *J. Am. Chem. Soc.* **138**, 10226–10231 (2016).

112. M. Yu *et al.*, Nitrogen-Doped Co_3O_4 Mesoporous Nanowire Arrays as an Additive-Free Air-Cathode for Flexible Solid-State Zinc-Air Batteries. *Adv. Mater.* **29**, 1602868 (2017).

113. H.-F. Wang *et al.*, Defect-rich carbon fiber electrocatalysts with porous graphene skin for flexible solid-state zinc–air batteries. *Energy Storage Mater.* **15**, 124–130 (2018).

114. T. Zhou *et al.*, Ultrathin Cobalt Oxide Layers as Electrocatalysts for High-Performance

Flexible Zn–Air Batteries. *Adv. Mater.* **31**, 1807468 (2019).

115. C.-Y. Su *et al.*, Atomic Modulation of FeCo-Nitrogen-Carbon Bifunctional Oxygen Electrodes for Rechargeable and Flexible All-Solid-State Zinc-Air Battery. *Adv. Energy Mater.* **7**, 1602420 (2017).
116. C. Guan *et al.*, Decorating Co/CoNx nanoparticles in nitrogen-doped carbon nanoarrays for flexible and rechargeable zinc-air batteries. *Energy Storage Mater.* **16**, 243–250 (2019).
117. Y. Jiang *et al.*, Multidimensional Ordered Bifunctional Air Electrode Enables Flash Reactants Shuttling for High-Energy Flexible Zn-Air Batteries. *Adv. Energy Mater.* **9**, 1900911 (2019).
118. D. Linden, *Handbook of Batteries* (McGraw-Hill, New York, 2004).
119. Y. Zhang *et al.*, Buckling in serpentine microstructures and applications in elastomer-supported ultra-stretchable electronics with high areal coverage. *Soft Matter*. **9**, 8062 (2013).
120. Y. Zhang *et al.*, Experimental and theoretical studies of serpentine microstructures bonded to prestrained elastomers for stretchable electronics. *Adv. Funct. Mater.* **24**, 2028–2037 (2014).
121. Y. Zhang, Y. Huang, J. A. Rogers, Mechanics of stretchable batteries and supercapacitors. *Curr. Opin. Solid State Mater. Sci.* **19**, 190–199 (2015).
122. M. Calderón-Santiago, F. Priego-Capote, B. Jurado-Gámez, M. D. Luque de Castro, Optimization study for metabolomics analysis of human sweat by liquid chromatography-tandem mass spectrometry in high resolution mode. *J. Chromatogr. A*. **1333**, 70–78 (2014).
123. Z. Suo, Reliability of Interconnect Structures. *Aerosp. Eng.*, 265–324 (2003).
124. Z. Suo, Mechanics of stretchable electronics and soft machines. *MRS Bull.* **37**, 218–225 (2012).
125. S. Xu *et al.*, Stretchable batteries with self-similar serpentine interconnects and integrated wireless recharging systems. *Nat. Commun.* **4**, 1543 (2013).
126. S. Qu *et al.*, Electrochemical approach to prepare integrated air electrodes for highly stretchable zinc-air battery array with tunable output voltage and current for wearable electronics. *Nano Energy*. **39**, 101–110 (2017).
127. L. Yin *et al.*, Highly Stable Battery Pack via Insulated, Reinforced, Buckling-Enabled Interconnect Array. *Small*. **14**, 1800938 (2018).
128. H. Lee *et al.*, A graphene-based electrochemical device with thermoresponsive microneedles for diabetes monitoring and therapy. *Nat. Nanotechnol.* **11**, 566–572 (2016).
129. A. M. Zamarayeva *et al.*, Flexible and stretchable power sources for wearable electronics. *Sci. Adv.* **3**, e1602051 (2017).
130. Y. Zhu, F. Xu, Buckling of Aligned Carbon Nanotubes as Stretchable Conductors: A New Manufacturing Strategy. *Adv. Mater.* **24**, 1073–1077 (2012).

131. T. Chen, Y. Xue, A. K. Roy, L. Dai, Transparent and Stretchable High-Performance Supercapacitors Based on Wrinkled Graphene Electrodes. *ACS Nano*. **8**, 1039–1046 (2014).

132. W. Weng *et al.*, A gum-like lithium-ion battery based on a novel arched structure. *Adv. Mater.* **27**, 1363–9 (2015).

133. Y. Zhang *et al.*, A mechanically driven form of Kirigami as a route to 3D mesostructures in micro/nanomembranes. *Proc. Natl. Acad. Sci.* **112**, 11757–11764 (2015).

134. Z. Song *et al.*, Origami lithium-ion batteries. *Nat. Commun.* **5**, 3140 (2014).

135. Z. Song *et al.*, Kirigami-based stretchable lithium-ion batteries. *Sci. Rep.* **5**, 10988 (2015).

136. J. S. Heo, J. Eom, Y.-H. Kim, S. K. Park, Recent Progress of Textile-Based Wearable Electronics: A Comprehensive Review of Materials, Devices, and Applications. *Small*. **14**, 1703034 (2018).

137. X. Wang, K. Jiang, G. Shen, Flexible fiber energy storage and integrated devices: recent progress and perspectives. *Mater. Today*. **00**, 1–8 (2015).

138. J. M. Lee *et al.*, Biscrolled Carbon Nanotube Yarn Structured Silver-Zinc Battery. *Sci. Rep.* **8**, 11150 (2018).

139. Y. Zhang *et al.*, High-Performance Lithium-Air Battery with a Coaxial-Fiber Architecture. *Angew. Chemie Int. Ed.* **55**, 4487–4491 (2016).

140. Y. Xu, Y. Zhao, J. Ren, Y. Zhang, H. Peng, An All-Solid-State Fiber-Shaped Aluminum-Air Battery with Flexibility, Stretchability, and High Electrochemical Performance. *Angew. Chemie Int. Ed.* **55**, 7979–7982 (2016).

141. Y. Xu *et al.*, Flexible, Stretchable, and Rechargeable Fiber-Shaped Zinc-Air Battery Based on Cross-Stacked Carbon Nanotube Sheets. *Angew. Chemie Int. Ed.* **54**, 15390–15394 (2015).

142. A. Sassolas, L. J. Blum, B. D. Leca-Bouvier, Immobilization strategies to develop enzymatic biosensors. *Biotechnol. Adv.* **30**, 489–511 (2012).

143. A. R. Pereira, J. C. P. de Souza, R. M. Iost, F. C. P. F. Sales, F. N. Crespilho, Application of carbon fibers to flexible enzyme electrodes. *J. Electroanal. Chem.* **780**, 396–406 (2016).

144. C. Wang *et al.*, Advanced Carbon for Flexible and Wearable Electronics. *Adv. Mater.* **31**, 1801072 (2019).

145. M. Parrilla, J. Ferré, T. Guinovart, F. J. Andrade, Wearable Potentiometric Sensors Based on Commercial Carbon Fibres for Monitoring Sodium in Sweat. *Electroanalysis*. **28**, 1267–1275 (2016).

146. H. Sun *et al.*, Novel graphene/carbon nanotube composite fibers for efficient wire-shaped miniature energy devices. *Adv. Mater.* **26**, 2868–2873 (2014).

147. Y. Xu *et al.*, Flexible, Stretchable, and Rechargeable Fiber-Shaped Zinc-Air Battery Based on Cross-Stacked Carbon Nanotube Sheets. *Angew. Chemie Int. Ed.* **54**, 15390–15394 (2015).

148. K. Wang *et al.*, High-Performance Cable-Type Flexible Rechargeable Zn Battery Based on MnO $_2$ @CNT Fiber Microelectrode. *ACS Appl. Mater. Interfaces*. **10**, 24573–24582 (2018).

149. A. Pendashteh, J. Palma, M. Anderson, J. J. Vilatela, R. Marcilla, Doping of Self-Standing CNT Fibers: Promising Flexible Air-Cathodes for High-Energy-Density Structural Zn–Air Batteries. *ACS Appl. Energy Mater.* **1**, 2434–2439 (2018).

150. Y. Zhang *et al.*, Vertically Oxygen-Incorporated MoS $_2$ Nanosheets Coated on Carbon Fibers for Sodium-Ion Batteries. *ACS Appl. Mater. Interfaces*. **10**, 35206–35215 (2018).

151. S. Gao *et al.*, Flexible MnS-Carbon Fiber Hybrids for Lithium-Ion and Sodium-Ion Energy Storage. *Chem. - A Eur. J.* **24**, 13535–13539 (2018).

152. C. Shen *et al.*, Flexible Sub-Micro Carbon Fiber@CNTs as Anodes for Potassium-Ion Batteries. *ACS Appl. Mater. Interfaces*. **11**, 5015–5021 (2019).

153. J. Hagberg *et al.*, Lithium iron phosphate coated carbon fiber electrodes for structural lithium ion batteries. *Compos. Sci. Technol.* **162**, 235–243 (2018).

154. W. Lu, M. Zu, J.-H. Byun, B.-S. Kim, T.-W. Chou, State of the Art of Carbon Nanotube Fibers: Opportunities and Challenges. *Adv. Mater.* **24**, 1805–1833 (2012).

155. M. D. Lima *et al.*, Biscrolling Nanotube Sheets and Functional Guests into Yarns. *Science (80-.).* **331**, 51–55 (2011).

156. J. S. Heo, J. Eom, Y.-H. Kim, S. K. Park, Recent Progress of Textile-Based Wearable Electronics: A Comprehensive Review of Materials, Devices, and Applications. *Small*. **14**, 1703034 (2018).

157. M. Sekar, M. Pandiaraj, S. Bhansali, N. Ponpandian, C. Viswanathan, Carbon fiber based electrochemical sensor for sweat cortisol measurement. *Sci. Rep.* **9**, 403 (2019).

158. S. Madhu *et al.*, Nanostructured SnO2 integrated conductive fabrics as binder-free electrode for neurotransmitter detection. *Sensors Actuators A Phys.* **269**, 401–411 (2018).

159. M. K.P.O., I. Shown, L.-C. Chen, K.-H. Chen, Y. Tai, Flexible sensor for dopamine detection fabricated by the direct growth of α-Fe2O3 nanoparticles on carbon cloth. *Appl. Surf. Sci.* **427**, 387–395 (2018).

160. P. Manickam, S. Madhu, R. E. Fernandez, C. Viswanathan, S. Bhansali, Fabric Based Wearable Biosensor for Continuous Monitoring of Steroids. *ECS Trans.* **77**, 1841–1846 (2017).

161. T. Guinovart, M. Parrilla, G. A. Crespo, F. X. Rius, F. J. Andrade, Potentiometric sensors using cotton yarns, carbon nanotubes and polymeric membranes. *Analyst*. **138**, 5208 (2013).

162. S. Wu, P. Liu, Y. Zhang, H. Zhang, X. Qin, Flexible and conductive nanofiber-structured single yarn sensor for smart wearable devices. *Sensors Actuators B Chem.* **252**, 697–705 (2017).

163. R. Kumar *et al.*, All-Printed, Stretchable Zn-Ag $_2$ O Rechargeable Battery via Hyperelastic Binder for Self-Powering Wearable Electronics. *Adv. Energy Mater.* **7**, 1602096 (2017).

164. M. E. Payne, A. Zamarayeva, V. I. Pister, N. A. D. Yamamoto, A. C. Arias, Printed, Flexible Lactate Sensors: Design Considerations Before Performing On-Body Measurements. *Sci. Rep.* **9**, 13720 (2019).

165. W. Zhang *et al.*, *Small*, in press, doi:10.1002/smll.201500783.

166. Y. Hu *et al.*, A Binder-Free and Free-Standing Cobalt Sulfide@Carbon Nanotube Cathode Material for Aluminum-Ion Batteries. *Adv. Mater.* **30**, 1703824 (2018).

167. S. Luo *et al.*, Binder-Free $LiCoO_2$ /Carbon Nanotube Cathodes for High-Performance Lithium Ion Batteries. *Adv. Mater.* **24**, 2294–2298 (2012).

168. Z.-D. Huang *et al.*, Self-assembled reduced graphene oxide/carbon nanotube thin films as electrodes for supercapacitors. *J. Mater. Chem.* **22**, 3591 (2012).

169. Y. Yang, J. Li, D. Chen, J. Zhao, A Facile Electrophoretic Deposition Route to the Fe_3O_4 /CNTs/rGO Composite Electrode as a Binder-Free Anode for Lithium Ion Battery. *ACS Appl. Mater. Interfaces*. **8**, 26730–26739 (2016).

170. Z. Khan *et al.*, Hierarchical urchin-shaped α-MnO2 on graphene-coated carbon microfibers: a binder-free electrode for rechargeable aqueous Na–air battery. *NPG Asia Mater.* **8**, e294–e294 (2016).

171. B. N. Joshi *et al.*, Flexible, Freestanding, and Binder-free SnO_x –ZnO/Carbon Nanofiber Composites for Lithium Ion Battery Anodes. *ACS Appl. Mater. Interfaces*. **8**, 9446–9453 (2016).

172. D. Sun *et al.*, New Binder-Free Metal Phosphide-Carbon Felt Composite Anodes for Sodium-Ion Battery. *Adv. Energy Mater.* **8**, 1801197 (2018).

173. A. K. Roy *et al.*, Preparation of a Binder-Free Three-Dimensional Carbon Foam/Silicon Composite as Potential Material for Lithium Ion Battery Anodes. *ACS Appl. Mater. Interfaces*. **8**, 7343–7348 (2016).

174. M. Li, R. Carter, A. Douglas, L. Oakes, C. L. Pint, Sulfur Vapor-Infiltrated 3D Carbon Nanotube Foam for Binder-Free High Areal Capacity Lithium–Sulfur Battery Composite Cathodes. *ACS Nano*. **11**, 4877–4884 (2017).

175. Z. Khan *et al.*, Carambola-shaped VO_2 nanostructures: a binder-free air electrode for an aqueous Na–air battery. *J. Mater. Chem. A*. **5**, 2037–2044 (2017).

176. Y. Khan, A. E. Ostfeld, C. M. Lochner, A. Pierre, A. C. Arias, Monitoring of Vital Signs with Flexible and Wearable Medical Devices. *Adv. Mater.* **28**, 4373–4395 (2016).

177. C. M. Lochner, Y. Khan, A. Pierre, A. C. Arias, All-organic optoelectronic sensor for pulse oximetry. *Nat. Commun.* **5**, 5745 (2014).

178. R. Xu *et al.*, Fabric-based stretchable electronics with mechanically optimized designs and prestrained composite substrates. *Extrem. Mech. Lett.* **1**, 120–126 (2014).

179. S. R. Steinhubl, E. D. Muse, E. J. Topol, The emerging field of mobile health. *Sci. Transl. Med.* **7**, 283rv3 (2015).

180. A. M. Gaikwad, A. C. Arias, D. A. Steingart, Recent Progress on Printed Flexible Batteries: Mechanical Challenges, Printing Technologies, and Future Prospects. *Energy*

Technol. **3**, 305–328 (2015).

181. W. Zeng *et al.*, Fiber-based wearable electronics: A review of materials, fabrication, devices, and applications. *Adv. Mater.* **26**, 5310–5336 (2014).
182. S.-Y. Lee *et al.*, Progress in flexible energy storage and conversion systems, with a focus on cable-type lithium-ion batteries. *Energy Environ. Sci.* **6**, 2414–2423 (2013).
183. K. Jost, G. Dion, Y. Gogotsi, Textile energy storage in perspective. *J. Mater. Chem. A*. **2**, 10776 (2014).
184. H. Lin *et al.*, Twisted aligned carbon nanotube/silicon composite fiber anode for flexible wire-shaped lithium-ion battery. *Adv. Mater.* **26**, 1217–1222 (2014).
185. J. Ren *et al.*, Elastic and Wearable Wire-Shaped Lithium-Ion Battery with High Electrochemical Performance. *Angew. Chemie*. **126**, 7998–8003 (2014).
186. S. Berchmans *et al.*, An epidermal alkaline rechargeable Ag-Zn printable tattoo battery for wearable electronics. *J. Mater. Chem. A*, 15788–15795 (2014).
187. P. G. Balakrishnan, R. Ramesh, T. Prem Kumar, Safety mechanisms in lithium-ion batteries. *J. Power Sources*. **155**, 401–414 (2006).
188. K. Braam, V. Subramanian, A Stencil Printed, High Energy Density Silver Oxide Battery Using a Novel Photopolymerizable Poly(acrylic acid) Separator. *Adv. Mater.* **27**, 689–694 (2015).
189. C. Yan *et al.*, Stretchable silver-zinc batteries based on embedded nanowire elastic conductors. *Adv. Energy Mater.* **4**, 1–6 (2014).
190. A. P. Karpinski, B. Makovetski, S. J. Russell, J. R. Serenyi, D. C. Williams, Silver–zinc: status of technology and applications. *J. Power Sources*. **80**, 53–60 (1999).
191. K. Raeissi, A. Saatchi, M. A. Golozar, Effect of nucleation mode on the morphology and texture of electrodeposited zinc. *J. Appl. Electrochem.* **33**, 635–642 (2003).
192. J. W. Gallaway *et al.*, A Lateral Microfluidic Cell for Imaging Electrodeposited Zinc near the Shorting Condition. *J. Electrochem. Soc.* **157**, A1279 (2010).
193. M. Chamoun *et al.*, Hyper-dendritic nanoporous zinc foam anodes. *NPG Asia Mater.* **7**, e178 (2015).
194. A. Lewandowski, K. Skorupska, J. Malinska, Novel poly (vinyl alcohol)– KOH – H 2 O alkaline polymer electrolyte. *Solid Sate Ionics*. **133**, 265–271 (2000).
195. C. C. Yang, Chemical composition and XRD analyses for alkaline composite PVA polymer electrolyte. *Mater. Lett.* **58**, 33–38 (2004).
196. A. A. Mohamad, A. K. Arof, Effect of storage time on the properties of PVA-KOH alkaline solid polymer electrolyte system. *Ionics (Kiel).* **12**, 57–61 (2006).
197. J. W. Gallaway *et al.*, An In Situ Synchrotron Study of Zinc Anode Planarization by a Bismuth Additive. *J. Electrochem. Soc.* **161**, A275–A284 (2013).
198. A. M. Gaikwad, H. N. Chu, R. Qeraj, A. M. Zamarayeva, D. A. Steingart, Reinforced Electrode Architecture for a Flexible Battery with Paperlike Characteristics. *Energy*

Technol. **1**, 177–185 (2013).

199. P. Arora, Z. (John) Zhang, Battery Separators. *Chem. Rev.* **104**, 4419–4462 (2004).
200. P. Suresh, D. H. Nagaraju, A. K. Shukla, N. Munichandraiah, Analysis of ac impedance of AgO-Zn cells: effects of state-of-charge, temperature and cycle-life. *Electrochim. Acta*. **50**, 3262–3272 (2005).
201. J.-P. Randin, Determination of state-of-discharge of zinc-silver oxide button cells. III. In situ impedance measurements of each electrode. *J. Appl. Electrochem.* **15**, 591–601 (1985).
202. J. Benavente, M. I. Vazquez, J. de Abajo, Effect of UV Light on Different Structural and Transport Parameters of Cellophane Membranes. *Sep. Sci. Technol.* **31**, 189–199 (1996).
203. B. Miller, Rotating Ring-Disk Study of the Silver Electrode in Alkaline Solution. *J. Electrochem. Soc.* **117**, 491 (1970).
204. R. F. Amlie, P. Rüetschi, Solubility and Stability of Silver Oxides in Alkaline Electrolytes. *J. Electrochem. Soc.* **108**, 813 (1961).
205. A. M. Gaikwad, J. W. Gallaway, D. Desai, D. A. Steingart, Electrochemical-Mechanical Analysis of Printed Silver Electrodes in a Microfluidic Device. *J. Electrochem. Soc.* **158**, A154 (2011).
206. Y. Shen, K. Kordesch, The mechanism of capacity fade of rechargeable alkaline manganese dioxide zinc cells. *J. Power Sources*. **87**, 162–166 (2000).
207. I. Manke *et al.*, In situ investigation of the discharge of alkaline Zn–MnO[sub 2] batteries with synchrotron x-ray and neutron tomographies. *Appl. Phys. Lett.* **90**, 214102 (2007).
208. J. W. Gallaway *et al.*, Real-time materials evolution visualized within intact cycling alkaline batteries. *J. Mater. Chem. A*. **2**, 2757 (2014).
209. C. P. Wales, The Microstructure of Sintered Silver Electrodes. *J. Electrochem. Soc.* **118**, 7 (1971).
210. C. P. Wales, The Microstructure of Sintered Silver Electrodes. *J. Electrochem. Soc.* **118**, 1021 (1971).
211. I. V Formation, P. Wales, OF THE SOCIETY TECHNOLOGY of AgO during Charges The Microstructure of Sintered Silver Electrodes, 1021–1026 (1971).
212. Y. Khan, A. E. Ostfeld, C. M. Lochner, A. Pierre, A. C. Arias, Monitoring of Vital Signs with Flexible and Wearable Medical Devices. *Adv. Mater.* **28**, 4373–4395 (2015).
213. Z. Song *et al.*, Kirigami-based stretchable lithium-ion batteries. *Sci. Rep.* **5**, 10988 (2015).
214. Z. Song *et al.*, Origami lithium-ion batteries. *Nat. Commun.* **5**, 1–6 (2014).
215. S. Xu *et al.*, Stretchable batteries with self-similar serpentine interconnects and integrated wireless recharging systems. *Nat. Commun.* **4**, 1543 (2013).
216. Y. Zhang *et al.*, Mechanics of ultra-stretchable self-similar serpentine interconnects. *Acta Mater.* **61**, 7816–7827 (2013).
217. C. Lv, H. Yu, H. Jiang, Archimedean spiral design for extremely stretchable

interconnects. *Extrem. Mech. Lett.* **1**, 29–34 (2014).

218. T. Gupta *et al.*, Improving the cycle life of a high-rate, high-potential aqueous dual-ion battery using hyper-dendritic zinc and copper hexacyanoferrate. *J. Power Sources*. **305**, 22–29 (2016).

219. H. L. Lewis, S. P. Wharton, in *The Twelfth Annual Battery Conference on Applications and Advances* (IEEE; http://ieeexplore.ieee.org/document/574089/), pp. 111–119.

220. A. Himy, Separators for high-rate, non-reserve zinc-silver oxide batteries. *Tech. Rep. ECOM-0310-1* (1967), (available at http://oai.dtic.mil/oai/oai?verb=getRecord&metadataPrefix=html&identifier=AD0665631).

221. A. P. Karpinski, B. Makovetski, S. J. Russell, J. R. Serenyi, D. C. Williams, Silver–zinc: status of technology and applications. *J. Power Sources*. **80**, 53–60 (1999).

222. J. D. MacKenzie, C. Ho, Perspectives on Energy Storage for Flexible Electronic Systems. *Proc. IEEE*. **103**, 535–553 (2015).

223. A. E. Ostfeld, A. M. Gaikwad, Y. Khan, A. C. Arias, High-performance flexible energy storage and harvesting system for wearable electronics. *Sci. Rep.* **6**, 26122 (2016).

224. S. Devan, V. R. Subramanian, R. E. White, Analytical Solution for the Impedance of a Porous Electrode. *J. Electrochem. Soc.* **151**, A905 (2004).

225. R. Ahmed, K. Reifsnider, in *ASME 2010 8th International Fuel Cell Science, Engineering and Technology Conference: Volume 2* (ASME, 2010; http://proceedings.asmedigitalcollection.asme.org/proceeding.aspx?articleid=1610599), pp. 167–175.

226. T. P. Dirkse, A potentiostatic study of the electrolytic formation of AgO. *Electrochim. Acta*. **34**, 647 (1989).

227. Y. Khan, A. E. Ostfeld, C. M. Lochner, A. Pierre, A. C. Arias, Monitoring of Vital Signs with Flexible and Wearable Medical Devices. *Adv. Mater.* **28**, 4373–4395 (2016).

228. S. L. Swisher *et al.*, Impedance sensing device enables early detection of pressure ulcers in vivo. *Nat. Commun.* **6**, 6575 (2015).

229. T. R. Ray *et al.*, Bio-Integrated Wearable Systems: A Comprehensive Review. *Chem. Rev.* **119**, 5461–5533 (2019).

230. Y. Liu, M. Pharr, G. A. Salvatore, Lab-on-Skin: A Review of Flexible and Stretchable Electronics for Wearable Health Monitoring. *ACS Nano*. **11**, 9614–9635 (2017).

231. J. R. Corea *et al.*, Screen-printed flexible MRI receive coils. *Nat. Commun.* **7**, 10839 (2016).

232. C. M. Lochner, Y. Khan, A. Pierre, A. C. Arias, All-organic optoelectronic sensor for pulse oximetry. *Nat. Commun.* **5**, 5745 (2014).

233. A. E. Ostfeld, A. C. Arias, Flexible photovoltaic power systems: integration opportunities, challenges and advances. *Flex. Print. Electron.* **2**, 013001 (2017).

234. Z. Wang, Z. Wu, N. Bramnik, S. Mitra, Fabrication of High-Performance Flexible

Alkaline Batteries by Implementing Multiwalled Carbon Nanotubes and Copolymer Separator. *Adv. Mater.* **26**, 970–976 (2014).

235. A. M. Gaikwad, D. A. Steingart, T. Nga Ng, D. E. Schwartz, G. L. Whiting, A flexible high potential printed battery for powering printed electronics. *Appl. Phys. Lett.* **102**, 233302 (2013).
236. W. Qiu *et al.*, High-performance flexible quasi-solid-state Zn–MnO_2 battery based on MnO_2 nanorod arrays coated 3D porous nitrogen-doped carbon cloth. *J. Mater. Chem. A*. **5**, 14838–14846 (2017).
237. Y. Zeng *et al.*, Achieving Ultrahigh Energy Density and Long Durability in a Flexible Rechargeable Quasi-Solid-State Zn-MnO_2 Battery. *Adv. Mater.* **29**, 1700274 (2017).
238. H.-W. Zhu *et al.*, Dip-coating processed sponge-based electrodes for stretchable Zn-MnO2 batteries. *Nano Res.* **11**, 1554–1562 (2018).
239. M. Kaltenbrunner, G. Kettlgruber, C. Siket, R. Schwödiauer, S. Bauer, Arrays of Ultracompliant Electrochemical Dry Gel Cells for Stretchable Electronics. *Adv. Mater.* **22**, 2065–2067 (2010).
240. G. Kettlgruber *et al.*, Intrinsically stretchable and rechargeable batteries for self-powered stretchable electronics. *J. Mater. Chem. A*. **1**, 5505 (2013).
241. G. M. Wu, S. J. Lin, C. C. Yang, Preparation and characterization of PVA/PAA membranes for solid polymer electrolytes. *J. Memb. Sci.* **275**, 127–133 (2006).
242. G. M. Wu, S. J. Lin, C. C. Yang, Alkaline Zn-air and Al-air cells based on novel solid PVA/PAA polymer electrolyte membranes. *J. Memb. Sci.* **280**, 802–808 (2006).
243. Z. Wang, X. Meng, Z. Wu, S. Mitra, Development of flexible zinc–air battery with nanocomposite electrodes and a novel separator. *J. Energy Chem.* **26**, 129–138 (2017).
244. J.-W. Rhim, M.-Y. Sohn, H.-J. Joo, K.-H. Lee, Pervaporation separation of binary organic-aqueous liquid mixtures using crosslinked PVA membranes. I. Characterization of the reaction between PVA and PAA. *J. Appl. Polym. Sci.* **50**, 679–684 (1993).
245. J. Song *et al.*, Interpenetrated Gel Polymer Binder for High-Performance Silicon Anodes in Lithium-ion Batteries. *Adv. Funct. Mater.* **24**, 5904–5910 (2014).
246. B. J. Hertzberg *et al.*, Effect of Multiple Cation Electrolyte Mixtures on Rechargeable Zn–MnO_2 Alkaline Battery. *Chem. Mater.* **28**, 4536–4545 (2016).
247. A. Kozawa, R. A. Powers, The Manganese Dioxide Electrode in Alkaline Electrolyte; The Electron-Proton Mechanism for the Discharge Process from MnO[sub 2] to MnO[sub 1.5]. *J. Electrochem. Soc.* **113**, 870 (1966).
248. S. W. Donne, G. A. Lawrance, D. A. J. Swinkels, Redox Processes at the Manganese Dioxide Electrode. *J. Electrochem. Soc.* **144**, 2949 (1997).
249. A. Kozawa, J. F. Yeager, Cathodic Reduction Mechanism of MnOOH to Mn(OH)[sub 2] in Alkaline Electrolyte. *J. Electrochem. Soc.* **115**, 1003 (1968).
250. D. Boden, C. J. Venuto, D. Wisler, R. B. Wylie, The Alkaline Manganese Dioxide Electrode. *J. Electrochem. Soc.* **114**, 415 (1967).

251. J. W. Gallaway *et al.*, Operando identification of the point of [Mn2]O4 spinel formation during γ-MnO2 discharge within batteries. *J. Power Sources*. **321**, 135–142 (2016).

252. S. W. Donne, G. A. Lawrance, D. A. J. Swinkels, Redox Processes at the Manganese Dioxide Electrode. *J. Electrochem. Soc.* **144**, 2954 (1997).

253. B. J. Hertzberg *et al.*, Effect of Multiple Cation Electrolyte Mixtures on Rechargeable Zn–MnO_2 Alkaline Battery. *Chem. Mater.* **28**, 4536–4545 (2016).

254. S. W. Donne, J. H. Kennedy, Electrochemical impedance spectroscopy of the alkaline manganese dioxide electrode. *J. Appl. Electrochem.* **34**, 159–168 (2004).

255. B. J. Landi, M. J. Ganter, C. D. Cress, R. A. DiLeo, R. P. Raffaelle, Carbon nanotubes for lithium ion batteries. *Energy Environ. Sci.* **2**, 638 (2009).

256. † Brian J. Landi *et al.*, Single Wall Carbon Nanotube−Nafion Composite Actuators (2002), doi:10.1021/NL025800H.

257. J. Ning, J. Zhang, Y. Pan, J. Guo, Surfactants assisted processing of carbon nanotube-reinforced SiO2 matrix composites. *Ceram. Int.* **30**, 63–67 (2004).

258. Y. Y. Huang, T. P. J. Knowles, E. M. Terentjev, Strength of nanotubes, filaments and nanowires from sonication-induced scission (2009) (available at http://arxiv.org/abs/0907.3176).

259. Y. Y. Huang, E. M. Terentjev, Y. Y. Huang, E. M. Terentjev, Dispersion of Carbon Nanotubes: Mixing, Sonication, Stabilization, and Composite Properties. *Polymers (Basel).* **4**, 275–295 (2012).

260. A. Kozawa, The Potential of the Manganese Dioxide Electrode and the Surface Composition of the Oxide. *J. Electrochem. Soc.* **106**, 79 (1959).

261. Z. Sonner *et al.*, The microfluidics of the eccrine sweat gland, including biomarker partitioning, transport, and biosensing implications. *Biomicrofluidics*. **9**, 031301 (2015).

262. P. J. Derbyshire, H. Barr, F. Davis, S. P. J. Higson, Lactate in human sweat: a critical review of research to the present day. *J. Physiol. Sci.* **62**, 429–440 (2012).

263. M. F. Bergeron, Heat cramps: Fluid and electrolyte challenges during tennis in the heat. *J. Sci. Med. Sport*. **6**, 19–27 (2003).

264. R. A. Robergs, F. Ghiasvand, D. Parker, Biochemistry of exercise-induced metabolic acidosis. *Am. J. Physiol. Regul. Integr. Comp. Physiol.* **287**, R502–R516 (2004).

265. D. Czarnowski, J. Langfort, W. Pilis, J. Gorski, Effect of a low-carbohydrate diet on plasma and sweat ammonia concentrations during prolonged nonexhausting exercise. *Eur. J. Appl. Physiol. Occup. Physiol.* **70**, 70–74 (1995).

266. D. Czarnowski, J. Gorski, J. Jozwiuk, a. Boron-Kaczmarska, Plasma ammonia is the principal source of ammonia in sweat. *Eur. J. Appl. Physiol. Occup. Physiol.* **65**, 135–137 (1992).

267. H. Liu, J. Deng, An amperometric lactate sensor employing tetrathiafulvalene in nafion film as electron shutle. *Electrochim. Acta*. **40**, 1845–1849 (1995).

268. B. Kowalewska, P. J. Kulesza, Application of Tetrathiafulvalene-Modified Carbon

Nanotubes to Preparation of Integrated Mediating System for Bioelectrocatalytic Oxidation of Glucose. *Electroanalysis*. **21**, 351–359 (2009).

269. A. MULCHANDANI, A. S. BASSI, A. NGUYEN, Tetrathiafulvalene-mediated Biosensor for L-lactate in Dairy Products. *J. Food Sci.* **60**, 74–78 (1995).
270. A. Weltin *et al.*, Polymer-based, flexible glutamate and lactate microsensors for in vivo applications. *Biosens. Bioelectron.* **61**, 192–199 (2014).
271. H. Liu, J. Deng, An amperometric lactate sensor employing tetrathiafulvalene in Nafion film as electron shuttle. *Electrochim. Acta*. **40**, 1845–1849 (1995).
272. J. Tkac, J. W. Whittaker, T. Ruzgas, The use of single walled carbon nanotubes dispersed in a chitosan matrix for preparation of a galactose biosensor. *Biosens. Bioelectron.* **22**, 1820–1824 (2007).
273. A. J. Bard, L. R. Faulkner, *Electrochemical methods : fundamentals and applications* (Wiley, 2001; https://www.wiley.com/en-us/Electrochemical+Methods%3A+Fundamentals+and+Applications%2C+2nd+Edition-p-9780471043720).
274. M. Alvarez-Icaza, U. Bilitewski, Mass production of biosensors. *Anal. Chem.* **65**, 525A-533A (1993).
275. D. S. Bindra *et al.*, Design and in vitro studies of a needle-type glucose sensor for subcutaneous monitoring. *Anal. Chem.* **63**, 1692–1696 (1991).
276. M. Ammam, J. Fransaer, Highly sensitive and selective glutamate microbiosensor based on cast polyurethane/AC-electrophoresis deposited multiwalled carbon nanotubes and then glutamate oxidase/electrosynthesized polypyrrole/Pt electrode. *Biosens. Bioelectron.* **25**, 1597–1602 (2010).
277. R. F. B. Turner, D. J. Harrison, R. V. Rajotte, H. P. Baltes, A biocompatible enzyme electrode for continuous in vivo glucose monitoring in whole blood. *Sensors Actuators B Chem.* **1**, 561–564 (1990).
278. J. M. Goran, J. L. Lyon, K. J. Stevenson, Amperometric Detection of l -Lactate Using Nitrogen-Doped Carbon Nanotubes Modified with Lactate Oxidase. *Anal. Chem.* **83**, 8123–8129 (2011).
279. I. A. Ges, F. Baudenbacher, Enzyme electrodes to monitor glucose consumption of single cardiac myocytes in sub-nanoliter volumes. *Biosens. Bioelectron.* **25**, 1019–24 (2010).
280. D. P. Hickey, R. C. Reid, R. D. Milton, S. D. Minteer, A self-powered amperometric lactate biosensor based on lactate oxidase immobilized in dimethylferrocene-modified LPEI. *Biosens. Bioelectron.* **77**, 26–31 (2016).
281. J. Trzebinski *et al.*, Hydrogel Membrane Improves Batch-to-Batch Reproducibility of an Enzymatic Glucose Biosensor. *Electroanalysis*. **23**, 2789–2795 (2011).
282. S. Munari, A. Bottino, G. Capannelli, Casting and performance of polyvinylidene fluoride based membranes. *J. Memb. Sci.* **16**, 181–193 (1983).
283. T. Guinovart, G. A. Crespo, F. X. Rius, F. J. Andrade, A reference electrode based on polyvinyl butyral (PVB) polymer for decentralized chemical measurements. *Anal. Chim.*

Acta. **821**, 72–80 (2014).

284. P. Yu *et al.*, Flexible Zn-Ion Batteries: Recent Progresses and Challenges. *Small*. **15**, 1804760 (2019).
285. B. Son *et al.*, Measurement and Analysis of Adhesion Property of Lithium-Ion Battery Electrodes with SAICAS. *ACS Appl. Mater. Interfaces*. **6**, 526–531 (2014).
286. A. J. Blake *et al.*, Creasable Batteries: Understanding Failure Modes through Dynamic Electrochemical Mechanical Testing. *ACS Appl. Mater. Interfaces*. **8**, 5196–5204 (2016).
287. A. M. Gaikwad, A. C. Arias, Understanding the Effects of Electrode Formulation on the Mechanical Strength of Composite Electrodes for Flexible Batteries. *ACS Appl. Mater. Interfaces*. **9**, 6390–6400 (2017).
288. H. Li, Z. Tang, Z. Liu, C. Zhi, Evaluating Flexibility and Wearability of Flexible Energy Storage Devices. *Joule*. **3**, 613–619 (2019).